Magnetic Properties and Photoluminescence in 3d–4f and in 4f Complexes

Zur Erlangung des akademischen Grades eines
DOKTORS DER NATURWISSENSCHAFTEN
(Dr. rer. nat.)
von der KIT-Fakultät für Chemie und Biowissenschaften
des Karlsruher Instituts für Technologie
genehmigte
DISSERTATION
von

M. Eng., Zhaoyang Jing

1. Referent: Prof. Dr. Mario Ruben

2. Referentin: Prof. Dr. Annie K. Powell

Tage der mündlichen Prüfung: 14.07.2025

Eidesstattliche Erklärung

Eidesstattliche Versicherung gemäß §.13 Absatz 2 Ziffer 3 der Promotionsordnung des Karlsruher Instituts für Technologie für die KIT-Fakultät für Chemie und Biowissenschaften:

1. Bei der eingereichten Dissertation zu dem Thema “Researchs on Structures and Magnetic Properties of Dysprosium Dinuclear Single Molecular Magnets” handelt es sich um meine eigenständig erbrachte Leistung.
2. Ich habe nur die angegebenen Quellen und Hilfsmittel benutzt und mich keiner unzulässigen Hilfe Dritter bedient. Insbesondere habe ich wörtlich oder sinngemäß aus anderen Werken übernommene Inhalte als solche kenntlich gemacht.
3. Die Arbeit oder Teile davon habe ich bislang nicht an einer Hochschule des In- oder Auslands als Bestandteil einer Prüfungs- oder Qualifikationsleistung vorgelegt.
4. Die Richtigkeit der vorstehenden Erklärung bestätige ich.
5. Die Bedeutung der eidesstattlichen Versicherung und die strafrechtlichen Folgen einer unrichtigen oder unvollständigen eidesstattlichen Versicherung sind mir bekannt.

Ich versichere an Eides statt, dass ich nach bestem Wissen die reine Wahrheit erklärt und nichts verschwiegen habe.

....

Ort und Datum Unterschrift

Contents

Abstract

Lanthanide elements have gained significant importance in modern technology due to their fascinating physical properties, including magnetism and luminescence. Lanthanide-based complexes are individual molecules comprised of lanthanide ions and organic ligands. The structural homogeneity, monodispersity of molecular material, and tunability through ligand engineering make them promising candidates for device applications. As luminescent materials, the unique f–f or d–f electronic transitions facilitate their use in OLEDs, bioimaging and anti-counterfeiting technologies. The magnetic anisotropy arising from spin–orbit coupling and crystal field effects enables certain lanthanide complexes to exhibit single-molecule magnet (SMM) behaviour, offering potential for applications in high-density data storage, molecular spintronics and quantum information processing. Furthermore, lanthanide complexes integrating both luminescence and SMM properties enable multifunctional devices, as they not only exhibit different properties within a single-phase material, but also facilitate significant interactions between these properties. Obtaining more lanthanide complexes with novel structures and thoroughly investigating their magnetic and optical properties can deepen understanding of structure–property relationships, thereby guiding the design of advanced molecular materials. The experimental section of the thesis is divided into three chapters, with the main content of each chapter as follows:

In Chapter 2, a series of isostructural $[Ln(NiL)_2]CF_3SO_3$ (**Ln_1**) complexes featuring linear Ni–Ln–Ni array have been synthesized, where L was a tripodal Schiff base ligand—tris(((2-hydroxy-3-methoxybenzyl)-amino)ethyl)amine. Direct current (DC) and alternating current (AC) magnetic susceptibility measurements were performed on these complexes to understand their magnetic properties. The role of Ni–Dy couplings on SMM property was further studied by a comparative study between **Dy_1** and its isostructural **$DyZn_2$** analog. Magnetic properties of **Y_1**, **Gd_1**, **Tb_1**, **Dy_1**, **Ho_1**, **Er_1** and **Yb_1** were further investigated using micro-SQUID. Open hysteresis loops were observed for **Gd_1**, **Tb_1**, **Dy_1**, **Ho_1**, and related to the intramolecular ferromagnetic couplings between Ni and the corresponding Ln ions.

Five additional Ni–Dy–Ni trinuclear complexes, $[Dy(NiL)_2]PF_6$ (**Dy_2**), $[Dy(NiL)_2]NO_3{\cdot}2H_2O{\cdot}3CH_3OH$ (**Dy_3**), $[Dy(NiL)_2]Cl{\cdot}4CH_3OH$ (**Dy_4**), $[Dy(NiL)_2]ClO_4{\cdot}2.5\,CH_3OH$ (**Dy_5**) and $[Dy(NiL)_2]BPh_4{\cdot}CH_3OH$ (**Dy_6**), differing in the counter-anions and lattice solvents, were synthesized by introducing salts containing different corresponding anions. Comparative studies across **Dy_1** – **Dy_6** demonstrated the influence of counter-anions on the molecular structures and the magnetic properties of these complexes, including the slow magnetic relaxation behaviours under both zero field and applied optimal fields.

In Chapter 3, the terminal Ni^{II} ions in **Dy_1** were successfully substituted with other divalent metal ions (Co^{II}, Fe^{II}, Zn^{II} and Mg^{II}) yielding new complexes $[Ln(CoL)_2CF_3SO_3]$ (**$LnCo_2$**, Ln = Y, Gd, Tb, Dy), $[Ln(FeL)_2CF_3SO_3]$ (**$LnFe_2$**, Ln = Y, Gd, Tb, Dy),

$Ln(ZnL)_2CF_3SO_3$ (**LnZn$_2$**, Ln = Ce, Pr, Nd, Sm, Eu, Gd, Tb, Dy) and $Ln(MgL)_2CF_3SO_3$ (**LnMg$_2$**, Ln = Pr, Nd, Sm, Eu, Gd). DC and AC magnetic studies were performed to explore the static and dynamic magnetic properties of the complexes on **LnCo$_2$** and **LnFe$_2$**. Ferromagnetic intramolecular Ln–Co/Fe couplings have been revealed in **GdCo$_2$**, **TbCo$_2$**, **DyCo$_2$** and **GdFe$_2$**. **GdCo$_2$**, **TbCo$_2$** and **DyCo$_2$** showed slow magnetic relaxations in the absence of applied magnetic field. Meanwhile, **YCo$_2$** turned out to be a field-induced SMM. Optical measurements performed on the solid-state samples of **LnZn$_2$** and **LnMg$_2$** revealed Ln^{III}-centered luminescence from **CeZn$_2$**, **NdMg$_2$**, **SmZn$_2$** and **SmMg$_2$** at room temperature. Significantly, intense Eu^{III}-centered emission in **EuZn$_2$** and **EuMg$_2$** was exclusively observed in the cryogenic temperature regime, a phenomenon attributed to the switching role of LMCT band.

In Chapter 4, a series of binuclear Ln(III) complexes—**Ln$_2$_MeCN** (Ln = Y, La, Ce, Pr, Nd, Sm, Eu, Gd, Tb, Dy, Ho)—composed of neutral Hbpp ligands (Hbpp = 3(5)-pyridine-1*H*-pyrazole) were synthesized. At room temperature, **Ce$_2$_MeCN**, **Sm$_2$_MeCN**, **Eu$_2$_MeCN**, **Tb$_2$_MeCN**, and **Dy$_2$_MeCN** exhibited their characteristic Ln^{III}-centered visible light emissions, while near infrared (NIR) emission was detected in **Nd$_2$_MeCN**. Notably, **Dy$_2$_MeCN** exhibited field-induced SMM behaviour and the crystal field splitting of eight Kramers doublets of the $^6H_{15/2}$ ground state was obtained from the high-resolution emission spectrum of the complex at 3.0 K. Two tetranuclear complexes **Dy$_4$_NO$_3$** and **Dy$_4$_Cl** with the deprotonated bpp^- anions as ligands were obtained under different reaction conditions. The tetranuclear complexes exhibited slow relaxation of magnetization under zero field. Their distinct SMM behaviours as well as that of **Dy$_2$_MeCN** were confirmed both through *ab initio* calculations and by structure-property relationships.

Zusammenfassung

Lanthanidelemente haben aufgrund ihrer faszinierenden physikalischen Eigenschaften, einschließlich Magnetismus und Lumineszenz, in der modernen Technologie an großer Bedeutung gewonnen. Lanthanidbasierte Komplexe sind Einzelmoleküle, die aus Lanthanidionen und organischen Liganden bestehen. Die strukturelle Homogenität, Monodispersität des molekularen Materials und die Anpassungsfähigkeit durch Ligandendesign machen sie zu vielversprechenden Kandidaten für den Einsatz in technischen Anwendungen. Als lumineszierende Materialien ermöglichen die einzigartigen f–f- oder d–f-Elektronenübergänge ihren Einsatz in OLEDs, der Bioimaging-Technologie und bei der Fälschungssicherung. Die magnetische Anisotropie, die aus dem Spin-Bahn-Kopplungseffekt und den Kristallfeldwirkungen resultiert, ermöglicht es bestimmten Lanthanidkomplexen, sich wie Einzelmolekülmagneten (SMMs) zu verhalten, was Potenzial für Anwendungen in der Hochdichtedatenspeicherung, der molekularen Spintronik und der Quanteninformationsverarbeitung bietet. Darüber hinaus ermöglichen Lanthanidkomplexe, die sowohl Lumineszenz- als auch SMM-Eigenschaften integrieren, multifunktionale Geräte, da sie nicht nur verschiedene Eigenschaften in einem einkristallinen Material aufweisen, sondern auch bedeutende Wechselwirkungen zwischen diesen Eigenschaften erleichtern. Die Gewinnung weiterer Lanthanidkomplexe mit neuartigen Strukturen und die eingehende Untersuchung ihrer magnetischen und optischen Eigenschaften können das Verständnis von Struktur-Eigenschafts-Beziehungen vertiefen und somit die Entwicklung fortschrittlicher molekularer Materialien leiten.

Der experimentelle Teil der Arbeit ist in drei Kapitel gegliedert, deren Hauptinhalte wie folgt zusammengefasst sind:

In Kapitel 2 wurde eine Serie isostruktureller $[Ln(NiL)_2]CF_3SO_3$ (**Ln_1**)-Komplexe mit linearer Ni–Ln–Ni-Anordnung synthetisiert, wobei L ein tripodal aufgebauter Schiff-Base-Ligand war – Tris(((2-Hydroxy-3-methoxybenzyl)-amino)ethyl)amin. Gleichstrom- (DC) und Wechselstrom- (AC) magnetische Suszeptibilitätsmessungen wurden durchgeführt, um die magnetischen Eigenschaften dieser Komplexe zu untersuchen. Die Rolle der Ni–Dy-Kopplung für das SMM-Verhalten wurde durch einen Vergleich zwischen **Dy_1** und seinem isostrukturellen **$DyZn_2$**-Analogon weiter untersucht. Die magnetischen Eigenschaften von **Y_1**, **Gd_1**, **Tb_1**, **Dy_1**, **Ho_1**, **Er_1** und **Yb_1** wurden zudem mittels Mikro-SQUID analysiert. Offene Hystereseschleifen wurden für **Gd_1**, **Tb_1**, **Dy_1** und **Ho_1** beobachtet und auf intramolekulare ferromagnetische Kopplungen zwischen Ni und den entsprechenden Ln-Ionen zurückgeführt.

Fünf weitere trinukleare Ni–Dy–Ni-Komplexe, $[Dy(NiL)_2]PF_6$ (**Dy_2**), $[Dy(NiL)_2]NO_3 \cdot 2H_2O \cdot 3CH_3OH$ (**Dy_3**), $[Dy(NiL)_2]Cl \cdot 4CH_3OH$ (**Dy_4**), $[Dy(NiL)_2]ClO_4 \cdot 2.5CH_3OH$ (**Dy_5**) und $[Dy(NiL)_2]BPh_4 \cdot CH_3OH$ (**Dy_6**), die sich in Gegenionen und Gitterlösemitteln unterscheiden, wurden durch Einführung verschiedener

Anionsalze hergestellt. Vergleichende Untersuchungen von **Dy_1** bis **Dy_6** zeigten den Einfluss der Gegenionen auf die molekulare Struktur und die magnetischen Eigenschaften dieser Komplexe, einschließlich langsamer magnetischer Relaxationsverhalten unter Nullfeld und optimal angelegtem Feld.

In Kapitel 3 wurden die terminalen Ni^{II}-Ionen in **Dy_1** erfolgreich durch andere zweiwertige Metallionen (Co^{II}, Fe^{II}, Zn^{II} und Mg^{II}) ersetzt, was zur Bildung neuer Komplexe führte: $[Ln(CoL)_2CF_3SO_3]$ (**LnCo$_2$**, Ln = Y, Gd, Tb, Dy), $[Ln(FeL)_2CF_3SO_3]$ (**LnFe$_2$**, Ln = Y, Gd, Tb, Dy), $Ln(ZnL)_2CF_3SO_3$ (**LnZn$_2$**, Ln = Ce, Pr, Nd, Sm, Eu, Gd, Tb, Dy) und $Ln(MgL)_2CF_3SO_3$ (**LnMg$_2$**, Ln = Pr, Nd, Sm, Eu, Gd). DC- und AC-magnetische Messungen wurden durchgeführt, um die statischen und dynamischen magnetischen Eigenschaften der **LnCo$_2$**- und **LnFe$_2$**-Komplexe zu untersuchen. In **GdCo$_2$**, **TbCo$_2$**, **DyCo$_2$** und **GdFe$_2$** wurden ferromagnetische intramolekulare Ln–Co/Fe-Kopplungen festgestellt. **GdCo$_2$**, **TbCo$_2$** und **DyCo$_2$** zeigten langsame magnetische Relaxationen ohne angelegtes Magnetfeld. **YCo$_2$** erwies sich als feldinduziertes SMM. Optische Messungen an Festkörperproben von **LnZn$_2$** und **LnMg$_2$** zeigten Ln^{III}-zentrierte Lumineszenz bei Raumtemperatur in **CeZn$_2$**, **NdMg$_2$**, **SmZn$_2$** und **SmMg$_2$**. Besonders intensiv war die Eu^{III}-zentrierte Emission in **EuZn$_2$** und **EuMg$_2$** im kryogenen Temperaturbereich, was auf die Schaltwirkung des LMCT-Bandes zurückgeführt wurde.

In Kapitel 4 wurde eine Serie binuklearer Ln^{III}-Komplexe – **Ln$_2$_MeCN** (Ln = Y, La, Ce, Pr, Nd, Sm, Eu, Gd, Tb, Dy, Ho) – mit neutralen Hbpp-Liganden (Hbpp = 3(5)-Pyridin-1*H*-pyrazol) synthetisiert. Bei Raumtemperatur zeigten **Ce$_2$_MeCN**, **Sm$_2$_MeCN**, **Eu$_2$_MeCN**, **Tb$_2$_MeCN** und **Dy$_2$_MeCN** ihre charakteristische Ln^{III}-zentrierte Lumineszenz im sichtbaren Bereich, während in **Nd$_2$_MeCN** Nahinfrarot-(NIR)-Emission beobachtet wurde. Besonders hervorzuheben ist das feldinduzierte SMM-Verhalten von **Dy$_2$_MeCN**. Die Kristallfeldaufspaltung der acht Kramers-Dubletts des $^6H_{15/2}$-Grundzustands wurde aus dem hochauflösenden Emissionsspektrum des Komplexes bei 3,0 K bestimmt. Zwei tetranukleare Komplexe, **Dy$_4$_NO$_3$** und **Dy$_4$_Cl**, mit deprotonierten bpp^--Anionen als Liganden wurden unter unterschiedlichen Reaktionsbedingungen erhalten. Diese tetranuklearen Komplexe zeigten eine langsame Relaxation der Magnetisierung im Nullfeld. Die unterschiedlichen SMM-Eigenschaften sowohl dieser Komplexe als auch von **Dy$_2$_MeCN** wurden sowohl durch ab-initio-Berechnungen als auch durch Struktur-Eigenschafts-Beziehungen bestätigt.

Chapter 1. Background

The objective of this chapter is to provide a brief introduction to the historical context and foundational knowledge relevant to the research topic explored in this thesis, and also to present recent advancements and emerging trends within the field. Furthermore, key experimental techniques and analytical methodologies utilized in the study are discussed here in order to provide a framework for interpreting the experimental findings and research conclusions.

1.1 Lanthanide elements and lanthanide complexes

The lanthanide elements, also known as the lanthanide metals or lanthanides (Ln), are a group of 15 metallic elements with atomic numbers ranging from 57 (lanthanum, La) to 71 (lutetium, Lu). As they are characterized by the progressive filling of their 4f electron orbitals, lanthanide elements are also referred to as 4f elements.

The 15 lanthanide metals plus two transition metal elements scandium (Sc) and yttrium (Y) from Group 3 of the periodic table are also collectively known as the rare earth elements (REEs) (Figure 1.1). This classification stems from their similar chemical properties and the tendency to coexist in mineral deposits. REEs exist primarily in the form of oxides in natural minerals, which is why they are referred to as "earth". Meanwhile, REEs are rarely found in concentrated deposits and difficult to extract in pure form due to their geochemical affinity.[1] In fact, the name "lanthanide" stems from lanthanum, the first element in the series, which itself is derived from the Greek word *lanthanein*, meaning "to lie hidden", highlighting the difficulty in isolating these elements. In addition, many REEs were first discovered in relatively uncommon minerals and therefore historically labelled as "rare". Nevertheless, lanthanides are not as rare as one might think. In fact, cerium (Ce), the most abundant lanthanide, is more plentiful in the Earth's crust than copper, while neodymium (Nd) and lanthanum (La) are more abundant than nickel. Table 1.1 lists the estimated abundance of lanthanides in the Earth's crust.[2] The abundance of promethium (Pm) is not included since Pm is radioactive and extremely rare, with all the isotopes being unstable.

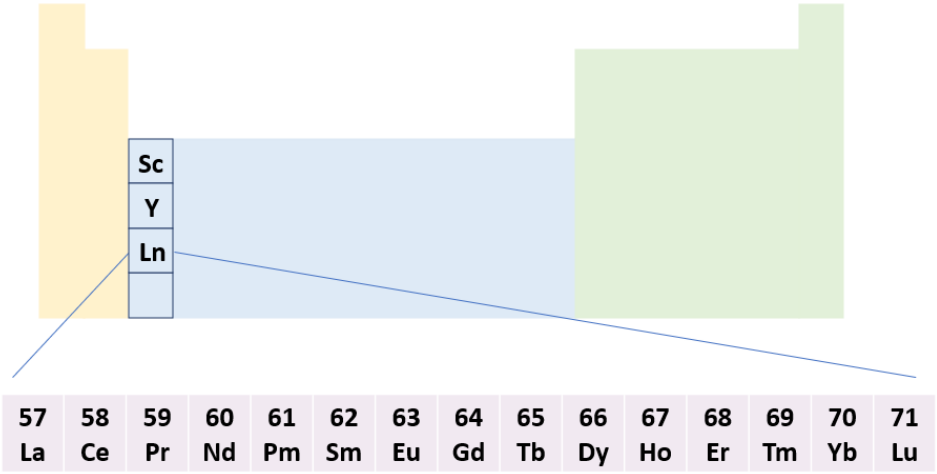

Figure 1.1 lanthanide series in the periodic table.

Table 1.1. Lanthanide elements and the estimated abundance (in mg/kg) in the Earth's crust.

La	Ce	Pr	Nd	Sm	Eu	Gd	Tb	Dy	Ho	Er	Tm	Yb	Lu
39	66.5	9.2	41.5	7.05	2	6.2	1.2	5.2	1.3	3.5	0.52	3.2	0.8

The general electronic configuration of a lanthanide atom is $[Xe]4f^n6s^2$, where $n = Z - 56$ (Z: atomic number), starting from Pr with $n = 3$. La, Ce, Gd and Lu are exceptions to the rule as their electron configurations taking the form of $[Xe]4f^{n-1}5d^16s^2$ (Table 1.2). The progressive filling of the 4f electron orbitals across lanthanide series leads to a gradual decrease in atomic radii from La (187.9 pm) to Lu (173.5 pm). This contraction arises because 4f electrons provide only incomplete shielding of the outer electrons from the steadily increasing nuclear charge. Notably, Eu and Yb atoms deviate significantly from this trend due to their unique electronic configurations. With their 4f orbitals being half-filled and full-filled respectively, Eu and Yb have only two 6s valence electrons in the conduction band, whereas the other lanthanide metals have three valence electrons in the 5d/6s conduction band. Therefore, the metallic bonding in Eu and Yb are much weaker, leading to larger atomic radii than the other lanthanides in the metallic state.

Table 1.2. Electron configurations and radii of lanthanide atoms and their trivalent ions.

Element	Atoms (Ln^0)		Trivalent ions (Ln^{III})	
	Electronic configuration	Radius (pm)	Electronic configuration	Radius (pm)
La	$[Xe]5d^16s^2$	187.9	[Xe]	116.0
Ce	$[Xe]4f^15d^16s^2$	182.5	$[Xe]4f^1$	114.3
Pr	$[Xe]4f^36s^2$	182.8	$[Xe]4f^2$	112.6
Nd	$[Xe]4f^46s^2$	182.1	$[Xe]4f^3$	110.9
Pm	$[Xe]4f^56s^2$	(181.0)	$[Xe]4f^4$	(109.5)
Sm	$[Xe]4f^66s^2$	180.4	$[Xe]4f^5$	107.9
Eu	$[Xe]4f^76s^2$	204.2	$[Xe]4f^6$	106.6
Gd	$[Xe]4f^75d^16s^2$	180.1	$[Xe]4f^7$	105.3
Tb	$[Xe]4f^96s^2$	178.3	$[Xe]4f^8$	104.0
Dy	$[Xe]4f^{10}6s^2$	177.4	$[Xe]4f^9$	102.7
Ho	$[Xe]4f^{11}6s^2$	176.6	$[Xe]4f^{10}$	101.5
Er	$[Xe]4f^{12}6s^2$	175.7	$[Xe]4f^{11}$	100.4
Tm	$[Xe]4f^{13}6s^2$	174.6	$[Xe]4f^{12}$	99.4
Yb	$[Xe]4f^{14}6s^2$	193.9	$[Xe]4f^{13}$	98.5
Lu	$[Xe]4f^{14}5d^16s^2$	173.5	$[Xe]4f^{14}$	97.7
Y	$[Kr]4d^15s^2$	180.1	[Kr]	101.9

The +3 oxidation state is the most common and stable ionic state for lanthanides. As shown in Table 1.2, the radii of Ln^{III} also exhibit a steady decrease across the series, same as their atom radii. The consistent reduction in both atomic and ionic radii known are as lanthanide contraction, a key feature which influences not only the physical and chemical properties of lanthanide elements but also post-lanthanide elements. For instance, this causes the 5d transition metals to have smaller atomic radii than they would without this effect, making their sizes comparable to those of the corresponding 4d transition metals. In addition, lanthanide contraction results in ionic radii of lanthanide metals, especially dysprosium and holmium, being close to that of yttrium, as shown in Table 1.2. This similarity enables yttrium ions to substitute for lanthanide metals in various compounds.

Although +3 oxidation state is dominant in lanthanide chemistry, other oxidation states are also accessible. Divalent lanthanide molecules have been reported for the entire series (except for Pm).[3] Eu^{II} is the most stable divalent ion, due to its half-filled $4f^7$ configuration, followed by Yb^{II}, Sm^{II} and Tm^{II}. On the other hand, Ce^{IV} and Tb^{IV} are the most common tetravalent ions.[4-6] While the half-filled $4f^7$ configuration contributes to the stability of Tb^{IV}, the high energy of 4f orbitals at the beginning of the lanthanide series facilitates the oxidation of Ce^{III}

to Ce^{IV}. Recently, the discovery of a molecule complex featuring Pr^{IV} marks a significant achievement in the exploration of non-trivalent lanthanide compounds.[7]

Lanthanides have a wide range of applications in various sectors owing to their unique magnetic, luminescent, and catalytic properties, among others.[8] For example, Ce-based catalysts are used in automotive catalytic converters and modern petroleum refining, Er is an essential ingredient in fiber optics for information transmission, Eu and Tb are widely used in light emitting diodes (LEDs) and display screens, Sm–Co and Nd–Fe–B strong permanent magnets are critical components of modern machinery, such as wind turbines. The crucial role played by lanthanides in advanced technologies has earned them the reputation of being the "vitamins of modern industry". Besides lanthanide alloys, oxides, and additives, lanthanide-based coordination complexes have also gained significant importance in modern technology. A prominent example is Gd complexes used as magnetic resonance imagery (MRI) contrast agents.[9] The unique advantage of lanthanide coordination complexes, including molecular-level tunability, structural homogeneity, monodispersity, enables precise design and fine-tuning of desired properties, making them versatile for applications.

Trivalent lanthanide ions are classified as hard Lewis acids due to their high charge density and relatively small ionic radii (particularly for heavy lanthanides). They prefer bonding with hard Lewis bases such as O and N. ligands like β-diketones, carboxylates, bipyridine and Schiff bases are therefore widely used in lanthanide complexes, whereas soft bases ligands with S- or P-donors are much less common, though not entirely absent.

The hard Lewis acid nature of Ln^{III} favors predominantly electrostatic interactions over covalent interactions with ligands, resulting in ionic bonds which lack directionality. Combined with the fact that the 4f orbitals are significantly shielded by outer $5s^2 5p^6$ electrons, lanthanide complexes exhibit weak geometry preference. This contrasts starkly with transition metals complexes where strong ligand field effects favor specific coordination configurations, such as octahedral for Cu^{II} and planar square for Ni^{II}. In addition, the high charge density facilitates the attraction of more ligands and mitigates the electrostatic repulsion between them, allowing for high coordination numbers. The coordination numbers are usually 8–10 for light Ln^{III} ions (La to Eu) and 7–9 for heavy Ln^{III} ions (Gd to Lu).

Selecting appropriate ligands to tune the structure of lanthanide complexes is crucial for obtaining compounds with excellent magnetic and optical properties. This is primarily because these properties are directly related to the energy level structure of lanthanide ions, which, in addition to being determined by the type of lanthanide ion itself, is also influenced by the ligand field.

The 4f orbitals of lanthanide ions exhibit strong angular dependence and are well-shielded by outer 5s and 5p orbitals. As a result, lanthanide ions retain a large unquenched orbital angular momentum, in contrast to transition-metal complexes, where strong ligand fields often lead to the quenching of orbital contributions. Furthermore, since the strength of spin–orbit coupling (SOC) is proportional to Z^4 (Z: atomic number), lanthanide ions exhibit extremely strong SOC.

As the SOC is much stronger than the crystal field effect, the total angular momentum quantum number *J*, derived from Russell-Saunders coupling (*L*-*S* coupling), becomes the primary quantum number for describing lanthanide ions, rather than the individual orbital angular momentum *L* and spin angular momentum *S*.

Atomic and ionic energy levels of lanthanide ions are characterized by a term symbol of the general form $^{2S+1}L_J$, where *J* can take any integer value between *L*+*S* and |*L*−*S*|. The energy of $^{2S+1}L_J$ is calculated as follows:

$$E(^{2s+1}L_J) = \left(\frac{\lambda}{2}\right)[J(J+1) - L(L+1) - S(S+1)] \qquad \text{Equation 1.1}$$

where λ is the spin–orbit coupling constant, and adopts + sign applies for lanthanides with less-than-half-filled shells and − sign for those with more-than-half-filled shells. The ground states are therefore determined to be $J = L-S$ for light lanthanides and $J = L+S$ for heavy lanthanides. The ground states for trivalent lanthanide ions are listed in Table 1.3. Gd^{3+} present quenched orbital momentum ($L = 0$). For La^{III} and Lu^{III}, both *L* and *S* equal to zero, as they do not process unpaired f electrons.

Table 1.3. $^{2S+1}L_J$ ground state for each trivalent lanthanide ion.

Ce	Pr	Nd	Pm	Sm	Eu	Gd	Tb	Dy	Ho	Er	Tm	Yb
$^2F_{5/2}$	$^3H_4$	$^4I_{9/2}$	$^5I_4$	$^6H_{5/2}$	$^7F_0$	$^8S_{7/2}$	$^7F_6$	$^6H_{15/2}$	$^5I_8$	$^4I_{15/2}$	$^3H_6$	$^2F_{7/2}$

The ground states are in line with the Hund's rule: 1. *S* takes the maximum value compatible with the Pauli exclusion principle; 2. *L* takes the maximum value as far as allowed by rule (1); 3. *J* takes the lowest possible value for lanthanide ions when the shell is less than half-filled, and the highest possible for those with a shell more than half-filled. For each Ln^{III}, the $^{2S+1}L_J$ ground state is well separated from the excited states (> 1500 cm^{-1}) with the only exceptions being Eu^{III} (ca. 300 cm^{-1}) and to a less extent, Sm^{III} (ca. 1000 cm^{-1}).

Compared to SOC, the crystal field effect is weaker and causes much less energy splitting (on the order of 10^2 cm^{-1}). Therefore, it is typically viewed as a perturbation on the energy splitting caused by SOC (Figure 1.2).[10] The perturbation lifts the degeneracy of $^{2S+1}L_J$ states, resulting in M_J sub-levels, also known as Stark sublevels. M_J corresponds to the azimuthal projection of *J*, taking integer values from $-J$ to *J*. The splitting between M_J sub-levels is typically comparable to thermal energy, leading to temperature dependant behaviours. The influence of crystal field on the magnetic and photophysical properties will be discussed in the upcoming chapters.

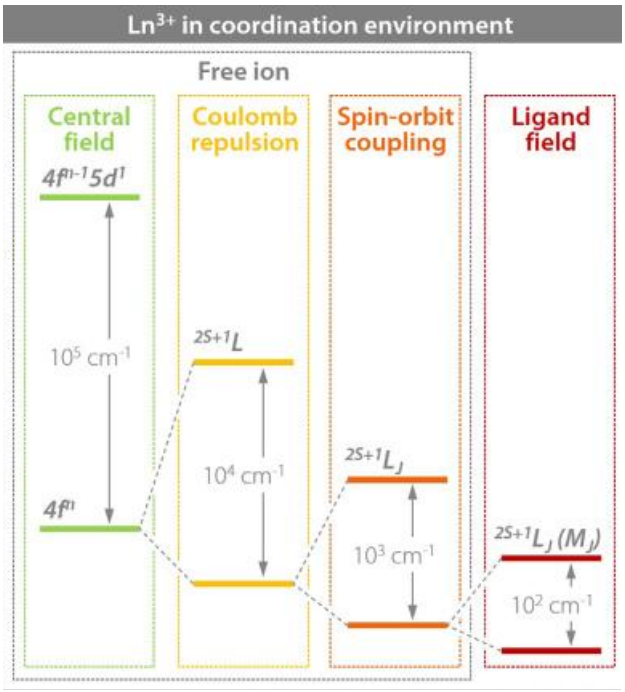

Figure 1.2 Contributions of different factors on the energy diagram of Ln^{III}. Reused with permission from reference 10, copyright Wiley-VCH Verlag GmbH & Co. KGaA.

1.2 Molecular magnetism and the role of lanthanide elements

1.2.1 Introduction of single-molecule magnets

Single-molecule magnets, as the name suggests, are magnets composed of individual molecules. Thousands of years ago, humans discovered naturally occurring magnetite and utilized it for navigation, divination, and other activities. In modern times, various inorganic magnetic materials such as alloys and ferrites have been developed and applied to multiple industrial fields including mechanical control and mineral processing. Following the advent of the first programmable general-purpose computer, ENIAC, in 1945, magnetic disks emerged as information storage devices and gradually gained widespread use. To date, although solid-state drives (SSDs) based on integrated circuits have become popular due to their higher read/write speeds, mechanical hard drives with magnetic media still hold an irreplaceable position in large-scale data storage thanks to their low cost and high storage density.

However, as the size of individual storage units in hard drives decreases, quantum effects become increasingly pronounced, pushing the storage density ever closer to its physical limits.[11] In recent years, the growth rate of storage capacity in individual hard drives has slowed down, falling below the pace predicted by Moore's Law. Single-molecule magnets exhibit similar hysteresis phenomena to traditional inorganic magnetic materials, meaning that

they tend to retain their magnetization after being magnetized. The difference lies in that the magnetism of single-molecule magnets stems from the quantum properties of individual complex molecules rather than macroscopic behaviour of aggregates. These structurally-uniform molecules can each form a separate nanoscale magnetic domain, allowing the dimensions of magnetic recording units to be reduced by tens to thousands of times in theory. Furthermore, manipulating the quantum behaviour of single-molecule magnets could lead to the development of spintronic devices such as molecular transistors and molecular spin valves, or quantum bits which are essential component for quantum computers.[12,13] In summary, due to their unique quantum properties and small physical dimensions, SMMs may play a significant role in the future of the information industry.

Slow magnetic relaxation behaviour is the hallmark characteristic of SMMs. Relaxation refers to the gradual process through which a physical system returns to its equilibrium state. In SMMs, magnetic relaxation primarily originates from individual molecules. These molecules exhibit a bistable state with equal magnetization magnitudes but opposite directions (magnetic quantum numbers $M_S = \pm S$), in the absence of an external magnetic field. The magnetic moments of the molecules are equally distributed between these two states, resulting in a net magnetization of zero (Figure 1.3).[14]

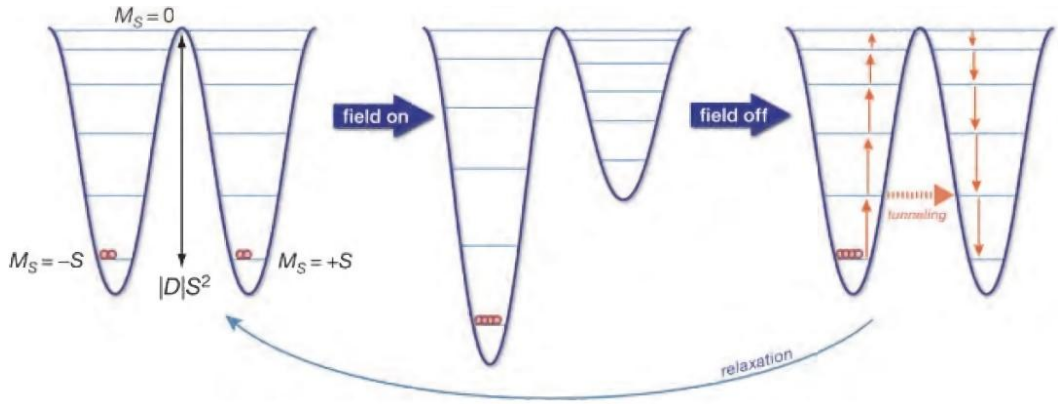

Figure 1.3. The double-well potential diagram of SMMs, and the illustration of magnetic relaxation process. Reused with permission from reference 14, copyright Royal Society of Chemistry.

When an external magnetic field is applied, the Zeeman effect splits the degenerate magnetic energy levels. The *Ms* states aligned parallel to the external magnetic field ($-S$) become lower in energy and more populated than the corresponding states aligned antiparallel to the external magnetic field ($+S$). As a result, the single-molecule magnet exhibits a non-zero magnetization, becoming magnetized.

Upon removal of the external magnetic field, the Zeeman splitting disappears, and $M_{\pm s}$ states become degenerate again. Some molecules in the $-S$ state will transition back to the $+S$ state. During this re-equilibration process, the molecules must overcome the energy barrier depicted in the double-well potential diagram. If the thermal energy of the system (k_BT) is

significantly higher than this energy barrier, the magnetic moments of the molecules can flip-flop rapidly. Otherwise, the flipping slows down, leading to the phenomenon of slow relaxation of magnetization.

The slow relaxation behaviour of single-molecule magnets is typically investigated through alternating current (AC) magnetic susceptibility experiments. When an alternating magnetic field is applied, if the magnetic relaxation time of the single-molecule magnet is shorter than the alternating period, the magnetic moment of the sample changes in-phase with the ac field. If the relaxation time is longer than the alternating period, the sample cannot keep up with the oscillation rate of the magnetic field, resulting in the non-zero out-of-phase magnetic susceptibility. According to the generalized Debye model[15], the ac magnetic susceptibility, expressed as a complex number χ_{AC}, is related to the relaxation time τ and the angular frequency of the ac magnetic field ω as:

$$\chi_{AC} = \chi_S + \frac{\chi_T - \chi_S}{1+(i\omega\tau)^{1-\alpha}} \qquad \text{Equation 1.2}$$

where χ_S stands for the adiabatic magnetic susceptibility, χ_T denotes the isothermal magnetic susceptibility, and α represents the degree of distribution of the relaxation time, ranging from 0 to 1, with larger values indicating broader distributions. The experimentally obtained χ_{AC} is given in the form of the in-phase component (χ') and the out-of-phase component (χ''), corresponding to its real part and imaginary part, respectively. Software such as CCFIT[16] or CCFIT2[17,18] can calculate the relaxation time τ based on the aforementioned equation. After obtaining relaxation times at various temperatures, the effective energy barrier U_{eff} of the single-molecule magnet can be determined using the Arrhénius formula:

$$\tau = \tau_0 \times \exp(U_{\text{eff}}/k_{\text{B}}T) \qquad \text{Equation 1.3}$$

where τ_0 is the pre-exponential factor, and k_{B} is the Boltzmann constant.

The effective energy barrier U_{eff} merely serves as an apparent representation of the energy required for relaxation. The actual relaxation processes in single-molecule magnets comprise phonon-dependent spin-lattice relaxations and quantum tunneling of magnetization which does not involve participation of phonons. The former can be further divided into the Orbach relaxation process, the Raman relaxation process, and the direct relaxation process, as shown in Equation 1.4:

$$\tau^{-1} = AT + CT^n + {\tau_0}^{-1}\exp\left(-\frac{U}{k_B T}\right) \qquad \text{Equation 1.4}$$

where the terms on the right side of the equation represent direct process, Raman process, and Orbach process, in sequence.[19]

When the flipping rate of the molecular magnetic moment is slower than the frequency of the applied alternating magnetic field, the spin system cannot fully catch up the changes in the magnetic field, causing the spin energy to transfer to the lattice through the spin-lattice relaxation process, and the system remains in a non-equilibrium state. Among these processes, both the Orbach process and the Raman process involve the participation of two phonons, but their mechanisms differ (Figure 1.4).[20] In the Raman process, the spin system undergoes non-

resonant phonon scattering, absorbing one phonon to reach a virtual intermediate state instead of a real energy level, and then emitting another phonon to return to the steady state. In contrast, the Orbach process involves absorbing one phonon to excite to a real intermediate state, and then emitting another phonon to decay back to the ground state energy level. The direct process occurs between energy levels with small energy differences, where the system undergoes magnetic moment reversal by absorbing or emitting a single phonon that matches the energy difference between the levels. For Kramers ions, such as Dy^{III} and Er^{III}, where the ground-state spin quantum numbers (M_J) are half-integers, the direct process is suppressed due to the presence of Kramers degeneracy under zero field.

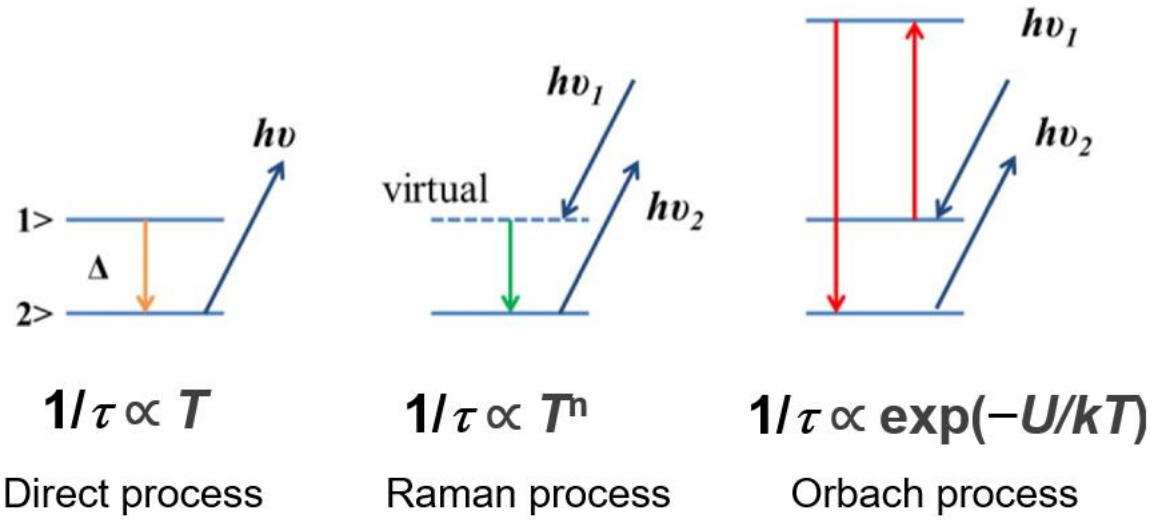

Figure 1.4. The phonon transfer and the relaxation time - temperature correlation in three types of spin-lattice relaxation. Reproduced with permission from reference 20, copyright Elsevier.

Quantum tunneling occurs between energy states that are equal in energy and have overlapping wave functions.[21] As quantum mechanics reveals, particles can tunnel directly between overlapping wave functions without the need for energy-driven transitions. In SMMs, the quantum tunneling of magnetization (QTM) refers to the magnetic moment changes its orientation by tunneling through an energy barrier, rather than going over it by thermal activation. Therefore, QTM functions as a "barrier-free channel" for the reversal of magnetic moment in single-molecule magnets, which can effectively reduce the observed effective energy barrier and even completely quench slow relaxation behaviour. In the absence of an external magnetic field, QTM can occur between degenerate spin states, e.g., $M_S = +S$ and $M_S = -S$. When an external magnetic field is applied, the Zeeman effect lifts the degeneracy of spin, thereby suppressing QTM. However, external magnetic fields with certain strengths can induce new quantum tunneling channels, e.g., the level crossing between $M_S = +S$ and $M_S = -(S-1)$, leading to enhanced QTM. This is particularly common in systems with dense multi-energy states due to hyperfine interactions from nuclear spins. Additionally, other factors that cause energy level crossings can also enhance QTM, such as the mixing of low-lying excited states into the ground state, hyperfine couplings, large transverse magnetic

anisotropy, and dipole-dipole interactions between neighboring spin carriers (see Chapter 1.2.3).

It is worth emphasizing that, although in Equation 1.4, the Orbach process term takes a form similar to the Arrhénius formula used to calculate the effective energy barrier, the two should not be simply conflated. This is because, in the former, the energy barrier U represents a gap between the ground state and a real excited state, including the excited M_J sublevels (e.g., Dy^{III}, Tb^{III}), SOC-induced excited states (e.g., Co^{II}, Fe^{III}) and exchange states in multi-spin systems. On the other hand, the effective energy barrier U_{eff} extracted by fitting τ versus T is lower than the energy barrier between the ground state and the first excited state for some SMMs. This suggests the presence of other relaxation processes, with or without the coexistence of the Orbach process. In high-performance SMMs, U_{eff} can be higher than the energy barrier between the ground state and the first excited state, indicating the occurrence of Orbach process through higher-order excited state(s).[22] Therefore, to enhance the effective energy barrier of SMMs, one can either increase the energy of the excited state reached by the Orbach process or suppress quantum tunneling and reduce the weakening of the energy barrier by other detrimental relaxation processes.

In the past thirty years, a large number of SMMs have been synthesized and studies. The major categories of them are introduced below.

1.2.2 Major categories of single-molecule magnets

Transition-metal based SMMs

In 1993, R. Sessoli and co-workers first discovered the single-molecule magnet behaviour in $\{Mn_{12}Ac\}$ (Figure 1.5), marking a significant milestone in the molecular magnetism.[23] Following this breakthrough, a series of polynuclear cluster-based SMMs composed of transition metals were subsequently identified, such as $\{V_4\}$[24], $\{Fe_8\}$[25], $\{Co_4\}$[26] etc. For single-molecule magnets with an integer ground state spin S, the theoretical maximum energy barrier is defined by $U = |D|S^2$ or $U = |D|(S^2-1/4)$ if S is a half-integer (D being the zero-field splitting parameter (ZFS)). In polynuclear cluster single-molecule magnets, the magnetic exchange coupling between transition-metal ions is typically stronger than spin-orbit coupling and the zero-field splitting of the individual transition metals. As a result, the slow magnetic relaxations are the processes of the entire molecular clusters rather than individual metal centers. D and S are thus parameters that describe overall properties of the multinuclear systems. For example, in $\{Mn_{12}Ac\}$, the total ground state spin S equals to 10, and D is approximately $-0.5\ cm^{-1}$, and the spin reversal energy barrier is 61 K. Due to the quadratic relationship, increasing the total spin ground state spins of molecular clusters was a major goal in the early stage of research on single-molecule magnets. In addition, the relatively predictable and controllable intramolecular interaction between transition-metal ions provided a convenient strategy to obtain clusters with large S values through molecular design.

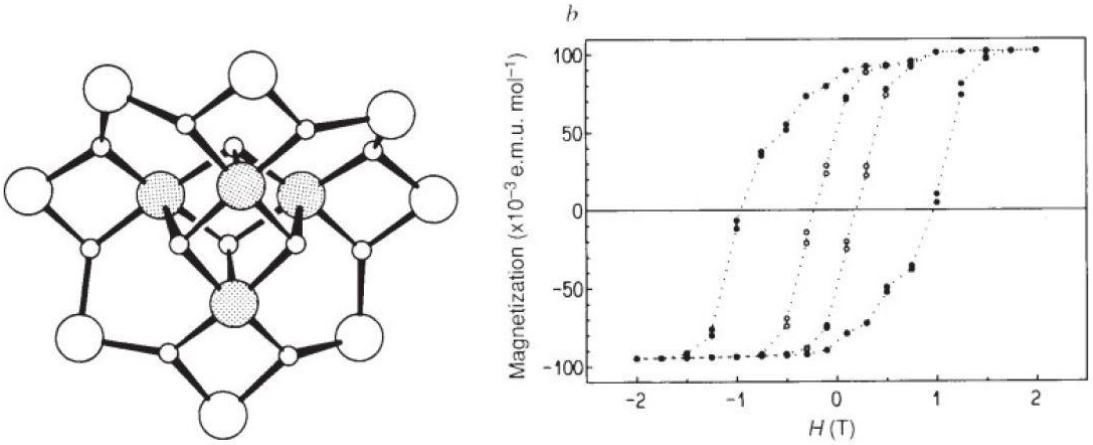

Figure 1.5. Molecular structure of the first SMM, {$Mn_{12}Ac$}, and its hysteresis loops recorded at 2.2 K (●) and 2.8 K (○). Reused with permission from reference 23, copyright Springer Nature.

However, as the nuclearity of molecular clusters increases, larger clusters tend to exhibit higher structural symmetry, which typically results in reduced magnetic anisotropy. Theoretical studies have also revealed that the effect of enhancing S on elevating the energy barrier in SMMs is limited because the ZFS parameter D is proportional to S^{-2}.[14,27] The development of transition-metal cluster SMMs has thus encountered a bottleneck. In 2011, Das et al. synthesized a {Mn_2Ni_3} cluster in which all metal centers were ferromagnetically coupled, resulting in a large total spin (S = 7).[28] However, the D value was only –0.32 cm^{-1}, and the measured effective energy barrier was merely 22 K.

There are also transition-metal SMMs with only one paramagnetic center, the majority of which are Co^{II} compounds. Depending on the sign of the D value, divalent cobalt can exhibit either easy-axis anisotropy (D < 0) or easy-plane anisotropy (D > 0). Co^{II} single-molecular magnets with easy-plane anisotropy exhibit slow magnetic relaxation behaviour only under an applied external magnetic field, classifying them as field-induced single-molecule magnets. In 2018, Hu et al. reported a field-induced single-ion magnet, [$CoL_2(CH_3CH_2O)_2$], with $|D|$ = 72.08 cm^{-1}.[29] Analysis of the EPR spectrum indicated that D is positive, corresponding to easy-plane anisotropy. This compound exhibited the longest relaxation time under a 1500 Oe field, with an effective energy barrier of 43.6 K. In 2016, Pavlov et al. reported two isomeric Co^{II} single-ion magnets, α-Co and β-Co, where the cobalt ions are coordinated in a trigonal prismatic geometry with six nitrogen atoms.[30] The D values for these compounds were –111 cm^{-1} and –74 cm^{-1}, respectively, with zero-field effective energy barriers of 180 cm^{-1} and 109 cm^{-1}.

Some low-valent transition metals can also form SMMs. In 2013, Zadrozny et al. reported a single ion magnet [K(crypt-222)][$Fe(C(SiMe_3)_3)_2$], where the monovalent iron ion is two-coordinated in a nearly perfect linear manner with a C–Fe^{I}–C angle of 179.2(2)° (Figure 1.6).[31] The Fe^{I} ion, with a high spin state of S = 3/2, possesses large unquenched orbital

angular momentum, giving it properties similar to lanthanide-based SMMs and a high energy barrier of U_{eff} = 226 cm^{-1} in a zero field. In 2015, S. Gao and co-workers reported $[Co(IMes)_2][BPh_4]$, which also features a linear, two-coordinate structure. The cobalt ion in this compound is in the +1 oxidation state with a d^8 configuration and S = 1, exhibiting an effective energy barrier of U_{eff} = 21.3 cm^{-1}.[32] Although low-valent, low-coordination transition-metal SMMs have the potential to outperform typical transition-metal- and even some lanthanide-based SMMs, they are generally difficult to prepare and are often sensitive to temperature and air.

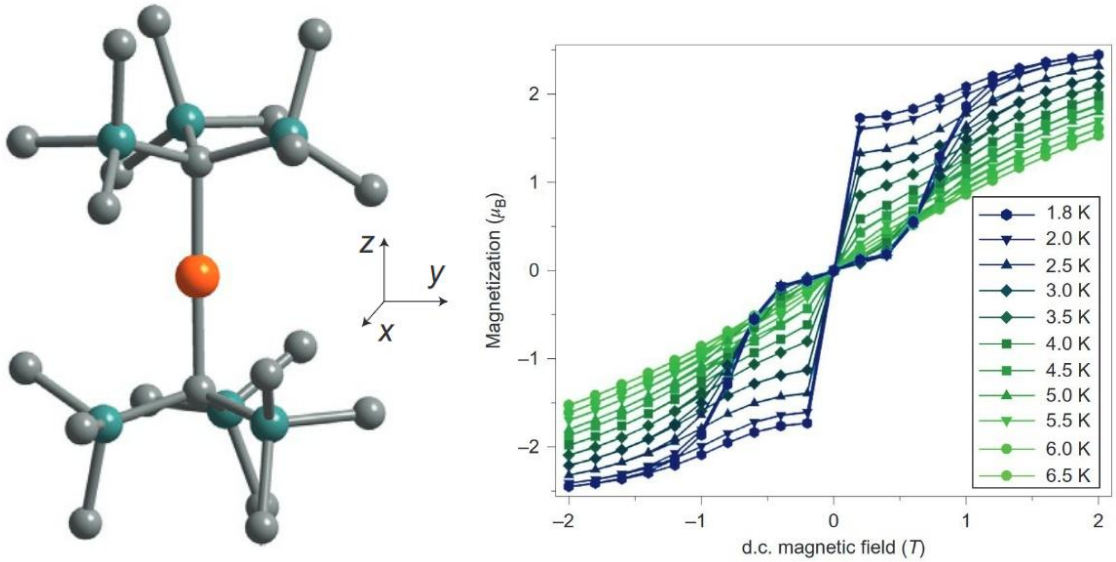

Figure 1.6. The structure of $[Fe(C(SiMe_3)_3)_2]^-$ anion (left), and magnetic hysteresis loops of $[K(crypt\text{-}222)][Fe(C(SiMe_3)_3)_2]$ at different temperatures (right). Reused with permission from reference 31, copyright Springer Nature.

Lanthanide-based SMMs

In 2003, Ishikawa et al. reported the first lanthanide-based SMM, $[NBu_4][TbPc_2]$ (Pc = phthalocyanine), which features a sandwich-like mononuclear structure (Figure 1.7).[33] In this complex, two Pc^{2-} rings each provide four nitrogen atoms to encapsulate the central Tb^{III} ion, creating a square antiprismatic coordination configuration. This compound exhibits a remarkable effective energy barrier U_{eff} of 331 K and demonstrates magnetic hysteresis at 1.7 K. It is also the first single-ion magnet.

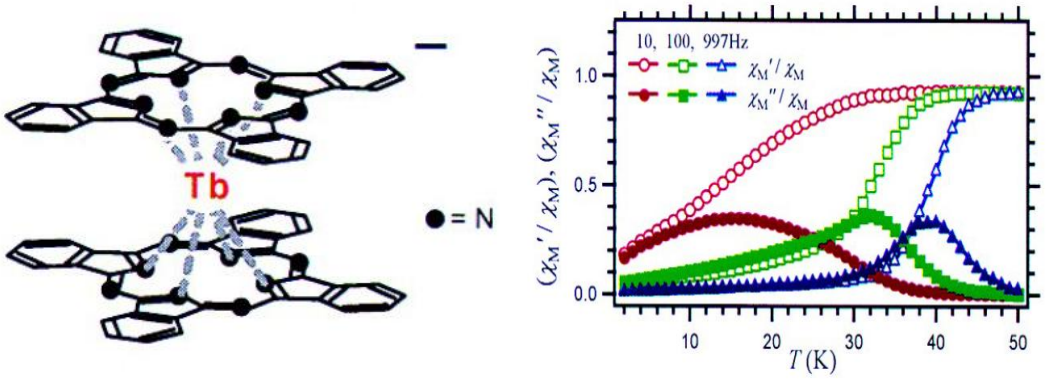

Figure 1.7. The structure of $[TbPc_2]^-$ anion (left), and the temperature dependence of the AC susceptibility of $[NBu_4][TbPc_2]$ at different frequencies (right). Reused with permission from reference 33, copyright American Chemical Society.

Lanthanide ions possess unique 4f electrons that are shielded by outer electron shells, allowing them to retain significant orbital angular momentum that is largely unaffected by external quenching effects. As a result, lanthanide ions can exhibit exceptionally large magnetic moments and substantial magnetic anisotropy. For example, being the most studied lanthanide in SMMs, Dy^{III} possesses a large total angular momentum (J = 15/2) and exhibits strong easy-axis anisotropy under an ideal ligand field, with the $\boldsymbol{g}$ tensor close to (0, 0, 20) in the effective spin S = 1/2 approximation. Additionally, Dy^{III} is a Kramers ion, characterized by the odd number of unpaired electrons (S = 5/2). According to Kramers' theorem, it ensures that the energy levels of Dy^{III} remain at least doubly degenerate in the absence of a magnetic field, regardless of the coordination environment. [34] This inherent degeneracy helps suppress the QTM effect, along with the strong anisotropy. Tb^{III} (J = 6) and Ho^{III} (J = 8) are also common in lanthanide-based SMMs due to their large total angular momenta. However, the non-Kramers nature (S = 3 for Tb^{III}, S = 2 for Ho^{III}) makes them prone to exhibiting large tunnel splitting between the ground pseudo-doublets, resulting in accelerated relaxation via QTM.

The SMM with the highest blocking temperature reported to date is $[(Cp^{iPr5})Dy(Cp^*)][B(C_6F_5)_4]$ (Figure 1.8).[35] This rare-earth metallocene compound exhibits open magnetic hysteresis loops up to 80 K, with an effective energy barrier of 1524 cm^{-1}. Theoretical studies have revealed that in $[(Cp^{iPr5})Dy(Cp^*)][B(C_6F_5)_4]$, not only is the magnetic axis of the ground state doublet aligned along the line connecting the centers of two cyclopentadienyl rings, but also the magnetic axes of the six excited doublet states are highly collinear with the ground state, with a maximum deviation angle of only 5.3°. As a result, the reversal of magnetic moment predominantly occurs through the higher-lying excited doublets rather than the lower-lying ones, leading to a large effective energy barrier. This ground-breaking achievement is of significant importance as it represents the first instance where the blocking temperature of a SMM has been elevated above the liquid nitrogen temperature (78 K) range. This demonstrates the potential for using SMMs to construct quantum computing

memory devices that can operate in the more affordable and accessible liquid nitrogen environment.

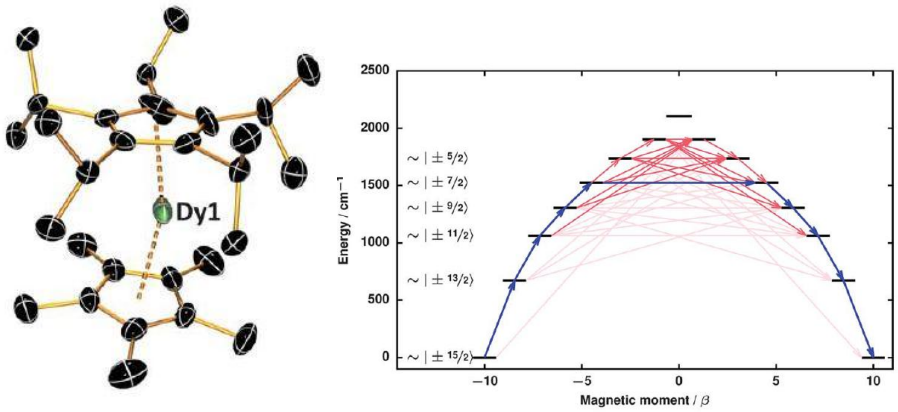

Figure 1.8. Molecular structure of [(Cp^{iPr5})Dy(Cp^*)][$B(C_6F_5)_4$] (left); and the relaxation mechanism (right). Blue arrows show the most probable relaxation route, and red arrows show transitions between states with less probable matrix elements; darker shading indicates a higher probability. Reused with permission from reference 35, copyright the American Association for the Advancement of Science.

The most commonly used metal elements in lanthanide-based SMMs are dysprosium (Dy), terbium (Tb), erbium (Er), and ytterbium (Yb). In recent years, there has been an increasing number of reports on SMMs composed of other lanthanide metal elements. For example, an acetato-bridged palladium-lanthanide tetranuclear heterometallic complex $(Pd_2Sm_2(H_2O)_2(CH_3COO)_{10})\cdot 2CH_3COOH$ reported in the year 2020 is the first samarium-based complex exhibiting slow magnetic relaxation.[36] In the same work, a unique and complete periodicity regarding the Kramers and non-Kramers nature of lanthanides in the slow magnetic relaxation of isostructural lanthanide-based complexes spanning the entire lanthanide series was reported for the first time, i.e., complexes containing Kramers lanthanide ions (Ln^{III} = Ce, Nd, Sm, Dy, Er, Yb) showed field-induced slow magnetic relaxation, characteristics of SMMs. In contrast, all complexes consisted of non-Kramers lanthanide ions (Ln^{III} = Pr, Tb, Ho, Tm) did not show any slow magnetic relaxation.

In addition, lanthanide compounds with unconventional valence states, primarily divalent Ln ions, are also theoretically investigated for their magnetic anisotropies. In the year 2019, two divalent metallocene complexes Ln-(Cp^{iPr5})$_2$ (Ln = Tb, Dy; Cp^{iPr5} = pentaisopropylcyclopentadienyl) were synthesized and characterized as the first ever SMMs based on a divalent lanthanide ion to show magnetic hysteresis.[37] Most notably, Tb-(Cp^{iPr5})$_2$, with Tb^{II} being a Kramers ion, is among the non-dysprosium SMMs presenting the highest spin reversal barriers (U_{eff} = 1205 cm^{-1}) and the highest blocking temperatures (T_B = 52 K), demonstrating the great potential for unconventional-valence lanthanide-based complexes to be candidates of high performance SMMs.

In addition to mononuclear lanthanide complexes, numerous polynuclear lanthanide complexes, including dinuclear ones, have also been investigated extensively for their slow magnetic relaxation properties over the years. The first example of polynuclear lanthanide

SMMs, reported in 2006, is a triangular $[Dy_3(\mu_3\text{-}OH)_2L_3Cl(H_2O)_5]Cl_3$ (L = *o*-vanillin) complex, exhibiting an effective energy barrier U_{eff} of 61.7 K.[38] A $\{Dy_{19}\}$ complex synthesized with tetrazole-functionalized calixarene represents a lanthanide-based SMM with high nuclearity.[39] In most of the polynuclear SMMs, the slow magnetic relaxation property originates from individual lanthanide ions, while the intramolecular interactions between lanthanide ions serve as an influencing factor on it.[40] The effects of them will be discussed later in Chapter 1.2.2.

In some rare cases, lanthanide-based complexes with metal-metal bonds between lanthanide centers showcase slow magnetic relaxation in relatively elevated temperatures. Gould et al. reported mixed-valence dilanthanide complexes $(Cp^{iPr5})_2Ln_2I_3$ (Ln = Gd, Tb, and Dy).[41] The direct metal-metal bond creates a strong exchange interaction pathway, which significantly enhances magnetic anisotropy by aligning the $4f^n$ electrons on two lanthanides to generate a high spin ground state and suppresses the QTM. The overall SMMs performance are thus enhanced with T_B of 72 K for the Dy complex and 65 K for the Tb complex among the highest blocking temperatures revealed for SMMs. Another notable example is the endohedral metallofullerene $Dy_2@C_{82}$ molecule, where a short Dy(II)−Dy(II) σ-bond was demonstrated for the first time.[42] The direct covalent bond induces strong antiferromagnetic coupling between the two divalent Dy^{II} ions, resulting in the highest 4f−4f exchange excited state (33.9 K) observed in Dy-SMMs. Such a strong coupling further leads to open magnetic hysteresis at zero field without an abrupt magnetization loss, along with a high magnetization blocking temperature (T_B) of 27.2 K. These complexes highlight the promising prospect for achieving high-performance dinuclear or polynuclear lanthanide-based SMMs by leveraging strong exchange couplings through metal-metal bonds.

d–f hybrid SMMs

In d–f hybrid single-molecule magnets, both d-block (transition metal) and f-block (lanthanide or actinide) elements coexist. The first d–f hybrid SMMs $[Cu^{II}LLn^{III}(hfac)_2]_2$ (Ln = Dy, Tb; H_3L = 1-(2-hydroxybenzamido)-2-(2-hydroxy-3-methoxy-benzylideneamino)ethane) were reported in 2004, one year after the report of the first lanthanide-based SMM $[NBu_4][TbPc_2]$. Since then, d–f hybrid complexes have always been an importance class of SMMs.[43] The majority of d–f hybrid SMMs consist of 3d transition metals and 4f lanthanide metals, also known as 3d–4f SMMs. Several 4d–4f SMMs and 3d–5f SMMs, e.g., the first 4d–4f SMM $[Ru^{III}_2Dy^{III}_2(OMe)_2(O_2CPh)_4(mdea)_2(NO_3)_2]$[44] and the trinuclear 3d–5f $\{UO_2Mn_2\}$ complex[45], have also been reported, though they are much less common compared to 3d–4f SMMs.

The flourishing of d–f SMMs is partly driven by the demand for structural design. For instance, transition metals can form metallacrowns, creating a high-symmetry coordination environment for the central lanthanide ion. In 2016, M. L. Tong and co-workers reported two d–f field-induced SMMs based on [15-metallacrown-6], i.e., $[LnCd_3(Hquinha)_3(n\text{-}Bu_3PO)_2I_3]\cdot 3EtOH\cdot 2H_2O$ (Ln = Ce; Nd) (Figure 1.9).[46] In this molecule, each of the three Hquinha ligands in the equatorial metallacrown plane bridges two Cd atoms and provides two

oxygen atoms at the 1,4-positions to coordinate with the central lanthanide, forming a structurally stable five-membered ring. The overall coordination geometry is nearly a perfect regular hexagon. The tri-*n*-butylphosphine oxide ligands on both sides of the plane, due to the steric hindrance of the substituents on phosphorus, axially coordinate to the central lanthanide, giving rise to an overall highly regular hexagonal bipyramidal coordination configuration. The O-Ce-O angles in the equatorial plane are 59.63° and 61.00°, while the axial O-Ce-O angle is 178.3°. The Continuous Shape Measures (CShM) value calculated using SHAPE 2.0[47] for the deviation from the D_{6h} symmetry is only 0.456, in line with the high coordination symmetry.

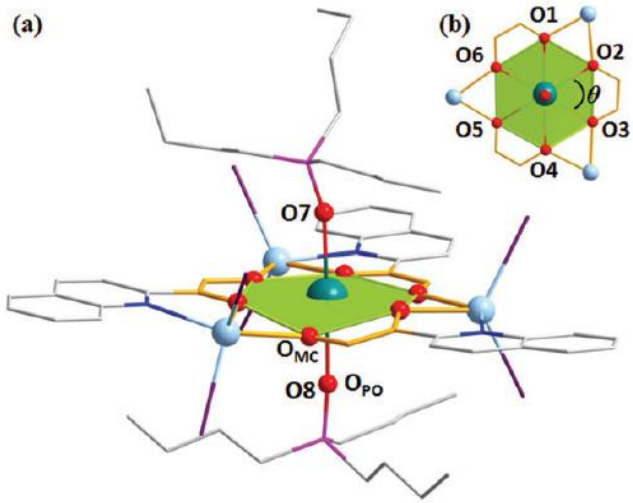

Figure 1.9. Side view (a) and top view (b) of the [15-metallacrown-6] core for $[CeCd_3(Hquinha)_3(n\text{-}Bu_3PO)_2I_3]\cdot 3EtOH\cdot 2H_2O$. Reused with permission from reference 46, copyright Royal Society of Chemistry.

In addition to the structural consideration, the moderate interaction between neighboring paramagnetic transition-metal ions and lanthanide ions—generally stronger than 4f–4f metal interactions but weaker than 3d–3d metal interactions—also promotes the development of 3d-4f hybrid complex, as this interaction can be utilized to enhance the performance of SMMs by suppressing QTM.[48-50] For example, Li et al. reported in 2015 three d–f hybrid SMMs $Dy^{III}_2M^{II}$ (M^{II} = Co^{II}, Ni^{II}, Cd^{II}), which feature the same perfect linear Dy−M−Dy arrangement.[51] The replacement of the diamagnetic Cd^{II} by paramagnetic ions led to a significant slowing of the relaxation, demonstrating the crucial role of the 3d–4f magnetic coupling in enhancing SMM behaviour. This research also demonstrated a widely adopted strategy for identifying the nature (ferro- or antiferromagnetic) of the 3d–4f coupling and its impact on SMM behaviour. The approach involves comparing the magnetic properties of paramagnetic 3d-ion-containing complexes with their diamagnetic analogs, where the 3d ion is replaced by diamagnetic substitutes such as Zn^{II}, Al^{III}, Co^{III}_{LS}.[52-54]

The slow magnetic relaxations in 3d–4f hybrid SMMs mainly originate from the spin reversal process of the 4f electrons in lanthanide ions due to the stronger magnetic anisotropy in lanthanides. And the magnetic interactions between 3d ions and 4f ions, if exist, are often treated as an influencing factor on that process. There are also exceptions. For instance, a $Co^{II}_2Dy^{III}_2$ complex reported by A. K. Powell and co-workers in 2012 demonstrated coexistence of distinct single-ion and exchange-based mechanisms.[55] The reason for magnet relaxation is the single-ion blocking of individual Dy^{III} ions at higher temperatures, which switches to exchanged-based blocking of the whole molecule at lower temperatures. In another 3d–4f ion-pair compound $[Dy(4\text{-MMNO})(H_2O)_5][Fe(CN)_6]$ (4-MMNO = 4-methylmorpholine N-oxide), two distinct relaxation processes from the $[Fe^{III}]_{LS}$ and Dy^{III} ions, respectively, are revealed.[56] These complexes highlight the complexity of interpreting magnetic properties in such d–f hybrid systems and underscore the need for careful analysis of the underlying mechanisms.

Radical-containing SMMs

Due to the presence of unpaired and spin-delocalized electrons in radicals, incorporating radical ligands into complexes can introduce strong interactions between the metal spin carriers and organic radicals. This can enhance the magnetic anisotropy of the metal ion or increase the overall spin value of the system, thereby leading to SMMs with high energy barriers. This approach is particularly effective for lanthanide complexes, as the diffuse spin orbitals of radical ligands are better able to penetrate into the core electron density of the deeply buried 4f orbitals.

In 2004, Ishikawa et al. oxidized the first rare earth single-ion magnet, $[TbPc_2]^-$, to obtain the neutral $[TbPc_2]^0$ molecule.[57] In $[TbPc_2]^0$, one of the phthalocyanine rings loses a single electron, becoming a π-radical, and the molecule transforms into a coupled system of Tb^{III} with S = 6 and a radical with S = 1/2. The effective energy barrier of this new system reaches 590 K, nearly double that of the original $[TbPc_2]^-$ anion (331 K).

In 2017, J. R. Long and co-workers reported two new series of organometallic N_2^{3-} radical-bridged dilanthanide complex salts: $[K(crypt\text{-}222)(THF)][(Cp^{Me4H}_2Ln(THF))_2(\mu\text{–}N_2)]$ (crypt-222 = 2.2.2-cryptand, THF = tetrahydrofuran, Cp^{Me4H} = tetramethylcyclopentadienyl, Ln = Tb (**1-Tb**), Dy(**1-Dy**)) and $[K(crypt\text{-}222)][(Cp^{Me4H}_2Ln)_2(\mu\text{–}N_2)]$, (Ln = Tb (**2-Tb**), Dy (**2-Dy**))[58]. The N_2^{3-} is located between two lanthanide centers, forming an overall Ln–radical–Ln linear structure (Figure 1.10). Magnetic susceptibility measurements reveal strong antiferromagnetic interaction between the two terminal lanthanide ions and the bridging N_2^{3-}radical in each complex, creating a ferrimagnetic system where the magnetic anisotropy in each of the aforementioned complexes is enhanced by the parallel alignment of the magnetic easy axes on two lanthanide ions. **1-Tb**, **1-Dy**, **2-Tb**, and **1-Dy** all reveal SMM property with effective energy barriers over 100 cm^{-1}. In particular, **2-Tb** exhibits 100s-blocking temperature up to 20 K, setting a record for both terbium-based and multinuclear SMMs at the time, and a coercive field of 7.9 T (at 10 K), which is still among the largest for any coordination compound to date. Notably, the relaxation barrier of **2-Tb** (U_{eff} = 276 cm^{-1}) is in excellent

agreement with the first excited exchange state, corresponding to a flip of a single Tb^{III} spin ($\Delta E = 12J_{Tb\text{-}rad} = 277\ cm^{-1}$). This demonstrates that the strong intramolecular Tb–radical interactions break the isolated state of the lanthanide ions, causing the relaxation via the exchange states rather than within individual metal centers.

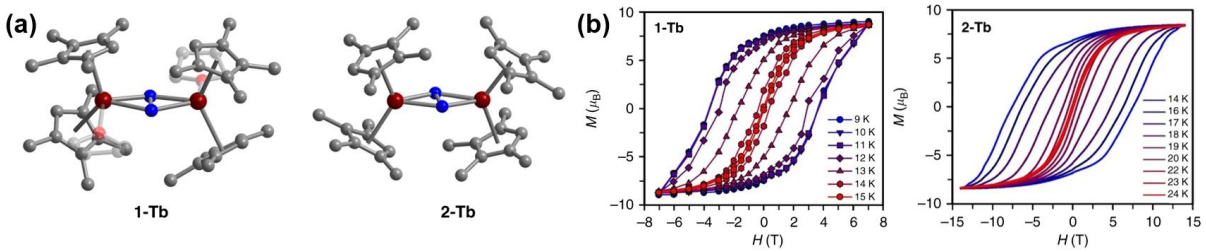

Figure 1.10. (a) Structure of structure of the N_2^{3-} radical-bridged anions in crystals of **1-Tb** and **2-Tb**; and (b) the hysteresis loops of **1-Tb** and **2-Tb**. Reused with permission from reference 58, licensed under [CC BY 4.0] (http://creativecommons.org/licenses/by/4.0/), source: https://www.nature.com/articles/s41467-017-01553-w.

The incorporation of radicals is not only limited to the lanthanide-based SMMs, radical-containing transition-metal-based SMMs have also been reported[59-61], highlighting the diversity of SMM systems that utilize radical ligands.

1.2.3 Influencing factors on the performance of lanthanide-based SMMs

As previously discussed, the advancement of transition-metal cluster single-molecule magnets has been hindered by their inherently small anisotropy. In contrast, many lanthanide ions possess strong magnetic anisotropy. Moreover, lanthanide ions can readily form single-ion magnets, which, due to their simpler structures, allow for easier tuning of magnetic properties through chemical means. Such advantages have promoted lanthanide-based SMMs as a research hotspot in molecular magnetism. Scientists have also identified numerous factors that influence the blocking temperature and effective energy barrier of SMMs, along with corresponding optimization strategies. These factors include the symmetry of the coordination environment around the spin centers, the charge distribution of the ligand field, the hyperfine interactions between nuclear and electron spins, as well as intermolecular or intramolecular electron spin interactions, etc. The following discussion will focus on lanthanide-based SMMs, detailing the respective effects of the aforementioned influencing factors.

Charge distribution of the ligand field

The SMM property of a paramagnetic metal complex are not only determined by the types of metals it contains but are also directly influenced by the distribution of charges around the

metal centers. For transition-metal complexes, the configuration of the ligand field directly determines whether the orbital angular momentum is quenched. For lanthanide ions, although the 4f electrons are largely shielded by outer electrons, the direction and strength of their anisotropy, as well as the probability of quantum tunneling, are still significantly affected by the surrounding charge distribution.

(1) Symmetry of the ligand field

The Hamiltonian operator acting on the angular momentum functions includes the spin-orbit coupling term $\widehat{H}_{SO}$, the exchange coupling term $\widehat{H}_{EX}$, the crystal field interaction term $\widehat{H}_{\mathrm{CF}}$, and the Zeeman effect term $\widehat{H}_{\mathrm{ZEE}}$,

$$\widehat{H} = \widehat{H}_{SO} + \widehat{H}_{CF} + \widehat{H}_{ZEE} + \widehat{H}_{EX} \qquad \text{equation 1.5}$$

in which $\widehat{H}_{CF} = \sum_{i=1}^{N} \sum_{k=2,4,6} \sum_{q=-k}^{k} \sigma_i^k B_{k\,i}^q \theta_k \hat{O}_{k\,i}^q$ equation 1.6

σ_i^k: orbital reduction parameters,

$B_{k\,i}^q (q \leq |k|)$: crystal field parameters (CFPs),

θ_k: operator equivalent factors,

$\hat{O}_{k\,i}^q$: for operator equivalents.

When $q = 0$, the CFPs are axial CFPs. When $q \neq 0$, they are transverse CFPs. To describe the ligand fields around transition metals, only the second-order and fourth-order CFPs ($k = 2, 4$) are required, whereas for lanthanides, the sixth-order parameters ($k = 6$) should also be included. The CFPs depend solely on the point group of the paramagnetic center, particularly the point group of the first coordination sphere. If the point group is C_1, all 27 B_k^q terms exist; otherwise, only terms where q is an even number are present. If the point group has a C_n rotation axis, further restrictions then apply, limiting q to $q = jn$, where j is an integer. In the presence of an S_n improper rotation axis, q vanishes if $2q/n$ is not an integer or if q/n is a half-integer. Therefore, for high-symmetry point groups such as $C_{\infty v}$, $D_{\infty h}$, D_{4d}, C_{5h}, D_{6d}, and C_n ($n > 6$), q is limited to 0, and the transverse crystal field parameters vanish. Since the transverse crystal field induces non-zero transverse anisotropy, which can induce fast QTM, engineering the symmetry of the ligand field around lanthanide centers is crucial for avoiding undesired QTM and acquiring high-performance SMMs.

M. L. Tong and co-workers summarized the selection rule of systematic absences of transverse crystal-field terms for a variety of point groups (Table 1.4).[62]

Table 1.4. Systematic absences of transverse crystal-field terms (k = 2, 4, 6). Reproduced with permission from reference 62, copyright Royal Society of Chemistry.

Point Group	C_n (n=)	σ_h	S_n (n=)	Selection Rule: B_k^q=0 when $\lvert q\rvert$ =
C_s	1	✓	—	1, 3, 5
C_1/S_2	1	—	2	—
C_1	1	—	—	—
C_2	2	—	—	1, 3, 5
C_3	3	—	—	1, 2, 4, 5
C_4	2, 4	—	—	1, 2, 3, 5, 6
C_5	5	—	—	1, 2, 3, 4, 6
C_6	2, 3, 6	—	—	1, 2, 3, 4, 5
C_n ($n \geq 7$)	≥7	—	—	All
C_{2h}	2	✓	—	1, 3, 5
C_{3h}	3	✓	3	1, 2, 3, 4, 5
C_{4h}	2, 4	✓	4	1, 2, 3, 5, 6
C_{5h}	5	✓	5	All
C_{6h}	2, 3, 6	✓	3, 6	1, 2, 3, 4, 5
S_4/D_{2d}	2	—	4	1, 2, 3, 5, 6
S_6/D_{3d}	3	—	6	1, 2, 4, 5
S_8/D_{4d}	2, 4	—	8	All
S_{10}/D_{5d}	5	—	10	1, 2, 3, 4, 6
S_{12}/D_{6d}	2, 3, 6	—	4, 12	All

In 2017, Y. Z. Zheng and co-workers reported a pentagonal bipyramidal SMM [Dy(O*t*-Bu)$_2$(py)$_5$][BPh$_4$] with a D_{5h} configuration.[63] In this complex, five pyridine molecules are positioned radially on the equatorial plane, while two axial tert-butoxide anions are nearly collinear with the metal center (O−Dy−O bond angle of 178.9°). Magnetic moment reversal in this compound occurs from the third and fourth excited states, yielding an effective energy barrier of 1261 cm^{-1}, which set a record for energy barriers at the time (Figure 1.11). In 2008, AlDamen et al. reported the first Er-based SMM, [Er(W$_5$O$_{18}$)$_2$].[64] In this complex, the Er ion is situated at the center of a square antiprism formed by two polyoxometalate ions, each providing four oxygen atoms from above and below, resulting in a D_{4d} symmetry. The energy barrier for this compound was measured to be 55.3 K. The above examples illustrate how an appropriate ligand field symmetry contributes to the enhanced slow magnetic relaxation.

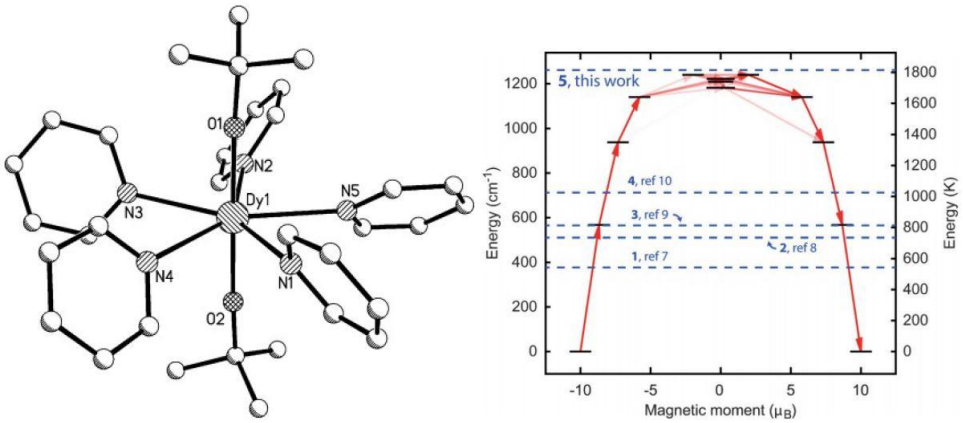

Figure 1.11. Molecular structure of $[Dy(OtBu)_2(py)_5]^+$ (left), and the relaxation mechanism (right). Opacity of the arrows give the relative transition propensity. Reused with permission from reference 63, copyright Wiley-VCH Verlag GmbH & Co. KGaA.

It is noteworthy that in complexes with configurations such as C_{3h}, C_{6h}, and D_{2d}, though not all B_k^q terms with $q \neq 0$ are quenched, the absence of most transverse CFPs can still lead to partial suppression of quantum tunneling. These complexes may also exhibit excellent SMM properties. For example, in 2014, J. Tang and co-workers reported the magnetic properties of two three-coordinate compounds, $Ln[N(SiMe_3)_2]_3$ (Ln = Dy, Er).[65] In these compounds, the three $N(SiMe_3)_2^-$ ligands form a triangular equatorial plane, with the Ln^{III} ion disordered above and below the center of the triangle, resulting in a C_{3v} configuration. In $Er[N(SiMe_3)_2]_3$, quantum tunnelling is effectively suppressed, with a reversal energy barrier reaching 122 K, and magnetic hysteresis loops can be observed at 1.9 K. In certain cases, even low-symmetry ligand fields may coincidentally result in a significant number of transverse CFPs being close to zero, leading to partial or complete suppression of QTM in the ground state. Given the profound impact of QTM on slow magnetic relaxation properties, calculating the CFPs for specific ligand fields is of great significance in the study of SMMs. *Ab initio* theoretical calculations based on the complete active space self-consistent field (CASSCF) method are frequently employed to determine these CFPs.[66] A detailed introduction to the relevant theoretical calculations will be provided in the following sections.

(2) Orientation of the ligand field

In the free ion state, trivalent rare earth metals exhibit distinct electron cloud shapes across different M_J sublevels (Figure 1.12).[67] Since the interaction between the electrons of rare earth ions and the external ligand field is relatively weak, these characteristic electron cloud shapes are largely preserved in the resulting complexes. Therefore, from an electrostatic model perspective, selecting appropriate ligand charge distributions can enhance the interaction between the ligand field and the metal's electron cloud, thereby improving magnetic anisotropy.

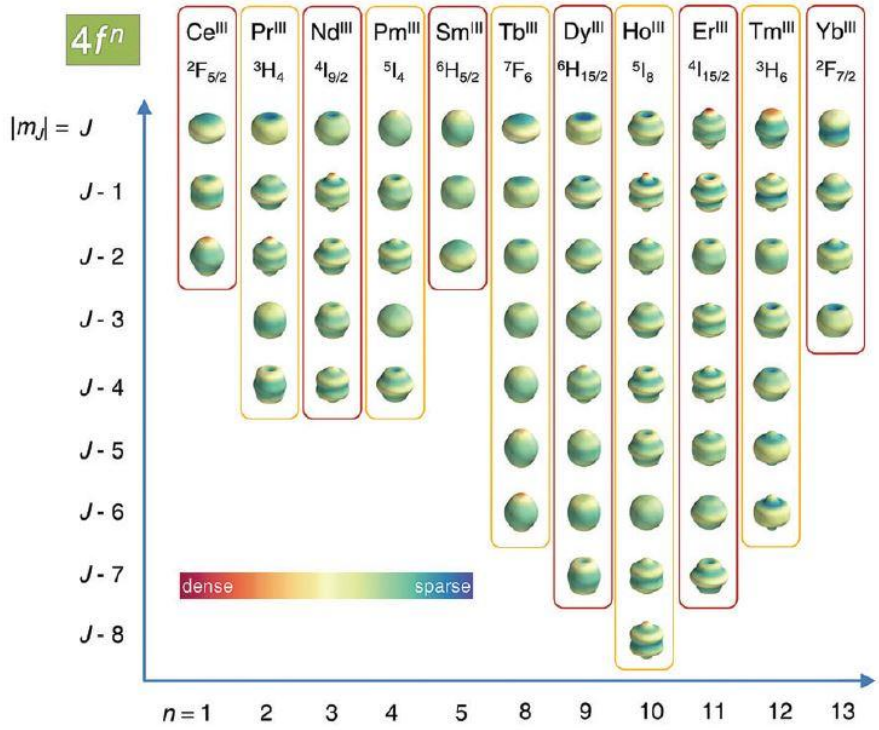

Figure 1.12. Visualization of the M_J-dependence angular distribution of charge density for Ln^{III} ions. Reused with permission from reference 67, copyright Royal Society of Chemistry.

For Dy^{III}, the ideal ground state $M_J = \pm 15/2$ has an oblate (flattened) electron cloud. In this case, electrostatic repulsion from axial ligands stabilizes the $M_J = \pm 15/2$ level, making it more energetically favorable. For Er^{III}, the $M_J = \pm 15/2$ level has a prolate (elongated) electron cloud, where charge interactions from the equatorial plane are more advantageous. This is evidenced by the $Ln[N(SiMe_3)_2]_3$ (Ln = Dy, Er) complexes discussed early.[65] While $Er[N(SiMe_3)_2]_3$ exhibits slow magnetic relaxation under zero field, $Dy[N(SiMe_3)_2]_3$ only exhibits weak χ_M'' signals under applied fields, with no peaks in the χ_M'' versus frequency plots revealed within the range of measurement. Theoretical calculations reveal that due to differences in the electron cloud shapes, the energies of the Stark sublevels for Er^{III} ions increase sequentially from $M_J = \pm 15/2$ to $M_J = \pm 1/2$ under the influence of equatorially coordinated ligands, while the trend for Dy^{III} ions is exactly the opposite (Figure 1.13). This results in Dy^{III} ions exhibiting anomalous non-easy-axis anisotropy (or easy-plane anisotropy), leading to rapid quantum tunnelling and very poor SMM property for $Dy[N(SiMe_3)_2]_3$ compared to its Er analogue.

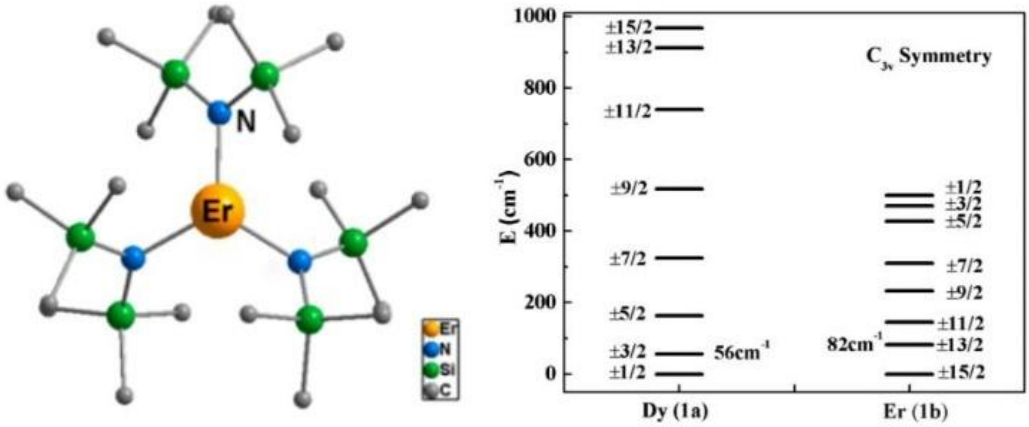

Figure 1.13. Molecular structure of $Er[N(SiMe_3)_2]_3$ (left); and energy diagrams showing the ground state M_J sublevels of both $Dy[N(SiMe_3)_2]_3$ and $Er[N(SiMe_3)_2]_3$ (right). Reused with permission from reference 65, copyright American Chemical Society.

(3) Strength of the ligand field

In some SMMs with low molecular symmetry and ligands that lack a clear axial or equatorial distinction, the direction of the metal's easy magnetization axis is often determined by the shortest and strongest coordination bond. If one bond is significantly stronger in strength than the other bonds, the complex can even be considered to possess a favorable $C_{\infty v}$ configuration, as demonstrated in a monometallic dysprosium bis(methanediide) SMM $[Dy(BIPM^{TMS})_2][K(18C6)(THF)_2]$ ($BIPM^{TMS}$ = $\{C(PPh_2NSiMe_3)_2\}^{2-}$) (Figure 1.14).[68] The linear coordination mode of the two methanediide centers provides a large build-up of negative charge along one single axis. Large energy gaps between the |15/2> ground state and all other doublets. Meanwhile, the three lowest energy Kramers doublets of the ground $^6H_{15/2}$ multiplet are essentially the pure |15/2>, |13/2> and |11/2> states quantized along the main C=Dy=C axis. Consequently, thermal relaxation proceeds mainly via the fourth and fifth doublets, where the wave functions are strongly mixed, and the main magnetic axes are perpendicular to that of the ground state, leading to high relaxation barriers (U_{eff}^1 = 501 cm^{-1}, U_{eff}^2 = 575 cm^{-1}).

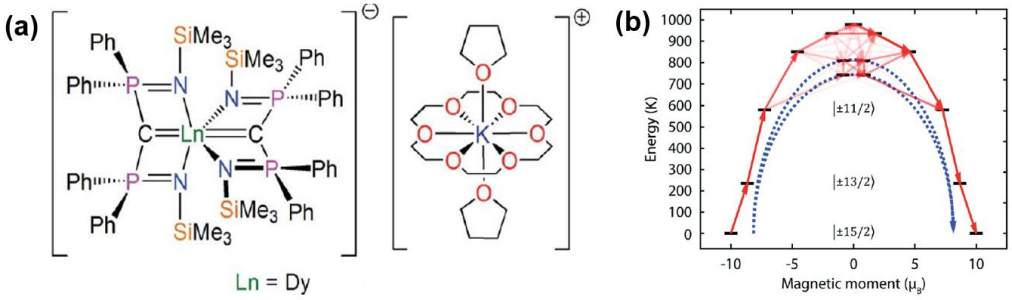

Figure 1.14. (a) Molecular structural scheme of $[Dy(BIPM^{TMS})_2][K(18C6)(THF)_2]$; and (b) calculate magnetic relaxation barrier. Reused with permission from reference 68, licensed under [CC BY 4.0] (http://creativecommons.org/licenses/by/4.0/), source:https://pubs.rsc.org/en/content/articlelanding/2016/sc/c5sc03111g

Another example is the tetranuclear dysprosium cluster SMM $[Dy_4K_2O(Ot\text{-}Bu)_{12}]\cdot C_6H_{14}$ reported by Blagg et al. in 2013 (Figure 1.15).[69] This molecule contains dysprosium ions with slightly different coordination environments and exhibits a double relaxation process, with energy barriers of 316 K and 692 K, respectively, and a blocking temperature of 5 K. Each dysprosium ion resides in a distorted octahedral structure formed by six oxygen atoms (four from μ_3-O^{t}Bu ligands, one from terminal tert-butoxide, and one μ_6 oxide), where the bond length between Dy and the terminal oxygen atom is significantly shorter than those with the bridging oxygen atoms. Theoretical calculations reveal that even in the absence of exceptionally high symmetry, the strong axial field offered by the terminal oxygen atom enhances the energy gap between M_J levels, reduces their mixing, and aligns the magnetic axes of the ground state and lower excited states along the Dy–terminal oxygen bonds, thereby increasing the reversal energy barrier.

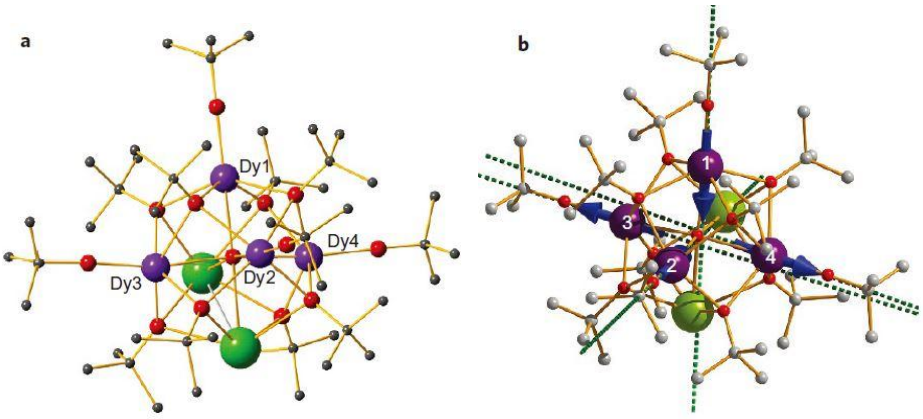

Figure 1.15. (a) Molecular structure of $[Dy_4K_2O(Ot\text{-}Bu)_{12}]\cdot C_6H_{14}$ (hydrogen atoms and the lattice hexane molecule are omitted); and (b) the directions of the easy axes of magnetization. Reused with permission from reference 69, copyright Springer Nature.

In summary, an appropriately symmetric molecular structure, ligand charge distribution aligned with the intrinsic electron cloud shape of the lanthanide ion, an enhanced crystal field strength along the easy axis, and reduced transverse crystal field strength collectively can significantly increase the likelihood of achieving high-performance SMMs. The ideal model compound $[DyO]^+$, predicted by N. F. Chibotaru and co-workers[70], integrates these advantages: (1) its monocoordinate structure exhibits $C_{\infty v}$ symmetry, effectively suppressing quantum tunneling; (2) all electrostatic interactions acting on the metal ion originate from the same direction—axial—eliminating competition from transverse fields; and (3) the Dy–O bond length is only 1.74 Å, indicating a strong interaction.[71] In this idealized compound, both the ground and excited state energy levels align with the Dy–O bond axis, and magnetic moment reversal occurs via the highest-energy excited doublet state, resulting in an energy barrier exceeding 3000 K.

Hyperfine interaction

The hyperfine interaction refers to the interaction between a nucleus and its surrounding electronic environment, which can be expressed as $H = I \cdot A_{hf} \cdot J$, where A_{hf} is the hyperfine interaction parameter, and I and J are the nuclear spin and total electron angular momentum quantum numbers, respectively.[72] Most lanthanide elements have isotopes with non-zero nuclear spins, and thus exhibit hyperfine couplings. Although energy level splitting caused by hyperfine interactions is generally small, much smaller than the splitting of M_J sublevels, an increasing number of experiments have shown that the resulting small hyperfine splitting can influence the properties of SMMs by affecting quantum tunneling of magnetization.

In 2017, M. Ruben, W. Wernsdorfer, and co-workers reported two dysprosium SMMs, $Et_4N[^{163}DyPC_2]$ and $Et_4N[^{164}DyPC_2]$, synthesized with isotopically enriched materials ($I = 0$ for ^{164}Dy vs. $I = 5/2$ for ^{163}Dy).[73] After diluting both samples with the diamagnetic Y^{III} to achieve a Dy content of 5%, the diamagnetically diluted samples ^{163}Dy-Y and ^{164}Dy-Y exhibited nearly identical χ_M'' versus frequency curves. Fitting to the Arrhénius equation yielded effective energy barriers of 34.5 K for ^{163}Dy-Y and 35.7 K for ^{164}Dy-Y. However, slight differences were observed at low temperatures: at 2 K, the peak of χ_M'' versus frequency plot for ^{163}Dy-Y appeared at 0.22 Hz, higher than the 0.1 Hz observed for ^{164}Dy-Y, indicating a faster quantum tunnelling rate for the former. This is because the hyperfine interaction introduced by the non-zero nuclear spin $I = 5/2$ for ^{163}Dy, in contrast to $I = 0$ for ^{164}Dy, leads to more energy level splitting and avoided hyperfine level crossings in the ground Stark sublevels near zero field, thereby facilitating rapid QTM. This is further confirmed by ultra-low temperature (0.03 K) measurements performed using micro-SQUID. The magnetic hysteresis loops of ^{163}Dy-Y sample displayed multiple steps within ±20 mT field (Figure 1.16), corresponding to hyperfine interaction-induced level crossings. These steps were entirely absent in ^{164}Dy-Y, which lacks nuclear spin. Similar phenomenon was also observed in dinuclear complexes—$[^{163}Dy_2(BTFA)_4(PHZP)_2]^0$ ($\mathbf{1}^{(I = 5/2)}$) and $[^{164}Dy_2(BTFA)_4(PHZP)_2]^0$ ($\mathbf{2}^{(I = 0)}$), where BTFA = 3-benzoyl-1,1,1-trifluoroacetone and PHZP = *N'*-[(*E*)-(pyrazin-2-yl)methylidene]pyrazine-2-carbohydrazonate.[74] While $\mathbf{1}^{(I = 5/2)}$ and $\mathbf{2}^{(I = 0)}$ exhibited almost the same magnetic properties at temperatures ≥ 2 K, the nuclear spin-bearing $\mathbf{1}^{(I = 5/2)}$ displayed much narrower hysteresis loops at 30 mK, demonstrating the role of hyperfine coupling in facilitating magnetic relaxation at the sub-Kelvin temperature range.

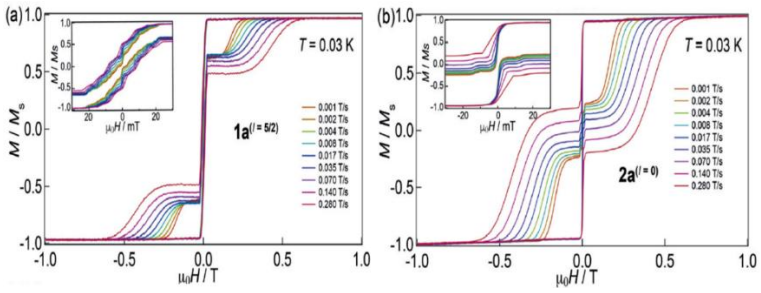

Figure 1.16. Magnetic hysteresis loops of ^{163}Dy-Y (a) and ^{164}Dy-Y (b), the top-left inset in (a) showing multiple quantum tunnelling steps in ^{163}Dy-Y. Reused with permission from reference 73, Copyright Wiley-VCH Verlag GmbH & Co. KGaA.

Intermolecular interaction

In the crystal lattices of SMMs, the shortest distances between neighboring molecules are typically around 10 Ångströms (Å). At such short distances, non-negligible dipolar-dipolar interactions between metal centers can arise, potentially creating an effective transverse magnetic field. This field can induce quantum tunnelling at low temperatures and even significantly altering the effective energy barrier for magnetic relaxation. To reduce the impacts of intermolecular interactions, two strategies are commonly employed. The first one is to dilute the paramagnetic molecules into a diamagnetic matrix, e.g., Y^{III} or Lu^{III} analogs, or to dissolve the molecules in a solution and test the resulting solution sample (often frozen at low measurement temperatures). By comparing the magnetic properties of diluted/frozen samples with those of the undiluted crystalline material, the contributions of intermolecular interactions can be systematically disentangled from the intrinsic magnetic relaxation dynamics in the single-molecule level. The second strategy is ligand engineering, e.g., introducing sterically bulky functional groups in the periphery of ligands to minimize intermolecular interactions. However, it is critical to note that these approaches may introduce subtle changes to the coordination environment. For instance, the molecular structure of a complex may differ between crystalline and solution states due to solvent effects or dynamic ligand rearrangements.[75,76] Therefore, careful consideration of the structural differences is essential when comparative studies are performed.

In 2013, Cosquer et al. reported a mononuclear dysprosium compound, $[Dy(hfac)_3(L^1)]$ (L^1 = 4,5-bis-(propylthio)tetrathiafulvalene-2-(2-pyridyl)benzimidazole).[77] While the pure crystalline sample exhibited no alternating current magnetic response, its frozen solution sample in the aprotic solvent CH_2Cl_2 revealed zero-field SMM behaviour with an energy barrier of 12 K. To further probe the role of intermolecular interactions, a modified ligand L^2 was synthesized by introducing a bulky, non-coordinating aromatic group to L^1 (Figure 1.17). This structural modification eliminated intermolecular hydrogen bonding observed in $[Dy(hfac)_3(L^1)]$. The resulting $[Dy(hfac)_3(L^2)]$ exhibited SMM behaviour under zero field with an energy barrier of 17 K, in solid state. Further investigations on the diamagnetically diluted sample $[Y_{0.93}Dy_{0.07}(hfac)_3(L^2)]$ demonstrated a significantly slower relaxation process in the temperature-independent regime, with relaxation rates nearly 30 times slower than those of the undiluted compound. This study employed various strategies to increase intermolecular distances, demonstrating the critical role of minimizing intermolecular interactions to preserve or enhance SMM properties.

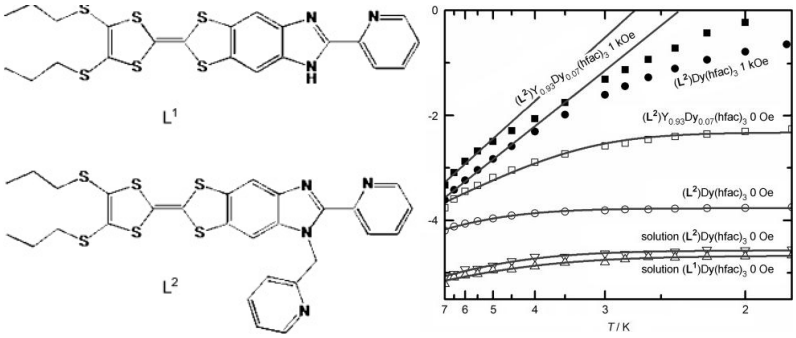

Figure 1.17. Structures of L^1 and L^2 (left); and Arrhénius plots of the relaxation times (right). Reused with permission from reference 77, copyright Wiley-VCH Verlag GmbH & Co. KGaA.

Some studies have loaded SMMs onto metal surfaces[78], encapsulated them within graphene nanotubes[79], or filled them into the pores of organic framework compounds[80], resulting in measured effective energy barriers or magnetic hysteresis loops at low temperatures that differ from those of pure crystalline samples. However, it is important to note that although these manipulations can quench intermolecular interactions, certain substrates or carriers exhibit coupling effects or charge transfer with the SMMs attached on them. Therefore, the changes in magnetic behaviour cannot be solely attributed to the effects of intermolecular interactions.

Intramolecular interaction

As previously discussed in the thesis, intramolecular interactions significantly influence the SMM properties of transition-metal clusters and d–f metal hybrid complexes. This section focuses specifically on the intramolecular interactions between lanthanide metal centers.

In 2011, M. Murugesu and co-workers reported dinuclear complex $Dy_2(valdien)_2(NO_3)_2$ (H_2valdien = N^1, N^3-bis(3-methoxysalicylidene)diethylenetriamine), which possesses a centrosymmetric molecular structure (Figure 1.18).[81] An antiferromagnetic interaction was confirmed between two dysprosium ions within the molecule, with their magnetic axes pointing in completely antiparallel directions. By comparing the temperature dependence of the imaginary part of the AC susceptibility (χ_M'') for samples with different levels of diamagnetic dilution (Dy content of 5%, 10%, 50%, respectively), the authors found that the diluted samples exhibited significant quantum tunneling phenomena at low temperatures, which were not observed in the sample containing 100% Dy content. When measuring the magnetic hysteresis loops at temperatures ranging from 0.04 K to 5 K, it was discovered that diluted samples showed distinct steps at zero field, whereas the steps in the undiluted sample appeared around ±0.3 T. The authors concluded that the antiferromagnetic interaction between the binuclear dysprosium ions acted like an internal “bias field” applied upon the dysprosium ions and this “bias field” shifted the QTM of individual isolated metal centers away from zero magnetic field to a small finite field, ±0.3 T in this case, thereby effectively suppressing zero-field tunneling.

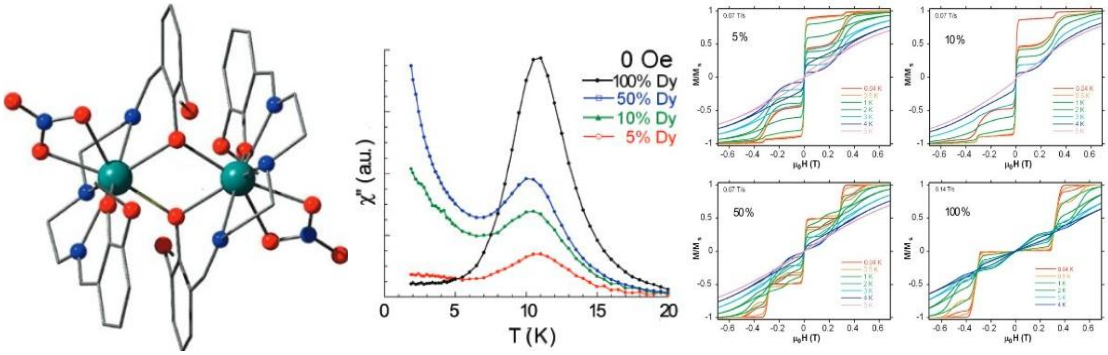

Figure 1.18. Molecular structure of $Ln_2(valdien)_2(NO_3)_2$ (left), temperature-dependent out-of-phase AC susceptibility curves (middle), and magnetic hysteresis loops (right) for samples with different dilution levels. Reused with permission from reference 81, copyright American Chemical Society.

While the weak Ln–Ln intramolecular coupling can generate exchange biasing, more frequently, however, it enhances QTM at lanthanide centers, since the coupled lanthanide ions exert effective transverse magnetic fields on each other — similar with the intermolecular couplings. This undermining effect is more pronounced when the magnetic easy axes are tilted. For example, when the aforementioned tetranuclear dysprosium cluster SMM $[Dy_4K_2O(O\textit{t}\text{-}Bu)_{12}]\cdot C_6H_{14}$ ({Dy_4K_2}, see page 28) is diluted by diamagnetic yttrium ions (yttrium ~ 95%) to give {DyY_3K_2} in a {Y_4K_2} matrix, the U_{eff} increases to 842 K, owing to the removal of both inter- and intra- molecular Dy–Dy couplings.[69] In addition, R. E. P. Winpenny and co-workers reported a dinuclear dysprosium compound $[hqH_2][Dy_2(hq)_4(NO_3)_3]\cdot MeOH$ (hqH = 8-hydroxyquinoline) in 2014, which doesn't reveal SMM property under zero applied field.[82] Two dysprosium ions in the complex exhibit distinct coordination environments and their magnetic easy axes are calculated to be 44° apart. Measurements on diamagnetic-doping samples and computational investigation reveal though the Dy ion in the "hq coordination pocket" is SMM active, the intramolecular interaction from the other Dy ion in the "NO_3^- coordination pocket" causes accelerated QTM at the Dy ion in the "hq coordination pocket", leading to the lack of SMM property. Later in 2017, the work reported by Lyu et al. on a structurally similar dinuclear complex $(HNEt_3)[Dy_2(MQ)_4(NO_3)_3]\cdot EtOH\cdot H_2O$ (MQ = 2-methyl-8-hydroxyquinoline), also supports the conclusion that intramolecular interactions promote quantum tunnelling when the easy axes on the metal ions are non-collinear.[83]

However, the distinction between collinear and non-collinear configurations remains poorly defined, making it challenging to predict the impact of intramolecular magnetic interactions on the SMM property based solely on molecular structure. For example, in the compound $[Dy_2ovph_2Cl_2(MeOH)_3]\cdot 3MeCN$ (H_2ovph_2 = pyridine-2-carboxylic acid [(2-hydroxy-3-methoxyphenyl)methylene] hydrazide) reported by Guo et al. in 2011, the two dysprosium ions exhibit identical coordination modes with the organic ligand $ovph_2^-$ in the transverse plane but differ in their coordination above and below the plane, where they are bound to

either two chloride ions or three methanol molecules.[84] This discrepancy introduces slight asymmetry in the overall molecular structure, resulting in an 8.79° angle between the magnetic axes of the two dysprosium ions. Although the magnetic axes in this case are not strictly collinear, micro-SQUID measurements and theoretical calculations indicate that the ferromagnetic interaction between the dysprosium ions suppresses quantum tunnelling.

1.2.4 Key experimental and theoretical techniques utilized to study SMMs

Superconducting Quantum Interference Device (SQUID) and Micro-SQUIDs

Superconducting Quantum Interference Device is a highly sensitive magnetometer utilizing the flux quantization properties of superconducting rings to achieve high-sensitivity measurements. The basic components of a SQUID are a superconducting loop and Josephson junctions. The superconducting loop allows current to flow without resistance below its critical temperature and enforces the quantization of magnetic flux. When an external magnetic field is applied, the loop responds by adjusting the circulating current to maintain flux quantization. A Josephson junction consists of two superconductors separated by a thin insulating barrier, allowing Cooper pairs to tunnel through the barrier. The phase difference across the junction depends on the magnetic flux threading the loop, leading to an interference effect that modulates the supercurrent in a periodic manner. Overall, a SQUID module can detect extremely small magnetic fields with high sensitivity.

The Magnetic Property Measurement System (MPMS) is one of the most used instruments for measuring the magnetic property of paramagnetic materials. One MPMS typically consists of a superconducting magnet, a sample chamber and probe, a SQUID detection system, a data acquisition and control system, a liquid helium-based cryostat, a magnetic field calibration system, and a sample rod with positioning system. Leveraging the ultra-sensitivity of SQUID sensors, MPMS can detect the extremely small magnetic moments (~10^{-9} emu) with high precision and low noise (~10^{-12} emu).[85] The cryostat enables MPMS to operate over a broad temperature range, from 1.8 K to 400 K, while the superconducting magnets are capable of generating magnetic fields of up to 7 T. Consequently, MPMS can collect the data of field- and temperature-dependent magnetic susceptibility (both DC and AC), as well as magnetization curves, including hysteresis loops.

Though being the workhorse of scientists for characterizing magnetic materials, MPMS based on conventional SQUID magnetometers are incapable of measuring samples at millikelvin temperatures and lack the sensitivity required to measure very small single crystals. To overcome these limitations, Wernsdorfer et al. developed a micro-SQUID setup which operates at temperatures ranging from 20 mK to 9 K.[86] The magnetometer, comprising an array of micro-SQUIDs, features a miniature design and high sensitivity, allowing the study on single crystals as small as 10 micrometers, which are placed directly on the array

(Figure 1.19). Furthermore, the external magnetic field can be applied in any direction of the micro-SQUID with a precision better than 0.1°, enabling the collection of angle-resolved magnetization data.

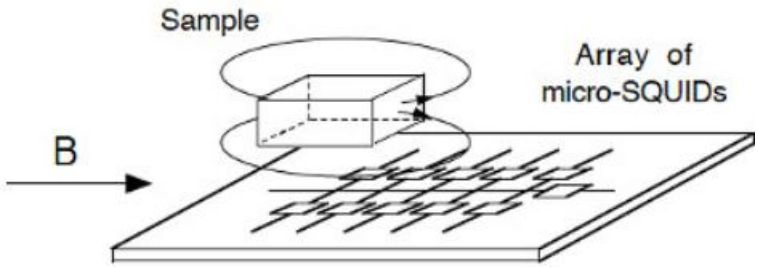

Figure 1.19. Schematic representation of the magnetometer developed in the W. Wernsdorfer group which is an array of micro-SQUIDs. Reused with permission from reference 86, copyright IOP Publishing.

CASSCF calculations and software PHI

To understand the molecular magnetism, specifically in the SMMs, accurate theoretical modeling of electronic structures, energy levels, and magnetic properties are required. The CASSCF (Complete Active Space Self-Consistent Field) method is one of the most powerful tools for this purpose. Being a type of *ab initio* (a Latin term meaning "from the beginning") calculations, CASSCF method solves the Schrödinger equation for molecular systems without empirical parameters, relying purely on fundamental physical constants.[87] Compared with some other ab initio calculation methods, like Hartree–Fock (HF) or Møller–Plesset perturbation theory (MP), CASSCF is specialized for multi-reference problems involving strong electron correlation as it uses a linear combination of configuration state functions (CSFs) to approximate the exact electronic wavefunction of an atom or molecule. At the same time, the focus on active molecular orbitals helps minimize computational cost compared to a full configuration interaction treatment, while maintaining a high level of accuracy. These features make CASSCF well-suited to study strongly correlated systems, such as transition-metal and lanthanide-metal complexes.

MOLCAS is a quantum chemistry software package designed for state-of-the-art quantum chemical calculations, with the key feature being the multiconfigurational approach, including CASSCF.[88] It performs CASSCF calculations based on the inputs of a set of atomic coordinates, which can come from experimentally determined crystal structures, optimized geometries by HF or density functional theory (DFT) calculations or hypothetical models constructed by users. Users can also define the active spaces and basis sets for each atom type to tune the calculations. After CASSCF calculations provide spin-free states and wavefunctions, restricted active space state interaction (RASSI-SO) can be invoked to compute spin-orbit coupling and interactions between CASSCF states. The results of RASSI

calculation for the ground and several excited spin-orbital multiplets can then be processed by SINGLE-ANISO, a module of MOLCAS, to generating the following quantities:

1. Parameters of pseudospin magnetic Hamiltonians, including all 27 crystal field parameters, the anisotropy of $\boldsymbol{g}$-tensor (diagonal elements g_x, g_y, g_z), the main axis and its direction in the Cartesian coordinate system, etc.

2. Static magnetic properties, including powder magnetic susceptibility function $\chi(T)$, Magnetization vector $\vec{M}(\vec{H})$ for specified directions of the applied magnetic field $\vec{H}$, powder magnetization M (H), etc.

It is noteworthy that the CASSCF approach has inherent limitations. First of all, it requires a carefully chosen active space. If it's too small, key orbitals are excluded, leading to an incomplete electronic description. Secondly, CASSCF completely neglects dynamic correlation. Dynamic correlation arises from instantaneous electron interactions and often stabilizes the ground state more than excited states. As a result, the energy splitting of states is often underestimated. CASPT2 (second-order perturbation theory) and NEVPT2 (N-electron valence state perturbation theory), both of which incorporate dynamic correlation, can provide a more complete picture of the electronic structure. However, they are also more computationally demanding.[89]

Since 2019, the launch of OpenMolcas, an open-source version of the original MOLCAS software, enhanced the accessibility to the powerful platform for the scientific community.[90,91] All *ab initio* calculation presented later in this thesis are performed on OpenMolcas platform following the CASSCF approach.

Software PHI is another versatile and powerful tool to study molecular magnetism.[92] Developed by the Chilton group, the program was designed primarily for the treatment of systems containing orbitally degenerate and strongly anisotropic ions, through the inclusion of spin-orbit (SO) coupling, crystal-field (CF) effects, Zeeman effects (ZEE) and also exchange couplings (EX) (Equation 1.5)

$$\hat{H} = \hat{H}_{SO} + \hat{H}_{CF} + \hat{H}_{ZEE} + \hat{H}_{EX} \qquad \text{Equation 1.5}$$

PHI can fit experimental data—including magnetization vs. field (M vs. H) plots, susceptibility vs. temperature (χ vs. T) plots, and EPR spectra—to extract important magnetic parameters such as exchange interactions, anisotropy, and $\boldsymbol{g}$-factors.

Beyond estimating unknown parameters from experimental data, PHI can also simulate magnetic behaviours on user-defined theoretical models. With customizable inputs such as spin values, coupling constants, magnetic anisotropies and crystal field parameters, the software facilities research on novel magnetic systems by predicting magneto-structural relations. In addition to M vs. H and χ vs. T plots, energy levels and transition probability between quantum states can also be simulated, which is vital for understanding the magnetic

relaxation processes in SMMs. For anisotropic systems, the zero-field average transition probability between states u and v is calculated through Equation 1.7:

$$T_{u,v} = \frac{1}{3}\sum_{\alpha=x,y,z}\left|\left\langle v\left(\sum_{l=1}^{N}\left(\widehat{H}_{ZEE}|_{B_\alpha=1}\right)\right)u\right\rangle\right|^2 \qquad \text{Equation 1.7}$$

where i stands for the i^{th} metal center, B_α denotes the magnetic field intensity for a single Cartesian direction, $\alpha \in$ x, y, z. The transition probabilities are in units of squared Bohr magnetons (μ_B^2). Transition-probability calculations are vital for understanding the magnetic relaxation in SMMs.

1.3 Optical properties of lanthanide complexes

1.3.1 Basics of photoluminescence (PL)

As stated in Chapter 1.1, lanthanides have found widespread applications owing to their unique luminescence properties. This section introduces the basics of luminescence, emphasizing particularly on the photoluminescence of lanthanide complexes. The distinctive characteristics of these photoluminescent complexes will be explored, drawing on the electronic structures of various lanthanides. Factors affecting quantum yield and strategies for achieving highly luminescent lanthanide complexes will also be examined. In addition, a range of excitation mechanisms will be elucidated. Finally, the key experimental facilities employed in this study will be presented.

Luminescence is the emission of light by a substance following the absorption of energy. Unlike thermal radiation, which arises from the thermal motion of particles within any matter above absolute zero kelvin, luminescence is triggered by electronic excitation. Depending on the excitation source, luminescence can be classified into various types, such as chemiluminescence (chemical reactions), electroluminescence (electric current), and photoluminescence (light absorption), piezoluminescence (mechanical pressure), magnetoluminescence (magnetic field), and so on.

In the case of photoluminescence (PL), a material first absorbs photons and gets excited from the singlet ground state S_0 to an excited singlet state Sn under light irradiation ($S_0 \rightarrow S_n$). When the material relaxes back to the ground state ($S_n \rightarrow S_0$), it reemits photons with energies similar to those absorbed. However, if the system undergoes intersystem crossing (ISC), where the excited electron transitions from a singlet state to a triplet state ($S_n \rightarrow T_n$), the subsequent relaxation from the triplet state to the ground singlet state ($T_n \rightarrow S_0$) typically occur in a longer timescale. The delay arises because this transition involves an electron spin flip and is spin-forbidden by quantum mechanics. The former process, occurring on a nanosecond

timescale, is known as fluorescence, while the latter, which can last from milliseconds to hours, is called phosphorescence (Figure 1.20).[93]

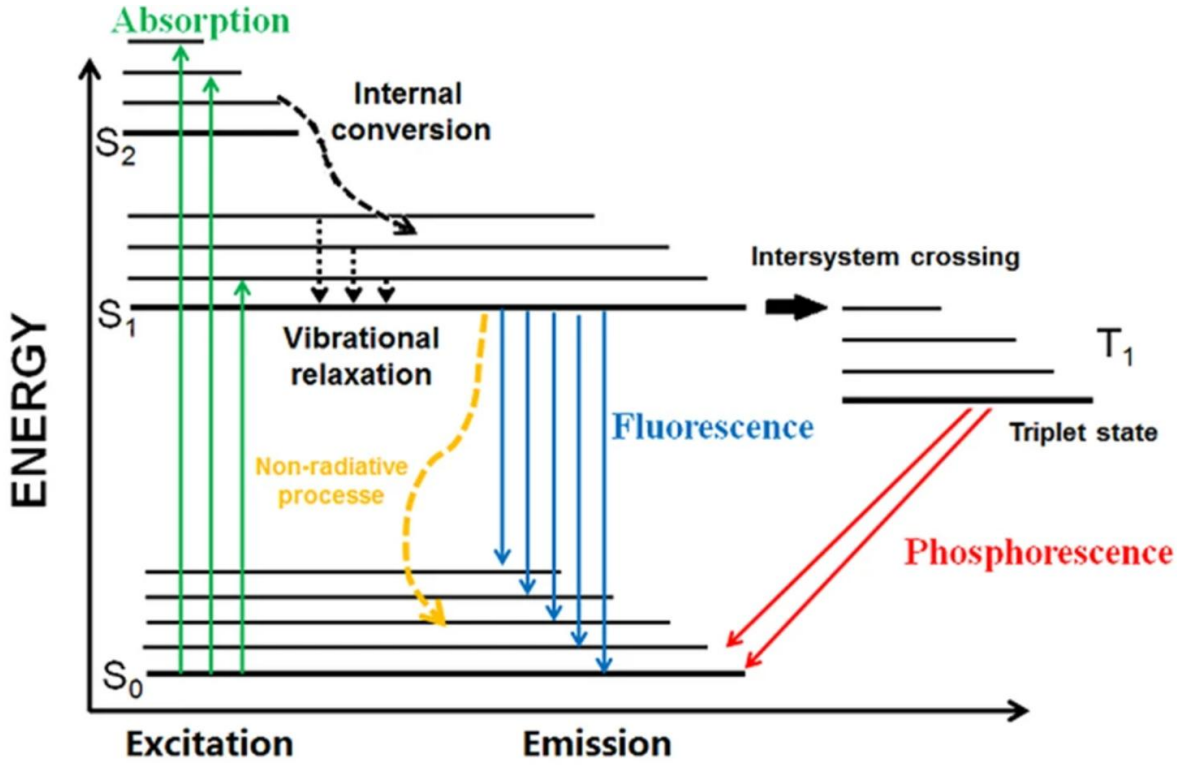

Figure 1.20. Jablonski diagram illustrating different transitions between a molecule's energy states. Reused from reference 93, licensed under [CC BY 4.0] (http://creativecommons.org/licenses/by/4.0/), source: https://link.springer.com/article/10.1007/s41104-021-00092-3.

As the ISC is from a high-lying singlet state to a low-lying triplet state, the emitted photon in phosphorescence always has a longer wavelength than the excited photon, leading to a redshift of the emission spectrum. The difference in energy or wavelength between the absorbed light (excitation) and the emitted light (emission) is termed Stokes shift. As illustrated in Figure 1.21, Stokes shift in photoluminescence also applies in fluorescence, though the shift is usually relatively small. Several effects lead to the shift, including the non-radiative processes, such as vibrational relaxation from the vibrational levels of the S_1 state, and internal conversion (IC) from high-lying S_n states (Figure 1.21, a).

The dynamics of photoluminescence decay are typically characterized by the lifetime τ, which represents the average time that a molecule stays in the excited state before emission takes place. Mathematically, τ is defined as the reciprocal of the decay rate constant k ($\tau = 1/k$) and corresponds to the time required for the luminescence intensity to decrease to $1/e$ (e being Euler's number, $1/e \approx 36.8\%$) of its initial value. The decay generally follows an exponential law (Figure 1.21, b). In a single-exponential decay model, the intensity $I(t)$ as a function of time t can be expressed as:

$$I(t) = I_0 \cdot e^{-t/\tau} \qquad \text{Equation 1.8}$$

I_0 : Initial luminescence intensity

$I(t)$: Luminescence intensity at time t

In real-world systems, such as heterogeneous materials and compounds with multiple decay pathways, a single-exponential decay model is not adequate to describe the photoluminescence kinetics. Instead, a multi-exponential model is required:

$$I(t) = I_1 \cdot e^{-t/\tau_1} + I_2 \cdot e^{-t/\tau_2} + \cdots \qquad \text{Equation 1.9}$$

Here, τ_i and I_i represent different lifetime components and their relative intensities, respectively.

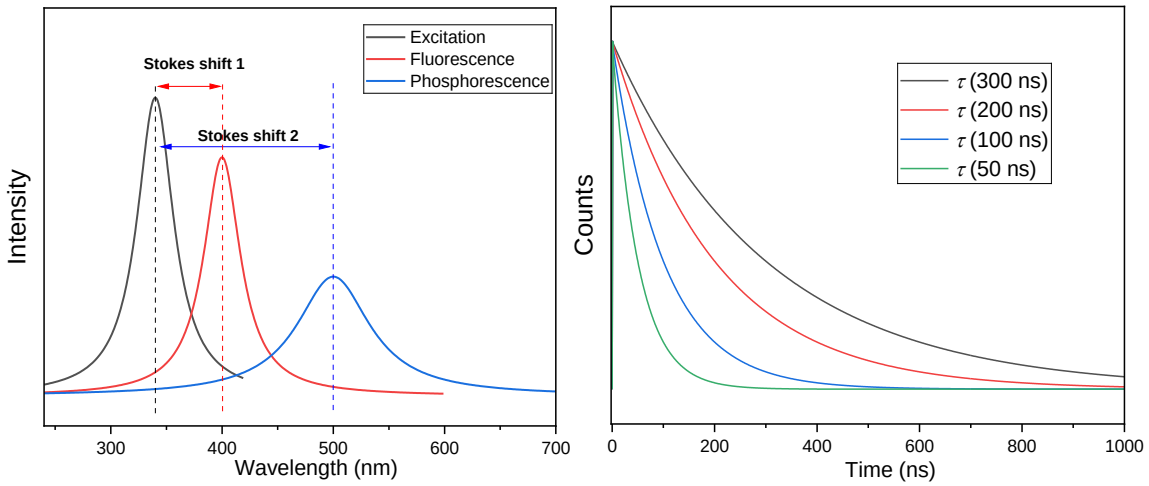

Figure 1.21. Illustrative Ex/Em spectra, showing Stokes shifts (left) and intensity decay plots of various lifetimes (right).

Another fundamental parameter in PL is photoluminescence quantum yield (PLQY or Φ), which quantifies the efficiency of a material in converting absorbed photons into emitted photons. Quantum yield is defined as the ratio of the number of photons emitted to the number of photons absorbed by the material. It is closely related to the luminescence lifetime (τ) and the radiative (τ_{rad}) and nonradiative ($\tau_{\text{non-rad}}$) lifetimes, as shown in Equation 1.X:

$$\Phi = \frac{\text{Number of Emitted Photons}}{\text{Number of Absorbed Photons}} = \frac{\tau}{\tau_{\text{rad}}} = \frac{\tau_{\text{non-rad}}}{\tau_{rad} + \tau_{\text{non-rad}}} \qquad \text{Equation 1.10}$$

High quantum yield is essential for achieving bright and efficient light emission in practical devices. The factors affecting PLQY of lanthanide complexes will be discussed in Chapter 1.3.2.

1.3.2 Characteristics of photoluminescence in lanthanide complexes

Lanthanide ions (e.g., Eu^{III}, Tb^{III}) emit light via 4f–4f electronic transitions, which are partially shielded by outer 5s/5p orbitals. This shielding drastically weakens the influences from external perturbations, such as ligand fields and solvent interactions, on the 4f electrons, suppressing Stark splitting and spectral broadening. This results in sharp, narrow emission bands of lanthanide complexes, unlike the broad, solvent-dependent emission of organic fluorophores (π–π*/n–π* transitions) or transition-metal complexes (d–d/metal–ligand charge transfer transitions). Meanwhile, according to Laporte Rule, in centrosymmetric environments, electric dipole transitions are only allowed if there is a change in the orbital angular momentum quantum number ($\Delta l = \pm 1$). For Ln^{III}, 4f–4f transitions occur with $\Delta l = 0$, making them Laporte-forbidden. This drastically extends the radiative lifetime (τ_{rad}), as the probability of photon emission via electric dipole transitions is extremely low. Many of these 4f–4f transitions are also spin-forbidden ($\Delta s \neq 0$), which further suppresses the radiative decay rate. Therefore, Ln^{III} ions exhibit significantly longer lifetime τ (microseconds to milliseconds), compared to the organic fluorophores or transition-metal complexes.

The emission properties of Ln^{III} ions also vary dramatically across the whole lanthanide series due to differences in 4f electron configurations and energy levels (Figure 1.22).[94-96] Trivalent lanthanide ions can be roughly categorized into two groups, the visible light emitters and the near-infrared (NIR) emitters, based on their characteristic emission bands. The most prominent visible light emitters are Eu^{III} ($4f^6$) and Tb^{III} ($4f^8$). Eu^{III} exhibit intense red emission, with the most pronounced emissive excited state being $^5D_0$, which lies ca. 17200 cm^{-1} above the ground state $^7D_0$. Tb^{III}, in contrast, displays green emission, with its primary emissive excited state $^5D_4$ located ca. 20500 cm^{-1} above the ground state $^7F_6$. Sm^{III} ($4f^5$), Dy^{III} ($4f^9$), Tm^{III} ($4f^{12}$) are also known for their visible light emissions. Their most significant emissive states are $^4G_{5/2}$, $^4F_{9/2}$ and $^1G_4$, respectively.

Nd^{III} ($4f^3$), Er^{III}($4f^{11}$), and Yb^{III}($4f^{13}$) all exhibit emissions in the NIR range. The characteristic NIR emissions for Nd^{III} ($4f^3$) locate at around 880, 1060, and 1330 nm, which correspond to the relaxations from the $^4F_{3/2}$ excited state to the $^4I_{9/2}$, $^4I_{11/2}$, $^4I_{13/2}$ states, respectively. In the case of Er^{III}, NIR emissions appear at around 820, 980, and 1530 nm, arising from the $^4I_{9/2}$, $^4I_{11/2}$, $^4I_{13/2}$ excited states transitioning to the $^4I_{15/2}$ ground states. As for Yb^{III} ($4f^{13}$), the most significant NIR emission locates at approximately 980 nm, corresponding to the $^2F_{5/2} \rightarrow {}^2F_{7/2}$ transition.

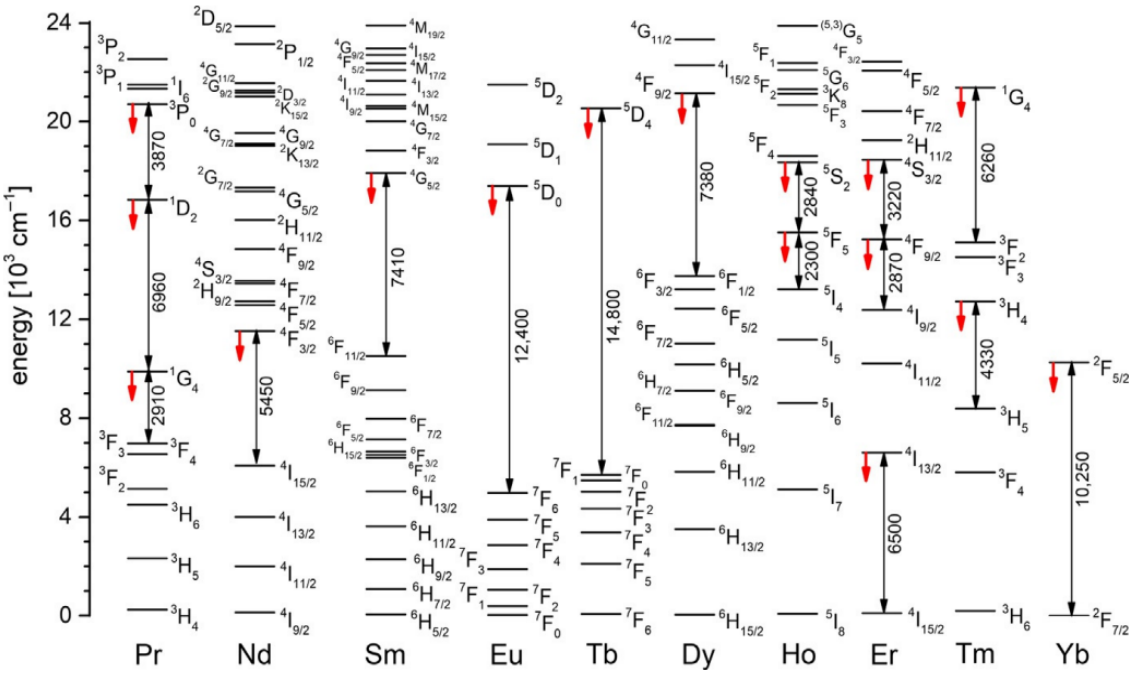

Figure 1.22. Partial energy level diagram of selected trivalent Ln ions (calculated energies for Ln^{III} (aq); exception: Yb^{III} in LaF_3) with red downward arrows indicating prominent emitting energies and the black double-headed arrows showing the energy gap between emitting level and next lower level (in cm^{-1}). Reused with permission from reference 94, copyright Elsevier.

It is noteworthy that labeling lanthanide ions as visible light or NIR emitters refers primarily to their most intense emission bands, not to an exclusive absence of f–f transitions in the other spectral region. For example, Sm^{III}, which is typically associated with visible emissions, can exhibit NIR bands (e.g., $^4G_{5/2} \rightarrow {}^6H_{13/2}$ and $^4G_{5/2} \rightarrow {}^6H_{15/2}$).[97] Meanwhile, the well-known NIR emitter Er^{III} can exhibit weak visible emissions (e.g., $^2H_{11/2} \rightarrow {}^4I_{15/2}$, $^4S_{3/2} \rightarrow {}^4I_{15/2}$).[98]

The distinct ion-specific emission profiles across the lanthanide series enables a wide range of applications. For example, the strong red emission from Eu^{III} and green emission from Tb^{III} are widely utilized in the display devices.[99,100] Meanwhile, Er^{III} plays a key role in the optical communication systems, as its 1530 nm emission ($^4I_{13/2} \rightarrow {}^4I_{15/2}$) falls within the telecommunication C-band, where silica optical fibers exhibit minimal loss.[101]

While most trivalent lanthanide ions display 4f–4f emissions, there are several notable exceptions. First of all, the Gd^{III} ion ($4f^7$) possesses exceptional stability due to its half-filled 4f shell. This stability results in a high-energy lowest excited state ($^6P_{7/2}$, ca. 32000 cm^{-1}), which lies above the singlet (S_1) and triplet (T_1) states of most organic ligands. Therefore, the energy cannot be transferred from the ligands to the gadolinium ions, leading to ligand-centered emission—either fluorescence or phosphorescence—rather than metal-centered luminescence in Gd complexes. Similar behaviour is observed in diamagnetic La^{III} ($4f^0$) and Lu^{III} ($4f^{14}$) complexes, which also lack low-lying excited states capable of accepting energy from ligands.

Secondly, Ce^{III} ($4f^1$) exhibits unique luminescence arising from 5d→4f transitions. Upon excitation, the single electron in the 4f orbital is promoted to the 5d orbit. A photon is emitted when the electron returns to the 4f orbital via radiative decay. As the 5d→4f transition is Laporte-allowed ($\Delta l = 1$), the emission can be intense and fast. Moreover, the 5d orbital is much more sensitive to the outer environment, leading to broad emission band and high sensitivity to the crystal field environment —behaviours reminiscent of the emission from transition-metal complexes.[102] More importantly, as the 5d level energy can be easily tuned through altering the crystal field, the emission wavelength of Ce^{III} is adjustable, covering the UV and Vis regions (~ 300 to 700 nm).[103-105] Together with its strong absorption and high quantum yield, luminescent Ce^{III} complexes are ideal for high-performance LEDs. Fang et al. reported the structural and PL properties of several tris(pyrazolyl)borate-based Ce^{III} complexes.[106] All of them exhibit blue 5d→4f transitions with high PLQY over 95% and short decay lifetimes of tens of nanoseconds (Figure 1.23). In addition to Ce^{III}, the 5d→4f transitions and their associated luminescence have also been studied on some divalent lanthanides, e.g. Eu^{II}, Yb^{II}, and Sm^{II}.[107,108]

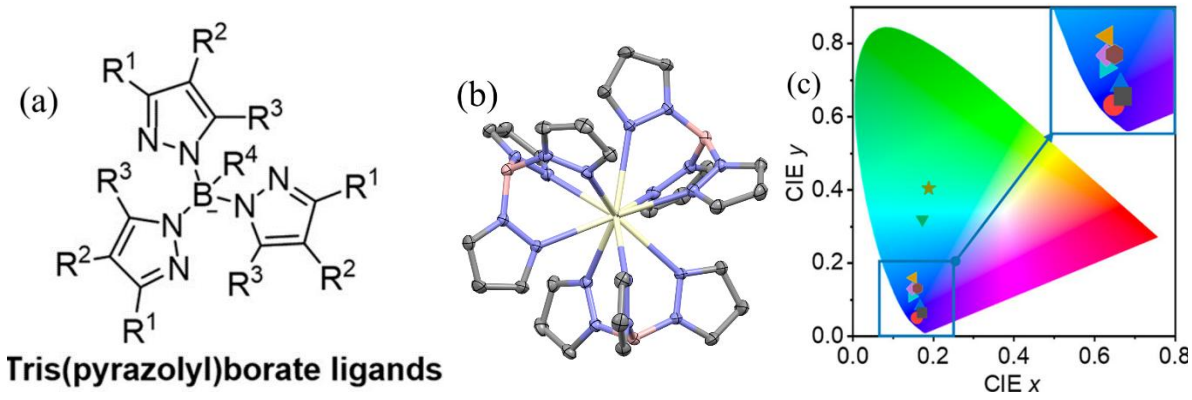

Figure 1.23. (a) Tris(pyrazolyl)borate) ligands. (b) Molecular structure of $Ce(Tp)_3$ (Tp^- = tris(pyrazolyl)borate). (c) CIE coordinates of the Ce^{III} complexes. Reused with permission from reference 106. Copyright (2021) American Chemical Society.

Lastly, though Pr^{III} ($4f^2$) and Ho^{III} ($4f^{10}$) possess potential 4f–4f transitions in the visible and NIR regions, they rarely display photoluminescence. This phenomenon arises from the combined effects of several factors, such as small energy gaps facilitating multi-phonon relaxation, inefficient energy transfer from ligand triplet states to metal emissive states, and non-radiative decay caused by energy migration between neighboring metal ions.[109,110]

Although direct excitation of the 4f–4f transition is possible for PL of lanthanide complexes, it is generally insufficient and impractical due to the weak absorption of light. This weak absorption arises again from the Laporte-forbidden nature of the 4f–4f electronic transitions, which is demonstrated by the very low value of molar extinction coefficients (ε ~1–10 $M^{-1}cm^{-1}$).

In contrast, organic ligands (chromophores) in complexes can act as antennae for light and sensitize the emission of lanthanides. The ligands, in particular aromatic or conjugated ones (e.g. 1,10-Phenanthroline, β-diketonates), have strong absorption bands in the ultraviolet (UV) or visible region and harvest excitation light efficiently. The absorbed energy is then transferred non-radiatively to the lanthanide ion via the ligand-to-metal energy transfer (LMET) process, typically occurring through the ligand's triplet excited state. Figure 1.24 schematically shows the mechanism, which is termed the antenna effect: photon absorption by ligands and subsequent energy transfer to the metal ion.[111] Via the antenna effect, the luminescence intensity of lanthanide complexes can be significantly enhanced, enabling their applications in fields such as bioimaging, sensing, and optoelectronics. In the meantime, as the emissions from lanthanide ions are typically observed in the visible or NIR region, large Stokes shifts are commonly observed in ligand-sensitized lanthanide complexes. In essence, the large Stokes shift arises from cumulative energy losses in the multi-step energy transfer process, including the energy dissipation from vibrational relaxations, IC, ISC and ligand-to-metal energy transfers.

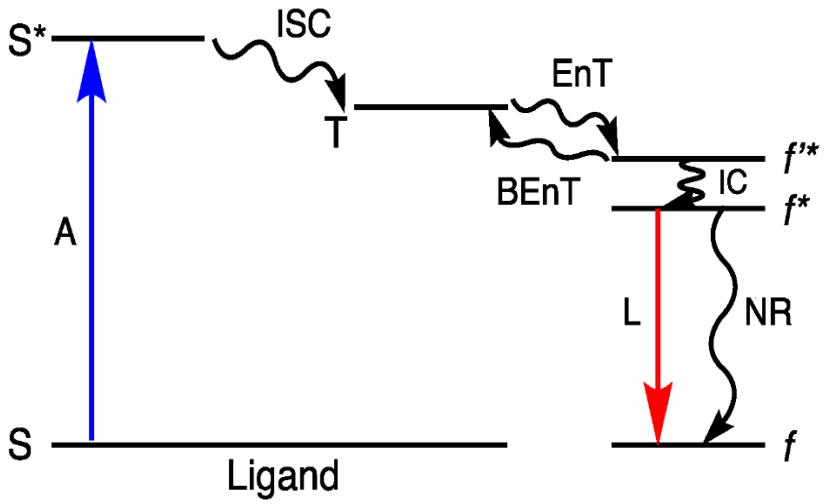

Figure 1.24. Schematic illustration of the energy migration process of Ln photoluminescence via antenna effect. S and S* represent ground and excited singlet states, respectively. The 4f states are denoted as *f* (ground state), *f** and *f'** (excited states). EnT and BEnT represent energy transfer and back energy transfer, respectively. NR denotes non-radiative decay. Blue arrow indicates light absorption process; red arrow shows luminescence process. Reused from reference 111, licensed under [CC BY 4.0] (http://creativecommons.org/licenses/by/4.0/), source: https://www.mdpi.com/1420-3049/25/9/2089.

The overall quantum yield for the ligand-sensitized luminescence of Ln^{III} (Φ_{Ln}^{L}) can be expressed as:

$$\Phi_{Ln}^{L} = \eta \times \Phi_{Ln}^{Ln} \qquad \text{Equation 1.11}$$

Here, η represents the sensitization efficiency and Φ_{Ln}^{Ln} represents intrinsic quantum yield for Ln^{III}.

Φ_{Ln}^{Ln} refers to the efficiency of the radiative decay process of a lanthanide ion from its excited state to its ground state. It is defined as:

$$\Phi_{Ln}^{Ln} = \frac{k_{rad}}{k_{\mathrm{rad}} + k_{\mathrm{non-rad}}} \qquad \text{Equation 1.12}$$

k_{rad}: radiative decay rate

$k_{non-rad}$: nonradiative decay rate

k_{rad} relies on several factors, for example, the lanthanide ion selection (e.g., Eu^{3+}/Tb^{3+} over Nd^{3+}/Yb^{3+}) and the local symmetry of ligand field. Meanwhile, $k_{non-rad}$ is dominated by the vibrational relaxation (via high-energy O-H, N-H, C-H bonds) and environmental quencher (e.g., O_2, water). Therefore, to achieve PL in lanthanide complexes, high-energy vibrations in ligands or solvents, which quench luminescence by dissipating energy as heat, should be minimized. Structurally rigid ligands should be prioritized to reduce vibrational/rotational motions. And the lanthanide center should be isolated from environmental quenchers. These strategies are more critical for NIR emitters, as the smaller energy gap ΔE of the radiative transitions drastically enhances $k_{\mathrm{non-rad}}$ as multi-phonon relaxation becomes highly efficient.

Regarding the sensitization efficiency η, it is evident that an optimal ligand-Ln^{III} distance is crucial for maximizing η. Because close proximity and orbital overlap are essential for effective LMET, and excessive separation will hinder this process. High ISC efficiency is another desired property to get bright PL materials, as it impacts how much energy are available to be transferred to lanthanides through the triplet state. Incorporating heavy atoms (e.g., Br, I) into the ligand or coordinating with metal ions can enhance ISC via spin-orbit coupling.[112]

Moreover, the triplet state energy of the "antenna" ligand should exceed the emissive states of the lanthanides for efficient LMET process. However, an excessively large energy gap ΔE between triplet state T_1 and the Ln^{3+} excited state can hamper LMET due to poor spectral overlap. On the other hand, a small ΔE facilitates the back energy transfer (BEnT) from lanthanides to ligands, particularly under thermal activation, which competes with metal-centered radiative emission and lowers η. For most Ln^{III} (e.g. Tb^{III}, Eu^{III}), empirical studies suggest the optimal range of ΔE is 2000 to 4000 cm^{-1}.[113] Due to the significant influence of the ligand's triplet state energy on PL properties, accurately determining the triplet state energy is a crucial step in studying the PL of lanthanide complexes.

As stated earlier, Gd^{III}, La^{III} and Lu^{III} complexes typically lack metal-centered luminescence, making them ideal for studying ligand-centered emission. Among them, Gd^{III} complexes exhibit a distinct tendency to favor phosphorescence over fluorescence at low temperatures. This arises from the paramagnetic enhancement effect: the large magnetic moment of Gd^{III} promotes spin-orbit coupling, thereby increasing the rate of ISC much significantly than La^{III} and Lu^{III}. The suppression of thermal quenching at cryogenic temperatures further stabilizes the triplet state, allowing phosphorescence to dominate. The

temperature-dependent phosphorescence spectra of Gd^{III} complexes provide a practical method to experimentally determine the T_1 energy levels of ligands. There are two commonly employed experimental approaches: the onset wavelength method and the shortest-wavelength peak method. In the former, the triplet energy is derived from the onset wavelength of the phosphorescence spectrum, defined as the point where emission intensity begins to rise from the baseline (Figure 1.25).[114] The latter can be used in systems with vibrational fine structure, where the triplet energy is extracted from the highest-energy (shortest-wavelength) peak in the spectrum, which corresponds to the 0-0 phonon transition.[115] This method is employed throughout this research, as the vibrational features are consistently resolvable and the shortest-wavelength peak provides higher precision.

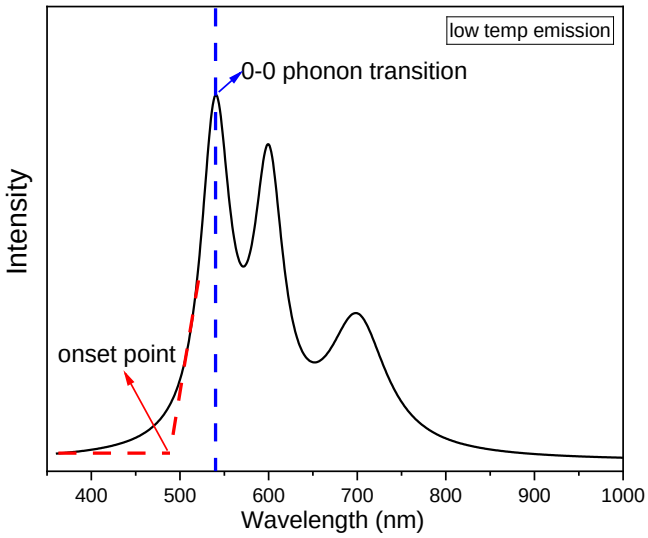

Figure 1.25. Illustrative low-temperature emission spectrum on a Gd complex with vibrational fine structure, showing the onset wavelength method (red) and the shortest-wavelength peak method (right) to extract the triplet state energy.

1.3.3 More energy transfer mechanisms in photoluminescent lanthanide complexes

Besides the ISC-mediated energy transfer pathway ($S_1 \rightarrow T_1 \rightarrow Ln$), direct energy transfer from the ligand's singlet excited state to the lanthanide ion ($S_1 \rightarrow Ln$) is also possible.[116] In such cases, the energy transfer occurs before ISC, allowing for a faster and potentially more efficient sensitization process. However, this direct singlet-to-lanthanide transfer is less common because the singlet state often relaxes too quickly to favor effective energy transfer.

There are several other energy transfer mechanisms in the sensitization of lanthanides' PL. The most important ones are charge transfer related, being ligand–ligand charge transfer

(LLCT), intra–ligand charge transfer (ILCT), ligand–metal charge transfer (LMCT), and metal-ligand charge transfer (MLCT).

LLCT involves the transfer of an electron from one ligand to another within the coordination sphere of the lanthanide complex. This mechanism is common in complexes with multiple ligands where one acts as an electron donor and another as an electron acceptor. The energy absorbed during this charge transfer can be transferred to the lanthanide ion, sensitizing its PL. LLCT can occur not only in hetero-ligand complexes, but also between two identical ligands. This is demonstrated in mononuclear Ln^{III} diradical complexes $[(DAD)_2Ln(BH_4)]$ (Ln = Yb, Lu; DAD = diazabutadiene) reported by Yan et al, which present LLCT transitions between DAD radical anions.[117]

Unlike LLCT, ILCT transitions happen exclusively within individual ligands. During LLCT, electron density redistributes within a single ligand, typically from an electron-rich group (e.g., amine group) to an electron-deficient group (e.g., carbonyl group) on the same molecule. The growing interest in ILCT-sensitized Ln^{III} PL in recent years is driven not only by its role as an alternative activation mechanism but also by its unique ability to enable visible-light excitation for NIR emitters, which circumvents high-energy UV irradiation that degrades biological samples or optical components. In an exemplary report by Zhang et al. in 2019, two dinuclear Yb^{III} complexes show high NIR PLQYs (> 1%) upon excitation with blue light at 420 nm, where the ILCT state and the classic triplet state of the bis-β-diketone ligands together participate in energy transfer processes to the Yb^{III} ions.[118]

LMCT involves the transfer of an electron from a coordinated ligand to the metal center. LMCT is especially relevant for easily reducible lanthanides (e.g., Eu^{III}, Yb^{III}, Sm^{III}). Since LMCT transitions are Laporte-allowed, their absorption bands are intense and broad compared to the weak, Laporte-forbidden f–f transitions—this facilitates efficient sensitization of lanthanide luminescence. However, LMCT can also quench emission, for example, it depletes the $^5D_0$ state nonradiatively through the "$^5D_0 \rightarrow$ LMCT state" channel when LMCT state lies lower in energy than the $^5D_0$ in an Eu complex.[119,120] The exact role of LMCT depends on its relative energy alignment and crossing-over not only with the lanthanide accepting states but also with the ligand's own singlet and triplet levels.[121-123] Therefore, tuning the LMCT energy level provides a key strategy for modulating the PL of lanthanide complexes.

Contrary to LMCT, in the MLCT transitions, an electron transfers from a metal-based orbital to a ligand-based orbital, typically the π* orbitals of an aromatic ligand. Similarly, the charge-transfer excited state can facilitate energy transfer to the lanthanide ion's 4f levels. MLCT is less common in lanthanide complexes compared to transition metal (in particular 4d and 5d metals, e.g., Ru, Ir) complexes due to the shielded nature of the 4f orbitals. It is also rarer compared to LMCT as the +4 oxidation state is less stable than +2 oxidation state for most lanthanides (except for Cerium). MLCT-mediated lanthanide PL is relevant primarily in d–f hybrid complexes, where the transition-metal complex moieties act as antenna chromophores for sensitization of lanthanide ions.[124,125]

In d–f hybrid complexes, energy migration may also happen directly between transition metals and lanthanide metals, thereby sensitizing the PL of lanthanides. For example, bimetallic 3d–4f complexes [LnCr] (Ln = Nd, Yb) reported by Imbert et al. reveal energy transfer from the $Cr(^2E)$ level to Nd^{III} and Yb^{III}, sensitizing their NIR luminescence.[126] The metal-metal energy transfer (MMET) can occur in heterometallic complexes containing different lanthanide ions, for example, from Eu^{III} to Yb^{III}.[127]

It is noteworthy that MMET does not only occur from an ion with a higher-lying emissive level to an ion with a lower-lying emissive level. One prominent counterexample is the cooperative sensitization (CS), where two low-energy ions jointly transfer energy to a high-energy acceptor. For instance, the CS process demonstrated by Panguluri et al. in a $[Eu_{9-x}Yb_x(BA)_{16}(OH)_{10}]Cl$ cluster (BA = benzoylacetonate, $x > 1$) cluster starts with the first Yb^{III} ion absorbing a 980 nm photon to populate its $^2F_{5/2}$ excited state, followed by a second Yb^{III} ion undergoing the same excitation. These two excited Yb ions (Yb*) then cooperatively transfer energy via the two-photon excited $[Yb_2^{**}Eu_{9-x}Yb_{x-2}]$ intermediate to Eu^{III}, populating its $^5D_1$ and $^5D_0$ levels and activating its characteristic red emission.[128] This CS process leads to the upconversion luminescence (UCL), — an anti-Stokes process where the absorbed photons are lower in energy than the emitted ones. While other UCL mechanisms exist which do not involve inter-ion energy transfer, they are not in the scope of this thesis.

More sensitization mechanisms have been identified in PL, such as: excimer-sensitized emission (originating from excited-state dimer formation through intermolecular π-orbital overlap) [129], excited-state-intramolecular-proton-transfer (ESIPT)-sensitized emission (emerging from photoinduced intramolecular proton transfer in keto-enol tautomeric system) [130], and aggregation-induced emission (AIE, stemming from restricted intramolecular motion in aggregated states) [131].

All the diverse sensitization mechanisms and energy transfer pathways advance the study of photoluminescent lanthanide complexes. These mechanisms are crucial in determining the overall luminescence efficiency, spectral characteristics, and temporal behaviour of lanthanide-based luminescent materials. Manipulating these energy transfer processes not only enables greater control over the photophysical properties of these complexes but also expands their practical applications in various technical domains.

1.3.4 Interplay between magnetism and optics in lanthanide complexes

Multifunctional materials, which exhibit two or more distinct physical properties—such as electrical, magnetic, or optical characteristics—are highly valuable for developing multi-responsive devices. Luminescent lanthanide SMMs, which combine luminescent functionalities and magnetic anisotropy, not only provide multifunctionality in single-phase material, but also pave the way for mutual modulation of their luminescent and magnetic properties. Moreover, most lanthanide SMMs are constructed using visible light emissive

Dy^{III} and Tb^{III} or NIR emissive Er^{III} and Yb^{III}, underscoring the great potential to obtain bifunctional luminescent materials. In this section, the correlation and interplay of magnetism and optics in lanthanide complexes will be explored, with a particular focus on photoluminescent SMMs.

M_J-splitting of lanthanide-based SMMs

The energy splitting of the ground multiplet plays a crucial role in the spin relaxation behaviour of lanthanide complexes. Determining the energy splitting of these sublevels is crucial for understanding magnetic relaxation mechanisms, such as the Orbach process, which involves transitions via excited states. Although computational methods, such as *ab initio* calculations using the CASSCF approach, can provide theoretical estimate of the energy splitting, their accuracy is limited, as discussed in Chapter 1.2.4. Meanwhile, the reliance on single crystal structure further constrains the application of CASSCF approach. The high-resolution PL spectroscopy, on the contrary, can determine the energy splitting experimentally of the investigated luminescent SMMs. This is achieved by the fact that the radiative transitions from the emissive excited states populate the ground state, including its M_J sublevels, and the energy differences from transitions to these M_J sublevels correspond to the energy splitting. To allow for clearer resolution of individual sublevels, PL measurements are typically performed at low temperatures to suppress thermal broadening. The energy splitting extracted from PL spectra can be further correlated with magnetic properties characterized by alternating current magnetometry, such as the energy barrier in the Orbach process, or with the energy splitting obtained from theoretical calculation, to gain deep insights into relaxation dynamics.

For example, M.L. Tong and co-workers reported a dinuclear zero field SMM $[Dy_2(bbpen)_2(tpcb)(MeOH)_2](BPh_4)_2$ (bbpen = N,N′-bis(2-hydroxybenzyl)-N,N′-bis(2-picolyl)ethylene diamine, tpcb = 1,2,3,4-tetra(pyridine-4-yl)cyclobutane).[132] The emission band corresponding to the $^4F_{9/2} \rightarrow {}^6H_{15/2}$ transition collected at 6 K exhibits a well-resolved structure, which is deconvoluted into eight peaks (Figure 1.26). These peaks correspond to the transitions to the eight degenerate doublets generated by the Stark splitting of $^6H_{15/2}$ sublevels. The energy separation between the second excited doublet and the ground doublet is calculated to be 1015 K, close to the experimental result (889 K obtained from Arrhénius law). Furthermore, the first two excited doulets obtained from the *ab initio* calculations (513 K for the 1st excited doublets, 970 K for the 2nd excited doublets) exhibit strong agreement with the fitting results of optical spectrum (574 K for the 1st excited doublets, 1015 K for the 2nd excited doublets), which validates the accuracy of *ab initio* calculations.

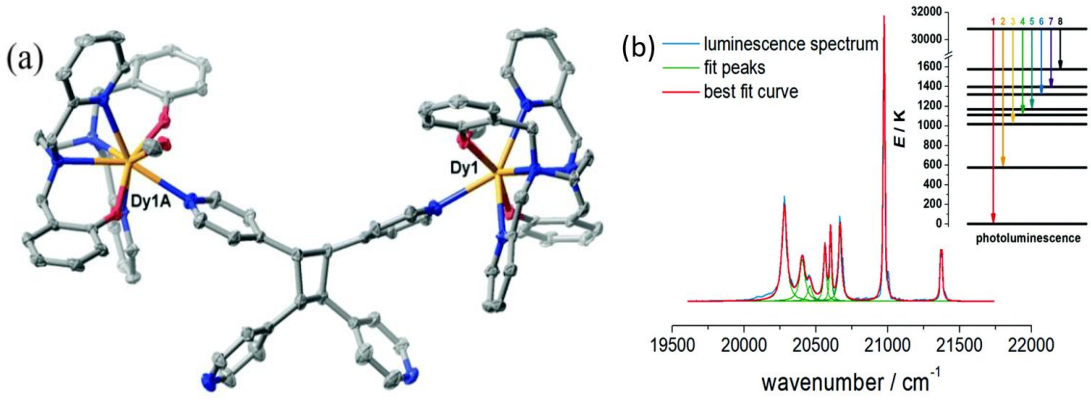

Figure 1.26. (a) molecular structure of $[Dy_2(bbpen)_2(tpcb)(MeOH)_2](BPh_4)_2$. (b) Deconvolution of fine $^4F_{9/2} \rightarrow {}^6H_{15/2}$ emission bands of $[Dy_2(bbpen)_2(tpcb)(MeOH)_2](BPh_4)_2$. Reused with permission from reference 132, copyright Royal Society of Chemistry.

Optical thermometers based on lanthanide complexes

The growing need to measure temperature at the nanoscale in fields—such as microelectronics and medical diagnostics—has driven the development of nanothermometers with micrometric or sub-micrometric spatial resolution.[133] Single molecules are ideal candidates for this purpose due to their small dimension, high sensitivity and localized response. By exploiting the temperature dependence of PL in lanthanide complexes, optical thermometers based on these materials can provide non-invasive contactless temperature sensing with high spatial resolution. The thermal probing capabilities of such complexes originates from various mechanisms, including temperature dependent lifetimes, emission intensities, and spectral shifts. Among these, optical thermometers based on ratiometric character, where the crucial thermometric parameters consist of the ratio between two distinct emission features, have attracted significant attention because they operate on intrinsic spectral ratios which remain robust under diverse experimental conditions.[134] One example of the ratiometric optical thermometers is the [Dy(bbpen)Cl] complex reported by Zanella et al.[135] The emission spectra of it reveal the characteristic $^4F_{9/2} \rightarrow {}^6H_{11/2,13/2,15/2}$ transitions of Dy^{III} (Figure 1.27, a). The most intensive $^4F_{9/2} \rightarrow {}^6H_{13/2}$ transition is selected to study luminescent thermometric features due to its larger signal-to-noise ratio. As shown in Figure 1.27, b–d, heating leads to a temperature-dependent intensity change due to the redistribution of the population on the M_J sublevels of the $^4F_{9/2}$ state: the longer-wavelength emission bands (e.g., 582.9–605 nm) decrease in intensity, while the shorter-wavelength bands (555–582.9 nm) intensify. The thermometric parameter Δ_T, defined as the integrated intensity ratio I_1/I_2 (where I_1 and I_2 correspond to the 555–582.9 nm and 582.9–605 nm spectral regions, respectively), exhibits three distinct linear regimes in the operational temperature range, demonstrating the potential of [Dy(bbpen)Cl] for thermometry across a wide temperature span.

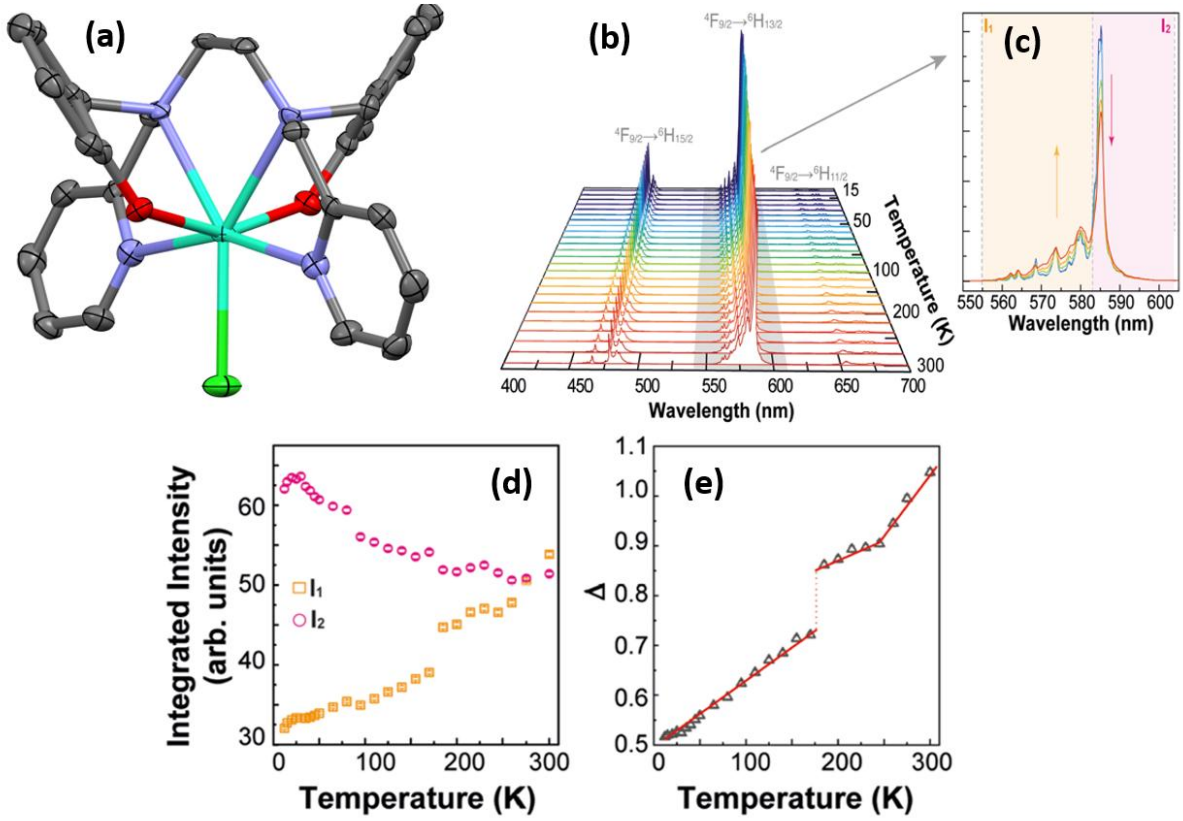

Figure 1.27. (a) Structure of [Dy(bbpen)Cl]. (b) Emission spectra of [Dy(bbpen)Cl] (12–300 K) upon excitation. (c) Magnification of the $^4F_{9/2}\rightarrow{}^6H_{13/2}$ transition displaying the temperature dependence I_1 and I_2 components. (d) Temperature dependence of I_1 and I_2 integrated areas. (e) Δ_T thermometric parameter. Reused from reference 135, licensed under [CC BY 4.0] (http://creativecommons.org/licenses/by/4.0/), source: https://onlinelibrary.wiley.com/doi/10.1002/anie.202306970?af=R.

The combination of optical thermometry with slow magnetic relaxation property in one complex can provide storage devices with self-monitoring ability, when the working temperature range of the optical thermometry overlaps with working temperature of the SMM. To achieve the overlapping is a challenging task, as the blocking temperatures of SMMs are typically very low. Nevertheless, significant progress has been made in designing lanthanide-SMM-based optical thermometers capable of operating in cryogenic regimes.[136] Notably, M. Murugesu and co-workers reported a dinuclear Dy^{III} complex $[Dy_2(bpm)(tfaa)_6]$ (bpm = 2,2′-bipyrimidine, tfaa =1,1,1-trifluoroacetylacetonate), which exhibits broad-range optical thermometry spanning 5–398 K, while its χ'' plot displays frequency-dependent shifting up to 12 K, indicative of slow relaxation of the magnetization behaviour in the thermometry temperature range.[137]

Light-induced change in magnetic properties

It is well established that light can affect magnetic properties (photo-magnetism) in transition-metal compounds via spin crossover (SCO) and electron transfer.[138-140] Such behaviours are less common in lanthanide complexes due to the shielded nature of the 4f orbitals. Nevertheless, photo-induced electron transfer can be achieved in ligands, thereby influencing the magnetic behaviour of lanthanide centers. Liao et al. reported the magnetic and luminescent dual responsive [Ln(L^{N6})(NO_3)$_2$](BPh_4)] [**1-Ln**, Ln = Dy, Tb, Eu, Gd, Y; L^{N6} = (3*E*,5*E*,10*E*,12*E*)-3,6,10,13-tetraaza-1,8(2,6)-dipyridinacyclotetradecaphane-3,5,10,12-tetraene] complexes, where organic radicals on L^{N6} are generated upon light according to EPR and UV−vis analyses.[141] Cyclic voltammetry measurements suggest PET from BPh_4^- to L^{N6}. The radical bearing **1-Dy*** presents not only weak ferromagnetic couplings between Dy^{III} ions and the L^{N6} radicals, but also markedly different magnetic relaxation behaviour from **1-Dy**.

Another pathway to influencing magnetic properties by light involves structural transformation in the ligands, including various photoisomerization (e.g., azobenzene derivatives), cycloaddition/dimerization (e.g., anthracene systems), or reversible pericyclic reactions (e.g., dithienylethenes).[142-145] Such photochemical reactions induce conformational or electronic changes in the ligand framework which can then be transmitted to the lanthanide ions. Both photo-induced electron transfer and photo-induced structural transformation provide a unique opportunity for rapid, remote and precise control of magnetic properties with high spatial and temporal resolution.[146] These methods often modify the color (photochromism) or luminescent properties of the complexes while modulating their magnetic properties, further enriching the research on lanthanide SMMs and their applications.

Magnetically induced change in optical properties

The photoluminescence in lanthanide complexes can be magnetically modulated via the Zeeman effect. Applied magnetic fields split the M_J sublevels, change their energy positions, and redistribute the population, thereby enabling magnetic control over emission intensity, polarization, and spectral profile. Ferreira et al. reported the photoluminescence for the SMM [Dy(acac)$_3$(H_2O)$_2$]·H_2O (acac = acetylacetonate) as a function of the external magnetic field.[147] The emission spectrum exhibits peak splitting, which follows the linear relationship $E = \mu_B g M_J H$ for $H < 10.0$ T. The splitting phenomenon not only enables quantitative magnetic field sensing, but also serves as a spectroscopic tool to investigate the magnetic anisotropy and the M_J sublevels of the lanthanide ions in luminescent SMMs. This presents a novel methodology for probing the electronic structure in luminescent lanthanide SMMs, complementary to conventional magnetic and EPR measurements.

In addition to the coexistence of the slow magnetic relaxation behaviour and the luminescent property, and beyond the magneto-luminescence and photo-magnetism, it has been demonstrated that luminescent lanthanide SMMs are versatile platforms for incorporating additional functionalities. For instance, studies have demonstrated their ability to host piezoelectricity and ferroelectricity.[148] Chirality-related effects, e.g., magneto-chiral

dichroism (MChD) and circularly polarized luminescence (CPL) are revealed in chiral luminescent lanthanide SMMs.[149,150] All these multifunctional capabilities and their promising applications have motivated the research on the magnetic and photophysical properties in lanthanide complexes. In the following section, the experimental methods for optical data collection used in this thesis will be introduced.

1.3.5 Variable temperature solid state photoluminescence measurements

PL spectroscopy, including excitation (ex) and emission (em) spectra, is the fundamental tool for understanding the PL properties of materials. In this work, the ex/em spectra are collected at the room temperature and the cryogenic range (e.g., 3.0 K). As previously discussed, lowering temperature can enhance the fluorescence intensity of lanthanides by suppressing non-radiative vibrational quenching, amplify phosphorescent emission in gadolinium complexes, and facilitate the resolution of M_J-sublevel-derived transitions by reducing thermal line broadening.

PL measurements are typically conducted in either solution state or solid state. In this work, all PL spectra are recorded in solid state, which allows for easier sample cooling and is more related to real-world application. Note that solid-state data can differ significantly from those in solution due to factors like intermolecular interactions (e.g., excimer formation, AIE), crystal packing, or lattice phonon modes.

Second- and higher-order artifacts originating from monochromator gratings and detector nonlinearities can interfere with the detection of genuine PL signals. They are signals at integer multiples of the excitation wavelength. For example, if the excitation source is at wavelength λ, second-order diffraction can appear at 2λ, third-order at 3λ, etc. They are typically recognizable since they feature structureless single peaks and appear at expected wavelengths. Meanwhile, the use of appropriate filters removes those peaks.

Experimentally, PL spectra are acquired using a Horiba Fluorolog-3 spectrofluorometer equipped with a 920 photomultiplier tube (PMT) detector (300–850 nm) and a nitrogen-cooled Hamamatsu NIR detector. Solid crystalline samples are mounted between two quartz plates with a drop of perfluorinated oil. Temperature control from 3.0 K to 300 K is achieved using a closed-cycle helium cryostat under high vacuum ($<10^{-5}$ mbar). Here, a 400 nm high pass cut-off filter is used for visible-region measurements to eliminate the second- and high order artifacts in ex/em spectra, when they obscure genuine PL signals. For the NIR detection, a 550 nm high pass cut-off filter is constantly placed on the optical path.

Chapter 2. Magnetic Properties of a series of Ni–Ln–Ni Trinuclear Complexes

2.1 Introduction

As mentioned in Chapter 1.2.1, single-molecule magnets (SMMs) with high spin reversal energy barriers and blocking temperatures T_B are highly sought after for their potential application in next generation information processing. Lanthanide ions, such as Dy^{III}, Tb^{III}, Er^{III}, Ho^{III}, are extensively employed in constructing high-performance SMMs due to their inherent large magnetic anisotropy and high magnetic moments. Among SMM candidates, 3d–4f hybrid complexes stand out as they not only retain the favorable properties of lanthanide ions but also gain additional versatility from the incorporation of diverse 3d ions. While some 3d–4f SMMs with diamagnetic 3d ions have demonstrated high energy barriers,[151-153] the most inspiring results are from 3d–4f SMMs featuring paramagnetic 3d ions. Several Fe^{II}–Dy–Fe^{II} or Co^{II}–Dy–Co^{II} trinuclear complexes, in which high spin Co^{II} and Fe^{II} coupled ferromagnetically with Dy^{III}, held the record for the highest energy barrier in 3d–4f SMMs for a long time,[48,52,154] until surpassed by two Ni–Ln complexes recently.[155,156] The new discoveries sparked my interest in Ni–Ln SMMs.

Most reported Ni–Ln SMMs either require an applied external field to show slow relaxation of magnetization or have low spin reversal energy barriers.[157-159] Despite the advances the effect of Ni^{II} ions in 3d–4f SMMs are not fully understood. The complexity of multi-metal systems with anisotropic spin centers hinders the quantitative evaluation of the magnetic couplings and their impacts. Though a comparative study on isostructural Ni^{II}–Ln and M–Ln (M being a diamagnetic ion, such as Zn^{II} or Mg^{II}) will give a qualitive indication whether the presence of Ni^{II} improves the SMM property in a certain system, only a few studies have been reported so far.[160,161] It is a very challenging task to obtain a Ni–Ln complex with an ideal structure, in which Ni^{II} ions can exert positive impacts on the SMM behaviour. This indicates the need for precise molecular design. There are several obstacles to be overcome: Firstly, it usually requires ferromagnetic couplings between 3d and 4f ions to increase the ground spin state *S*, but when the coupling is weak, the magnetic directions of the paramagnetic 3d ions can flip-flop easily, and create a fluctuating field, thereby enhancing the rate of magnetization relaxation associated with the lanthanide centers.[162] Besides, in some dinuclear or polynuclear lanthanide SMMs, when the easy axes of different metal centers inside one molecule are tilted, or parallel but not colinear, the metal centers will apply transverse magnetic fields (or moments) to each other which can induce fast QTM.[81,83] Lastly, the paramagnetic Ni^{II} ion can have either uniaxial anisotropy ($D < 0$) or easy-plane anisotropy ($D > 0$), a mismatch of the anisotropies between Ni^{II} and lanthanide ions is unfavorable for obtaining high performance Ni^{II}–Ln SMMs.[163] Therefore, the control over the magnetic anisotropies and their relative orientations is crucial for utilizing the d–f coupling to harness desirable SMM characteristic.

I noticed two trinuclear Zn–Ln–Zn (Ln = Tb and Gd) linear complexes reported in 2020 and 2023, synthesized using a tripodal Schiff base ligand tris(((2-hydroxy-3-methoxybenzyl)-amino)ethyl)amine (H_3L, Figure 2.1)[164,165]. The central lanthanide ions were uniaxial anisotropic and exhibited slow relaxation of magnetization. Meanwhile, the low nuclearity and high symmetry of the structure allow easier interpretation of the magnetic behaviour. These facts motivated me to synthesize similar complexes where the diamagnetic Zn^{II} ions were replaced by paramagnetic Ni^{II} ions.

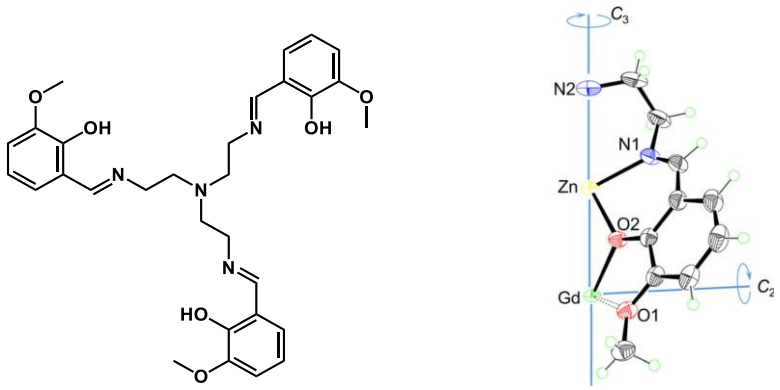

Figure 2.1. (Left) The molecular structure of ligand H_3L. (Right) Ortep drawing with atom labeling of the independent part of reported Zn–Gd–Zn cation at the 50% probability level.

Herein, a series of isostructural $[Ln(NiL)_2]CF_3SO_3$ (**Ln_1**, Ln = Y, Ce, Pr, Nd, Sm, Eu, Gd, Tb, Dy, Ho, Er, Tm, Yb) were synthesized, characterized, and their static and dynamic magnetic properties were studied. A comparative study between **Dy_1** and the isostructural **DyZn2** revealed the role of Ni^{II} on SMM property. Magnetic properties of **Y_1**, **Gd_1**, **Tb_1**, **Dy_1**, **Ho_1**, **Er_1** and **Yb_1** have also been investigated using micro-SQUID. The open hysteresis loops observed for **Gd_1**, **Tb_1**, **Dy_1**, **Ho_1** were related to the cooperative behaviour between the Ni and Ln ions.

A second series of five Ni–Dy–Ni trinuclear complexes, $[Dy(NiL)_2]PF_6$ (**Dy_2**), $[Dy(NiL)_2]NO_3{\cdot}2H_2O{\cdot}3CH_3OH$ (**Dy_3**), $[Dy(NiL)_2]Cl{\cdot}4CH_3OH$ (**Dy_4**), $[Dy(NiL)_2]ClO_4{\cdot}2.5\,CH_3OH$ (**Dy_5**) and $[Dy(NiL)_2]BPh_4{\cdot}CH_3OH$ (**Dy_6**), differing in the composition of counterions and lattice solvents relative to **Dy_1**, were synthesized and characterized. Comparative studies across **Dy_1** – **Dy_6** demonstrated the influence of counter-anions on the structural and magnetic properties of these complexes. Ferromagnetic Dy–Ni intramolecular couplings were present in **Dy_1** – **Dy_6**. The slow relaxation of magnetization properties of all the complexes were investigated and compared, under both zero field and applied optimal fields. Moreover, a "partial dilution" experiment, where **Dy_1** molecules were dispersed in **Y_1** matrix, was conducted to explore the role of intermolecular interaction in **Dy_1**.

Theoretical calculations were conducted to elucidate the relaxation processes in **Dy_1** – **Dy_6**. Strategies to increase spin reversal barriers in Ni–Ln complexes were proposed,

supported by calculations on hypothetical models and analyses of the structure-magnetic property correlations in previously reported Ni–Ln SMMs.

2.2 Synthesis details

General procedures

All chemicals and reagents purchased from commercial sources (Sigma-Aldrich, TCI chemicals, abcr) were of reagent grade and used without further purification. Ligand H_3L was synthesized by a simple condensation reaction of tris(2-aminoethyl)amine (tren) and *O*-vanillin in methanol. All the Ln–Ni complexes were synthesized by either slow evaporation of the solvents or slow diffusion of layered solutions under air atmosphere. For **Ln_1**, **Dy_2**, and **Dy_3**, the methanol solution of lanthanide salts was layered on top of the methanol solution containing H_3L and the corresponding Ni salts in long test tubes, allowing slow mixing of the reactants to grow large crystals. Due to the high solubility of compound **Dy_4** in methanol, a more straightforward slow evaporation method was used to grow the crystals of **Dy_4** from a more concentrated methanol solution. In the cases of **Dy_5** and **Dy_6**, $Dy(ClO_4)_3$ aqueous solution and $NaBPh_4$ were used to introduce the ClO_4^- and BPh_4^- counter-anions, respectively, where the $Ni(ClO_4)_2$, $Dy(BPh_4)_3$, and $Ni(BPh_4)_2$ are not on stock in the lab and less common commercially. $NiCl_2{\cdot}6H_2O$ and $DyCl_3{\cdot}6H_2O$ (for **Dy_6**) were used as the sources of metal ions in the slow diffusion. The successful syntheses of the pure desired products indicated that chloride ions wouldn't participate in the formation of complexes in the presence of ClO_4^- or BPh_4^-, which is in line with the high solubility observed for **Dy_4** in its crystal growth process.

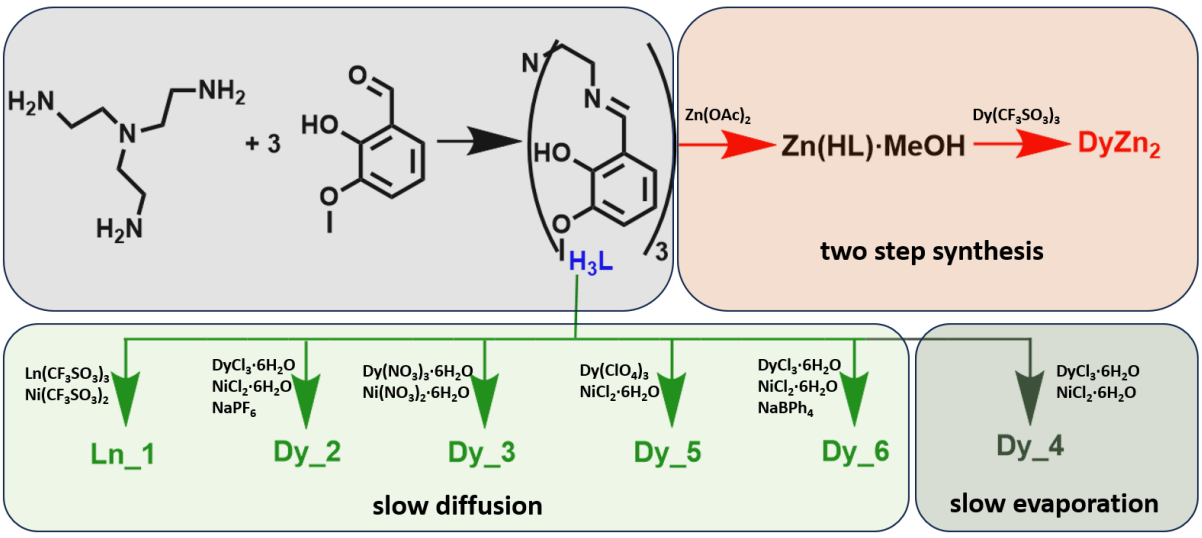

Scheme 2.1. Synthetic routes of **Ln_1**, **Dy_2** – **Dy_6** and **DyZn2**.

The Zinc-containing Complex **DyZn$_2$** was synthesized in two steps following a previously reported protocol.[164,165] Zn(HL)·MeOH was prepared first by stirring H_3L and zinc acetate in methanol. The obtained zinc *ligand complex* was further reacted with dysprosium triflate in an ethanol/methanol solution with the presence of NEt_3 in an oven at 45 ℃. All our attempts to get **DyZn$_2$** in one step, either by slow diffusion or by slow evaporation, failed to give the expected compound, demonstrating the different reactivity of Zn^{II} and the necessity of the two-step synthesis protocol.

Syntheses of nickel(II) trifluoromethanesulfonate

Slightly excessive trifluoromethanesulfonic acid (1.80 g, 12.0 mmol) was added dropwise to a clear green solution of $Ni(OAc)_2{\cdot}4H_2O$ (1.24 g, 5.0 mmol) in MeCN (100 mL) at room temperature. After stirring for 1 hour, the mixture was concentrated under reduced pressure to around 15 mL, and diethyl ether (100 mL) was added. The resulted blue precipitation was then filtrated and washed with cold diethyl ether and hexane. After drying in an oven at 60 °C overnight, 1.12g $Ni(CF_3SO_3)_2$ (FW = 548.63, yield 62.7 %) was obtained.

Syntheses of Tris(((2-hydroxy-3-methoxybenzyl)-amino)ethyl)amine (H_3L)

Three equivalents of *O*-vanillin (2.28 g, 15.0 mmol) was added to a clear colorless solution of tris(2-aminoethyl)amine (0.73g, 5.0 mmol) in MeOH (15 mL) at room temperature. The resulting yellow solution was stirred for 4 hours. During the stirring, thick yellow precipitate started to form. The precipitate was filtered, washed with cold MeOH and diethyl ether and dried in an oven at 60 °C overnight to give 2.12 g H_3L ($C_{30}H_{36}O_6N_4$, FW = 548.63, yield 77.1%).

Synthesis of $[Ln(NiL)_2]CF_3SO_3$ (**Ln_1**, Ln = Y, Ce, Pr, Nd, Sm, Eu, Gd, Tb, Dy, Ho, Er, Tm, Yb)

H_3L (27.5 mg, 0.05 mmol) and $Ni(CF_3SO_3)_2$ (18.0 mg, 0.05 mmol) were dissolved together in 12 mL methanol. After adding triethylamine (15.0 mg, 0.15 mmol), the solution was stirred for 10 mins and subsequently transferred to a 20 mL long test tube. Then, a 4 mL methanol solution of 0.025 mmol $Ln(CF_3SO_3)_3$ was carefully layered on top of the previous solution. Crystals with hexgonal prism shape formed after 4 to 7 days (yield 24.1–31.2%). The color for all **Ln_1** is green, with the only exception of **Eu_1** being brownish-red. Anal. Calcd for **Dy_1** ($DyNi_2C_{61}H_{66}F_3N_8O_{15}S$, FW = 1520.17 g·mol^{-1}): C, 48.20; H, 4.38; N, 7.37. Found: C, 48.25; H, 4.33; N, 7.39.

Synthesis of $[Dy(Ni_2)]PF_6$ (**Dy_2**)

H_3L (27.5 mg, 0.05 mmol) and $NiCl_2·6H_2O$ (12.0 mg, 0.05 mmol) were dissolved together in 14 mL methanol. After adding triethylamine (15.0 mg, 0.15 mmol), the solution was stirred for 10 mins and subsequently transferred to a 20 mL long test tube. Then, a 4 mL methanol solution of $DyCl_3·6H_2O$ (9.4 mg, 0.025 mmol) and $NaPF_6$ (6.0 mg, 0.036 mmol) was carefully layered on top of the previous solution. Green crystals with hexgonal prism shape formed after 2 days (yield 28.3%). Anal. Calcd for **Dy_2** ($DyNi_2C_{60}H_{66}F_6N_8O_{12}P$, FW = 1516.06 $g·mol^{-1}$): C, 47.53; H, 4.39; N, 7.39. Found: C, 47.40; H, 4.35; N, 7.44.

Synthesis of $[Dy(NiL)_2]NO_3·2H_2O·3CH_3OH$ (**Dy_3**)

H_3L (27.5 mg, 0.05 mmol) and $Ni(NO_3)_2·6H_2O$ (14.5 mg, 0.05 mmol) were dissolved together in 12 mL methanol. Following the addition of triethylamine (15.0 mg, 0.15 mmol), the solution was stirred for 10 mins and then transferred to a 20 mL long test tube. Subsequently, a 4 mL methanol solution of $Dy(NO_3)_3·6H_2O$ (11.4 mg, 0.025 mmol) was carefully layered on top of the previous solution. Green crystals with rod shape formed after 2 days (yield 33.8%). Anal. Calcd for **Dy_3** ($DyNi_2C_{63}H_{82}N_9O_{20}$, FW = 1565.26 $g·mol^{-1}$): C, 48.34; H, 5.28; N, 8.05. Found: C, 47.30; H, 5.17; N, 7.92.

Synthesis of $[Dy(NiL)_2]Cl·4CH_3OH$ (**Dy_4**)

H_3L (55.0 mg, 0.1 mmol) and $NiCl_2·6H_2O$ (24.0 mg, 0.1 mmol) were dissolved together in 12 mL methanol. The solution was first stirred for 10 mins after adding triethylamine (30.0 mg, 0.30 mmol), and then for another 10 mins upon the addition of $DyCl_3·6H_2O$ (18.8 mg, 0.05 mmol). Slow evaporation of the final yellow solution at room temperature gave green crystals with rod shape after 3 days (yield 16.1%). Anal. Calcd for **Dy_4** ($DyNi_2C_{64}H_{82}ClN_8O_{16}$, FW = 1534.72 $g·mol^{-1}$): C, 50.09; H, 5.39; N, 7.30. Found: C, 49.35; H, 5.20; N, 7.23.

Synthesis of $[Dy(NiL)_2]ClO_4·2.5CH_3OH$ (**Dy_5**)

Caution: perchlorate salts are potentially explosive and should be handled with extreme care.

H_3L (27.5 mg, 0.05 mmol) and $NiCl_2·6H_2O$ (12.0 mg, 0.05 mmol) were dissolved together in 12 mL methanol. After adding triethylamine (15.0 mg, 0.15 mmol), the solution was stirred for 10 mins and subsequently transferred to a 20 mL long test tube. Then, a 4 mL methanol solution containing 16.5μL 50 % $Dy(ClO_4)_3$ aqueous solution (25.0 mg, 0.027 mmol) was carefully layered on top of the previous solution. Green crystals with rod shape formed after 4 days (yield 30.3%). Anal. Calcd for **Dy_5** ($DyNi_2C_{62.5}H_{75}ClN_8O_{18.5}$, FW = 1549.67 $g·mol^{-1}$): C, 48.44; H, 4.88; N, 7.23. Found: C, 48.12; H, 4.77; N, 7.16.

Synthesis of $[Dy(NiL)_2]BPh_4 \cdot CH_3OH$ (**Dy_6**)

H_3L (27.5 mg, 0.05 mmol) and $NiCl_2 \cdot 6H_2O$ (14.5 mg, 0.05 mmol) were dissolved together in 12 mL methanol. After adding triethylamine (15.0 mg, 0.15 mmol), the solution was stirred for 10 mins and subsequently transferred to a 20 mL long test tube. A 4 mL methanol solution of $DyCl_3 \cdot 6H_2O$ (9.4 mg, 0.025 mmol) and $NaBPh_4$ (15 mg, 0.042 mmol) was then carefully layered on top of the previous solution. Green crystals with rod shape formed after 3 days (yield 27.0%). Anal. Calcd for **Dy_6** ($DyNi_2C_{85}H_{91}BN_8O_{13}$, FW = 1723.38 $g \cdot mol^{-1}$): C, 59.24; H, 5.32; N, 6.50. Found: C, 59.30; H, 5.29; N, 6.39.

Synthesis of $Dy(ZnL)_2CF_3SO_3$ (**$DyZn_2$**)

Step 1: H_3L (1.1 g, 2.0 mmol) and $Zn(OAc)_2$ (0.37 g, 2.0 mmol) were dissolved in 20 mL methanol. The solution was evaporated to dryness, and the resulting orange oil was dissolved in 20 mL methanol and dried again. This procedure was repeated 5 times to remove the acetate anions. The resulting oil is then used directly in the next step.

Step 2: Oily product (66.0 mg) prepared from the first step was dissolved in 4 mL methanol together with $Dy(CF_3SO_3)_3$ (30.5 mg, 0.05 mmol). Then a 1 mL ethanol solution containing triethylamine (60.0 mg, 0.6 mmol) was added into the former methanol solution. The mixture solution was stirred for 5 mins and left to stand in an incubator at 45℃. Yellow hexagonal prismatic crystals were obtained after 2 days (yield 35.4%). Anal. Calcd for **$DyZn_2$** ($DyZn_2C_{61}H_{66}F_3N_8O_{15}S$, FW = 1533.56 $g \cdot mol^{-1}$): C, 47.78; H, 4.34; N, 7.30. Found: C, 46.89; H, 4.43; N, 7.21.

2.3 Molecular structures

The single crystal structures of the six nickel-containing **Dy_1** – **Dy_6** and **$DyZn_2$** were determined by SC-XRD techniques. Powder-XRD measurements confirmed the phase purity of their bulky samples (Figure S1–S5). Powder-XRD measurements were also performed on all the **Ln_1** (Ln = Y, Ce, Pr, Nd, Sm, Eu, Gd, Tb, Dy, Ho, Er, Tm, Yb) complexes. The similar powder-XRD spectra of all the **Ln_1** indicated that all of them are isostructural (Figure S6). In the following discussion, the structure of **Dy_1** will be described in detail as a representative for **Ln_1** series of complexes. The structures of **Dy_2** – **Dy_6** and **$DyZn_2$** complexes are also presented in this section.

Seven Dy complexes **Dy_1** – **Dy_6** and **$DyZn_2$** reported in this chapter can be categorized into two groups based on the symmetries of the M–Dy–M (M = Ni, Zn) trinuclear structures. The first group comprises **Dy_1**, **Dy_2** and **$DyZn_2$**, which have strictly linear main structures with the ∠Ni–Dy–Ni in **Dy_1** and **Dy_2**, ∠Zn–Dy–Zn in **$DyZn_2$** all being 180°. In the

second group, ∠Ni–Dy–Ni in **Dy_3** – **Dy_6** slightly deviates from 180°, leading to not fully linear but lightly bent Ni–Dy–Ni trinuclear structures (Table 2.1).

Table 2.1 the angles (°) of M–Dy–M in the complexes **Dy_1 – Dy_6** and **$DyZn_2$**

First group		Second group	
Dy_1	180	**Dy_3**	176.63
Dy_2	180	**Dy_4**	177.12
$DyZn_2$	180	**Dy_5**	176.81
		Dy_6	173.51

The complexes—**Dy_1**, **Dy_2** and **$DyZn_2$**— in the first group all crystalize in the *R*32 space group, trigonal crystal system, with Z = 3. The detailed crystallographic information is provided in Table S1. Since **$DyZn_2$** is isomorphic to **Dy_1**, and **Dy_2** has the similar $[Dy(NiL)_2]^+$ main structure with **Dy_1** (see later), only the structure of **Dy_1** will be described in detail and the structural difference regarding **Dy_2** and **$DyZn_2$** will be added for comparison. In **Dy_1**, two deprotonated H_3L ligands each encapsulate one Ni^{II} in the inner N_3O_3 coordination pocket formed by three imine–N and three μ_2-O(phenoxy). The two resulting $[NiL]^-$ units subsequently sandwich a Dy^{III} from opposite directions with their phenol–O (Figure 2.2). Six uncoordinated methoxy groups lie equatorially around the central Dy^{III} ion and shield it from the environment. The Ni–N, Ni–O and Dy–O bond distances are 2.090(4) Å, 2.062(3) Å, and 2.346(3) Å, respectively. The intramolecular Dy–Ni distance is 3.2442(8) Å. A 3-fold rotation axis passes through the linear Ni–Dy–Ni array and three additional *C*2 axes lie perpendicular to the 3-fold principal axis. Hence, the $[Dy(NiL)_2]^+$ cation has D_3 symmetry and each asymmetric unit of **Dy_1** contains one sixth of the cation.

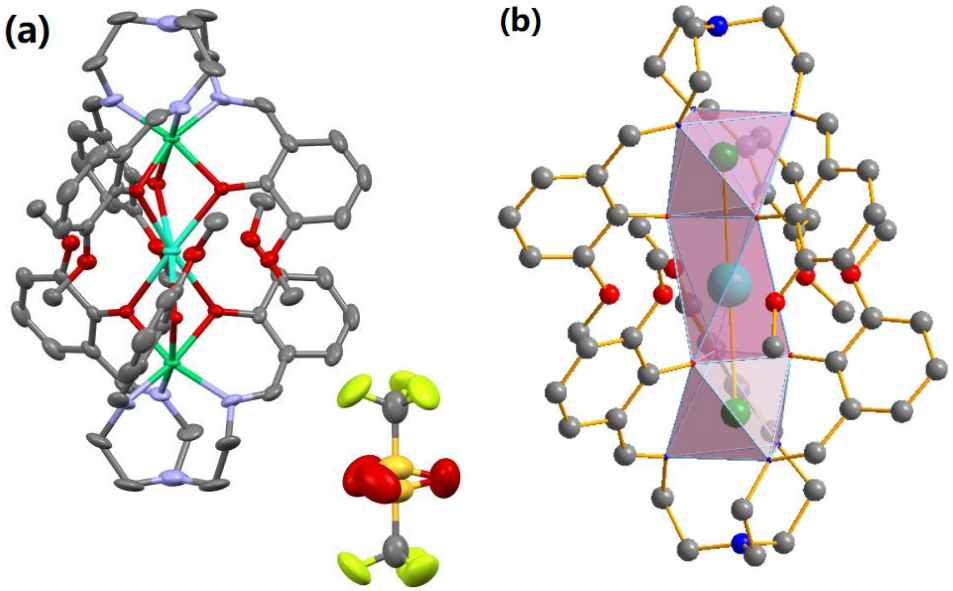

Figure 2.2. (a) Molecular structures of **Dy_1**; (b) the $[Dy(NiL)_2]^+$ cation with coordination polyhedrons around metal centers. H atoms are omitted for the sake of clarity. Colour code: Dy, cyan; O, red; N, blue; C, grey; S, orange; F, yellow; Ni, green.

The coordination polyhedron around Ni^{II} is close to regular octahedron, with the opposite N_3 and O_3 triangular faces both being equilateral. At variance, the polyhedron around the six-coordinated Dy^{III} departs more from regular octahedron as shown by the continuous shape measures (CShM) calculated on SHAPE 2.1 program (Table S2, S3).[47] In fact, the coordination geometry of Dy^{III} is better described as axially elongated trigonal antiprism, with the twist angle θ = 44.95°, the dihedral angle φ = 67.73° (θ and φ in Figure 2.3, for a regular octahedron, θ and φ both equal to 60°). The triflate ions in the lattice, which balance the charges, not only locate along the 3-fold axes, but also disorder in a head to head manner so that the disordered anions feature the D_3 molecular symmetry as well. All the $[Dy(NiL)_2]^+$ cations in the crystal lattice are arranged in the same direction (Figure S7). The closest intermolecular Dy···Dy and Dy···Ni distances between neighboring molecules are 11.87 Å and 11.76 Å, respectively, long enough to quench intermolecular Dy···Dy and Dy···Ni interactions. In comparison, the closest intermolecular distance between two terminal Ni^{II} ions is relatively shorter (9.32 Å) as a result of the linear shape of $[Dy(NiL)_2]^+$ cations.

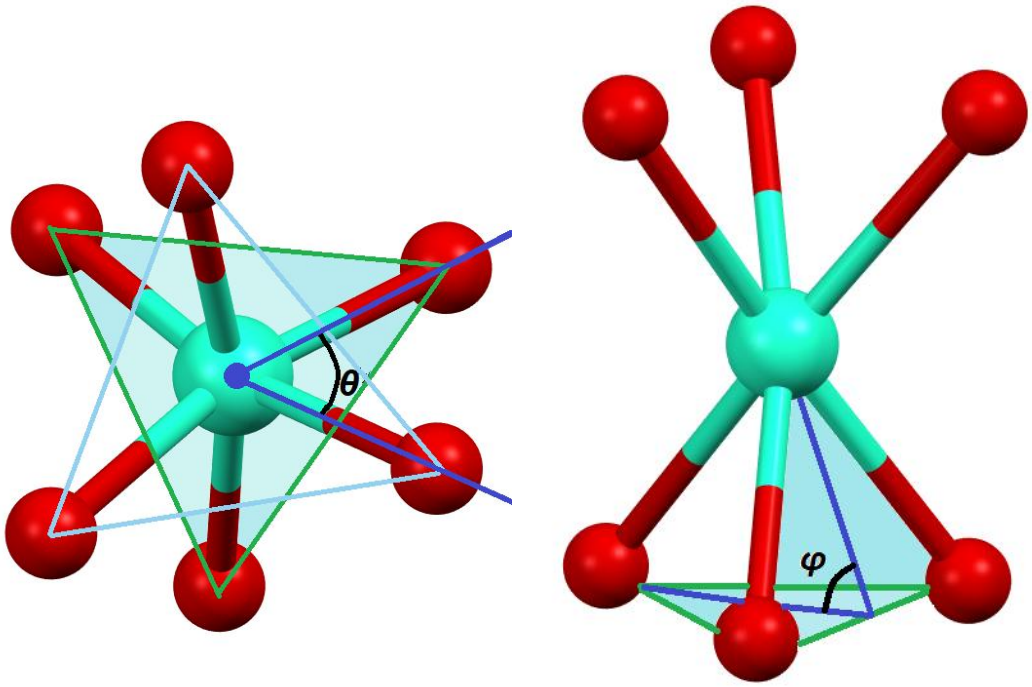

Figure 2.3. Top view (left) and side view (right) of the coordination structure around Dy^{III} in **Dy_1**. Colour code: Dy, cyan; O, red.

Dy_2 has almost identical $[Dy(NiL)_2]^+$ main structures as **Dy_1**, as shown by the bond lengths and bond angles (Table S4), including similar θ and φ angles (θ = 43.96°, φ = 67.55°). The only major difference between **Dy_1** and **Dy_2** lies in the counter-anions. Instead of one triflate ion, there is a hexafluorophosphate ion in **Dy_2** for each $[Dy(NiL)_2]^+$ cation (Figure 2.4, a). The hexafluorophosphate ion is not disordered, which is quite reasonable, because unlike the triflate, the O_h symmetric hexafluorophosphate ion can fulfill the D_3 symmetry

without disordering. The replacement of the counter-anions doesn't impact the packing pattern or the unit size of **Dy_2** much, as shown in the close unit cell parameters and similar PXRD spectrum of **Dy_1** and **Dy_2**. (Table S1, Figure S1). The closest intermolecular Dy···Dy, Dy···Ni and Ni···Ni distances from neighboring molecules for **Dy_2** are 11.84 Å, 11.67 Å and 9.25 Å in sequence.

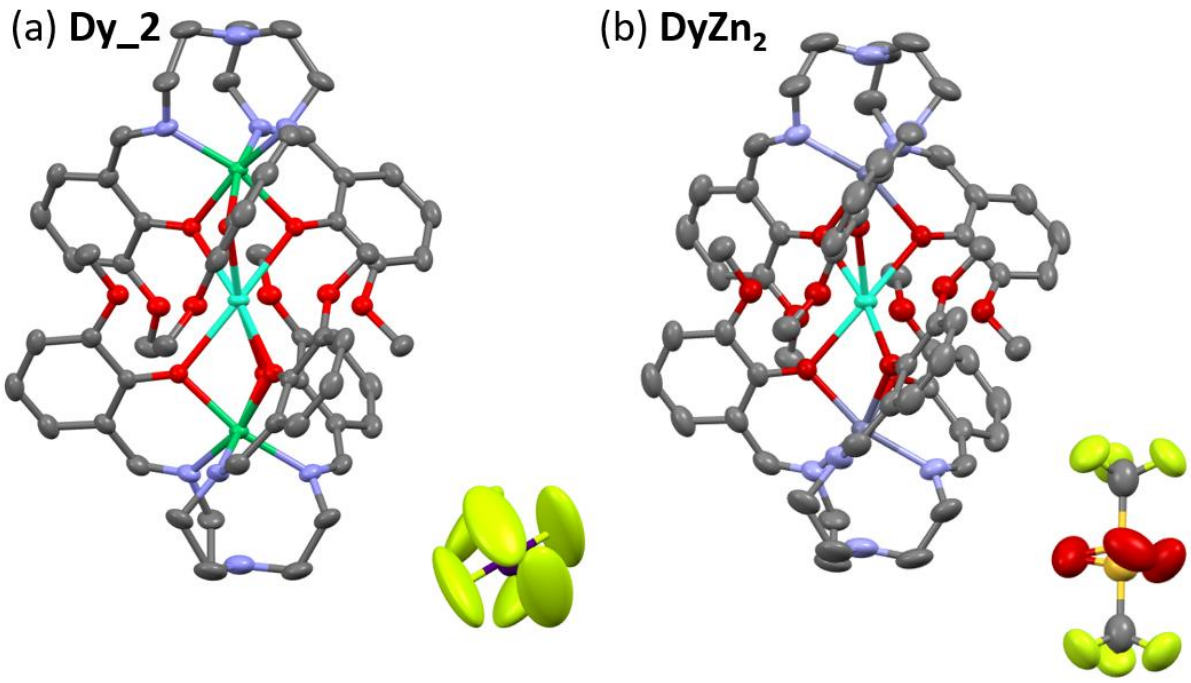

Figure 2.4. Molecular structures of **Dy_2** (a) and **DyZn$_2$** (b). H atoms are omitted for the sake of clarity. Colour code: Dy, cyan; O, red; N, blue; C, grey; P, purple; F, yellow; Ni, green; S, orange; Zn, navy blue.

The zinc ions in **DyZn$_2$** have larger radii compared to nickel ions in **Dy_1** and **Dy_2**, leading to longer Zn–O and Zn–N distances, being 2.155(3) Å and 2.129(4) Å, respectively. The Dy–O bond length is 2.349(3) Å, almost the same as that in **Dy_1** and **Dy_2**, regardless of the change in the transition metals (Table S4). In **DyZn$_2$**, the coordination environment around Dy^{III} is measured by twist angle θ = 37.64° and dihedral angle φ = 67.39°, so that as the trigonal antiprism geometry is similarly elongated along the C_3 axis as that in **Dy_1** and **Dy_2**, the twist angle θ in **DyZn$_2$** differs moderately (Figure 2.4, b). In all three complexes, no hydrogen bonds or other weak interactions is found between the trinuclear cations and the counter-anions, as shown in the packing diagrams (Figure 2.5).

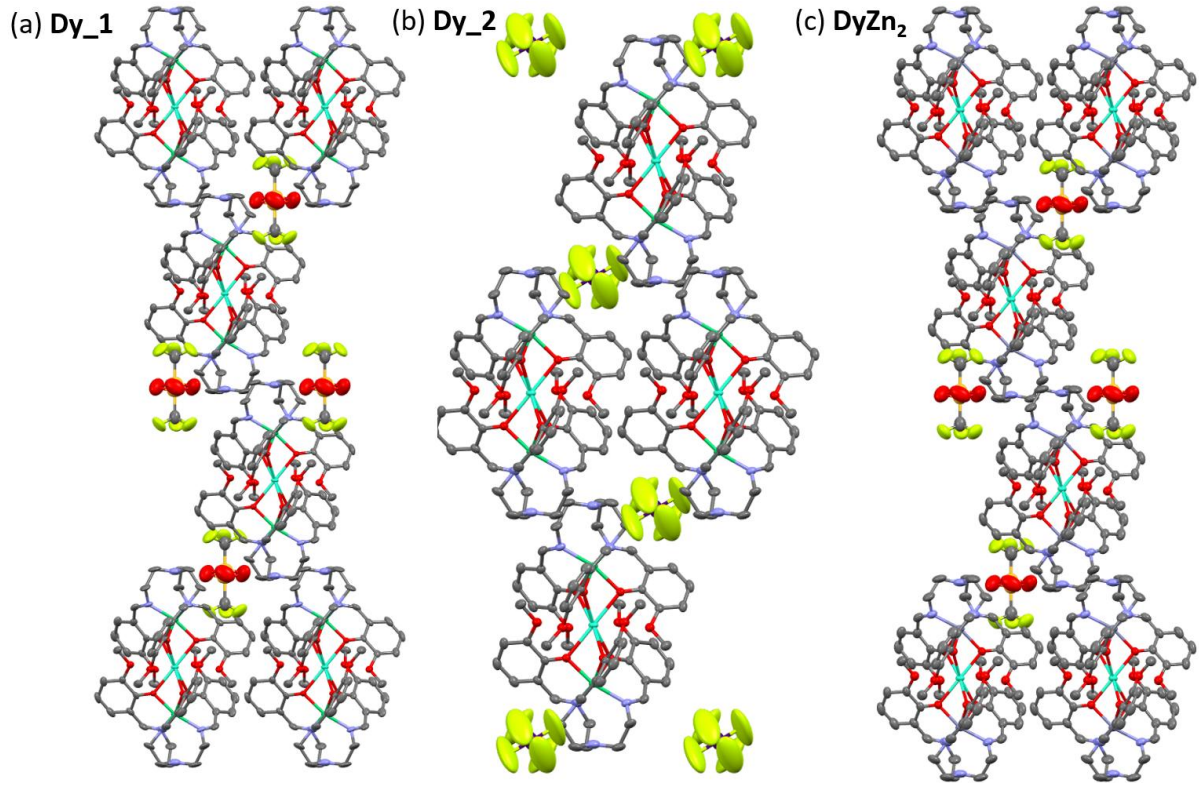

Figure 2.5. The packing diagram of **Dy_1** (a), **Dy_2** (b), and **DyZn2** (c) along the direction of *a* axis.

As described in some other M–Ln–M complexes formed by *O*-vanillin containing tripodal ligands, the twisting of H_3L around the 3d ion leads to chiral Δ or Λ configuration,[166,167] and the assembly of two ML^- pairs in one molecule may further yield homochiral Δ-Δ or Λ-Λ configuration, or meso Δ-Λ configuration. **Dy_1**, **Dy_2**, and **DyZn2** all have homochiral configurations (Figure S8). However, Flack parameter close to 0.5, which indicates the presence of merohedral twins, is observed in every measured crystal (Table S1). Therefore, at least with the current synthetic methods, no enantiomerically pure single crystals are obtained for **Dy_1**, **Dy_2**, and **DyZn2**.

In the second group, complexes **Dy_3** and **Dy_4** both crystalize in the less symmetric $P2_1/n$ space group, monoclinic crystal system, with Z = 4. They share similar unit cell parameters (Table S5), and similar $[Dy(NiL)_2]^+$ main structures, just like the case of **Dy_1** and **Dy_2**. Due to the lowering of crystallographic symmetry, one asymmetric unit now consists of a whole $[Dy(NiL)_2]^+$ cation, a counter-anion (nitrate for **Dy_3**, chloride for **Dy_4**), and several lattice solvents. The $[Dy(NiL)_2]^+$ cations lose the C_3 and C_2 rotation axes, because the Ni–Dy–Ni angles deviate from 180°. As a consequence, the two terminal Ni^{II} ions inside one $[Dy(NiL)_2]^+$ cation are no longer crystallographically equivalent, though their coordination geometries are still both closest to octahedron (Table S6). Meanwhile, though the central Dy^{III} ions remain six-coordinated by oxygen atoms from phenoxy groups, there are slight differences in the Dy–O bond lengths. The Dy–O bond lengths range from 2.320(3) Å to 2.380(3) Å in **Dy_3** and 2.332(3) Å to 2.383(3) Å in **Dy_4** (Table S7). SHAPE analysis

reveals that the coordination geometries around the Dy^{III} ions in **Dy_3** and **Dy_4** are nearly identical to each other, while being both closest to octahedral shape (Table S8). The closest intermolecular Dy···Dy, Dy···Ni and Ni···Ni distances from neighboring molecules in **Dy_3** are 10.40 Å, 9.54 Å and 8.39 Å, respectively. In **Dy_4**, these intermolecular distances are basically the same (Dy···Dy, 10.41 Å; Dy···Ni, 9.52 Å; Ni···Ni, 8.38 Å), since **Dy_4** has similar packing mode and unit parameters with **Dy_3**. O–H···O hydrogen bonds exist between the nitrate ions and neighboring water molecules in the lattice of **Dy_3** (Figure 2.6, a). In **Dy_4** there are O–H···O hydrogen bonds between methanol molecules and O–H···Cl hydrogen bonds between the chloride counter-anions and methanol molecules (Figure 2.6, b). No hydrogen bonds are found between the $[Dy(NiL)_2]^+$ main structure and the surrounding solvent molecules or counter-anions in either **Dy_3** or **Dy_4**.

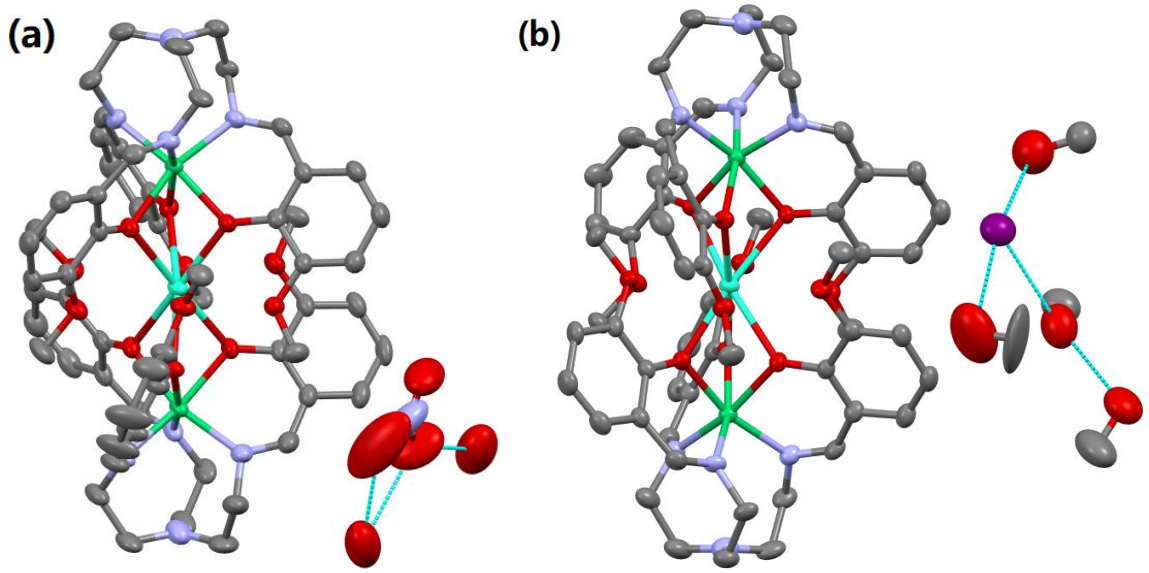

Figure 2.6. Molecular structures of **Dy_3** (a) and **Dy_4** (b). H atoms are omitted for the sake of clarity. Colour code: Dy, cyan; O, red; N, blue; C, grey; Cl, purple; Ni, green. The hydrogen bonds are shown as light blue dash lines.

Dy_5 crystalizes in the $P\bar{1}$ space group, triclinic crystal system, with Z = 2 (Table S5). The ∠Ni–Dy–Ni is 176.81°. The Dy–O bond lengths range from 2.316(2) Å to 2.382(2) Å (Table S7). The closest intermolecular Dy···Dy, Dy···Ni and Ni···Ni distances from neighboring molecules in **Dy_5** are 10.29 Å, 9.53 Å and 8.60 Å, respectively.

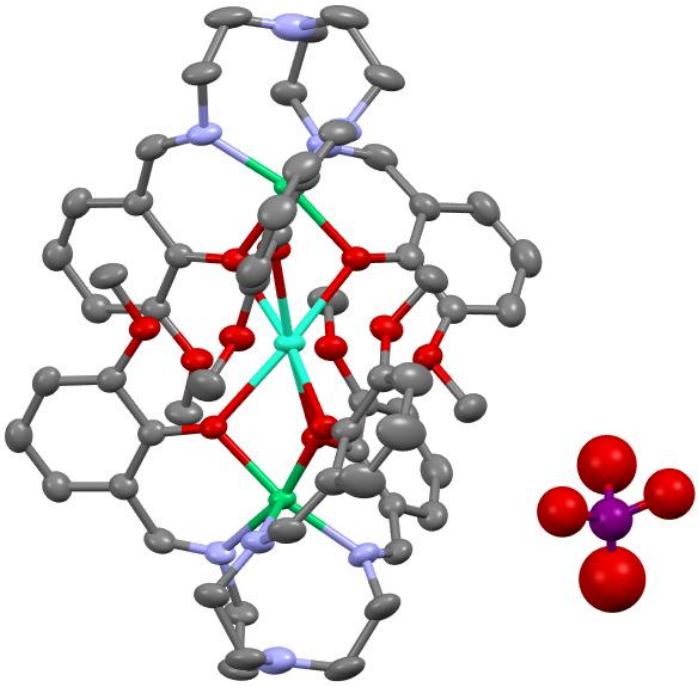

Figure 2.7. Molecular structures of **Dy_5**. H atoms are omitted for the sake of clarity. Colour code: Dy, cyan; O, red; N, blue; C, grey; Cl, purple; Ni, green.

Dy_6 crystalizes in the $P2_1/n$ space group, monoclinic crystal system, with Z = 4, the same as **Dy_3** and **Dy_4**, but its unit parameters are very different (Figure 2.8, Table S5). The unit volume of **Dy_6** is 7593.7(2) $Å^3$, remarkably larger than the 6403.63(14) $Å^3$ of **Dy_3** and the 6446.1(2) $Å^3$ of **Dy_4**, as a direct result of the large size of the tetraphenylborate anions in the lattice. The closest intermolecular Dy···Dy, Dy···Ni and Ni···Ni distances in **Dy_6** are 11.18 Å, 9.53 Å and 8.76 Å, respectively. The bulky tetraphenylborate anions also impact the packing mode of **Dy_6** in a sense that the $[Dy(NiL)_2]^+$ cations in **Dy_3** – **Dy_5** align basically along the same direction, but the cations show apparently two arrangement directions in the lattice of **Dy_6** (Figure 2.9). The ∠Ni–Dy–Ni in **Dy_6** is 173.51°, the smallest in the not strictly linear group **Dy_3** – **Dy_6**. The Dy–O bond lengths lie in the range from 2.329(2) Å to 2.367(2) Å (Table S7).

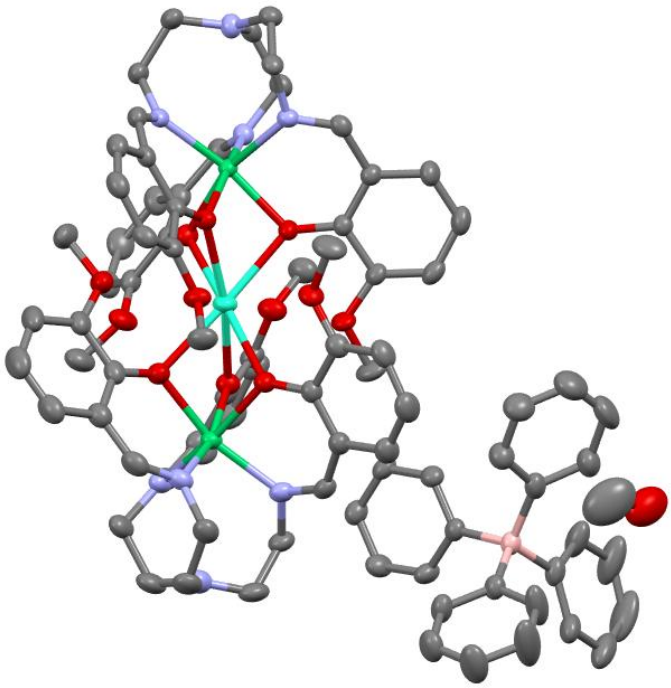

Figure 2.8. Molecular structures of **Dy_6**. H atoms are omitted for the sake of clarity. Colour code: Dy, cyan; O, red; N, blue; C, grey; B, pink; Ni, green.

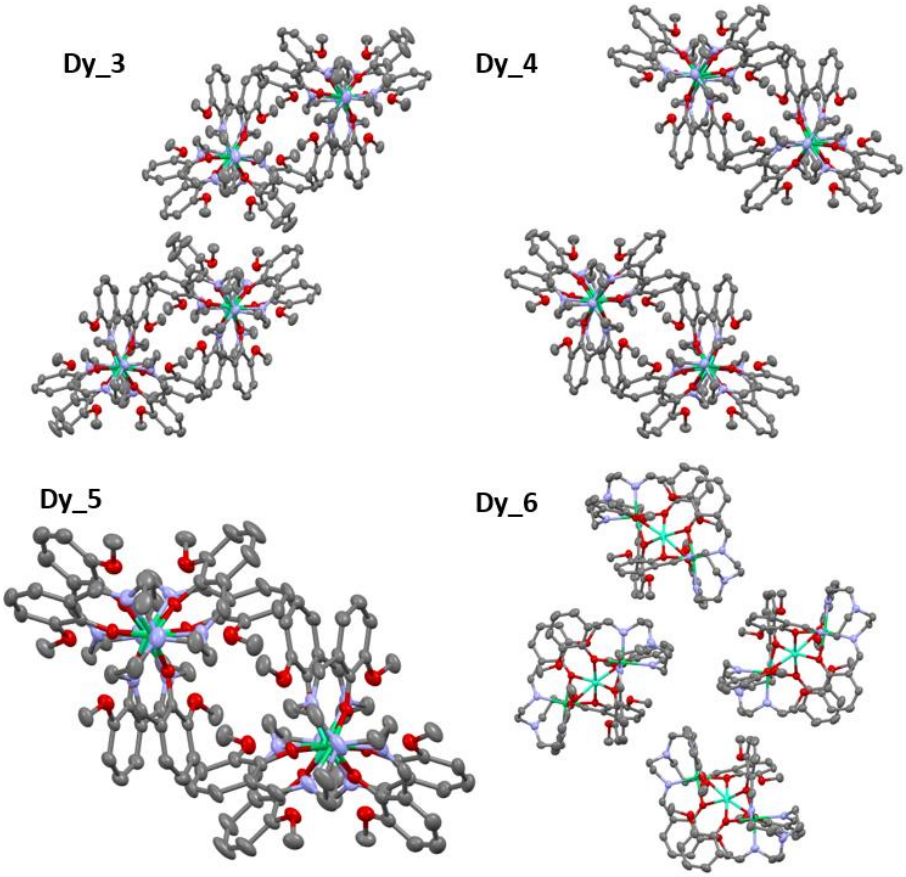

Figure 2.9. The packing diagram of **Dy_3** − **Dy_6** complexes along the direction of c axis. Only the $[Dy(NiL)_2]^+$ cations are shown for clarity.

Unlike the *R*32 space group for **Dy_1** and **Dy_2**, neither the $P2_1/n$ group for **Dy_3**, **Dy_4** and **Dy_6**, nor the $P\bar{1}$ group for **Dy_5** is a polar space group, so no chiral crystals are expected for these complexes. In fact, **Dy_3** – **Dy_6** are racemates with half of the $[Dy(NiL)_2]^+$ cations in one unit cell having Δ-Δ configuration and the other half having Λ-Λ configuration (Figure S9).

In the previous paragraphs the structures of **Dy_1** – **Dy_6** were introduced in detail, including similarities and differences among these samples. However, the most surprising feature is the full linearity versus nonlinearity depending on the different counter-anions present in the crystal lattice. Especially, since **Dy_1** – **Dy_3**, **Dy_5**, and **Dy_6** are synthesized in the same manner, the formation of the different crystal structures here is dictated by the nature of the counter-anions, not by the synthetic approaches. This counter-anion induced structural change occurs, first of all, by the symmetric structures of triflate and hexafluorophosphate ions. They can align their symmetry axes, C_3 axis in triflate and S_6 axis in hexafluorophosphate, along with the C_3 axis of the unit cell, so that the crystals are able to preserve the overall 3-fold symmetry. In principle, the equilateral triangular nitrate ions in **Dy_3** and the spherical chloride ions in **Dy_4** can also align their symmetry axes along C_3 axes of the unit cells and do not break the overall symmetry of the lattices. **Dy_5** can also satisfy the requirements of D_3 symmetry if the perchlorate ions disorder in a head-to-head manner similar to the triflate ions in **Dy_1**. But in these complexes the additional solvent molecules, in particular the low symmetric methanol molecules, hinder the formation of higher symmetric crystal structures. The absence or presence of the additional lattice solvents in the current work is tentatively attributed to the sizes of the counter-anions — triflate and hexafluorophosphate ions are big enough to function as templates to prompt highly symmetric structures and/or to exclude methanol molecules from the crystal lattice by steric hindrance effect, while nitrate, chloride and perchlorate ions are not. Nevertheless, the possibility shouldn't be ruled out that, under certain synthetic conditions, fully linear $[Dy(NiL)_2]NO_3$, $[Dy(NiL)_2]Cl$ or $[Dy(NiL)_2]ClO_4$ complexes could also be achieved. In fact, in 2016, M-X, Yao et. al published the synthesis of $[Dy(NiL)_2]NO_3{\cdot}3H_2O$ by slowly diffusing tert-Butylmethylether into a $MeOH/CHCl_3$ mixture solution containing H_3L, $Ni(NO_3)_2$, $Dy(hfac)_3{\cdot}6H_2O$, in the presence of NEt_3.[168] Their compound crystalizes in $P\bar{1}$ space group with the Ni–Dy–Ni angle being 177.08°. Although the Ni–Dy–Ni array is also not strictly linear, the fact that in this thesis and in their paper, two different crystallographically-pure $[Dy(NiL)_2]NO_3{\cdot}$solvents complexes were obtained by different procedures reveals the dependence of the final trinuclear structure on the synthetic conditions.

2.4 Magnetic properties of **Ln_1**

2.4.1 Static magnetic properties

Direct current (DC) magnetic susceptibility data were collected for all the **Ln_1** samples in the temperature range of 2–300 K under an external field of 1000 Oe using a Quantum Design MPMS-XL SQUID magnetometer. The samples were ground and fixed in a gelatine capsule using small amounts of eicosane to avoid any movement of the sample. The data obtained were corrected for diamagnetic contributions of the eicosane, the gelatine capsule and the sample holder. Diamagnetic corrections for the samples were estimated using Pascal's constants. The sample preparation and data correction methods are consistent for all the DC susceptibility measurements in this thesis.

The $\chi_M T$ value for **Y_1** stands at 2.525 $cm^3mol^{-1}K$ at 300 K and drops very slowly to 2.360 $cm^3mol^{-1}K$ at 6 K. Below 6 K, the $\chi_M T$ value begins to decrease at an accelerated rate, and finally reaches 2.143 $cm^3mol^{-1}K$ at 2.0 K (Figure 2.10). Because Y^{III} is diamagnetic, only the two Ni^{II} (S = 1) ions contribute to the molar paramagnetic susceptibility. Meanwhile, as the two Ni^{II} at the two opposite ends are not directly bridged by coordination atoms, the room temperature $\chi_M T$ value can be seen as a sum of the value for two uncoupled Ni^{II} ions. Therefore, an isotropic Landé factor g of 2.25 can be estimated according to the equation

$$\chi_M = \frac{N_A g^2 \beta^2}{3k_B} S(S+1) \qquad \text{Equation 2.1}$$

where N_A is Avogadro's constant, β is bohr magneton, k_B is the Boltzmann's constant. A g-factor around 2.2 is plausible for Ni^{II} in octahedral coordination spheres, as similar values were often reported in previous works.[169,170] The first very gradual and then accelerated decrease in the $\chi_M T$ is also a normal behaviour for nickel complexes, which originates from the small anisotropy of Ni^{II}, and the related zero field splitting. As stated in the Chapter 2.1, the weak anisotropy, including the sign of D, can be an influencing factor for the SMM performance of 3d–4f hybrid complexes. Here, however, it is hard to determine unambiguously the sign of D for Ni^{II} from DC magnetic susceptibility measurements, since it is proven that the temperature dependence of $\chi_M T$ is generally not very sensitive to the sign of D.[171]

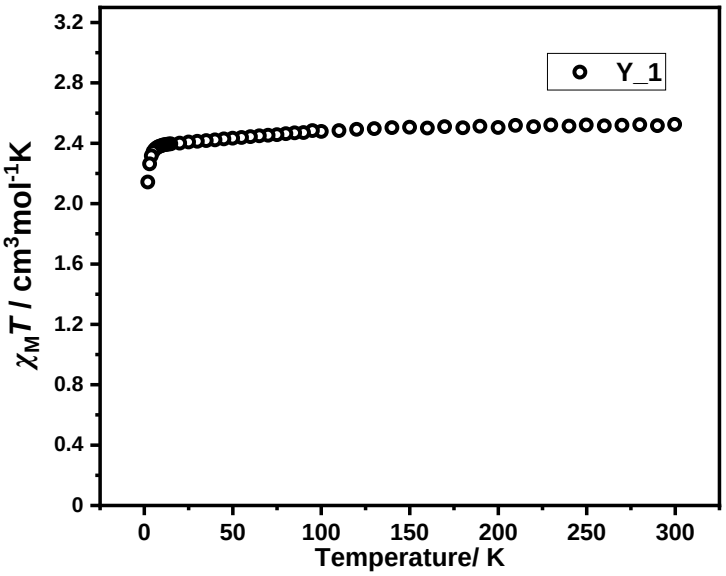

Figure 2.10. The plot of $\chi_M T$ versus T for **Y_1** under an applied field of 1000 Oe.

The $\chi_M T$ value for **Gd_1** also decreases slowly from an initial 10.36 cm^{3}mol^{-1}K at 300 K to a minimum of 10.28 cm^{3}mol^{-1}K at 105 K. The value at 300 K corresponds to the value expected for uncoupled two Ni^{II} (1.26 cm^{3}mol^{-1}K, S = 1, g_{Ni} = 2.25) and one Gd^{III} (7.88 cm^{3}mol^{-1}K, J = 7/2, g_J = 2). Upon further cooling the sample, $\chi_M T$ rises first gradually, and then at a faster speed starting from around 30 K. After reaching a maximum of 16.61 cm^{3}mol^{-1}K at 3.0 K, the $\chi_M T$ value drops slightly to 16.55 cm^{3}mol^{-1}K at 2.0 K (Figure 2.11). Since Gd^{III} is almost isotropic with its half-filled [Xe]4f^7 configuration, the increase of $\chi_M T$ indicates the presence of Gd–Ni intramolecular ferromagnetic coupling. The slight drop at 2.0 K is either due to possible weak intermolecular interaction, or a consequence that the effect of the intramolecular ferromagnetic coupling doesn't compensate the effect of the decrease in the susceptibility of Ni^{II}.

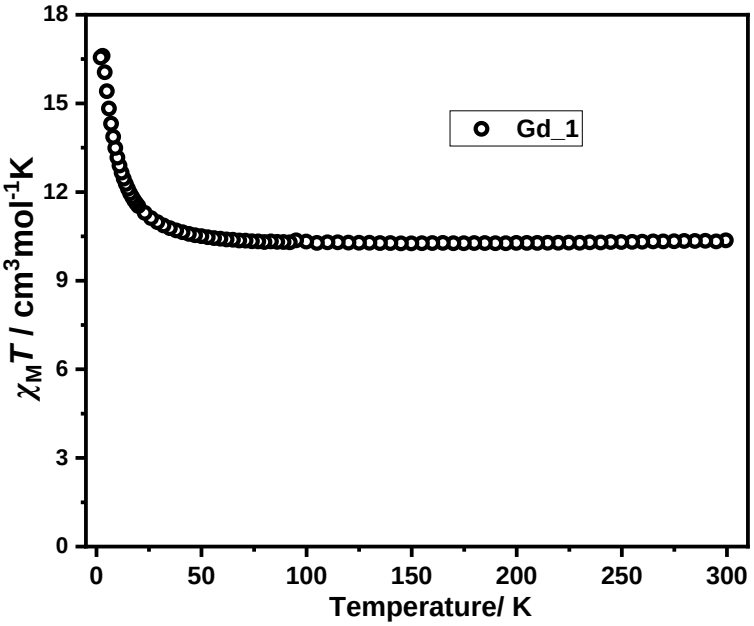

Figure 2.11. The plot of $\chi_M T$ versus T for **Gd_1** under an applied field of 1000 Oe.

The temperature-dependent $\chi_M T$ plots for the rest of **Ln_1** are shown in Figure 2.12. Their room temperature $\chi_M T$ values are listed in Table 2.2, together with the theoretical values for uncoupled two high spin state Ni^{II} (S = 1, g_{Ni} = 2.25) and one Ln^{III} in the free-ion approximation. The experimental room temperature values of **Ln_1** are always close to the theoretical ones, except for **Eu_1** and **Sm_1**. The deviations occur because the free-ion approximation assumes only the ground $^{2S+1}\Gamma_J$ state is thermally populated, whereas the energy separation of the first excited states and the ground states are small enough in Sm^{III} (~ 1000 cm^{-1}) and Eu^{III} (~300 cm^{-1}) for the thermal population of the excited states. Lowering the temperature leads to gradual decrease of the $\chi_M T$ values in the beginning, which can be attributed to the combined effect of the thermal depopulation of excited Stark sublevels of the lanthanide ion and zero field splitting of Ni^{II}. For **Dy_1**, **Tb_1**, **Ho_1**, **Sm_1** and **Pr_1**, upturns in the plots were observed in the low temperature regime. Similar to the case of **Gd_1**, the upturns clearly indicate that ferromagnetic intramolecular interactions between Ni^{II} and Dy^{III}, Tb^{III}, Ho^{III}, Sm^{III} or Pr^{III} operates at low temperature. The temperatures at inflection points, the corresponding $\chi_M T$ value at these points, and the maximum $\chi_M T$ value in the low temperature regime for these complexes are listed in Table S9.

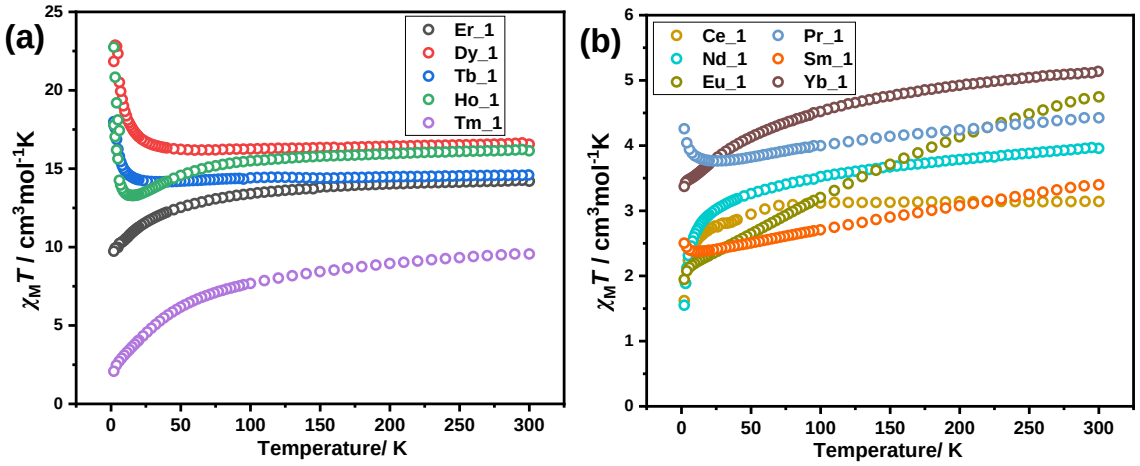

Figure 2.12. The plots of $\chi_M T$ versus T for (a) **Er_1**, **Dy_1**, **Tb_1**, **Ho_1**, **Tm_1** and (b) **Ce_1 Pr_1**, **Nd_1**, **Sm_1**, **Eu_1**, **Yb_1** under an applied field of 1000 Oe.

Table 2.2. The experimental room temperature $\chi_M T$ values and the theoretical values for two uncoupled Ni^{II} (S = 1, g_{Ni} = 2.25) and one Ln^{III} for **Ln_1**.

complexes	Experimental value ($cm^3mol^{-1}K$)	Theoretical value for Ln^{III} ($cm^3mol^{-1}K$)	Theoretical value for **Ln_1** ($cm^3mol^{-1}K$)
Ce_1	3.14	0.80	3.32
Pr_1	4.43	1.60	4.12
Nd_1	3.97	1.64	4.16
Sm_1	3.40	0.09	2.61
Eu_1	4.47	0.00	2.52
Tb_1	14.60	11.82	14.34
Dy_1	16.68	14.17	16.69
Ho_1	16.14	14.07	16.59
Er_1	14.20	11.48	14.00
Tm_1	9.56	7.15	9.67
Yb_1	5.14	2.57	5.09

On the contrary, the $\chi_M T$ values decrease monotonously as the temperature is lowered across the entire measured range for **Ce_1**, **Nd_1**, **Eu_1**, **Er_1**, **Tm_1** and **Yb_1**. Their minimum $\chi_M T$ values at 2.0 K are listed in Table S10. Although an intramolecular coupling between these lanthanide ions and Ni^{II} cannot be completely ruled out based on the absence of upturns, it should be either antiferromagnetic in nature or very weak in strength. In fact, the $\chi_M T$ values for Ce^{III}, Eu^{III}, Tm^{III} and Yb^{III} are often lower than 4 $cm^3mol^{-1}K$ under 10 K as previously reported.[36,172] The low values and the inherent temperature dependency of $\chi_M T$

make it difficult, if not impossible, to determine the nature of the coupling with Ni^{II} by DC magnetic susceptibility measurements, when no direct evidence for ferromagnetic couplings is observed, like in the current study. The Ln^{III} are then divided into the "ferro group" and the "uncertain group" according to if ferromagnetic coupling with Ni^{II} is confirmed. In the "ferro group", Gd^{III} is basically isotropic, Dy^{III}, Tb^{III}, Ho^{III}, and Pr^{III} have oblate-shaped electron density of the ground state, only Sm^{III} have prolate-shaped electron density. In the "uncertain group", the light lanthanide ions, Ce^{III} and Nd^{III}, are oblate, while the heavier ones, including Er^{III}, Tm^{III}, Yb^{III} are all prolate. **Eu_1** is out of the discussion since Eu^{III} is diamagnetic in its ground state. I tentatively propose two influencing factors on the Ln–Ni couplings in the current trinuclear structure. Firstly, the oblate ions tend to have ferromagnetic coupling with Ni^{II}. The axial coordination field render these ions easy-axis anisotropic with the easy axis of magnetization pointing to the Ni^{II}, thus creating ferromagnetic dipolar interaction. Then, the nature of coupling depends also on the radius of Ln^{III}. Larger Ln^{III} can have exchange coupling with the Ni^{II} through the overlapping of electron clouds. The exchange coupling can be ferro- or antiferromagnetic varying from one lanthanide element to another, and holds the potential to reverse the effect of dipolar coupling. That could explain why the oblate Ce^{III} and Nd^{III} are in the "uncertain group", while the prolate Sm is in the "ferro group".

2.4.2 Dynamic magnetic properties

To explore whether the samples show SMM behaviours, alternating current (AC) susceptibility measurements were performed on all the **Ln_1** complexes at 2.0 K, first under a zero field and an applied field of 1000 Oe with a 3 Oe oscillating field at frequencies from 1 to 1000 Hz. If any signs for slow relaxation of magnetization were detected, an applied field-dependent AC susceptibility measurement were then done to find out the optimal applied field.

No out-of-phase susceptibility (χ_M'') different from zero was observed for **Y_1**. This is an expected result, because Ni^{II} ions only has weak anisotropy and small magnetic moment. The SMM behaviour was exhibited in **Dy_1** and **Tb_1**. The detailed results and discussion for **Dy_1** will be given in Chapter 2.5 along with the other dysprosium containing complexes. As shown in Figure 2.13, χ_M'' signals of **Tb_1** rose in the high oscillation frequency region under zero field and applied fields, but no peaks could be observed, indicating that the spin relaxation rates exceeded the range of measurement.

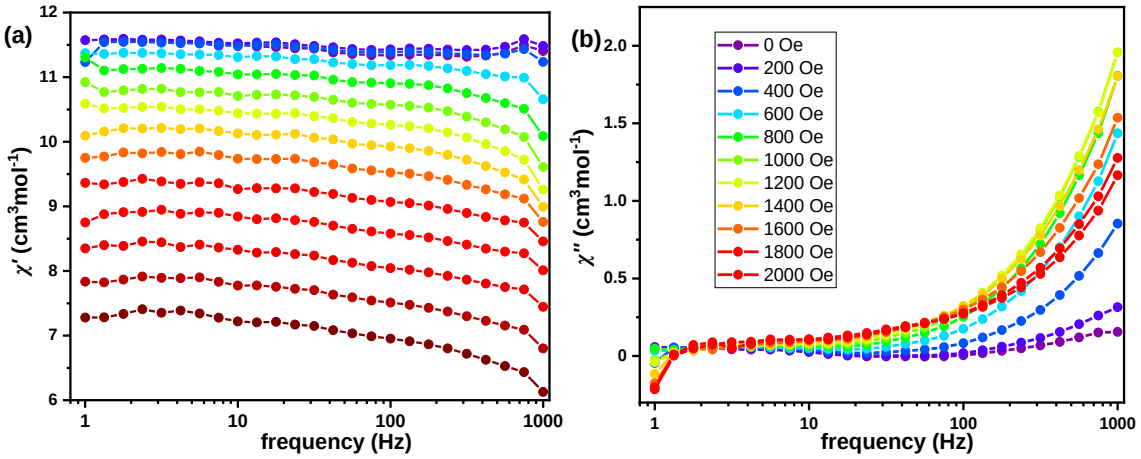

Figure 2.13. Frequency dependency of the in-phase (a) and out-of-phase (b) component of the magnetic susceptibility for **Tb_1** under varying external magnetic fields.

No χ_M'' signals different from zero was revealed for the other **Ln_1**, irrespective of the 1000 Oe applied field.

2.5 Magnetic properties of **Dy_1** – **Dy_6** and **DyZn$_2$**

2.5.1 Static magnetic properties

The bulk magnetic properties of **Dy_1** – **Dy_6** were collected on their polycrystalline samples. DC susceptibility measurements revealed room temperature $\chi_m T$ values of 16.68, 17.07, 16.94, 16.50, 16.59, 16.65 $cm^3mol^{-1}K$ for **Dy_1** – **Dy_6**, respectively, in good agreement with the theoretical value of 16.59 $cm^3mol^{-1}K$ for uncoupled two high spin state Ni^{II} ions (1.21 $cm^3mol^{-1}K$, $S = 1$, $g = 2.2$) and one Dy^{III} ion (14.17 $cm^3mol^{-1}K$, $S = 5/2$, $L = 5$, $^6H_{15/2}$, $g_J = 4/3$) (Figure 2.14). The $\chi_m T$ values dropped slightly upon lowering the temperature from 300 K to 60 K, followed by pronounced upward trends in the low temperature region. The maximum $\chi_m T$ values for **Dy_1** – **Dy_6** were 22.88, 21.90, 28.20, 25.05, 24.08, and 22.99 $cm^3mol^{-1}K$, respectively. For each complex, the initial decrease was due to the gradual thermal depopulation of excited Stark levels of the Dy ions while the upturn in the low temperature regime was indicative of intramolecular ferromagnetic coupling between Dy^{III} and Ni^{II} centers.[168] The similar variable-temperature magnetic susceptibility profiles for **Dy_1** – **Dy_6** demonstrated that the variations in the counter-anions and the accompanying subtle structural changes, including the Ni–Dy–Ni angles and local coordination polyhedral around Dy^{III} and Ni^{II} ions, only exert a minimal impact on the anisotropies of the metal centers and the strength of intramolecular Dy–Ni interactions**.** On the contrary, $\chi_m T$ value of **DyZn$_2$** only exhibited monotonous decrease from 14.16 $cm^3mol^{-1}K$ at room temperature to 11.63 $cm^3mol^{-1}K$ at 2.0

K. Since zinc ions are diamagnetic, the monotonous decrease originated from the thermally induced depopulation of the M_J sublevels of Dy^{III} ions.

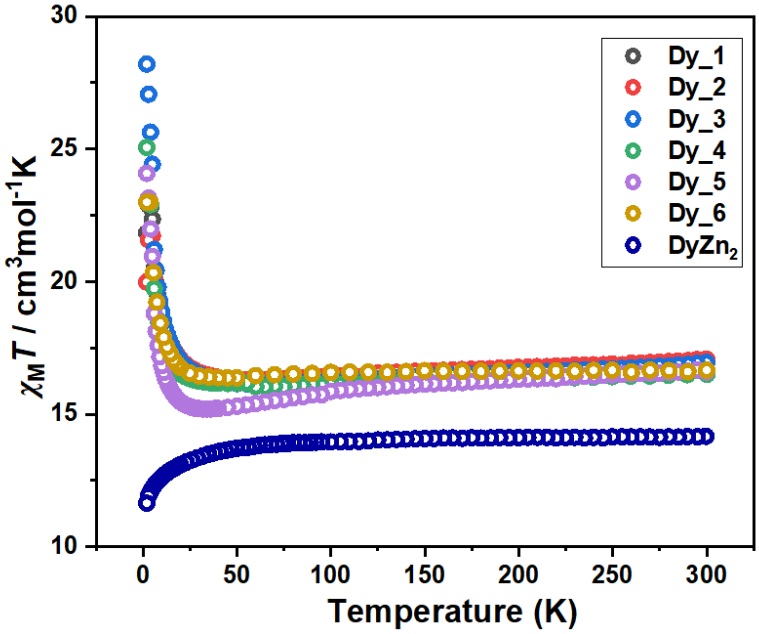

Figure 2.14. The $\chi_M T$ *versus* T plots for **Dy_1 – Dy_6**, and **DyZn$_2$** under an applied field of 1 kOe.

Isothermal field dependent magnetization (M versus H) measurements are conducted on **Dy_1** – **Dy_4** and **DyZn$_2$** at 2.0, 4.0, 6.0, 8.0, and 10 K in the range of 0 to 7.0 T (Figure S10). At 2.0 K, the magnetizations first increase rapidly below 1.0 T, and then continue to increase over the whole field range steadily to reach 9.44, 9.54, 9.08, 9.17, and 5.07 $N\mu_B$ at the highest field, very close to the theoretical sum value of two Ni^{II} ($2 \times gS = 2 \times 2.2 \times 1 = 4.4\ N\mu_B$) and one Ising type Dy^{III} ($1/2 \times gJ = 1/2 \times 4/3 \times 15/2 = 5.0\ N\mu_B$) for **Dy_1** – **Dy_4** and two diamagnetic Zn^{II} and one Dy^{III} for **DyZn$_2$**. However, the plots show no signs of saturation even at the highest field 7.0 T and the lowest temperature 2.0 K, indicating the presence of the large magnetic anisotropy of Dy^{III} in all the five complexes, and/or the low-lying exited states induced by weak intramolecular interactions in **Dy_1** – **Dy_4**.[173] At higher temperatures, the magnetizations also rise monotonously upon the increase of external fields, though at more gradual slopes, mainly due to the increased thermal perturbation.

2.5.2 Dynamic magnetic properties

AC susceptibility measurements were performed on **Dy_1** – **Dy_6** and **DyZn$_2$** first under a zero field at frequencies from 1 to 1500 Hz. All seven samples showed frequency dependent behaviours under zero field, but **DyZn$_2$** did not show any out-of-phase AC susceptibility (χ_M'') versus frequency peaks within the range of measurement at lowest possible temperature, so the energy barriers could only be extracted for **Dy_1** – **Dy_6** (Figure 2.15 and Figure 2.16, a).

The χ_M'' versus frequency peaks for **Dy_1** – **Dy_6** can be observed until 2.6 K, 2.4 K, 3.2 K, 3.3 K, 3.3 K and 2.3 K, respectively. Relaxation time at each temperature is obtained with the help of CCFIT2[17,18] using the generalized Debye model (Table S11–S16). All the ln(τ/s) versus 1/T plots of **Dy_1** – **Dy_6** exhibited practical linear relations with no signs of QTM. Therefore, all the data were fitted following the Arrhénius equation

$$\tau^{-1} = {\tau_0}^{-1}\, exp\left(-\frac{U_{eff}}{k_B T}\right) \qquad \text{Equation 2.2}$$

with τ representing the relaxation time, τ_0 the pre-exponential factor and k_B the Boltzmann constant.

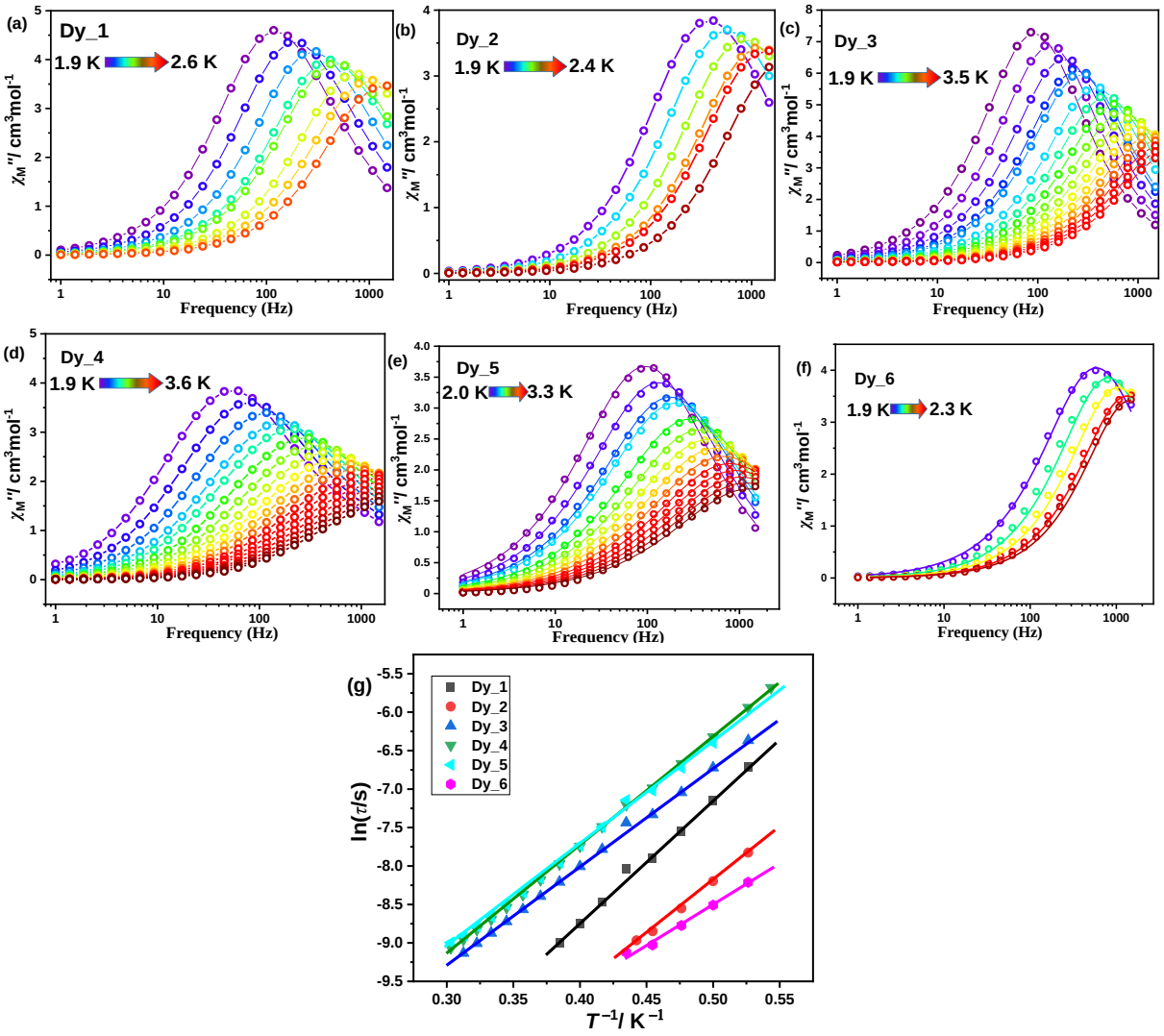

Figure 2.15. (a)–(f) Temperature dependence of the out-of-phase AC susceptibility (χ_M'') under zero field for complex **Dy_1** – **Dy_6**. The lines are a guide for the eye. (g) ln(τ) versus T^{-1} plots under zero field, the lines are the fitting results from Arrhénius equation.

The results are listed in Table 2.3. The effective energy barriers U_{eff}/k_B for **Dy_1** – **Dy_6** are moderate, spanning from 10.31(0.64) K to 15.89(0.48) K. The values of τ_0 are in the reasonable range for SMMs (10^{-6}–10^{-12} s).[174-176] The α parameters span from 0.076 to 0.118 for **Dy_1**, 0.086 to 0.128 for **Dy_2**, 0.047 to 0.052 for **Dy_3**, and 0.102 to 0.154 for **Dy_6**, showing narrow distributions of the relaxation times. In **Dy_4** and **Dy_5**, α values range from 0.206 to 0.239, and 0.243 to 0.315 respectively, indicating relatively broader distributions of the relaxation times.

Table 2.3. The effective energy barriers and the pre-exponential factors of **Dy_1** – **Dy_6**.

Complex	under zero field		under optimal field	
	U_{eff}/k_B (K)	τ_0 (s)	U_{eff}/k_B (K)	τ_0 (s)
Dy_1	15.89(0.48)	2.815×10^{-7}	46.21(0.48)	1.366×10^{-7}
Dy_2	13.84(0.35)	2.712×10^{-7}	45.63(1.13)	1.215×10^{-9}
Dy_3	12.95(0.15)	1.886×10^{-6}	131.10(1.87)	4.801×10^{-9}
Dy_4	14.18(0.08)	1.502×10^{-6}	10.14(0.32)	2.686×10^{-5}
Dy_5	13.54(0.19)	1.954×10^{-6}	13.29(0.23)	1.575×10^{-5}
Dy_6	10.31(0.64)	1.170×10^{-6}	18.29(0.14)	9.131×10^{-7}

The absence of peaks within the frequency range of measurement in **DyZn$_2$** indicates fast QTM, which can be understood from the perspective of coordination geometry. According to the rules of systematic absences of transverse crystal-field parameters (CFPs), the B_k^q ($|q|$ = 1, 2, 4, 5) terms in the spin Hamiltonian $\hat{H}_{CF} = \sum_{k=2,4,6}\sum_{q=-k}^{k} B_q^k \hat{O}_q^k$ vanish under the D_3 local symmetry around Dy^{III}.[62] However, the other transverse CFPs $B_4^{\pm3}$, $B_6^{\pm3}$and $B_6^{\pm6}$ remain non-zero and they contribute to the non-diagonal elements in the crystal-field matrix, resulting in possible QTM. If θ = 60°, not 37.64°, the symmetry will ascend into D_{3d}, but that still doesn't help quench the $B_4^{\pm3}$, $B_6^{\pm3}$*and* $B_6^{\pm6}$ terms. The fast QTM in **DyZn$_2$** is further confirmed as the relaxation peak of **DyZn$_2$** moved into the range of measurement when a small external field (200 Oe) was applied, due to the suppression of QTM (Figure 2.16, a). The optimal field was found to be 1500 Oe. The χ_M'' versus frequency peak can be observed up to 4.7 K under the optimal field and the relaxation times at each temperature are listed in Table S17. Arrhénius fitting gave U_{eff}/k_B = 12.08(0.19) K, τ_0 =1.268×10^{-5} s. The large α values (0.48 to 0.69) indicated the coexistence of multiple relaxation processes. In comparison to **DyZn$_2$**, the Ni-containing **Dy_1** exhibited superior SMM properties with its longer relaxation time and larger energy barrier. As the theoretical calculations demonstrated that the minor difference in the twist angle θ has negligible impact on the magnetic properties, *vide infra*, the significantly enhanced SMM performance of **Dy_1** is associated with the Dy–Ni ferromagnetic coupling in

it. This positive effect from Dy–Ni coupling can be attributed to the collective contribution of multiple key features. First of all, the ferromagnetic interaction between Ni and Dy creates a large ground spin state S_{total}. Secondly, the intramolecular interaction creates an internal bias field on Dy center that suppresses the fast QTM. Besides, as indicated from the negative axial zero field splitting parameters (D), Ni^{II} ions are also uniaxial anisotropic, the same as the central Dy^{III}, *vide infra*. Combined with the last point that the Dy^{III} center and two terminal Ni^{II} form a linear arrangement, a perfect collinearity of all the easy axes of magnetization within a molecule is achieved. This leads to enhanced overall magnetic anisotropy while significantly minimizing the detrimental effects from internal transverse magnetic fields.

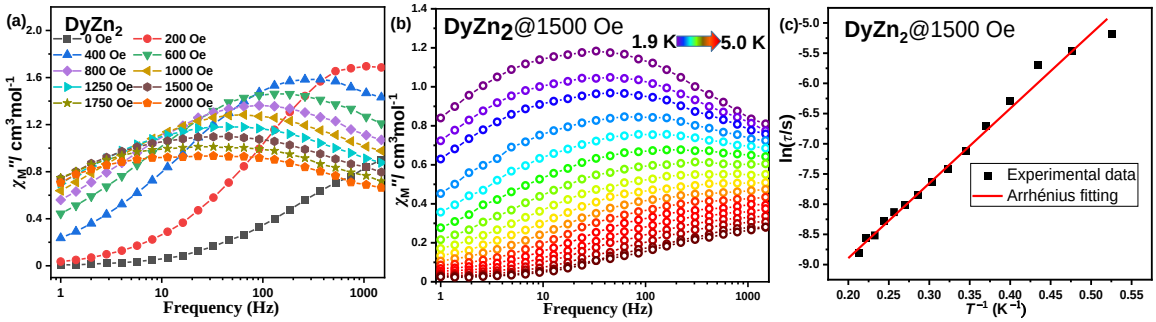

Figure 2.16. (a) χ_M'' under varied external magnetic fields at 2.0 K for **$DyZn_2$**. (b) temperature dependence of χ_M'' under 1500 Oe external field for **$DyZn_2$**. The lines are a guide for the eye. (c) ln (τ) versus T^{-1} plot and fitting result under 1500 Oe external field.

The SMM performance of **Dy_1** – **Dy_6** was further investigated under optimal fields, which were determined to be 1500 Oe for **Dy_1**, **Dy_3** – **Dy_6**, and 2000 Oe for **Dy_2** (Figure S11). The measured data are summarized in Figure 2.17. Intriguingly, obvious differences were present in the structurally similar pair **Dy_1** and **Dy_2**, and were even more pronounced among the non-fully linear **Dy_3** – **Dy_6**. The highest temperatures of exhibiting a peak in the χ_M'' versus frequency plots followed a sequence of **Dy_3** (13.0 K) > **Dy_1** (6.8 K) > **Dy_4** (6.6 K) > **Dy_6** (3.6 K) > **Dy_5** (3.5 K) > **Dy_2** (3.2 K), while the effective energy barriers are in the order of **Dy_3** > **Dy_1** ≈ **Dy_2** > **Dy_6** > **Dy_5** > **Dy_4** (Table 2.3). In addition, the ln(τ/s) versus 1/T plots of **Dy_1** – **Dy_3** exhibited curvatures in the low temperature region, which indicated the coexistence of multiple relaxation mechanisms.[177] The different SMM performances between fully linear **Dy_1** and **Dy_2** may come from subtle variations in bond lengths and bond angles presented in Chapter 2.3. As for **Dy_3** – **Dy_6**, since their $[Dy(NiL)_2]^+$ cations are no longer strictly D_3 symmetric, the variations in bond lengths and bond angles around the metal ions are more significant, which are likely to induce larger changes in their electronic energy level structures. The varying intermolecular interactions arising from the different space groups and packing modes of **Dy_3** – **Dy_6** could also exert different impacts on the slow relaxation behaviours. Overall, it is manifested that unlike under zero field, the slow relaxation behaviours under optimal applied fields are more sensitive to slight structural changes in the Ni–Dy–Ni complexes.

To the best of my knowledge, the energy barrier in **Dy_3** under the optimal magnetic field is among the highest reported for Ni–Dy SMMs, second only to two complexes where the central Dy ion is in D_{5h} coordination symmetry.[155,178] This unique large energy motivated me to compare **Dy_3** with the previously reported nitrate-containing complex $[Dy(NiL)_2]NO_3{\cdot}3H_2O$.[168] Because only an energy barrier of 14.17 K under zero field was reported for $[Dy(NiL)_2]NO_3{\cdot}3H_2O$, I repeated the synthesis and collected AC magnetic susceptibility data under applied fields. The PXRD spectrum of the product matched well with the simulated spectrum based on the reported single crystal structure (Figure S12). The optimal field for $[Dy(NiL)_2]NO_3{\cdot}3H_2O$ was also determined to be 1500 Oe. Under this field, $[Dy(NiL)_2]NO_3{\cdot}3H_2O$ showed U_{eff} of 119.20(3.10) K and τ_0 of 1.266×10^{-8} s (Figure S13). The similar U_{eff} and τ_0 values of **Dy_3** and $[Dy(NiL)_2]NO_3{\cdot}3H_2O$ suggested that the difference in their space groups and lattice solvents didn't play any important role in the SMM performance under zero field or under an optimal field. Hence, the high energy barrier under an optimal field in **Dy_3**, compared to **Dy_1**, **Dy_2** and especially **Dy_4** – **Dy_6**, came likely from the nitrate ions and the associated phonon vibrations. To verify the hypothesis, additional physical measurements and more sophisticated theoretical efforts on phonon spectra and spin-phonon couplings are required, which is beyond the scope of the current work.

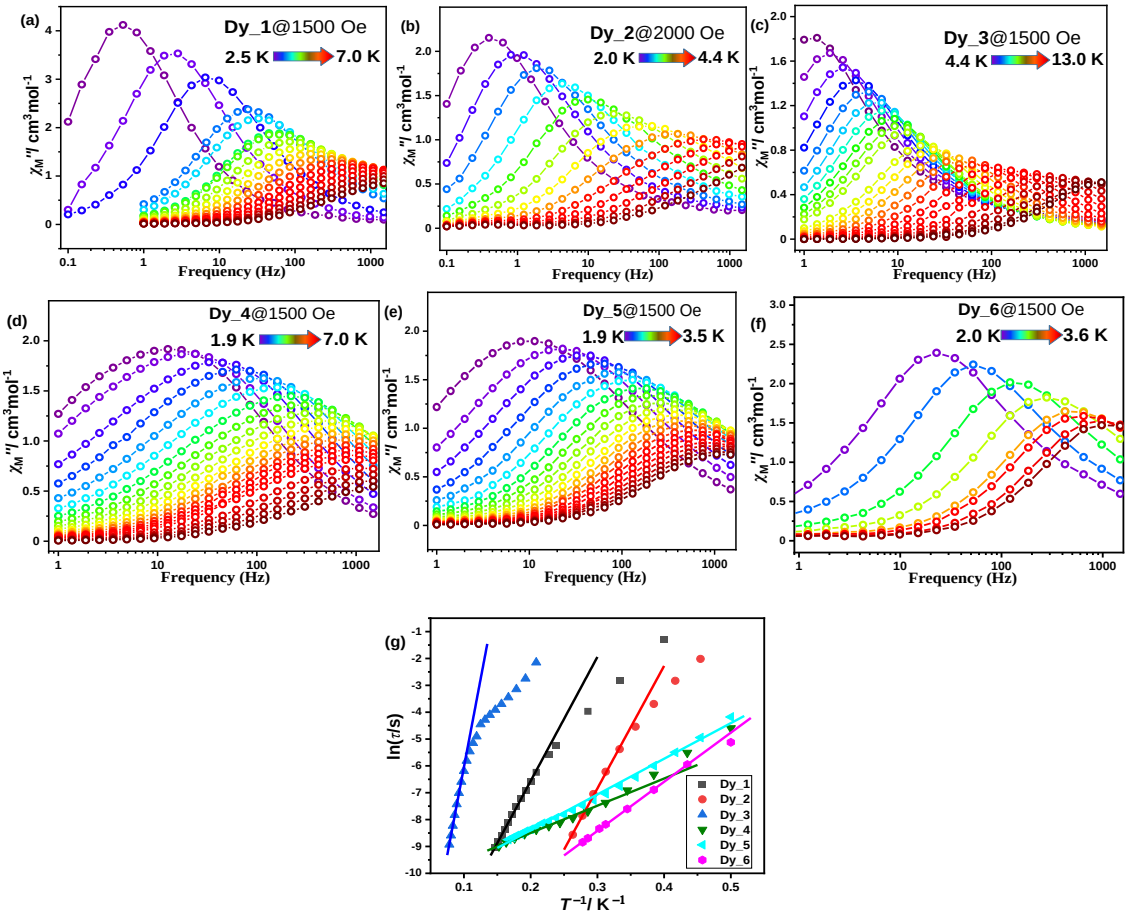

Figure 2.17. (a)–(f) temperature dependence of the out-of-phase AC susceptibility (χ_M'') under optimal applied fields for complex **Dy_1** – **Dy_6**. The lines are a guide for the eye. (g) ln (τ) versus T^{-1} plots under optimal applied fields, the lines are the fitting results from Arrhénius equation.

The intermolecular coupling is an important factor on the dynamic of magnetic relaxation in SMMs. As demonstrated in many reports, intermolecular interaction is frequently an origin of rapid QTM, and dilution in antimagnetic matrix can mitigate QTM by cancelling the intermolecular interaction.[179] Unlike the dilution of mononuclear SMMs, dilution of the 3d–4f complexes with both 3d and 4f ions being paramagnetic in a fully diamagnetic matrix is a challenging task. Thus, the impact of intermolecular couplings in such systems is rarely unveiled. To explore the impact of intermolecular interaction in **Dy_1**, a dilution in the isostructural $[Y(ZnL)_2]CF_3SO_3$ matrix, for instance, is desired. However, though the $[Y(ZnL)_2]CF_3SO_3$ complex may be prepared in the manner of preparing **DyZn2**, the instability of the trinuclear complexes in organic solvents hinders the co-crystallization of **Dy_1** and $[Y(ZnL)_2]CF_3SO_3$. As an alternative, $[Dy_{0.1}Y_{0.9}(NiL)_2]CF_3SO_3$ (hereafter referred to as **1***) was prepared, in which the intermolecular Dy–Dy interactions were largely quenched by diamagnetic Y ions, while intermolecular Ni–Ni interactions could still remain. PXRD spectrum of **1*** confirmed that the sample was isostructural to **Dy_1** (Figure S14). Room temperature $\chi_m T$ value of **1*** was 3.782 $cm^3mol^{-1}K$, close to the theoretical value of 3.837 $cm^3mol^{-1}K$ when the ratio of Dy:Y was exactly 1:9. The "partially diluted" **1*** exhibited faster relaxation under zero field than its pure $[Dy(NiL)_2]CF_3SO_3$ counterpart, since only at temperatures ≤ 2.0 K a peak in the χ_M'' versus frequency plot was observed (Figure 2.18). When the performances under optimal applied fields were compared, the energy barrier (U_{eff}/k_B = 35.37(0.65) K, $\tau_0 = 1.795\times10^{-7}$ s) of **1*** was still lower than 46.21(0.48) K of **Dy_1** (Table 2.3). In the "partially diluted" sample, spins of Ni ions in $[Y(NiL)_2]^+$ components flip-flop easily and serve as magnetic fluctuation in the surroundings, inducing faster relaxation on the neighboring $[Dy(NiL)_2]^+$ through the aforementioned intermolecular Ni···Ni interactions. By contrast, in $[Dy(NiL)_2]CF_3SO_3$, all Ni ions are more or less "pinned" by the ferromagnetic coupling with the central Dy ions within individual molecules, so their fluctuation isn't as vigorous as in the "partially diluted" sample. Though the "pinning effect" on Ni^{II} by Dy^{III} is hard to quantify experimentally, similar phenomenon is already confirmed for several Fe^{II} and Fe^{III} complexes with Mössbauer spectroscopy.[48,180,181]

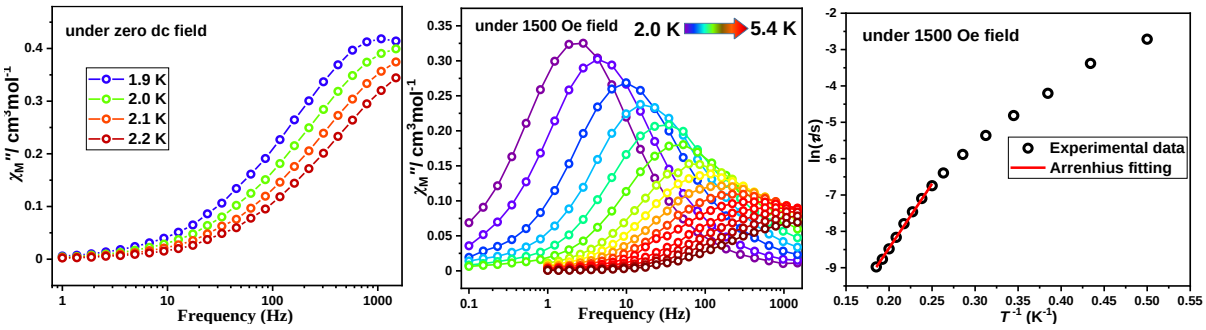

Figure 2.18. Temperature dependence of the out-of-phase AC susceptibility (χ_M'') under zero field (left) and optimal field (middle) for **1***. The lines are a guide for the eye. Right, ln (τ) versus T^{-1} plot for **1*** under optimal fields, the red line is the linear fitting result.

2.6 Micro-SQUID measurements on **Ln_1**

Sub-Kelvin studies of **Ln_1** (Ln = Gd, Dy, Tb, Ho, Er, Yb) were carried out employing micro-SQUID arrays. In all cases, the field was aligned along the easy axis of the crystal, employing the transverse field method. The studies were carried out on single crystals with the field applied along the principal anisotropic axis. Hysteresis loops were obtained at different sweep rates and temperatures, ranging from 5 K to 30 mK and from 0.5 to 128 mT/s. Open hysteresis loops were observed for the **Gd_1**, **Tb_1**, **Dy_1** and **Ho_1** complexes, while **Er_1**, **Yb_1** and **Y_1** analogues revealed close loops at the lowest temperature and fastest sweep rate. To investigate further whether the observed behaviour for the **Gd_1**, **Tb_1**, **Dy_1** and **Ho_1** systems is a cooperative behaviour between the Ni and Ln ions, the nickel-free analogues, i.e., **DyZn2**, $[Tb(NiL)_2]CF_3SO_3$ (**TbZn2**) and $[Gd(NiL)_2]CF_3SO_3{\cdot}0.5H_2O$ (**GdZn2**) were investigated using micro-SQUID. **TbZn2** and **GdZn2** were synthesized according to reported procedures.[164,165] A **HoZn2** analogue, however, could not be obtained despite multiple attempts, likely due to the reduced ionic radius of Ho^{III}.

Micro-SQUID studies of the **Gd_1** revealed open loops with very sharp transitions at a base temperature of 30 mK (Figure 2.19, a). The temperature dependence of the loops was also investigated, leading to open loops up to 300 mK temperature (Figure 2.19, b). The loops are found to be highly sweep-rate and temperature dependent; hence, the system is an SMM. Upon sweeping the external magnetic field at 30 mK, the magnetization loss at zero field is minimal, considerably smaller than the magnetization loss at around ±800 Oe (±0.08 T), demonstrating large zero-field residual magnetization.

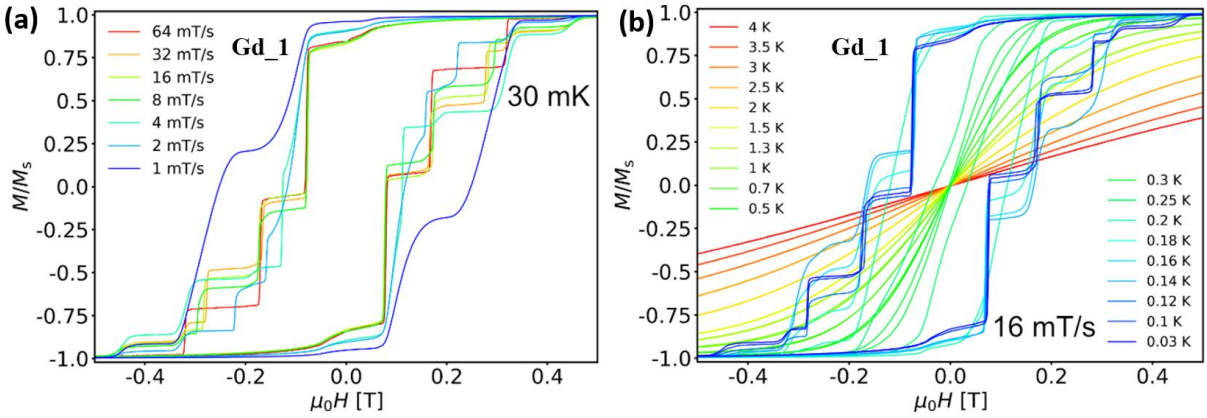

Figure 2.19. Hysteresis loops collected in a single crystal of **Gd_1** with the applied field along the easy axis of the crystal. (a) Field sweep study at 30 mK and sweep rates from 64 down to 1 mT/s; (b) Temperature-dependent loops with a sweep rate of 16 mT/s from 30 mK up to 4 K.

GdZn$_2$, the zinc-substituted counterpart of **Gd_1**, also revealed open hysteresis loop featuring sweep-rate and temperature dependent sharp crossings (Figure 2.20). The SMM characteristics reflects local magnetic anisotropy at the Gd^{III} centers, in agreement with prior studies on **GdZn$_2$**.[165] Notably, while **Gd_1** showed substantial coercive fields, **GdZn$_2$** displayed minimal coercivity at comparable temperatures, as evidenced by its waist-restricted hysteresis loops. The significant magnetization loss near zero field originates from rapid QTM process, whereas its absence in **Gd_1** indicates that the zero-field QTM in **Gd_1** is mitigated by Ni–Gd intramolecular ferromagnetic coupling. The increased ground spin state in **Gd_1** ($S_{\mathbf{Gd\_1}} = S_{Gd} + 2S_{Ni}$), and the reduced transition probability of simultaneously flipping three spins—one on Gd^{III} and two on Ni^{II}—in the ground level crossing (versus a single spin on Gd^{III} in **GdZn$_2$**) can both contribute to the mitigation of the zero-field QTM.

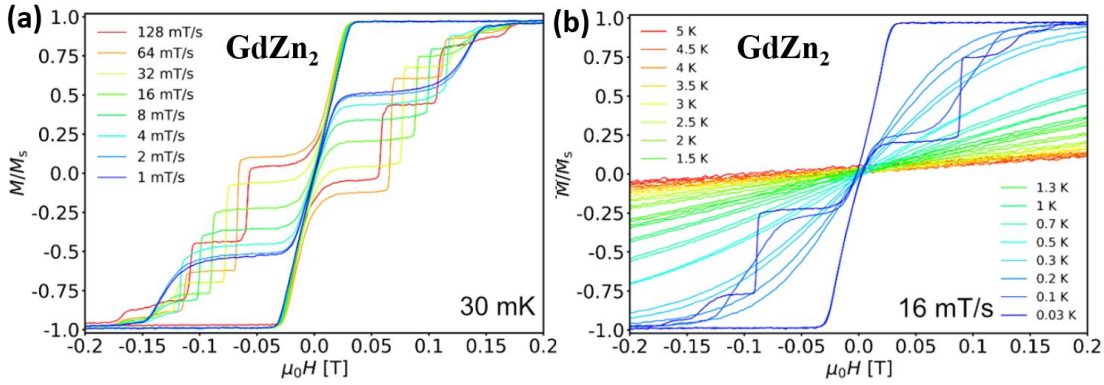

Figure 2.20. Hysteresis loops collected in a single crystal of **GdZn$_2$** with the applied field along the easy axis of the crystal. Field sweep study at 30 mK and sweep rates from 128 down to 1 mT/s (a). Temperature-dependent loops with a sweep rate of 16 mT/s from 30 mK up to 5 K (b).

Dy_1 exhibited open loops with the largest coercive field (±0.5 T) among the investigated complexes (Figure 2.21). The loops are sweep-rate dependent, consistent with the loops of SMMs (Figure 2.21, a). The temperature dependence of the loops revealed open loops up to 2.5 K (Figure 2.21, b).

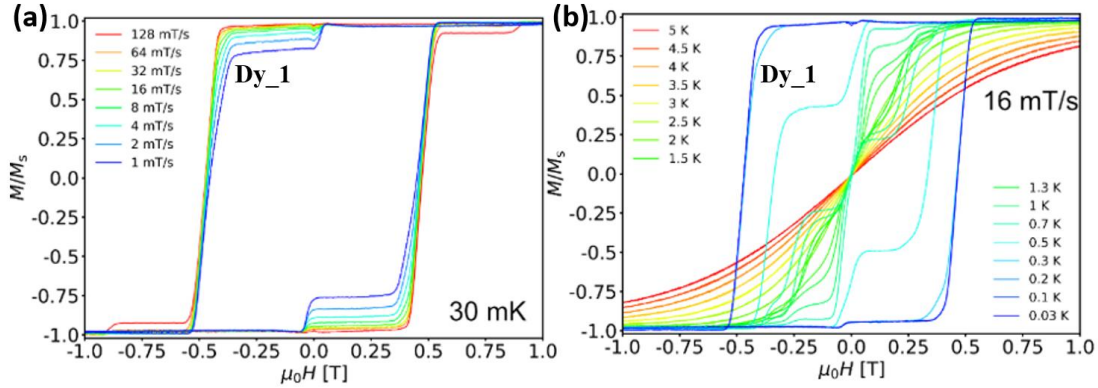

Figure 2.21. Hysteresis loops collected in a single crystal of **Dy_1** with the applied field along the easy axis of the crystal. (a) Field sweep study at 30 mK and sweep rates from 128 down to 1 mT/s; (b) Temperature-dependent loops with a sweep rate of 16 mT/s from 30 mK up to 5 K.

In stark contrast to **Dy_1**, complexes **Y_1** and **DyZn$_2$** exhibited completely closed hysteresis loops (Figure 2.22); hence, the open loops observed in **Dy_1** originate not from isolated Dy^{III} or Ni^{II} ions alone, but rather from the cooperative Ni–Dy interactions. The closed loops of **DyZn$_2$** further corroborate the fast QTM observed in its AC susceptibility measurements (see Chapter 2.5.2).

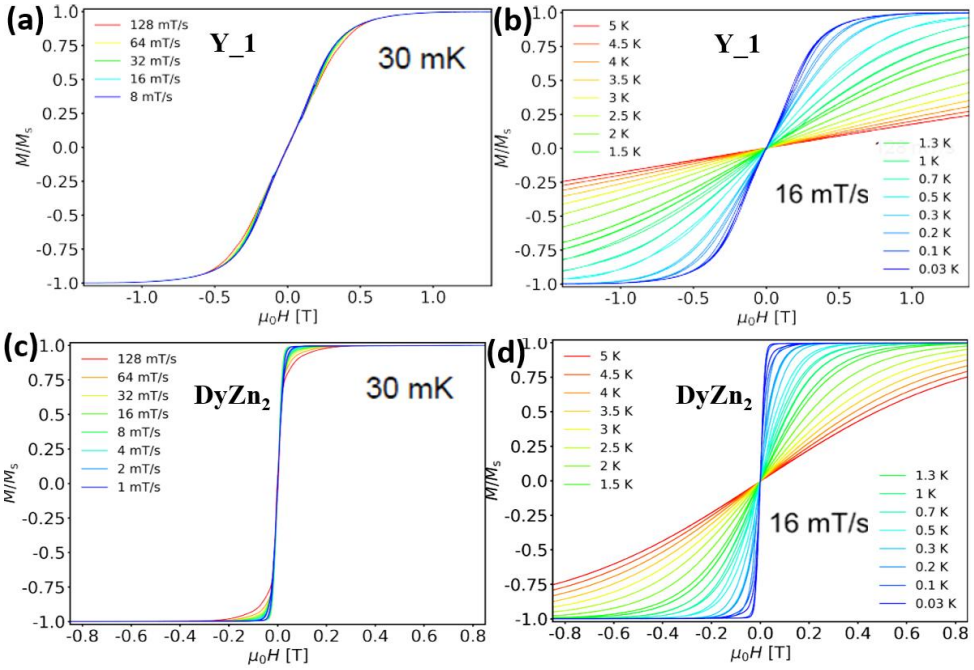

Figure 2.22. Hysteresis loops collected in a single crystal of **Y_1** and **DyZn$_2$** with the applied field along the easy axis of the crystal. Field sweep study at 30 mK and sweep rates from 128 down to 1 mT/s for **Y_1** (a) and **DyZn$_2$** (c); Temperature-dependent loops with a sweep rate of 16 mT/s from 30 mK up to 5 K for **Y_1** (b) and **DyZn$_2$** (d).

In the **Tb_1** analogue, the loops at a base temperature of 30 mK revealed open loops with a single sharp transition near zero field (Figure 2.23, a). The loops were sweep-rate dependent, consistent with the loops of SMMs. The temperature dependence of the loops revealed open loops up to 500 mK (Figure 2.23, b). Likewise, **Ho_1** also showed open hysteresis loops at temperatures up to 500 mK (Figure 2.23, c–d). Notably, both **Tb_1** and **Ho_1** exhibited substantial magnetization loss near zero field, indicating intense QTM at the zero-field level crossings, in stark contrast to **Dy_1** and **Gd_1**. This phenomenon can be rationalized through Kramers' theorem—**Tb_1** and **Ho_1** can be seen as non-Kramers "giant spin" systems, since the sum of one integer J_{Ln} (J_{Ln} = 6 for Tb^{III}, 8 for Ho^{III}) and two integer S_{Ni} (S_{Ni} = 1) yields an integer total, whereas **Dy_1** and **Gd_1** (J_{Ln} = 15/2 for Dy^{III}, 7/2 for Gd^{III}) are Kramers "giant spin" systems with intrinsic doubly degenerate ground states under zero field. The small openings in the hysteresis loops of **Tb_1** and **Ho_1** likely arise from hyperfine interactions with the ^{159}Tb and ^{165}Ho nuclear spins, which broaden the zero-field level crossings by splitting the otherwise degenerate electronic ground states.

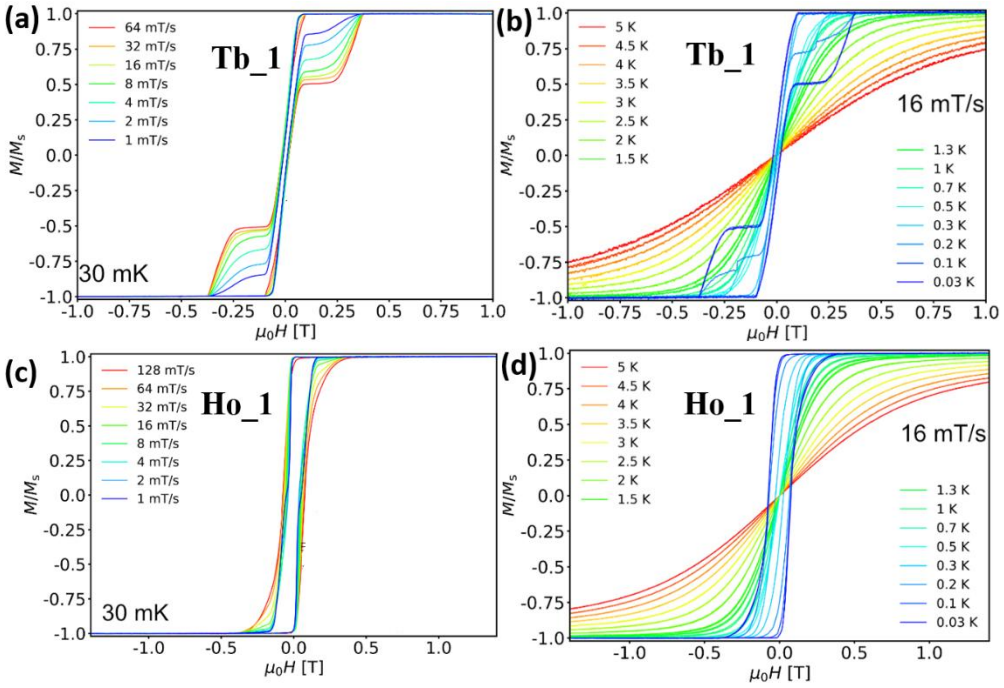

Figure 2.23. Hysteresis loops collected in a single crystal of **Tb_1** and **Ho_1** with the applied field along the easy axis of the crystal. Field sweep study at 30 mK and sweep rates from 128 down to 1 mT/s for **Tb_1** (a) and **Ho_1** (c); Temperature-dependent loops with a sweep rate of 16 mT/s from 30 mK up to 5 K for **Tb_1** (b) and **Ho_1** (d).

The hysteresis loops of **$TbZn_2$** were completely closed, revealing no SMM characteristics. Similar to the case of **$DyZn_2$**, the D_3 local symmetry around Tb^{III} allows non-negligible transverse CFPs $B_4^{\pm 3}$, $B_6^{\pm 3}$and $B_6^{\pm 6}$. Along with the non-Kramers nature of Tb^{III}, QTM-mediated fast magnetic relaxation is expected for **$TbZn_2$**.

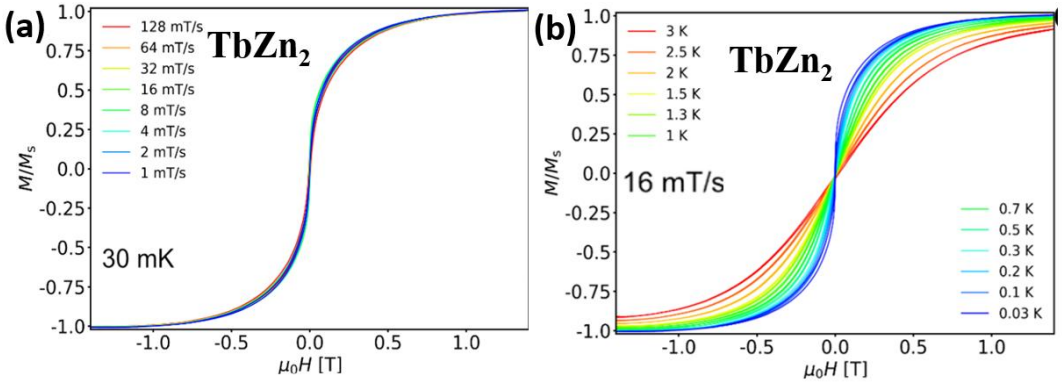

Figure 2.24. Hysteresis loops collected in a single crystal of **$TbZn_2$** with the applied field along the easy axis of the crystal. (a) Field sweep study at 30 mK and sweep rates from 128 down to 1 mT/s; (b) Temperature-dependent loops with a sweep rate of 16 mT/s from 30 mK up to 3 K.

Micro-SQUID investigation on the **Er_1** and **Yb_1** analogues revealed closed loops; therefore, neither of them is SMM under the current working conditions (Figure 2.25). In

Yb_1 and **Er_1**, the prolate electron density of Yb^{III} and Er^{III} favors easy-plane anisotropy instead of easy-axis anisotropy, which is incompatible with their axial coordination geometry. The mismatch not only disrupts ferromagnetic Ni–Ln coupling by orienting the lanthanide easy-plane perpendicular to the Ni···Ln vector, but also enhances single-ion QTM on lanthanide centers. This dual mechanism accounts for the absence of open hysteresis loops.

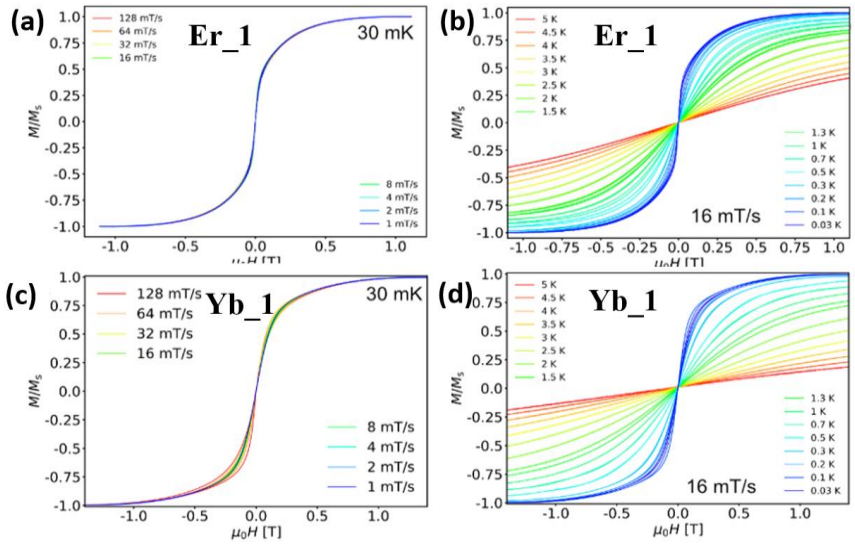

Figure 2.25. Hysteresis loops collected in a single crystal of **Er_1** and **Yb_1** with the applied field along the easy axis of the crystal. Field sweep study at 30 mK and sweep rates from 128 down to 1 mT/s for **Er_1** (a) and **Yb_1** (c); Temperature-dependent loops with a sweep rate of 16 mT/s from 30 mK up to 5 K for **Er_1** (b) and **Yb_1** (d).

In summary, open hysteresis loops were revealed in **Gd_1**, **Dy_1**, **Tb_1**, and **Ho_1**, where the ferromagnetic intramolecular Ni–Ln couplings promote "giant spin" behaviour rather than isolated metal-center property. The match between electron density of the lanthanide centers and the axial coordination is essential for the "giant spin" behaviour, as demonstrated by the lack of it in **Yb_1** and **Er_1**, where prolate electron clouds of Yb^{III} and Er^{III} violate the requirement. Furthermore, **Gd_1** and **Dy_1** exhibited enhanced coercivity and remanence owing to effective mitigation of zero-field QTM through: (i) the formation of "giant spin" (versus **$GdZn_2$**, **Y_1** and **$DyZn_2$**) and (ii) the protected degeneracy of Kramers systems (versus non-Kramers **Tb_1** and **Ho_1**).

2.7 Theoretical analysis of the magnetic properties

2.7.1 *Ab initio* calculations by the CASSCF methods

To gain deeper understanding of the magnetic behaviours in the samples, *ab initio* calculations were conducted on **Dy_1**, **Dy_3** and **$DyZn_2$** using CASSCF method on the

OPENMOLCAS platform. **Dy_1** and **Dy_3** were selected as the representatives of the fully linear and quasi linear Ni–Dy–Ni complexes respectively, and **DyZn$_2$** was analyzed to illustrate the effects from different transition metals. For the calculation on Dy^{III}, the Dy^{III} fragment was calculated keeping the experimentally determined structure of the corresponding compound, excluding counter-anions and solvents, and the paramagnetic Ni^{II} ions were replaced by the diamagnetic Zn^{II}. For the calculation on Ni^{II}, central Dy^{III} was replaced by Y^{III}, and the other Ni^{II} was by Zn^{II}. More details are listed in the Supporting Information.

In all three samples calculated, Dy^{III} ions are uniaxial anisotropic with their easy axes of magnetization closely aligned along the M–Ln–M direction. The energy gaps between the first excited Kramers doublets (KDs) and the ground KDs are 72.87 cm^{-1} for **Dy_1**, 47.64 cm^{-1} for **Dy_3**, both significantly larger than the effective energy barriers of ca.14 K (9.73 cm^{-1}) extracted for **Dy_1** – **Dy_6** under zero field; therefore, the magnetic relaxations in these samples are unlikely through the KDs of individual Dy^{III} (Table S27). The same theoretical energy gap for **DyZn$_2$** also exceeds its experimental U_{eff} (39.76 cm^{-1} vs. 8.39 cm^{-1}). This discrepancy can be attributed to the coexistence of multiple relaxation mechanisms, as indicated by the large α values. Comparing the Landé factors (***g***) and the transverse CFPs of individual Dy^{III} in **Dy_1** and **DyZn$_2$**, no significant difference which favors the suppression of QTM in **Dy_1** is observed (Table S28). Hence, the enhanced SMM performance of **Dy_1** is ascribed to the Dy–Ni interactions, not the structural modifications around Dy^{III} centers, e.g., the twisting angle θ. Furthermore, the Ni^{II} ions in both **Dy_1** and **Dy_3** display weak uniaxial magnetic anisotropy, which can be judged from their negative axial zero field splitting parameters D and anisotropic g values (Table S29). Consequently, the Ni^{II} ions have paramagnetic ground spin state $S = 1$, as the $m_S = \pm 1$ sublevels are lower in energy than the diamagnetic $m_S = 0$ sublevel. The easy axes of magnetization on Ni^{II} ions are roughly along the lines connecting the centers of N_3 face and the centers of the O_3 face in their N_3O_3 coordination polyhedra, approximately colinear with the easy axes of their neighboring Dy^{III} ions.

2.7.2 Exchange energy states modelled by PHI

Both $\chi_M T$ versus T and M versus H plots of **Dy_1** were fitted simultaneously in the software PHI[92], with the CFPs for Dy^{III} and Ni^{II} obtained from *ab initio* calculations as input. The best fitting result was obtained when the ferromagnetic coupling parameter $J_{Dy–Ni}$ was equal to 1.013 cm^{-1} (in the $H = -2JS_1S_2$ convention) (Figure S15). The asymmetry in **Dy_3** complicates such a fitting for **Dy_3** as two distinct $J_{Dy–Ni}$ values should be considered. Nevertheless, similar strength of the Dy–Ni ferromagnetic couplings can be anticipated for **Dy_1** – **Dy_6** due to the minimal variations in the $[Dy(NiL)_2]^+$ cations. Based on $J_{Dy–Ni}$, the exchange spectrum of **Dy_1** was calculated and the resulting relevant states were exhibited in Figure 2.19, together with the possible relaxation pathways and their qualitative transition

probabilities. The states 1 and 2 are the ground bistable states dominated by $|1, 15/2, 1\rangle$ and $|-1, -15/2, -1\rangle$ ($|m_{S,Ni1}, m_{J,Dy}, m_{S,Ni2}\rangle$), respectively. The energies and the percentage composition of the excited exchange states 1–10 are summarized in Table 2.4. The energy gaps between states 3 and 4, or states 5 and 6, and the ground states are 7.262 (10.45 K) and 7.398 cm^{-1} (10.65 K), respectively. These values align with the U_{eff} obtained for **Dy_1** – **Dy_6**. Meanwhile, the percentage composition of the excited exchange states 3–6 show they are highly mixed with m_J levels of opposite signs. Such mixing not only reduces the magnetic moment of the excited states, but also facilitates greatly the relaxation between $|m_J = \pm 15/2\rangle$, namely the magnetic reversal on Dy^{III}. These two facts both contribute to the large transition probabilities between state 3 and 4, 5 and 6 (Table S30). There are excited exchange states with higher energies, but as their related transition probabilities are much less than the ones for states 3–6, these states are believed irrelevant in the SMM performance. I then conclude that the relaxations in **Dy_1** – **Dy_6** under zero field take place in the low-lying excited exchange states (Figure 2.26).

Table 2.4. Calculated energy levels (cm^{-1}) and the compositions of major wave functions for the 10 lowest states for **Dy_1** using CASSCF/RASSI-SO with OPENMOLCAS.

States	E/cm^{-1}	major wave functions
1	0.000	92.04%|1, 15/2, 1>+7.54%|1, 9/2, 1>
2	3.787E−13	92.04%|−1, −15/2, −1>+7.54%|−1, −9/2, −1>
3	7.262	38.14%|−1, −15/2, 0>+38.14%|0, −15/2, −1>+7.68%|1, 15/2, 0>+7.68%|0, 15/2, 1>
4	7.262	38.14%|1, 15/2, 0>+38.14%|0, 15/2, 1>+7.68%|−1, −15/2, 0>+7.68%|0, −15/2, −1>
5	7.398	27.96%|−1, −15/2, 0>+27.96%|0, −15/2, −1>+17.95%|1, 15/2, 0>+17.95%|0, 15/2, 1>
6	7.398	27.96%|1, 15/2, 0>+27.96%|0, 15/2, 1>+17.95%|−1, −15/2, 0>+17.95%|0, −15/2, −1>
7	10.60	45.73%|1, −15/2, −1>+45.73%|−1, −15/2, 1>+3.98%|1, −9/2, −1>+3.98%|1, −9/2, −1>
8	10.60	45.73%|1, 15/2, −1>+45.73%|−1, 15/2, 1>+3.98%|1, 9/2, −1>+3.98%|1, 9/2, −1>
9	10.60	45.76%|1, −15/2, −1>+45.73%|−1, −15/2, 1>+3.98%|1, −9/2, −1>+3.98%|1, −9/2, −1>
10	10.60	45.76%|1, 15/2, −1>+45.73%|−1, 15/2, 1>+3.98%|1, 9/2, −1>+3.98%|1, 9/2, −1>

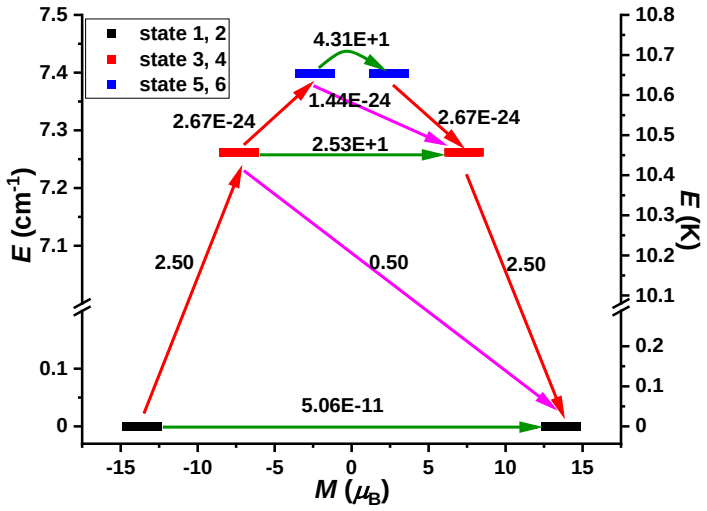

Figure 2.26. spectrum of the low-lying exchange states in complex **Dy_1**. Each exchange state is placed in agreement with its magnetic moment (bold lines). The numbers on each arrow denotes the qualitative transition probabilities.

2.8 Strategies to improve spin reversal barriers in Ni–Ln complexes

Since the low energy barrier between these excited exchange states and the ground states is the limiting factor of the reversal barrier of magnetization, creating stronger Ni–Dy coupling is a strategy to improve the SMM behaviour in similar systems. With that in mind, a hypothetical study is performed on PHI[92] to explore the influence of the intramolecular coupling. It is conducted by assuming that the $J_{Dy–Ni}$ in **Dy_1** is 2.026 cm^{-1}, doubled from the original strength, while the other parameters remain constant. The energy gaps between states 3 and 4, as well as states 5 and 6, and the ground states are 12.20 cm^{-1} and 12.76 cm^{-1}, respectively—both less than twice their original values. Meanwhile, the transition probabilities between states 3 and 4 (3.55) and states 5 and 6 (44.6) remain significantly high (Table 2.5). Considering that the $J_{Ln–Ni}$ in Ni–Ln complexes is typically limited to a few wavenumbers, merely increasing the coupling strength does not appear to be an effective strategy for enhancing U_{eff}.

Increasing the anisotropy of Ni^{II} may be another possible way to improve the SMM performance of **Dy_1**. To test this hypothesis, the parameter D is adjusted to −1.374 cm^{-1}, doubling its original value of −0.687 cm^{-1}, and E is set to 0, replacing its original value of 0.007 cm^{-1}. All other parameters remain unchanged. The energy of states 3 and 4 increases slightly to 9.32 cm^{-1}. The transition probabilities between states 3 and 4 is 24.03, even larger than before. The corresponding energy and transition probabilities for states 5 and 6 are 9.46 cm^{-1} and 25.25 (Table 2.5). Therefore, most of the spins will relax via the same low-lying excited exchange states. Since the magnetic anisotropy of Ni^{II} is generally weak, it is not practical to obtain large U_{eff} by merely adjusting the anisotropy of Ni^{II}.

In the next attempt, the transverse CFPs $B_4^{\pm 3}$, $B_6^{\pm 3}$and $B_6^{\pm 6}$, which could contribute to QTM on Dy^{III}, are set to zero. With this modification, the energies of the low-lying excited states 3 and 4, 5 and 6 remain almost unchanged, but the transition probabilities between them decrease significantly (Table 2.5). This highlights a strategy to mitigate spin transitions via low-lying exchange states by eliminating the unfavorable transverse CFPs on the lanthanide ion. In fact, the first transition involving the reverse of the spin state of Dy^{III} with probability over 0.1 is now the spin transition between states 13 and 14 (energy = 18.4 cm^{-1}, transition probability = 1.14). When the rhombic zero-field splitting parameter E of Ni^{II} ions is also set to zero, the first transition probability over 0.1 is observed between states 25 and 26 (transition probability = 5.22), which are 71.5 cm^{-1} high in energy. In this hypothetical scenario, the Ni^{II} ions exhibit stronger axial anisotropy and are less prone to spin relaxation, which further stabilizes the spin states of Dy^{III} they interact with.

Table 2.5. Selected calculation results for different hypothetical scenarios.

Changed settings	J_{Dy-Ni}= 2.026 cm^{-1}	$D = -1.374$ cm^{-1} $E = 0$ cm^{-1}	$B_4^{\pm 3}$, $B_6^{\pm 3}$, $B_6^{\pm 6} = 0$	$B_4^{\pm 3}$, $B_6^{\pm 3}$, $B_6^{\pm 6} = 0$ $E = 0$ cm^{-1}
Energy of states 3 and 4	12.20 cm^{-1}	9.32 cm^{-1}	7.43 cm^{-1}	7.43 cm^{-1}
Transition probability between states 3 and 4	3.55	24.03	0.1367E−04	0.1734E−05
Energy of states 5 and 6	12.76 cm^{-1}	9.46 cm^{-1}	7.58 cm^{-1}	7.58 cm^{-1}
Transition probability between states 5 and 6	44.6	25.25	0.12	0.1063E−03

With all the hypothetical experiments performed for different scenarios, it can be deduced that in a Ni–Ln complex where the anisotropies of Ln^{III} and Ni^{II} are both easy-axis and colinear, the spin relaxation through low-lying exchange states can be suppressed by carefully designing the coordination symmetry around Dy^{III} to quench the adverse transverse CFPs. On that basis, reducing rhombic zero-field splitting parameter E of Ni^{II} can further enhance the suppression effect.

To gain deeper insights on the general strategy to improve spin reversal barriers in Ni–Ln complexes, the Ni–Ln SMMs with U_{eff} over 50 K reported in the literatures are listed in Table 2.6. Two of the ten complexes in the table require applied magnetic fields to exhibit U_{eff} over 50 K. Among the remaining compounds, $Tb_2Ni_2(HL^2)_2(\mu_3\text{-}OMe)_2(CH_3CN)_2(NO_3)_4\cdot 4H_2O$ and $Dy_2Ni_2(HL^2)_2(\mu_3\text{-}OMe)_2(CH_3CN)_2(NO_3)_4\cdot 4H_2O$ are isostructural, both featuring butterfly shaped $\{Ln_2M_2\}$ cores. CASSCF calculations illustrated that the energy separations between

the ground and the first excited doublets (>150 cm^{-1}) were much higher than their experimentally derived U_{eff}. In contrast, relaxation paths with blocking barriers close to the U_{eff} were present in the calculated exchange spectrum. Complexes with $\{Ln_2M_2\}$ butterfly shaped cores represent a major category of 3d–4f SMMs and many such $\{Ln_2Ni_2\}$ SMMs have been reported so far. In these $\{Ln_2Ni_2\}$ SMMs, most of which exhibit effective energy barriers lower than 30 K, the coordination environments of Ln ions deviate significantly from ideal high-symmetry environments (Table S31). Considering this phenomenon along with the previous discussion of $Tb_2Ni_2(HL^2)_2(\mu_3\text{-}OMe)_2(CH_3CN)_2(NO_3)_4\cdot 4H_2O$ and $Dy_2Ni_2(HL^2)_2(\mu_3\text{-}OMe)_2(CH_3CN)_2(NO_3)_4\cdot 4H_2O$, it is reasonable to infer that in Ni–Ln complexes where the coordination environments around Ln ions are not of particular high symmetries, magnetic relaxations through low-lying excited exchange states constituent the primary factor limiting the improvement of SMM performance.

$[Dy_2Ni_2(L^1)_{10}(bipy)_2]$ and $[Dy_2Ni_2(bipy)_2(C_6H_5COO)_{10}]$ possess similar Ni–Dy–Dy–Ni arrays. Two or more relaxation processes are reported in $[Dy_2Ni_2(L^1)_{10}(bipy)_2]$. One process at higher temperatures is ascribed to the relaxation through spin-orbit states of individual Dy^{III} ions, as the measured energy barrier (73 cm^{-1}) is in good agreement with the calculated barrier involving first excited KDs of Dy^{III} ions (61 cm^{-1}). Another process at lower temperatures is associated with the reversal of exchange states, where the low-energy barrier of exchange type is calculated to be ca. 8 cm^{-1}. The energy barrier extracted from experimental results for $[Dy_2Ni_2(bipy)_2(C_6H_5COO)_{10}]$ is reported to be 39.9 cm^{-1}, in the same order of the calculated energy separations between the ground and the first excited KDs of individual Dy^{III} (84.4 cm^{-1}). It is noteworthy that the intramolecular Dy–Dy and Dy–Ni interactions in $[Dy_2Ni_2(bipy)_2(C_6H_5COO)_{10}]$ are calculated to exhibit comparable strengths, making it complicated to assess of the specific effect from Dy–Ni interactions.

$[Ni_2Dy_3(HL^3)_4]Cl$ contains a central linear $\{Dy_3\}$ unit and two terminal Ni^{II}. The central Dy^{III} has distorted square antiprism geometry while the other two possess trigonal dodecahedron geometry. Two thermally activated relaxation processes are present, among which the one occurring at higher temperatures shows a typical Arrhénius-like behaviour with U_{eff} = 85 K. No *ab initio* calculations have been reported to elucidate the mechanism of the magnetic relaxation. At last, $HoNi_5(quinha)_5F_2(dfpy)_{10}$, $[DyNi_5(quinha)_5F_2(dfpy)_{10}](ClO_4)\cdot 2EtOH$ and $[Ni_2Dy(TTTT^{Me})_2(DMF)]BPh_4$ have far superior energy barriers relative to other Ni–Ln SMMs. The first two are metallacrowns with each central Ln^{III} ion surrounded equatorially by a [15-MC_{Ni}-5] ring. $[Ni_2Dy(TTTT^{Me})_2(DMF)]BPh_4$, where $TTTT^{Me}$ stands for a tripodal Schiff base, has a quasi linear array of Ni–Dy–Ni, similar with the trinuclear complexes reported in this work. However, besides six oxygen atoms from two $TTTT^{Me}$ ligands, the central Dy^{III} ion is further coordinated by an extra DMF molecule. The common structural feature of them is the compressed pseudo pentagonal bipyramid coordination environment (D_{5h}) around Dy^{III} ions. While the incorporation of paramagnetic Ni^{II} ions is found to induce unusual temperature- and field-dependent magnetic dynamics in the low temperature region by providing low-lying exchange states, the relaxations at high temperatures are predominantly governed by individual Ln^{III} centers of these complexes.

Overall, to achieve high-energy-barrier Ni–Ln SMMs, it is essential to address the challenge posed by low-lying excited exchange states. One effective approach is to fine-tune the coordination geometry around the Ln^{III} ion. Additionally, enhancing the ferromagnetic coupling between Ni^{II} and Ln^{III}, increasing the uniaxial anisotropy of the Ni^{II}, and optimizing the alignment between Ni^{II} and Ln^{III} ions are possible ways to further boost the energy barriers.

Table 2.6. The data of Ni–Ln SMMs with the U_{eff} over 50 K reported in literature.

Complexes	H_{DC}/ kOe	U_{eff}/K	τ_0/s	Geometries	CshM value	Ref.
$HoNi_5(quinha)_5F_2(dfpy)_{10}$	0	825.1	$3.3(5) \times 10^{-13}$	pentagonal bipyramid (D_{5h})	0.552	49
$[DyNi_5(quinha)_5F_2(dfpy)_{10}](ClO_4)\cdot 2EtOH$	0	1526(16)	$3.7(7) \times 10^{-12}$	pentagonal bipyramid (D_{5h})		155
$[Dy_2Ni_2(L^1)_{10}(bipy)_2]$	0	105(1)	1.85×10^{-11}	mono-capped triangular prism (C_{2v})	0.246*	182
$[Dy_2Ni_2(bipy)_2(C_6H_5COO)_{10}]$	0	57.06	1.80×10^{-8}	triangular dodecahedron (D_{2d})	1.058	174
$Tb_2Ni_2(HL^2)_2(\mu_3\text{-}OMe)_2(CH_3CN)_2(NO_3)_4\cdot 4H_2O$	0	86.2	2.3×10^{-7}	capped square antiprism (C_{4v})	3.600*	183
$Dy_2Ni_2(HL^2)_2(\mu_3\text{-}OMe)_2(CH_3CN)_2(NO_3)_4\cdot 4H_2O$	0	56.6	3.3×10^{-8}	capped square antiprism (C_{4v})	3.532*	183
$[Dy_2Ni(C_7H_5O_2)_8]\cdot(C_7H_6O_2)_2$	1.5	55.19	5.21×10^{-8}	square antiprism (D_{4d})	0.727*	51
$[Ni_2Dy_3(HL^3)_4]Cl$	0	$U_1 = 53.5$ $U_2 = 85$	$\tau_1 = 2.3 \times 10^{-8}$ $\tau_2 = 5.9 \times 10^{-7}$	trigonal dodecahedron (D_{2d}) square-antiprism (D_{4d})		184
$[Ni_2Dy(TTTT^{Me})_2(DMF)]BPh_4$	0 0.3	582 582	$1.4(4) \times 10^{-11}$ $1.3(4) \times 10^{-11}$	pentagonal bipyramid (D_{5h})	0.987	178
$Dy_4Ni_8(\mu_3\text{-}OH)_8(L^4)_8(OAc)_4(H_2O)_4\cdot 3.25EtOH\cdot 4CH_3CN$	1	81.14(3)	$6.21(2) \times 10^{-11}$	square-antiprism (D_{4d})	0.833 0.830 0.694 0.506	185

*calculated by the author from the provided cif files

H_2quinha = quinaldichydroxamic acid;

dfpy = 3,5-difluoropyridine;

HL^1 = 3, 5-dichlorobenzoic acid;

bipy = 2, 2'-bipyridine;

C_6H_5COO = benzoate;

H_3L^2 = 2-(2, 3-dihydroxpropyliminomethyl)-6-methoxyphenol;

$C_7H_6O_2$ = salicylic aldehyde;

H_4L^3 = (E)-2, 2'-(2-hydroxy-3-((2-hydroxyphenylimino)methyl)-5-methylbenzylazanediyl)diethanol; H_3TTTT^{Me} = 2, 2', 2"-(((nitrilotris-(ethane-2, 1-diyl))tris-(azanediyl))tris(methyl-methylene))tri-phenol; H_2L^4 = 4-bromo-2-[(2-hydroxypropylimino)methyl]phenol.

Chapter 3. Magnetic and Photoluminescent Properties of $[Ln(ML)_2]CF_3SO_3$ (M = Zn, Mg, Co, Fe) Trinuclear Complexes

3.1 Introduction

In Chapter 2, a series of $\{LnNi_2\}$ trinuclear complexes with fully linear or quasi-linear Ni–Ln–Ni array was investigated magnetically. All the dysprosium containing complexes behaved as single molecular magnets under zero external field. Theoretical calculations using CASSCF method, using the coordinates obtained from the single-crystal diffraction studies, and the simulations on the M/H and $\chi T/T$ plots proved that the intramolecular couplings play a key role in the SMM property of the dysprosium complexes. Furthermore, micro-SQUID measurements revealed open hysteresis loops in Gd, Dy, Tb, Ho containing complexes, where Ln–Ni are ferromagnetically coupled.

These findings motivated me to further investigate magnetic properties on more samples with the same linear trinuclear configuration. In this chapter, the terminal Ni^{II} ions were successfully substituted with other paramagnetic 3d ions (Co^{II} and Fe^{II}), yielding new complexes $[Ln(CoL)_2CF_3SO_3]$ (**LnCo$_2$**, Ln = Y, Gd, Tb, Dy) and $[Ln(FeL)_2CF_3SO_3]$ (**LnFe$_2$**, Ln = Y, Gd, Tb, Dy). DC and AC magnetic studies were performed to unravel the static and dynamic magnetic properties of the complexes.

The photoluminescence of lanthanide complexes is another important subject of interest and Schiff base ligands are well known for their sensitization ability. Recently, M. Ruben and co-workers performed spectral hole burning (SHB) studies of prototypical C_{3v} symmetric [Eu(trensal)] (H_3trensal = 2,2',2''-Tris(salicylideneimino)triethylamine) complex.[186] The studies revealed narrow optical linewidth (2.8 MHz at 4.2 K) of the $^5D_0 \rightarrow {}^5F_0$ transition centered around 580 nm and long nuclear spin lifetimes up to 460 ± 80 s. Since ligand H_3L is structurally similar to H_3trensal, and the central lanthanide ion in M–Ln–M core has a similar D_3 symmetric coordination environment, it is supposed interesting to conduct photoluminescence investigations on the trinuclear complexes and analyze the effects of structural differences. However, no photoluminescence is observed in the $\{LnNi_2\}$ trinuclear complexes reported in the former chapter, as it is quenched by the Ni^{II} ions through the paramagnetic quenching effect.[187] Replacing the paramagnetic Ni^{II} ions with diamagnetic divalent ions is a strategy to remove the paramagnetic quenching effect. Consequently, two sets of trinuclear complexes—$Ln(ZnL)_2CF_3SO_3$ (**LnZn$_2$**, Ln = Ce, Pr, Nd, Sm, Eu, Gd, Tb, Dy) and $Ln(MgL)_2CF_3SO_3$ (**LnMg$_2$**, Ln = Pr, Nd, Sm, Eu, Gd)—were prepared to study the photoluminescence of the lanthanide ions.

3.2 Synthesis details

General procedures

All commercially purchased (Sigma-Aldrich, TCI chemicals, abcr) chemicals and reagents were of reagent grade and used without further purification. Ligand H_3L is synthesized by the condensation reaction as described in Chapter 2.2.

The syntheses of **LnM2** are successfully achieved using three different procedures (Scheme 3.1). To start with, **LnZn2** (Ln = Ce, Pr, Nd, Sm, Eu, Gd, Tb, Dy) are synthesized with a two-step scheme, modified from the procedures previously published.[164,165] **LnMg2** are obtained by slow evaporation of methanolic solutions in ambient environment. At last, **LnCo2** and **LnFe2** are prepared under inert atmosphere, since Co^{II} and Fe^{II} ions can be easily oxidized to the corresponding trivalent ions in the methanolic solution in the presence of L^{3-} and form the precipitation of charge-neutral $Co^{III}L$ or $Fe^{III}L$ mononuclear complexes.[188] It is also worthy to note, even after the formation of **LnCo2** or **LnFe2** single crystals in the mother liquid, exposure to oxygen will cause the disappearance of the desired product and the emergence of $Co^{III}L$ or $Fe^{III}L$ complexes. This is because the crystals can re-dissolve in methanol solution and then decompose into smaller ions. Therefore, crystals of the target complexes are collected soon after their formation. Once harvested from the solution, the crystals can remain stable in the dry environment for a long time.

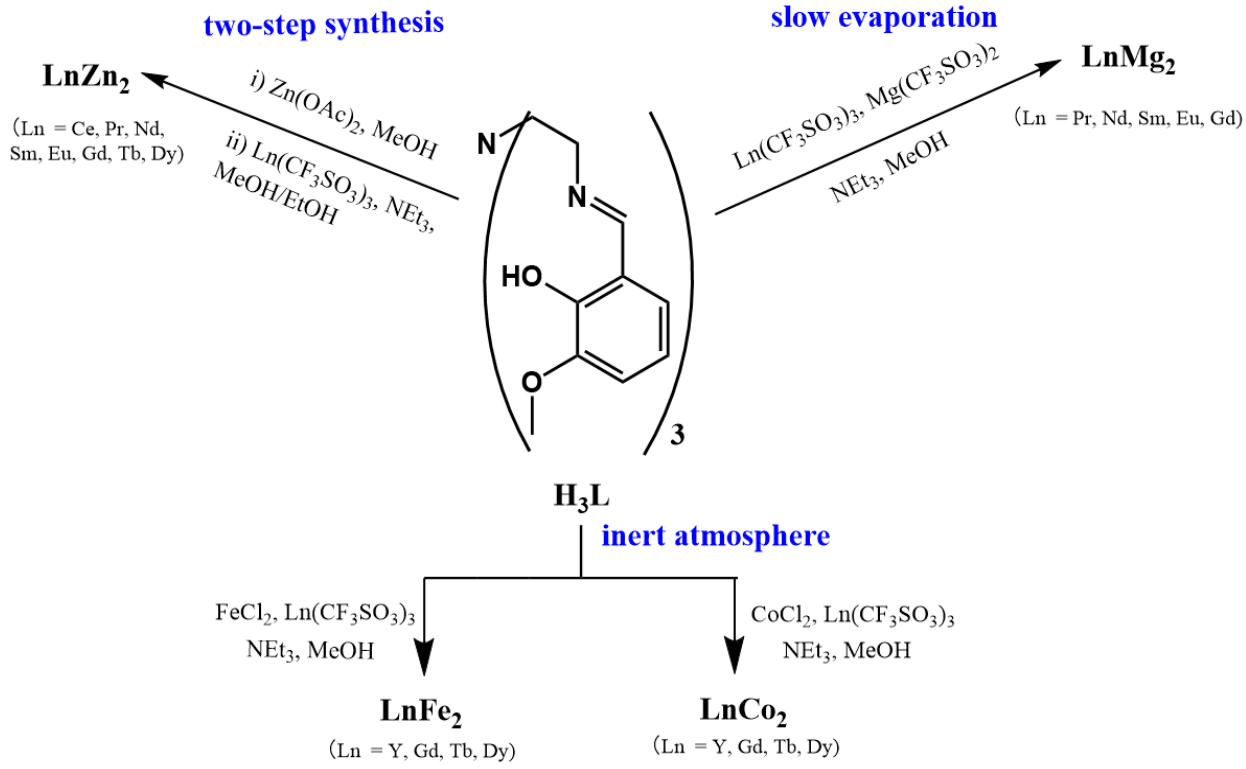

Scheme 3.1. the synthetic routes to synthesize LnM_2 (M = Zn, Mg, Co, Fe) trinuclear complexes.

Syntheses of magnesium trifluoromethanesulfonate

Slightly excessive trifluoromethanesulfonic acid (3.00 g, 20.0 mmol) was added dropwise to a clear colorless aqueous solution of magnesium carbonate (0.76 g, 9.0 mmol) at room temperature. After stirring for 1 hour at 80 °C, volatiles were removed under reduced pressure at 80 °C. The resulted residue was then washed with cold diethyl ether and hexane. After drying in an oven at 60 °C overnight, magnesium trifluoromethanesulfonate (2.10 g, yield 72.7 %) was obtained as white crystalline solid.

Synthesis of $Ln(ZnL)_2CF_3SO_3$ (**$LnZn_2$**, Ln = Ce, Pr, Nd, Sm, Eu, Gd, Tb, Dy)

Step 1: H_3L (1.1 g, 2.0 mmol) and equimolar $Zn(OAc)_2$ (0.367 g, 2.0 mmol) were dissolved in 20 mL methanol. The solution was evaporated to dryness, and the resulting orange oil was dissolved in 20 mL of methanol and dried again. This procedure was repeated 5 times to remove the acetate anions. The resulting oily product is then used directly in the next step.

Step 2: 66 mg of the oily product from last step was dissolved in 4 mL of methanol together with 0.05 mmol of $Ln(CF_3SO_3)_3$ (Ln = Ce, Pr, Nd, Sm, Eu, Gd, Tb, Dy). Then a 1 mL ethanol solution containing triethylamine (60 mg, 0.6 mmol) was added into the former methanol solution. The resulting solution was stirred for 5 minutes and left to stand in an incubator at 45 °C. Hexagonal prismatic crystals were formed after 2 days. Solid impurity was observed only in the synthesis of **$DyZn_2$**, and it was removed by manual separation as described in Chapter 2.2. Attempts were also made to prepare **$HoZn_2$**, **$ErZn_2$** and **$YbZn_2$**, but the results are not fruitful. This fact indicates that Dy^{III} ion is at the demarcation point, and **$LnZn_2$** complexes of lanthanide ions featuring ionic radii smaller than the Dy^{III} radius cannot be obtained by the current method. The color of **$EuZn_2$** is orange, while the other **$LnZn_2$** exhibit varying shades of yellow.

Synthesis of $Ln(MgL)_2CF_3SO_3$ (**$LnMg_2$**, Ln = Pr, Nd, Sm, Eu, Gd)

H_3L (55.0 mg, 0.10 mmol) and 32.2 mg $Mg(CF_3SO_3)_2$ (0.10 mmol) and 30 mg triethylamine (0.30 mmol) were stirred together in 12 mL methanol for 10 minutes till a clear yellow solution was formed. Next, slightly excessive $Ln(CF_3SO_3)_3$ (36.0 mg, 0.06 mmol) salt was added to the solution. After stirring for another 10 minutes, the solution was filtered and left undisturbed for slow evaporation at ambient temperature. Hexagonal prism shaped crystals were collected after aweek. Attempts to prepare **$CeMg_2$**, **$TbMg_2$**, **$DyMg_2$**, and **$HoZn_2$** using the same synthetic method were not successful, probably due to the mismatch in the size of these ions. The color of **$EuMg_2$** is dark red, while the other **$LnMg_2$** exhibit varying shades of yellow.

Synthesis of $Ln(CoL)_2CF_3SO_3$ (**$LnCo_2$**, Ln = Y, Gd, Tb, Dy)

H_3L (110 mg, 0.20 mmol) and triethylamine (60 mg, 0.60 mmol) were stirred in 35 mL methanol for 60 minutes in a three-neck flask under a continuous argon flow. Slightly excess $CoCl_2$ (31.2 mg, 0.24 mmol) and $Ln(CF_3SO_3)_3$ (36.0 mg, 0.12 mmol) were quickly added into the solution under the protection of argon. After three minutes of stirring, the metal salts fully dissolved and the solution turned into orange color. Then the stirring and the introduction of argon were stopped and the flask was kept still in an ice bath to allow for the crystallization of **$LnCo_2$**. After 60 minutes, orange crystalline product was formed and collected by vacuum filtration.

Synthesis of $Ln(FeL)_2CF_3SO_3$ (**$LnFe_2$**, Ln = Y, Gd, Tb, Dy)

110 mg H_3L (0.20 mmol) and 60 mg triethylamine (0.60 mmol) were stirred in 35 mL methanol for 60 minutes in a three-neck flask under a continuous argon flow. Slightly excessive $FeCl_2$ (31.0 mg, 0.24 mmol) and $Ln(CF_3SO_3)_3$ (36.0 mg, 0.12 mmol) were added together into the solution rapidly under the protection of argon, and the solution turned into purple. Once the metal salts were fully dissolved, the stirring and the introduction of argon were stopped. After around five minutes, purple crystalline product was observed at the bottom of the flask. It was collected by vacuum filtration without further delay.

3.3 Molecular structures

The molecular structures of **$DyZn_2$**, **$EuMg_2$**, and **YCo_2** were determined by performing SC-XRD studies (Figure 3.1 and 3.2). Powder-XRD spectra were collected on all the **LnM_2** (M = Zn, Mg, Co, Fe) samples obtained, and compared with the simulated spectra of **$DyZn_2$**, **$EuMg_2$**, and **YCo_2** (Figure S16–S19). The results showed that the **LnM_2** (M = Zn, Mg, Co, Fe) samples had the same linear trinuclear structure, regardless of the different metal ions. Moreover, FT-IR (ATR) measurements performed on **$DyZn_2$**, **$EuMg_2$**, **$LnCo_2$**, **$LnFe_2$** (Ln = Y, Gd, Tb, Dy) provided further proof on the purity and the structural similarity of these samples (Figure S20).

$EuMg_2$ crystalizes in the *R*32 space group, trigonal crystal system, with Z = 3. The detailed crystallographic information is provided in Table S32. Continuous shape measures (CShM) analyses performed on the coordination polyhedrons around Mg^{II} indicate that Mg^{II} ions are situated in a nearly octahedral coordination environment (Table S33). The bond length is 2.206(2) Å for Mg–N, and 2.057(2) Å for Mg–O. The distorted trigonal antiprismatic six-coordinated sphere around the central Eu^{III} ion is axially elongated, with the twist angle θ = 38.86°, the dihedral angle φ = 68.68° (see Chapter 2.3 for the definition of θ and φ). The six Eu–O bonds have a bond length of 2.4284(18) Å.

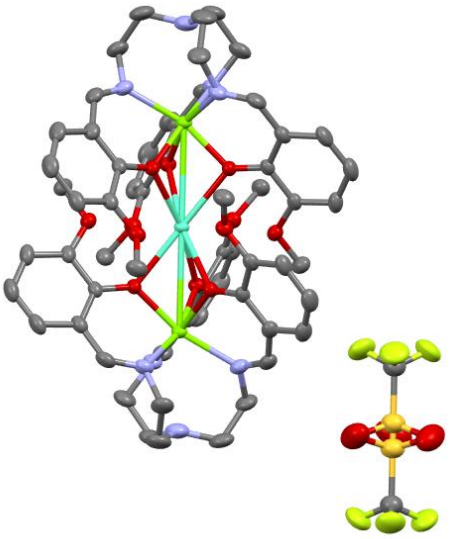

Figure 3.1. Molecular structure of **EuMg$_2$**. H atoms are omitted for the sake of clarity. Colour code: Eu, cyan; O, red; N, blue; C, grey; S, orange; F, yellow; Mg, green.

YCo$_2$ is isostructural to **EuMg$_2$**, with basically the same unit cell parameters as that of **EuMg$_2$** (Table S34). The coordination polyhedrons around Co^{II} deviate slightly from regular octahedron (Table S35). The Co–N and Co–O bond lengths are 2.132(3) Å and 2.091(2) Å, respectively. Central Y^{III} ion is also located in a distorted axially elongated trigonal antiprismatic coordination sphere. The twist angle θ around Y^{III} is 40.88°, while the dihedral angle φ is 67.00°.

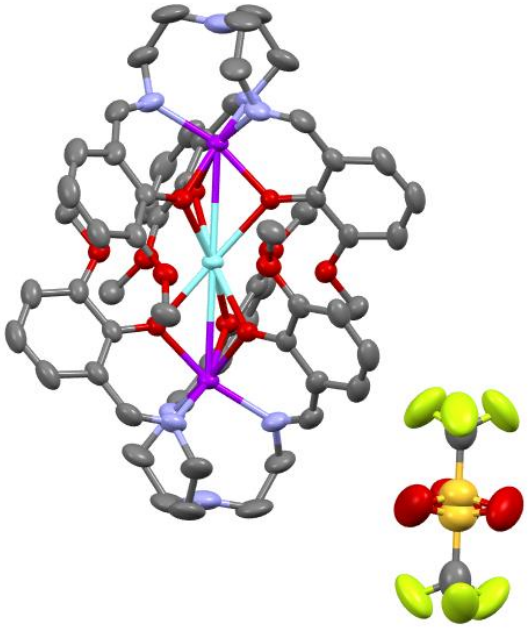

Figure 3.2. Molecular structures of **YCo$_2$**. H atoms are omitted for the sake of clarity. Colour code: Y, aqua blue; O, red; N, blue; C, grey; S, orange; F, yellow; Co, purple.

The structure of **$DyZn_2$** is already shown and discussed in the Chapter 2.3. Here only some parameters of it are listed in Table 3.1 for the comparative study with **$EuMg_2$**, **YCo_2**, and **Dy_1**. As it is shown by the comparison among **Ln_1** (Ln = Gd, Tb, Dy, Ho, Er, Yb) in Chapter 2.3, the radii of lanthanide ions influence the Ln–O bond lengths but do not significantly affect the coordination spheres of the terminal divalent metal ions, so the differences among the bond lengths of M–O and M–N in Table 3.1 come mainly from the nature of M^{II} ions, while the Ln–O bond lengths follow the trend of the ionic radii of lanthanides.

Table 3.1. Selected bond lengths (Å) and bond angles (°) for **$EuMg_2$**, **$DyZn_2$**, **YCo_2**, and **Dy_1**

	Ln–O	M–O	M–N	θ	φ
$EuMg_2$	2.4284(18)	2.057(2)	2.206(2)	38.86	68.68
$DyZn_2$	2.349(3)	2.155(3)	2.129(4)	37.64	67.39
YCo_2	2.3219(19)	2.091(2)	2.132(3)	40.88	67.00
Dy_1	2.346(3)	2.062(3)	2.090(4)	44.95	67.73

3.4 Magnetic properties of $[Ln(CoL)_2]CF_3SO_3$

3.4.1 Static magnetic properties

Direct current (DC) magnetic susceptibility measurements of **$LnCo_2$** (Ln = Y, Gd, Tb, Dy) were performed on polycrystalline samples in the temperature range of 2 to 300 K under DC field of 1000 Oe. As shown in Figure 3.3, the $\chi_M T$ value for **YCo_2** is 6.06 $cm^3mol^{-1}K$ at 300 K. The value is considerably larger than 3.74 $cm^3mol^{-1}K$ expected for the combined contributions of two uncoupled high spin isotropic Co^{II} (1.87 $cm^3mol^{-1}K$, S = 3/2, g = 2.0) and one diamagnetic Y^{III}. The large value is attributed to the presence of unquenched orbital contribution and spin-orbit coupling in Co^{II}. Upon lowering the temperature, $\chi_M T$ value first remains almost constant in the high temperature regime, and then exhibits a gradual decrease starting from around 150 K. At 2.0 K, $\chi_M T$ value of 3.40 $cm^3mol^{-1}K$ was observed. The decrease in the low temperature-regime can be attributed to the intrinsic magnetic anisotropy of Co^{II} ions.

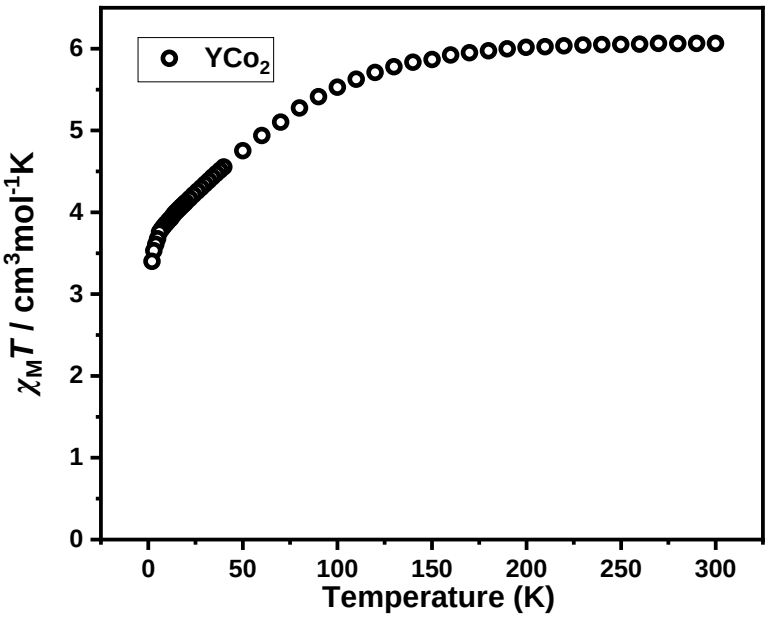

Figure 3.3. Plot of $\chi_M T$ versus T for **YCo$_2$** under an applied DC field of 1000 Oe.

The $\chi_M T$ versus T data for **GdCo$_2$**, **TbCo$_2$**, and **DyCo$_2$** are plotted in Figure 3.4. Their $\chi_M T$ values at 300 K are 14.28, 19.82, 20.83 $cm^3mol^{-1}K$, respectively. Assuming that two Co^{II} and one Ln^{III} are all uncoupled, and the contribution of the two Co^{II} is equal to that in **YCo$_2$** (6.06 $cm^3mol^{-1}K$), the contributions from Gd^{III}, Tb^{III}, Dy^{III} are calculated to be 8.22, 13.76 and 14.77 $cm^3mol^{-1}K$ in the corresponding **LnCo$_2$**, close to their respective theoretical values for a single uncoupled ion. The $\chi_M T$ values for **GdCo$_2$**, **TbCo$_2$**, and **DyCo$_2$** remain almost constant until 150 K. In the low temperature region, however, the values decrease at a noticeable rate before starting to rise after reaching minimum values at around 40 K. The first decrease is attributed to the thermal depopulation of excited Stark sublevels of the Dy^{III} or Tb^{III}, and intrinsic anisotropy of Co^{II}. And the following rise indicates the presence of Gd–Co, Tb–Co and Dy–Co intramolecular ferromagnetic couplings. Maximum values are observed at 3.0 K rather than 2.0 K for all three complexes, suggesting a weak intermolecular interaction operates at 2.0 K. However, the presence of it cannot be definitely confirmed, as the phenomenon might also result from the decrease in Co^{II} susceptibility outweighing the effect of intramolecular ferromagnetic coupling.

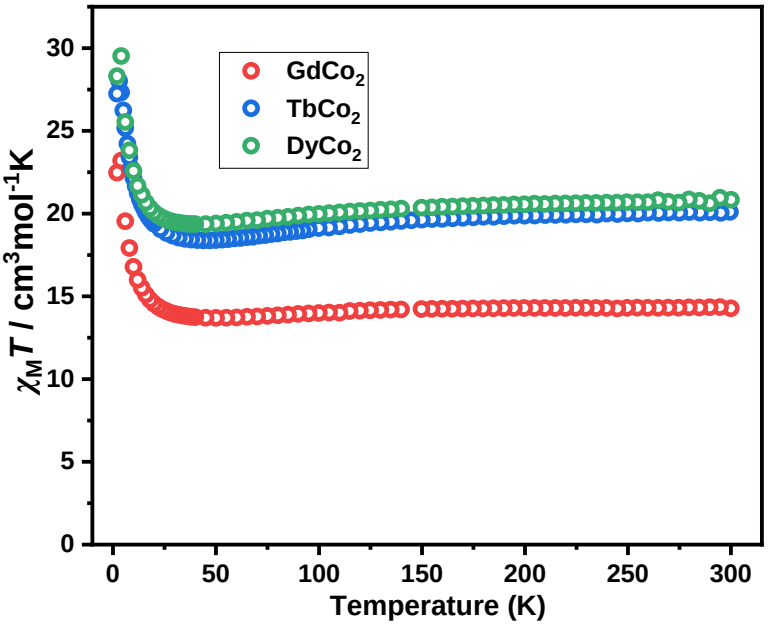

Figure 3.4. Plots of $\chi_M T$ vs. T for **GdCo$_2$**, **TbCo$_2$**, **DyCo$_2$** under an applied field of 1 kOe.

3.4.2 Dynamic magnetic properties

Alternating current (AC) susceptibility measurements were performed on all four **LnCo$_2$** complexes at 2.0 K, first under a zero field and then under an applied field of 1000 Oe with a 3 Oe oscillating field at frequencies from 1 to 1500 Hz. If any signs for slow relaxation of magnetization were detected, an applied field-dependent AC susceptibility measurement were then performed to find out the optimal applied field. The determination of the optimal field is based on a comprehensive consideration of the relaxation time and intensity of χ_M''.

The slow relaxation of magnetization behaviour is observed for **YCo$_2$** only under an applied field; therefore, **YCo$_2$** is a field-induced SMM. The optimal field is determined to be 1500 Oe as shown in Figure S21. Figure 3.5 displays the in-phase (χ') and out-of-phase (χ'') components of the magnetic susceptibility under this optimal field. The χ_M'' vs. frequency peaks are observed in the temperature range of 1.9 K to 2.5 K. The results were shown up to 3.0 K since the relaxation time could be still extracted with a high degree of confidence.

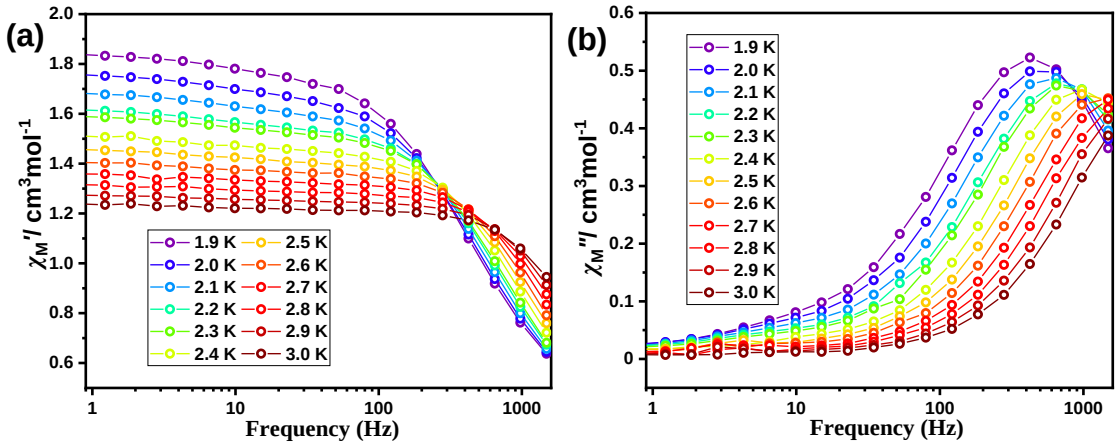

Figure 3.5. Frequency dependency of the in-phase (a) and out-of-phase (b) components of the magnetic susceptibility for **YCo_2** under 1500 Oe applied field. The solid lines are guide for the eye.

The Cole–Cole plot (χ_M'' vs. χ_M') is fitted by the software CCFIT according to the generalized Debye model (Figure 3.6, a). The detailed fitting results, including the extracted τ and α are given in Table S38. α values are relatively larger at low temperatures and smaller at high temperatures, ranging from 0.240 to 0.108, indicating a broader distribution of relaxation times at low temperatures. The relaxation times τ obtained are plotted versus T^{-1} in Figure 3.6, b. It could be seen that the data points were not distributed along a straight line, which indicates that the Orbach process is unlikely to exist in this case. In fact, it is frequently documented that the magnetic relaxations in Co^{II} field-induced SMMs occur through virtual states instead of real excited states. Therefore, only Raman, direct and QTM processes are considered in the fitting, as in the following equation:

$$\tau^{-1} = AT + CT^n + {\tau_{QTM}}^{-1} \qquad \text{Equation 3.1}$$

The best fitting result is A = 861 s^{-1} K^{-1}, C = 32.8 s^{-1} K^{-n}, and n = 5.6. n falls within the normal range for Raman processes.[189,190] The coexistence of the Raman and direct processes were also in line with the relatively broad distribution of the relaxation times. Attempts to include a QTM term do not improve the fitting result, but lead to overparameterization.

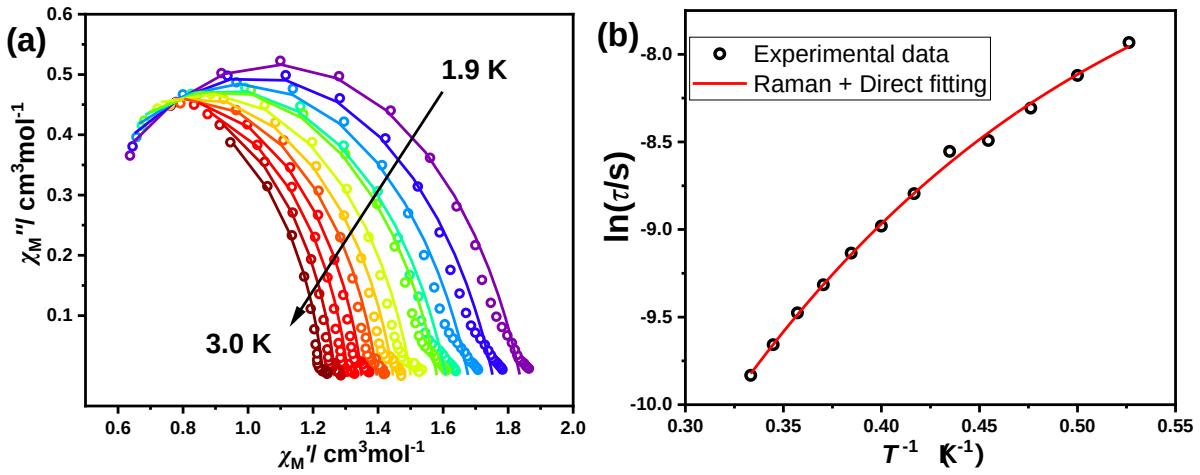

Figure 3.6. (a) the Cole–Cole (χ_M'' vs. χ_M') plot of **YCo$_2$** under a 1500 Oe applied field, the lines are the best fitting result to generalized Debye model; **(**b) the temperature-dependent relaxation time and the corresponding best fitting result obtained using the Raman and direct relaxation mechanisms

GdCo$_2$ reveals slow relaxation of magnetization behaviour under zero DC field as χ_M'' rises in the high frequency region (Figure S22). Unfortunately, no χ_M'' versus frequency peak is observed under zero DC field, as the magnetic relaxation is too fast, probably due to fast QTM. Applying a 200 Oe external field shifted the peak into the operating frequency range of the instrument. From the field versus relaxation time plots, an optimal field of 600 Oe is obtained, under which the magnetic relaxation is the slowest. Under the optimal field the χ_M'' vs. frequency peaks are observed up to 2.35 K at 1497 Hz (Figure 3.7). The results are shown up to 2.7 K since the relaxation time can be still extracted with a high degree of confidence.

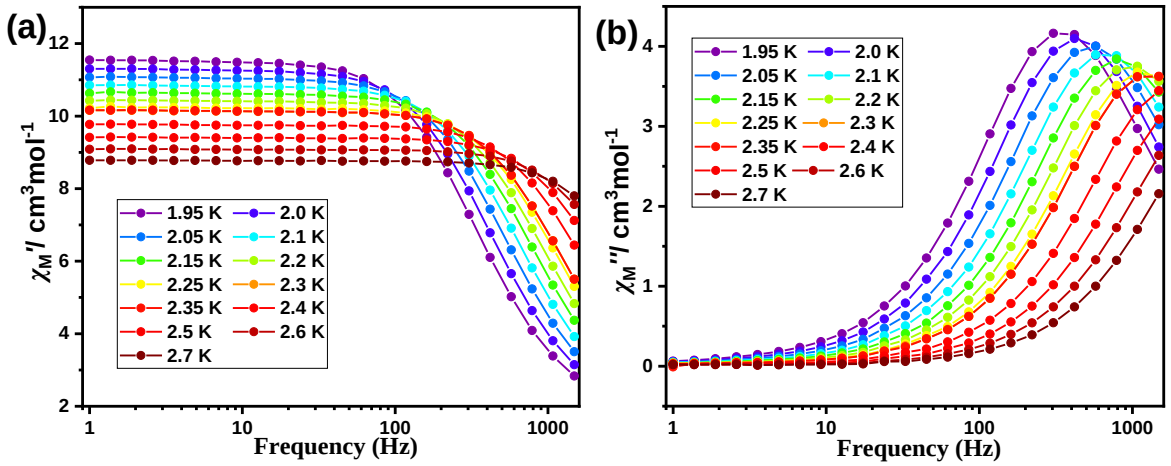

Figure 3.7. Frequency dependency of the in-phase (a) and out-of-phase (b) components of the magnetic susceptibility for **GdCo$_2$** under 600 Oe applied DC field. The solid lines are guide for the eye.

The Cole–Cole plot (χ_M'' vs. χ_M') is fitted by the software CCFIT according to the generalized Debye model (Figure 3.8, a). The detailed fitting results are given in Table S39. α values are in the range from 0.02 to 0.09, indicating a narrow distribution of relaxation times at the measured temperatures. The relaxation times τ are plotted versus T^{-1}, exhibiting nearly a straight line in accordance with Arrhénius behaviour (Figure 3.8, b). Fitting to the Arrhénius equation— $\tau^{-1} = \tau_0{}^{-1} exp(-U_{eff}/k_B T)$ —provides the effective energy barrier U_{eff}/k_B= 15.7 K, and τ_0 = 1.35 × 10^{-7} s. The value of τ_0 is in the reasonable range for SMMs.[174-176] The data is also fitted to the Raman and direct processes. The fitting converges at A = 0 s^{-1} K^{-1}, C = 24.1 $s^{-1}K^{-n}$, and n = 6.9. The fitting results demonstrate that the magnetic relaxation for **GdCo$_2$** under 600 Oe field is either through Orbach process or through Raman process. In the former case, the relaxation is likely going through the low-lying excited exchange states, similar to the situation for **Dy_1** in Chapter 2, while in the latter case the relaxation tends to originate from the intrinsic magnetic anistropy of Co^{II}. The narrow distribution of relaxation times for **GdCo$_2$** (in contrast to the broad distribution for **YCo$_2$**) is more aligned with the first assumption.

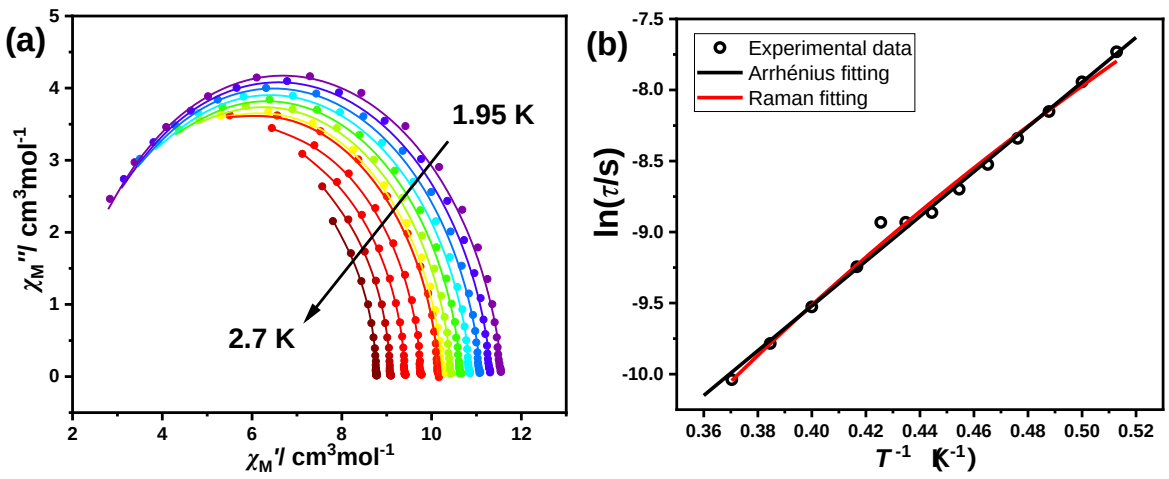

Figure 3.8. (a) the Cole–Cole (χ_M'' vs. χ_M') diagram of **GdCo$_2$** under 600 Oe applied field, the lines are the best fitting result to generalized Debye model; **(**b) the temperature dependent relaxation time and the best results from Arrhénius and Raman fitting, respectively.

Similar to **GdCo$_2$**, **TbCo$_2$** also reveals slow relaxation of magnetization behaviour under zero DC field as χ_M'' rises in the high frequency region though no χ_M'' versus frequency peak is observed under zero field in the measurable frequency range 0.1 to 1500 Hz) of our instrument (Figure S23). Applying external DC fields shifted the peak into the range of measurement, and the optimal field is determined to be 3000 Oe. Under higher external fields, the relaxation times remain essentially the same, but the intensity of magnetic susceptibility decreases. Under 3000 Oe field, the χ_M'' vs. frequency peak is observed up to 5.4 K at 999 Hz (Figure 3.9). The results are shown up to 6.0 K since the relaxation time can still be extracted with a high degree of confidence.

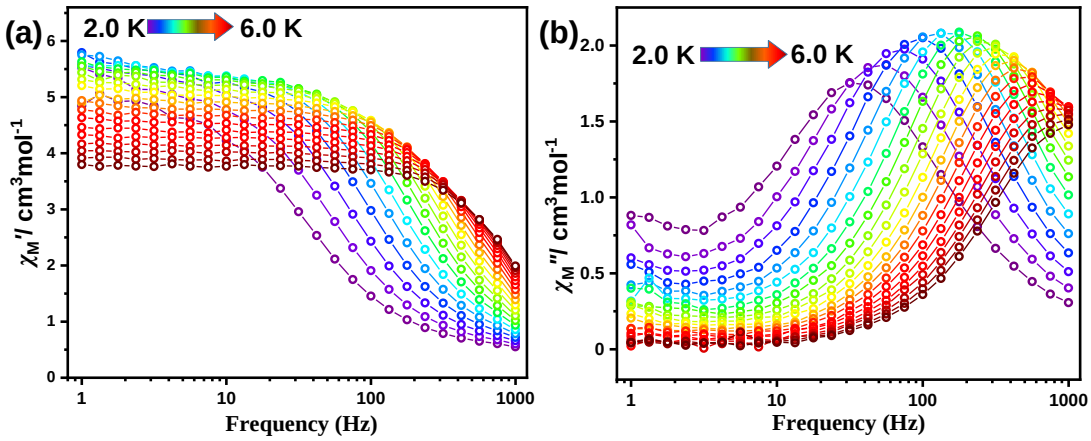

Figure 3.9. Frequency dependency of the in-phase (a) and out-of-phase (b) components of the magnetic susceptibility for **TbCo$_2$** under 3000 Oe applied field. The solid lines are guide for the eye.

The Cole–Cole plot (χ_M'' vs. χ_M') is fitted by the software CCFIT according to the generalized Debye model (Figure 3.10, a). The detailed fitting results are given in Table S40. α values are relatively larger at low temperatures and smaller at high temperatures, ranging from 0.04 at 6.0 K to 0.25 at 2.0 K, indicating a broader distribution of relaxation times at low temperatures. The relaxation times τ are plotted versus T^{-1}, exhibiting a linear diagram in accordance with Arrhénius behaviour (Figure 3.10, b). Fitting to the Arrhénius equation $\tau^{-1} = {\tau_0}^{-1} exp(-U_{eff}/k_BT)$ provides the effective energy barrier U_{eff}/k_B= 10.0 K, and τ_0 = 3.52 × 10^{-5} s. The value of τ_0 is in the reported range for SMMs. Attempts are also made to fit the data according to Raman process, direct processes or a combination of the two. However, no reasonable results are obtained, which is expected since the τ versus T^{-1} plot does not reveal clear curvatures. The Arrhénius behaviour and the low effective energy barrier for **TbCo$_2$** under 3000 Oe field implies that the magnetic relaxation is most likely through the low-lying excited exchange states.

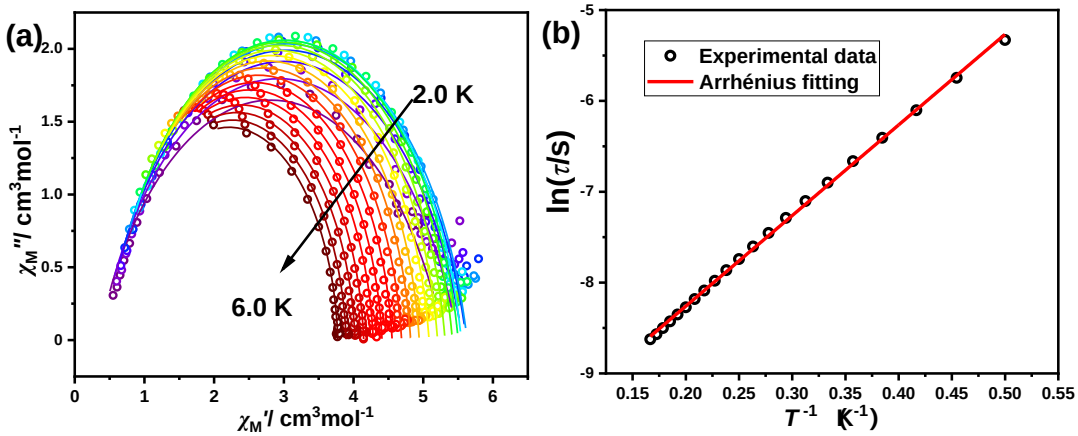

Figure 3.10. (a) the Cole–Cole (χ_M'' vs. χ_M') diagram of **TbCo$_2$** under 3000 Oe applied field, the lines are the best fitting result to generalized Debye model; **(**b) the temperature dependence of relaxation time and the best fitting results.

DyCo2 also reveals slow relaxation of magnetization behaviour under zero DC field as χ_M'' rises in the high frequency region but χ_M'' versus frequency peak is out of the frequency range of measurement (Figure 3.11, a), as observed for **GdCo2** and **TbCo2**. The temperature-dependent χ_M'' plot collected at the oscillation frequency of 999 Hz exhibit an upturn in the low temperature region starting from around 4 K, again confirming the presence of the slow relaxation of magnetization in **DyCo2** (Figure 3.11, b). Unfortunately, no clear peaks can be observed after applying external fields (Figure 3.11, a). Therefore, no more temperature-dependent AC magnetic susceptibility measurements are carried out on **DyCo2**.

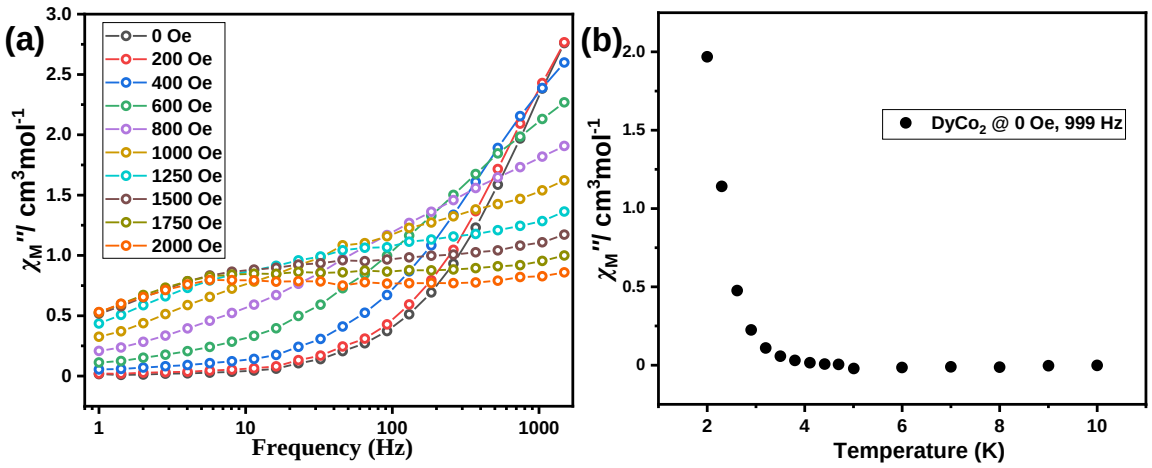

Figure 3.11. (a) out-of-phase susceptibility (χ_M'') versus frequency plot for **DyCo2** under different external fields. The lines are guides for the eye. (b) temperature-dependent χ_M'' plot measured at 999 Hz.

3.5 Magnetic properties of $[Ln(FeL)_2]CF_3SO_3$

3.5.1 Static magnetic properties

Direct-current (DC) magnetic susceptibility measurement of **LnFe2** (Ln = Y, Gd, Tb, Dy) were performed on polycrystalline samples in the temperature range of 2 to 300 K under DC field of 1000 Oe. The $\chi_M T$ versus T plot for **YFe2** is shown in Figure 3.12. The $\chi_M T$ value for the complex is 7.21 $cm^3mol^{-1}K$ at 300 K, in agreement with two uncoupled high spin-state Fe^{II} (2 × 3.63 $cm^3mol^{-1}K$, $S = 2$, $g_{Fe} = 2.2$). Here a g-factor around 2.2 is reasonable for high spin-state Fe^{II} in octahedral coordination spheres, as similar values were often reported in previous works.[191,192] Upon lowering the temperature, $\chi_M T$ values first decrease slowly to 6.68 $cm^3mol^{-1}K$ at 20 K, and then drop fast to finally reach 4.55 $cm^3mol^{-1}K$ at 2.0 K, as a result of the magnetic anisotropy of Fe^{II}.

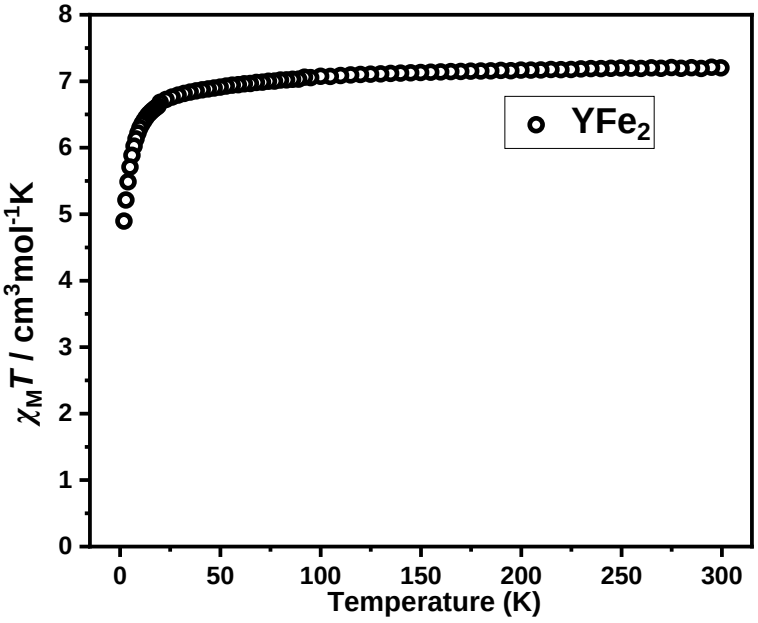

Figure 3.12. Plot of $\chi_M T$ versus T for **YFe$_2$** under an applied field of 1000 Oe.

The $\chi_M T$ versus T data for **GdFe$_2$**, **TbFe$_2$**, **DyFe$_2$** are plotted in Figure 3.13. Their $\chi_M T$ values at 300 K are 15.23, 18.02, 21.99 $cm^3mol^{-1}K$, respectively. Assuming the two Fe^{II} and one Ln^{III} are all uncoupled, and the contribution of the two Fe^{II} is equal to that in **YFe$_2$** (7.21 $cm^3mol^{-1}K$), the contributions from Gd^{III}, Tb^{III}, Dy^{III} are 8.02, 10.81 and 14.78 $cm^3mol^{-1}K$, respectively, for the corresponding **LnFe$_2$**, close to the theoretical values of individual Ln^{III} (7.88, 11.80, 14.17 $cm^3mol^{-1}K$). Upon lowering the temperature, $\chi_M T$ values for **GdCo$_2$**, **TbCo$_2$**, **DyCo$_2$** remain roughly constant in the high temperature range. Different behaviours are revealed as at low temperatures, $\chi_M T$ values for **TbFe$_2$** and **DyFe$_2$** drop to 11.86 and 14.56 $cm^3mol^{-1}K$, respectively, whereas $\chi_M T$ value for **GdFe$_2$** rises to a maximum of 25.24 $cm^3mol^{-1}K$ at 4 K before drops slightly at 2.0 K. The rise for **GdFe$_2$** is a clear indication of the presence of Gd–Fe intramolecular ferromagnetic couplings. The differences of $\chi_M T$ values between **TbFe$_2$** and **YFe$_2$** and **DyFe$_2$** and **YFe$_2$** at the same temperatures are calculated to investigate the nature of Tb–Fe and Dy–Fe couplings respectively in **TbFe$_2$** and **DyFe$_2$** (Figure S24). Both Δ(**TbFe$_2$-YFe$_2$**) and Δ(**DyFe$_2$-YFe$_2$**) remain almost constant above 20 K, and decrease monotonously at low temperatures to moderate values at 2.0 K, akin to the $\chi_M T$ plots for many dysprosium or terbium mononuclear complexes. Therefore, it is safe to rule out the possibility of strong Tb–Fe or Dy–Fe ferromagnetic couplings in these samples. This is in stark contrast with **TbCo$_2$**, **DyCo$_2$**, and **Tb_1**, **Dy_1** (see Chapter 2.4.1), but not unusual, because high spin Fe^{II} is more likely to exhibit exchange coupling with neighbouring lanthanide ions due to its greater number of unpaired electrons and larger magnetic moment.

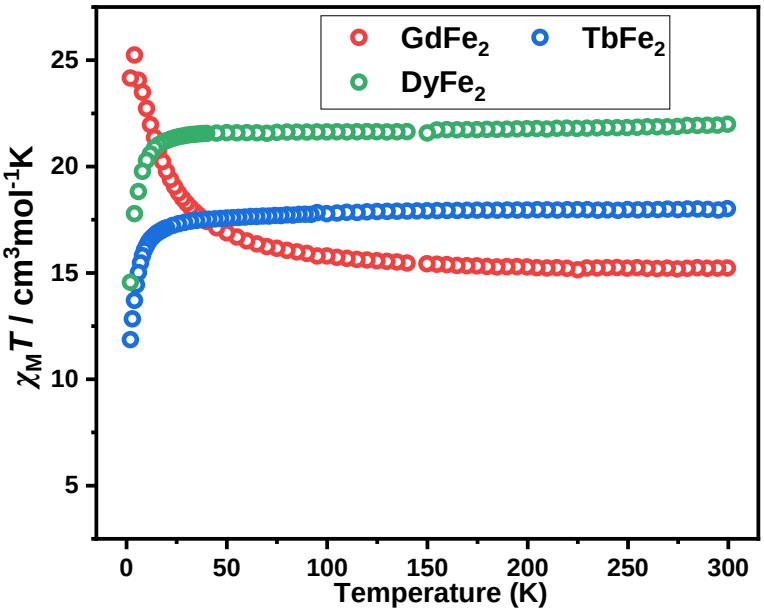

Figure 3.13. Plots of $\chi_M T$ vs. T for **GdFe$_2$**, **TbFe$_2$**, **DyFe$_2$** under an applied field of 1 kOe.

3.5.2 Dynamic magnetic properties

The alternating current (AC) susceptibility measurements were performed on all four **LnFe$_2$** complexes at 2.0 K, under a zero field and an applied field of 1000 Oe with a 3 Oe oscillating AC field at frequencies from 1 to 1000 Hz. Only **TbFe$_2$** exhibits peaks in the χ_M'' versus frequency plot under the applied field. The optimal field was determined to be 3000 Oe from applied field-dependent AC susceptibility measurements shown in Figure S25. Under the optimal field, the χ_M'' vs. frequency peak was observed up to 2.5 K at 999 Hz (Figure 3.14). The results were shown up to 3.5 K since the relaxation time could be still extracted with a high degree of confidence.

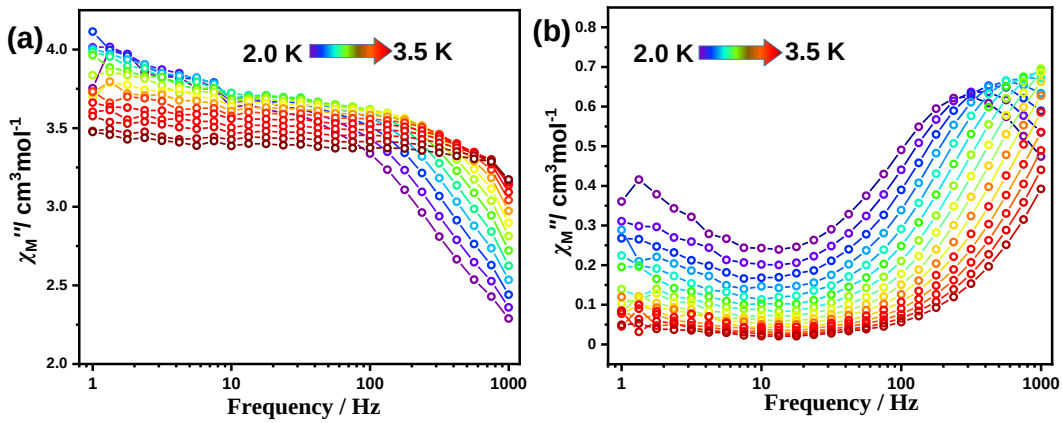

Figure 3.14. Frequency dependency of the in-phase (a) and out-of-phase (b) component of the magnetic susceptibility for **TbFe$_2$** under 3000 Oe applied field. The solid lines are guide for the eye.

In the Cole-Cole plot (χ_M'' vs. χ_M') of **TbFe$_2$**, in addition to data points forming near-semicircular curves, there are some scattered data points, most of which were collected at oscillation frequencies below 10 Hz, appearing on the right side of the plot (Figure 3.15, a). These scattered data points may be artificial signals, signals of another relaxation process of **TbFe$_2$** complexes, or signals originating from impurities. Regardless of their origin, these data points do not exhibit clear patterns and cannot be fitted. Therefore, only the data points with oscillation frequency ≥ 10 Hz are fitted by the software CCFIT according to the generalized Debye model. The detailed fitting results are given in Table S41. α values are relatively larger at low temperatures and smaller at high temperatures, ranging from 0.09 at 3.5 K to 0.29 at 2.0 K, indicating a broader distribution of relaxation times at low temperatures than at high temperatures. Fitting the τ versus T^{-1} plot to the Arrhénius equation $\tau^{-1} = \tau_0^{-1} exp(-U_{eff}/k_BT)$ provides the effective energy barrier U_{eff}/k_B = 10.8 K, and τ_0 = 2.26 × 10^{-6} s. The value of τ_0 is in the expected range for SMMs. Attempts are also made to fit the data assuming the dominance of Raman and direct processes. The best fitting result is A = 0 s^{-1}K^{-1}, C = 120s^{-1} K^{-n}, and n = 4.2.

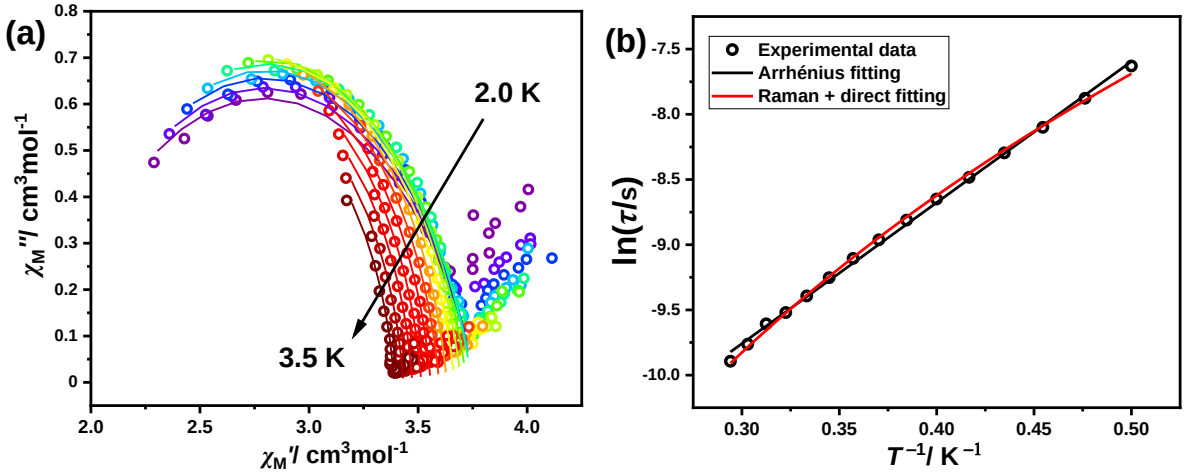

Figure 3.15. (a) the Cole–Cole (χ_M'' vs. χ_M') diagram of **TbFe$_2$** under 3000 Oe applied field, the lines are the best fitting result to generalized Debye model; **(**b) the temperature-dependent relaxation time and the best results from Arrhénius and Raman fitting, respectively.

3.6 Optical properties of [Ln(MgL)$_2$]CF$_3$SO$_3$ and [Ln(ZnL)$_2$]CF$_3$SO$_3$

3.6.1 Photoluminescence of [Gd(MgL)$_2$]CF$_3$SO$_3$ and [Gd(ZnL)$_2$]CF$_3$SO$_3$

The photoluminescence (PL) characteristics of [Gd(MgL)$_2$]CF$_3$SO$_3$ (**GdMg$_2$**) and [Gd(ZnL)$_2$]CF$_3$SO$_3$ (**GdZn$_2$**) were investigated in the solid-state using a Horiba Fluorolog

spectrometer with R920 photomultiplier tube detector. The solid crystalline samples were placed in between two fused-quartz glass plates with a drop of perfluorinated oil.

Figure 3.16 illustrates the photophysical data obtained for **GdMg$_2$** and **GdZn$_2$** at room temperature. Following the excitation in the wavelength range of 360 nm to 420 nm, both complexes exhibit emission (fluorescence) corresponding to the $^1\pi\pi^*$ state. The emission bands are centered at 444 nm for **GdMg$_2$** and 470 nm for **GdZn$_2$**.

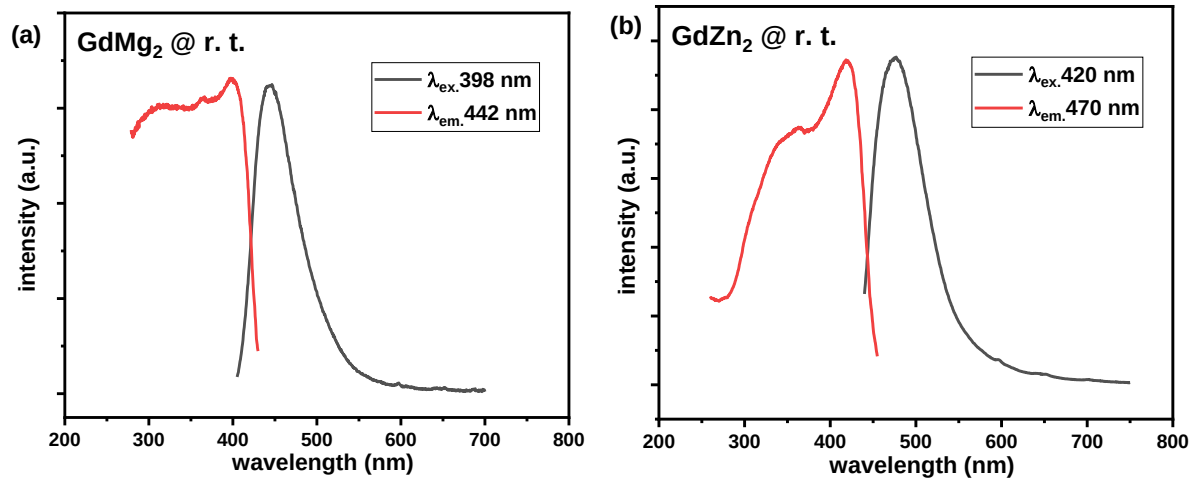

Figure 3.16. Emission and excitation spectra of **GdMg$_2$** (a, $\lambda_{ex.}$ = 398 nm, $\lambda_{em.}$ = 442 nm) and **GdZn$_2$** (b, $\lambda_{ex.}$ = 420 nm, $\lambda_{em.}$ = 470 nm) at room temperature.

Lowering the temperature to 3.0 K, the emission spectra change dramatically. Broad structured phosphorescence bands, extending from 475 nm to 700 nm for **GdMg$_2$** and 500 nm to 700 nm for **GdZn$_2$**, appear and dominate the spectra. In contrast, the fluorescence bands, which remain basically at the same position as at room temperature, become relatively rather weak though visible. The structured phosphorescence bands enable the determination of the 0–0 phonon transition energy from the $^3\pi\pi^*$ state by examining the position of the shortest-wavelength peak. The triplet state energy of L^{3-} are therefore calculated to be 19960 cm^{-1} in **GdMg$_2$** (501 nm), and 18832 cm^{-1} in **GdZn$_2$** (531 nm). Note that the triplet energy of **GdMg$_2$** is 1128 cm^{-1} higher than the energy obtained for **GdZn$_2$**. The excitation spectra for **GdMg$_2$** and **GdZn$_2$** collected at the phosphorescence bands have similar shape, albeit differ slightly in the peak maxima values. The excitation bands at 3.0 K peak at 398 nm for **GdMg$_2$** and 408 nm for **GdZn$_2$**, both slightly blue shifted in comparison to their corresponding room temperature spectra.

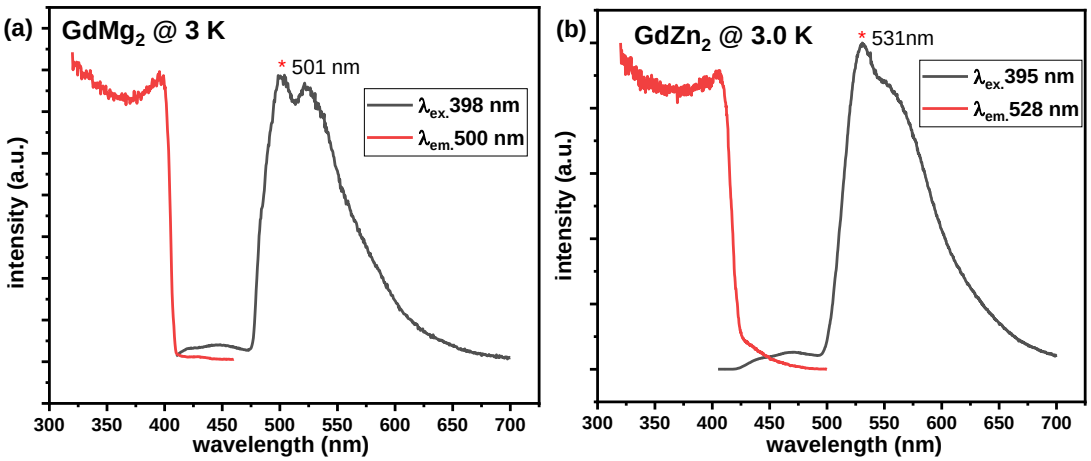

Figure 3.17. Emission and excitation spectra of **$GdMg_2$** (a, $\lambda_{ex.}$ = 398 nm, $\lambda_{em.}$ = 500 nm) and **$GdZn_2$** (b, $\lambda_{ex.}$ = 395 nm, $\lambda_{em.}$ = 528 nm) at 3.0 K.

The general trend that the excitation and emission peaks appear at shorter wavelengths in **$GdMg_2$** as compared to **$GdZn_2$**, at both room temperature and 3.0 K, is due to the difference between Mg^{2+} and Zn^{2+}. The smaller Mg^{2+} has larger ionic potential and thus elevates the energy of the ligand-related excitation levels more significantly.

3.6.2 Photoluminescence of and $[Ce(ZnL)_2]CF_3SO_3$

At room temperature, **$CeZn_2$** exhibits a broad emission band centered at 570 nm, with a shoulder at around 470 nm, upon excitation at 400 nm (Figure 3.18). The shoulder is attributed to the fluorescence of the ligand L^{3-}, since it is located at the same position as the fluorescence peak in **$GdZn_2$**. The main part of the broad emission, on the contrary, arises from metal center. It is well known that unlike most lanthanide ions, Ce^{III} ions feature characteristic 5d–4f emissions since the 5d orbitals are low enough in energy to be accessible via optical excitation. The excitation spectrum for the broad emission monitored at 570 nm displays a pattern similar to those of **$GdMg_2$** and **$GdZn_2$** at room temperature, indicating the sensitization of the Ce^{III}-based luminescence by ligand L^{3-}.

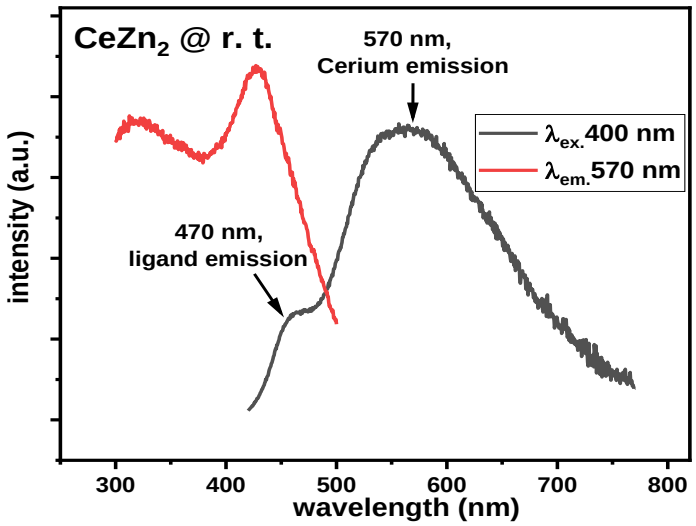

Figure 3.18. Emission and excitation spectra of **CeZn$_2$** ($\lambda_{ex.}$ = 400 nm, $\lambda_{em.}$ = 570 nm) at room temperature.

Variable-temperature emission spectra are collected on **CeZn$_2$** at temperature from 180 K to 10 K (Figure S26). Upon lowering the temperature, the intensity of the ligand-based fluorescence peak deceased gradually, while the broad band splits into two peaks. The emission /excitation spectra of **CeZn$_2$** at 3.0 K are shown in Figure 3.19, a. The two distinct peaks in the emission spectrum are centered at at 534 nm and 573 nm. The energies of the two emission peaks are calculated to be 18727 cm^{-1} and 17452 cm^{-1}, respectively. The energy difference, 1275 cm^{-1}, corresponds to the splitting between two 4f ground levels ($^2F_{5/2}$ and $^2F_{7/2}$) of Ce^{III}. The excitation spectra monitored at the two emission peaks are identical in shape and position, and similar to the excitation spectra measured for **GdZn$_2$** at 3.0 K (Figure 3.17, b), indicating that the 5d–4f emission can be sensitized by ligand L^{3-} via antenna effect. The small shoulders in the excitation spectra at around 420 nm and 460 nm are tentatively attributed to the 4f–5d excitations of Ce^{III}.

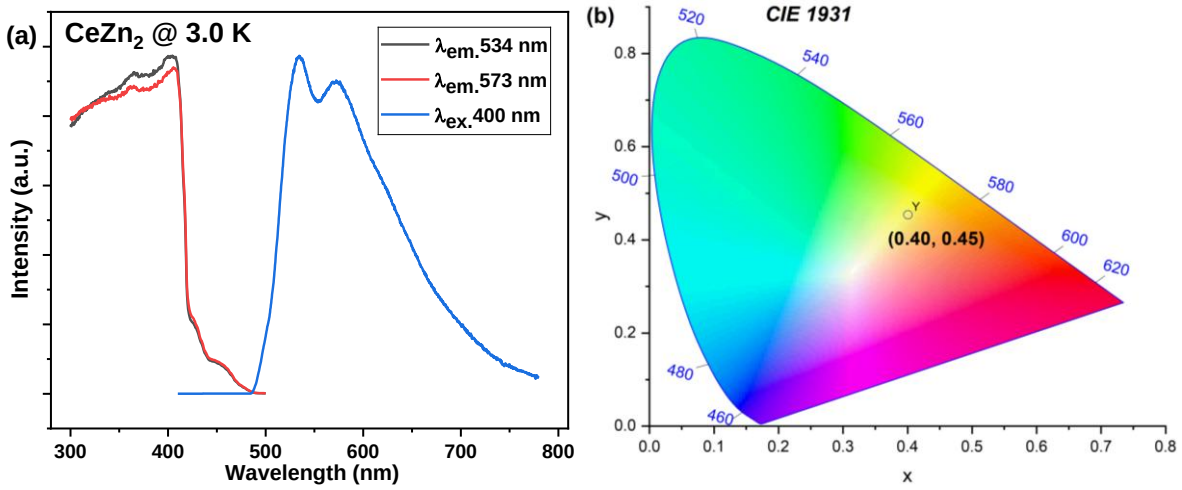

Figure 3.19. (a) Emission ($\lambda_{ex.}$ = 400 nm) and excitation ($\lambda_{em.}$ = 534 and 573 nm) spectra of **CeZn$_2$** at 3.0 K; (b) The CIE 1931 chromaticity diagram of **CeZn$_2$** under $\lambda_{ex.}$400 nm at room temperature.

The CIE 1931 coordinates of the room temperature emission are (0.40, 0.45), demonstrating the ability of **CeZn2** to serve as a yellow emitting material (Figure 3.19, b).

3.6.3 Photoluminescence of $[Nd(MgL)_2]CF_3SO_3$

The photoluminescence of Nd^{III} complexes typically occurs in the near-infrared (NIR) region as the energy difference between the emissive $^4F_{3/2}$ and the ground $^4I_{9/2}$ state is around 10400 cm^{-1}. The room temperature luminescence characteristics of **NdMg2** is investigated on its solid sample using a Horiba Fluorolog spectrometer with a Hamamatsu NIR detector for the NIR region.

Upon excitation at the ligand absorption at 390 nm, three sets of emission peaks can be clearly detected in the NIR region (Figure 3.20, a). The emission peaks are centered at 900, 1060, and 1350 nm corresponding to the energy transitions from $^4F_{3/2}$ to $^4I_{9/2}$, $^4I_{11/2}$, and $^4I_{13/2}$, respectively. The excitation spectrum collected by monitoring the emission at 1086 nm is comparable to the one observed for **GdMg2**; i.e., the intensity reaches its maximum around 400 nm and then rapidly decreases as the wavelength increases (Figure 3.20, b). These results demonstrate that the sensitization of NIR emission of Nd^{III} in **NdMg2** is via the antenna effect. It is also worthy to note that since NIR emissions in lanthanide complexes are more susceptible to quenching by high-energy vibrational modes, lowering the temperature to suppress non-radiative relaxation processes is often necessary for detecting these emissions. In this regard, the observation of NIR emissions in **NdMg2** at the room temperature demonstrates not only is ligand L^{3-} capable of sensitizing NIR emission of lanthanides, but also the overall structure of the trinuclear complex effectively isolates the central Ln^{III} from surrounding high-energy vibration modes.

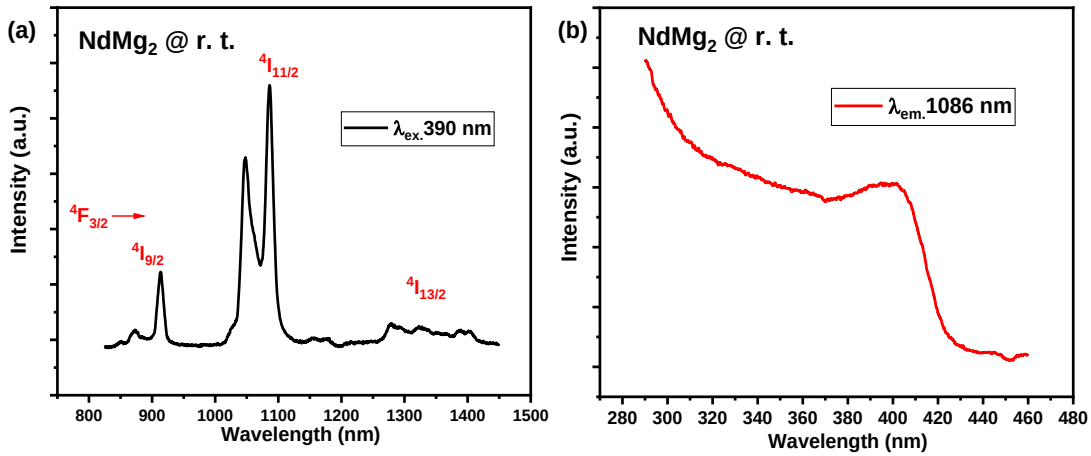

Figure 3.20. Emission (a, $\lambda_{ex.}$ = 390 nm) and excitation (b, $\lambda_{em.}$ = 1086 nm) spectra of **NdMg2** at room temperature.

3.6.4 Photoluminescence of $[Sm(MgL)_2]CF_3SO_3$ and $[Sm(ZnL)_2]CF_3SO_3$

The solid-state photoluminescence spectra of **$SmMg_2$** and **$SmZn_2$** are collected at room temperature and at 3.0 K (Figure 3.21 and 3.22). For both samples, four sets of emission peaks are observed in the range of wavelength from 540 nm to 750 nm, corresponding to the energy transitions from $^4G_{5/2}$ to $^6H_{5/2}$, $^6H_{7/2}$, $^6H_{9/2}$ and $^6H_{11/2}$. Besides the Sm^{III} centered emission, a weak ligand centered emission band at around 470 nm is also visible in **$SmZn_2$** at room- and low-temperatures.

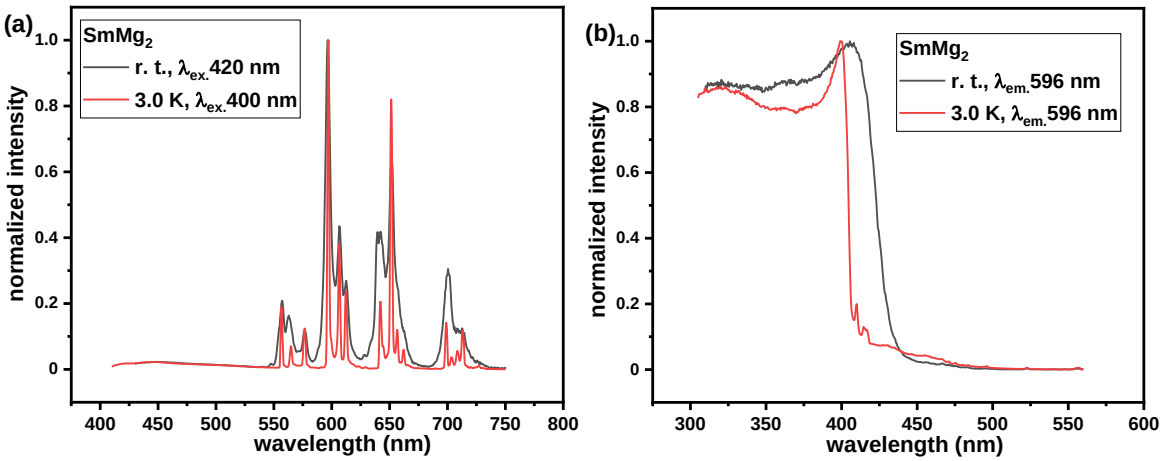

Figure 3.21. Normalized emission (a) and excitation (b) spectra of **$SmMg_2$** at room temperature (black) and 3.0 K (red).

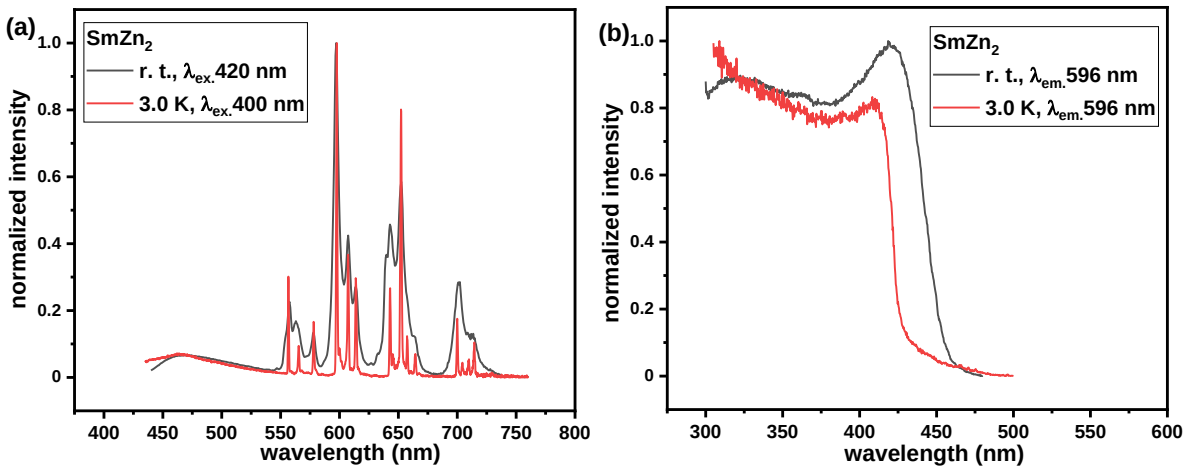

Figure 3.22. Normalized emission (a) and excitation (b) spectra of **$SmZn_2$** at room temperature (black) and 3.0 K (red).

3.6.5 Photoluminescence of $[Eu(MgL)_2]CF_3SO_3$ and $[Eu(ZnL)_2]CF_3SO_3$

Figure 3.23 presents the solid-state photoluminescence spectra of **EuMg$_2$** and **EuZn$_2$** collected at room temperature, under various excitation wavelengths. Both complexes exhibit dominant ligand–centered broad emissions with the maximum intensity below 550 nm. Faint Eu^{III}–centered emissions are only observed around 614 nm and 650 nm, corresponding to the $^5D_0 \rightarrow {}^5F_2$ and the $^5D_0 \rightarrow {}^5F_3$ transitions, respectively.

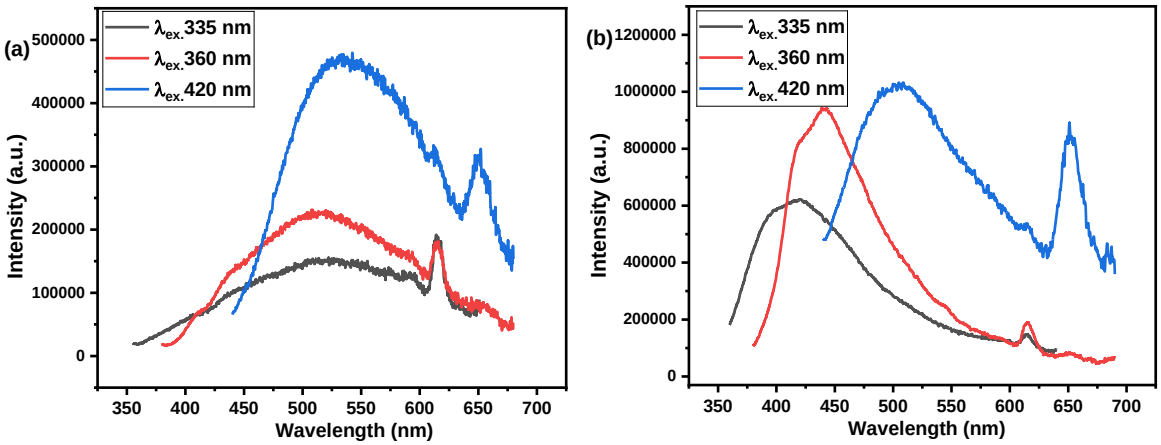

Figure 3.23. Emission spectra of **EuZn$_2$** (a) and **EuMg$_2$** (b) at room temperature.

At 3.0 K, both **EuMg$_2$** and **EuZn$_2$** exhibit distinct Eu^{III}-centered f–f emission peaks. The emission spectra are collected under excitation wavelength of 422 nm for **EuZn$_2$** and 410 nm for **EuMg$_2$** (Figure 3.24). Five sets of emission peaks are observed in the range of wavelength from 570 nm to 720 nm, corresponding to the energy transitions from $^5D_0$ to $^5F_0$, $^5F_1$, $^5F_2$, $^5F_3$, and $^5F_4$ respectively. In both samples, the $^5D_0 \rightarrow {}^5F_2$ transition around 614 nm, which is ED-allowed and hypersensitive to the local symmetry, is the most intense emission. The presence of a sharp and narrow $^5D_0 \rightarrow {}^7F_0$ emission peak at 578 nm is in line with the non-centrosymmetric coordination environment around the Eu^{3+} ion, since the $^5D_0 \rightarrow {}^7F_0$ transition is strictly forbidden in centrosymmetric systems. A broad peak spanning from around 500 nm to over 700 nm is also observable in **EuMg$_2$**, which is presumably ligand–associated. The drastic variation of the photoluminescence behaviours between room temperature and low temperature reveals strong temperature dependence of emission of **EuMg$_2$** and **EuZn$_2$** complexes, a phenomenon unseen in previously studied **SmMg$_2$** and **SmZn$_2$**.

The acceptor levels of Eu^{III} ($^5D_0$, 17300 cm^{-1}, 578 nm) and Sm^{III} ($^4G_{5/2}$, 17980 cm^{-1}, 556 nm) are close in energy. Therefore, ligands capable of sensitizing fluorescence of Sm^{III} are generally also able to sensitize fluorescence of Eu^{III}. In the meanwhile, the triplet levels of L^{3-}, determined from the low temperature photoluminescence spectra of **GdZn$_2$** (18832 cm^{-1}, 532 nm) and **GdMg$_2$** (19960 cm^{-1}, 501 nm), are suitable to allow effective energy transfer to both Eu^{III} and Sm^{III}. Especially for **EuMg$_2$**, the calculated energy gap between the triplet level T_1 and the

emissive level $^5D_0$ (2660 cm^{-1}) is much larger than the energy gap necessary for back energy transfer (1850 cm^{-1}).[193] Nevertheless, while **SmMg$_2$** and **SmZn$_2$** exhibit significant luminescence from Sm^{III} ions at room temperature, **EuMg$_2$** and **EuZn$_2$** display only faint Eu^{III}-centered luminescence. It is speculated that certain nonradiative deactivation processes, such as ligand-to-metal charge transfer (LMCT), may be present in the Eu complexes.

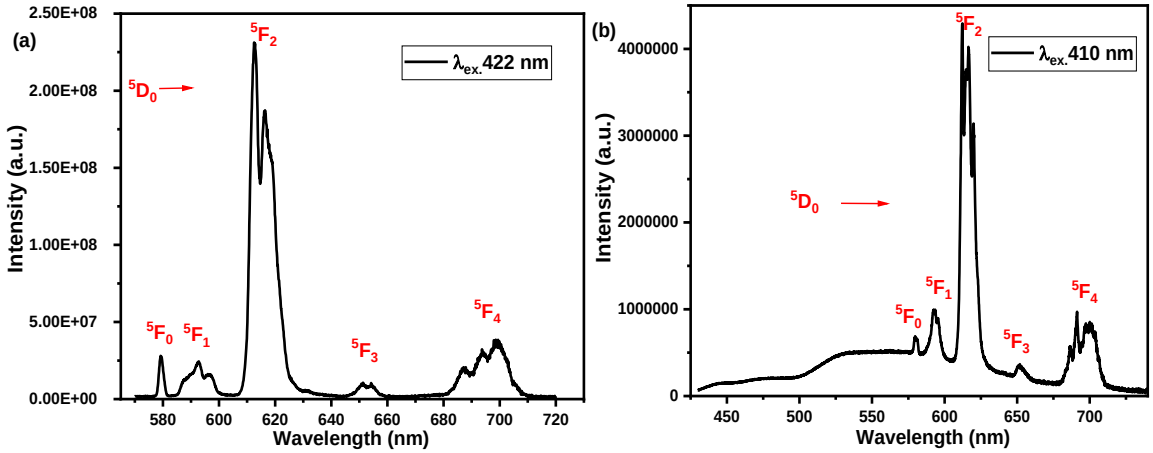

Figure 3.24. Emission spectra of **EuZn$_2$** (a) and **EuMg$_2$** (b) at 3.0 K.

Moreover, the excitation spectra of the Eu^{III}-centered emission at 3.0 K are collected at the emission wavelength of 614 nm (Figure 3.25). The pattern of the excitation spectra is entirely different from that of the Sm^{III}-centered emission in **SmMg$_2$** and **SmZn$_2$**, and the Gd^{III}-centered emission in **GdMg$_2$** and **GdZn$_2$**, suggesting an energy transfer pathway different from the pathway involved in the conventional antenna effect. The excitation spectrum of the broad emission in **EuMg$_2$** (red line in Figure 3.25, b), in contrast, indicates the involvement of the ligands' excited singlet state.

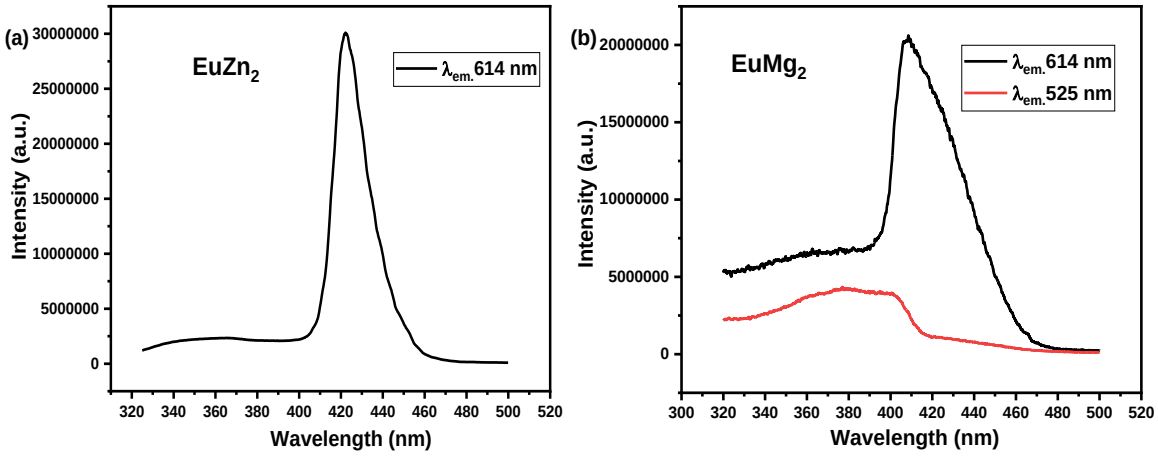

Figure 3.25. Excitation spectra of **EuZn$_2$** (a) and **EuMg$_2$** (b) at 3.0 K.

3.6.6 UV-vis absorption spectra

Besides the unique photoluminescence behaviours, Eu-containing complexes **$EuZn_2$** and **$EuMg_2$** also display significantly different colors relative to their counterparts. As shown in Figure 3.26, **$EuZn_2$** is orange and **$EuMg_2$** is dark red, while **$GdZn_2$** and **$GdMg_2$** are both yellow. The color variations indicate distinct light absorption behaviours. Motivated by these facts, the solid-state UV-vis absorption spectra of **$EuMg_2$**, **$EuZn_2$** are collected and compared with their corresponding Gd complexes. The measurement is also conducted on **$SmZn_2$** to illustrate the photoluminescence in Sm-containing samples.

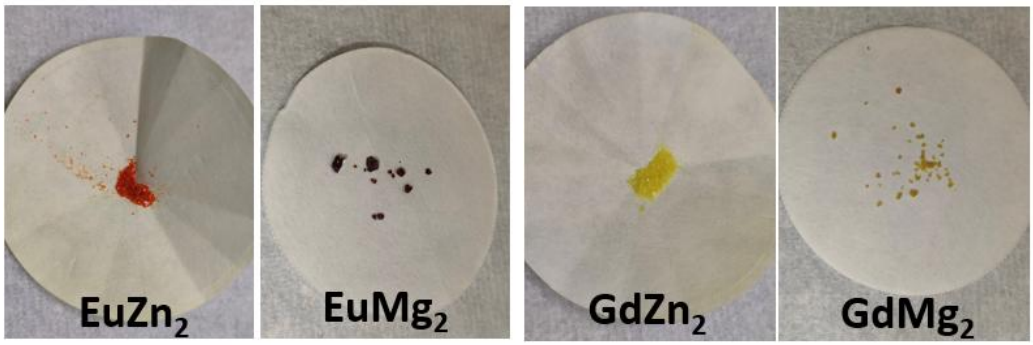

Figure 3.26. Colors of **$EuMg_2$**, **$EuZn_2$**, **$GdZn_2$** and **$GdMg_2$** under sun light.

It can be seen from Figure 3.27 that the in addition to the absorption peaks at around 400 nm and 280 nm, which are common for all measured samples, **$EuZn_2$** and **$EuMg_2$** also exhibit structureless absorption bands above 400 nm. The additional absorption bands are responsible for the unique color of the Eu complexes. Their origin is ascribed to the LMCT process, which is also reported for some Eu complexes with Schiff base ligands.[194] Compared to **$EuZn_2$**, **$EuMg_2$** exhibits a red shifted absorption maximum and a broader band extending to longer wavelength, which may explain the presence of a broad emission peak in **$EuMg_2$** at 3.0 K. The energy ranges of LMCT are estimated from the onset rise absorption at the high and low energy sides of the bands for **$EuZn_2$** (400 nm, 25000 cm^{-1}; 650 nm, 15385 cm^{-1}) and **$EuMg_2$** (400 nm, 25000 cm^{-1}; 700 nm, 14286 cm^{-1}). The energy of LMCT bands is not only close to the excited singlet state of the ligand but also overlapped with the triplet state and the emissive excited states of trivalent Eu ions. Consequently, various energy transfer processes, including excited singlet to LMCT, back energy transfer from triplet to LMCT, and back energy transfer from Eu^{III} to LMCT, can be active at room temperature and quench the Eu^{III}-centered photoluminescence. At low temperature, the role of LMCT bands switches from quenching to sensitizing the europium emissions as the strongest europium emissions are obtained when the excitation wavelengths fall within the high energy region of LMCT bands. This role transition

induces temperature dependent emissions–at room temperature, the luminescence is dominated by ligand-centered emission, whereas at low temperature, it comes mainly from Eu^{III} ions.

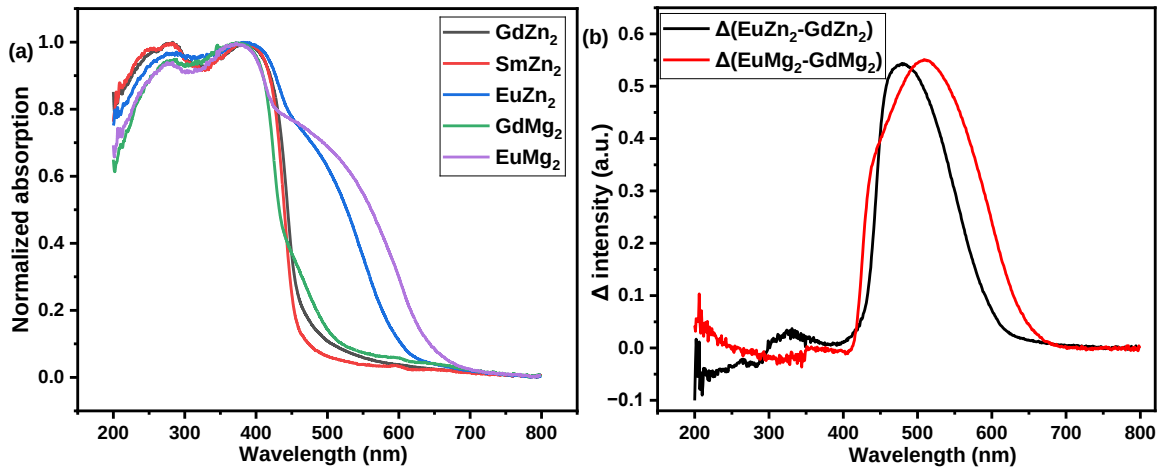

Figure 3.27. a, normalized UV-vis absorption spectra of **$EuMg_2$**, **$EuZn_2$**, **$GdZn_2$**, **$GdMg_2$** and **$SmZn_2$**; b, difference in absorption spectra.

As stated in Chapter 1.3.3, trivalent samarium complexes may also undergo LMCT processes. Here, however, no LMCT band is detected for **$SmZn_2$**, consistent with the strong Sm^{III}-centered emission in Sm complexes at room temperature (Figure 3.27, a). Figure 3.28 illustrates the Jablonski energy diagram detailing photophysical processes in **$EuMg_2$**, **$EuZn_2$**, **$SmMg_2$** and **$SmZn_2$**. While Sm^{III}-centered emissions are sensitized by the antenna effect via the triplet state, distinct Eu^{III}-centered emissions only appear at low temperatures by exciting into the LMCT band.

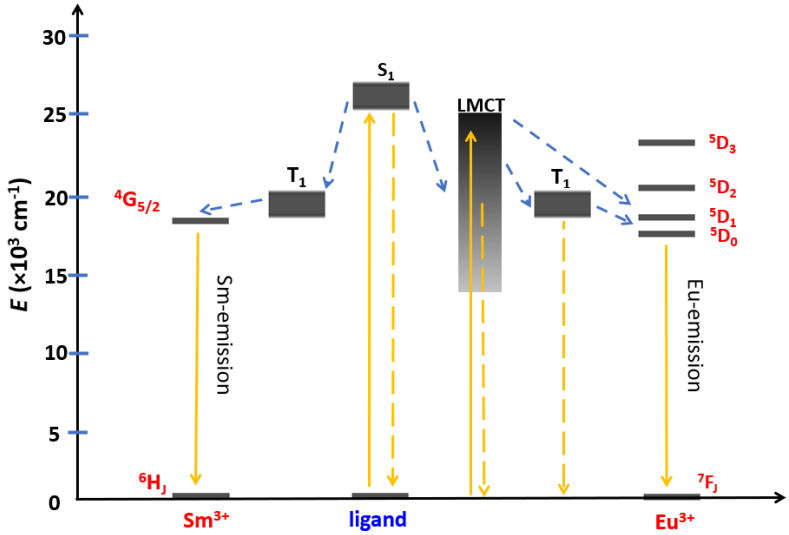

Figure 3.28. Generalized energy level diagram of **$EuMg_2$**, **$EuZn_2$**, **$SmMg_2$** and **$SmZn_2$**. Dashed and solid lines represent the nonradiative and radiative processes, respectively.

Chapter 4. Magnetic and Photoluminescence Properties of Lanthanide Complexes Composed of pyrazole-based Ligands

4.1 Introduction

In Chapter 2 and Chapter 3, the molecular structures, magnetic properties and photoluminescence behaviours of M–Ln–M (M = Mg, Fe, Co, Ni, Zn) heteronuclear complexes synthesized with a tripodal Schiff base ligand tris(((2-hydroxy-3-methoxybenzyl)-amino)ethyl)amine (H_3L) have been elucidated. Some of the complexes, particularly those containing paramagnetic 3d ions, exhibit slow relaxation of magnetization behaviour. However, the paramagnetic 3d metal ions in the complexes can quench the potential Ln-centered photoluminescence. In the meantime, the relatively low triplet energy of H_3L prevents it from sensitizing the luminescence of Dy^{III} and Tb^{III} ions via antenna effect. These limitations shifted the focus of this study to complexes composed exclusively of lanthanide metals and alternative ligands.

3(5)-Pyridine-1*H*-pyrazole, hereafter referred to as Hbpp (Figure 4.1), is a conjugated multidentate ligand, which holds the potential to form various metal complexes through versatile coordination modes and sensitize the metal-centered luminescence.[195-197] For example, Kaizaki and coworkers reported a series of dinuclear Fe^{II} complexes [{Fe(NCS)(py-X)}$_2$(bpp)$_2$], in which the deprotonated symmetrical bpp^- anion coordinated with two iron^{II} ions.[198] Zheng et al., reported a mononuclear Ir^{III} complex (**Ir-Py)** featuring bpp^- as a monodentate ancillary ligand.[199] **Ir-Py** showed efficient green emission peaking ($\lambda_{max.}$) at 499 nm. In contrast, to the best of our knowledge, the photoluminescence and SMM characteristics of lanthanide complexes composed of Hbpp are yet to be reported.

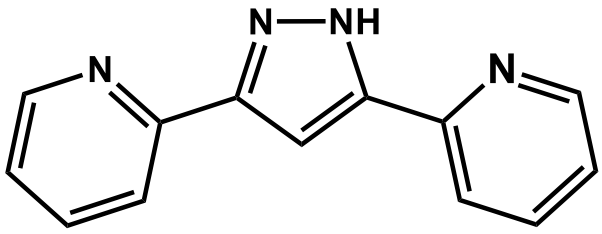

Figure 4.1. The molecular structure of ligand Hbpp.

Herein, the syntheses and structures of a series of binuclear Ln(III) and tetranuclear Dy(III) complexes, respectively, composed of Hbpp and bpp^- ligands are presented. See Table 4.1 for details.

Table 4.1. Details of binuclear and tetranuclear Ln(III) complexes studied in this chapter.

Entry	Binuclear Ln^{III} complexes	Tetranuclear Dy^{III} complexes
1	$[Y(Hbpp)_2(NO_3)_3]_2 \cdot 2CH_3CN$ (**Y_2_MeCN**)	$[Dy_4(bpp)_4(OH)_4(NO_3)_4] \cdot 2CH_3CH_2OH$ (**Dy_4_NO_3**)
2	$[La(Hbpp)_2(NO_3)_3]_2 \cdot 2CH_3CN$ (**La_2_MeCN**)	$[Dy_4(bpp)_4(CH_3CH_2OH)_2(OH)_2Cl_6] \cdot 3CH_3CH_2OH$ (**Dy_4_Cl**)
3	$[Ce(Hbpp)_2(NO_3)_3]_2 \cdot 2CH_3CN$ (**Ce_2_MeCN**)	
4	$[Pr(Hbpp)_2(NO_3)_3]_2 \cdot 2CH_3CN$ (**Pr_2_MeCN**)	
5	$[Nd(Hbpp)_2(NO_3)_3]_2 \cdot 2CH_3CN$ (**Nd_2_MeCN**)	
6	$[Sm(Hbpp)_2(NO_3)_3]_2 \cdot 2CH_3CN$ (**Sm_2_MeCN**)	
7	$[Eu(Hbpp)_2(NO_3)_3]_2 \cdot 2CH_3CN$ (**Eu_2_MeCN**)	
8	$[Gd(Hbpp)_2(NO_3)_3]_2 \cdot 2CH_3CN$ (**Gd_2_MeCN**)	
9	$[Tb(Hbpp)_2(NO_3)_3]_2 \cdot 2CH_3CN$ (**Tb_2_MeCN**)	
10	$[Dy(Hbpp)_2(NO_3)_3]_2 \cdot 2CH_3CN$ (**Dy_2_MeCN**)	
11	$[Ho(Hbpp)_2(NO_3)_3]_2 \cdot 2CH_3CN$ (**Ho_2_MeCN**)	

Characteristic Ln^{III}-centered visible light emissions are observed in **Ce_2_MeCN**, **Sm_2_MeCN**, **Eu_2_MeCN**, **Tb_2_MeCN**, and **Dy_2_MeCN**, while near infrared (NIR) emission is detected in **Nd_2_MeCN**. Notably, **Dy_2_MeCN** exhibited field-induced SMM behaviour and the crystal field splitting of the Kramers doublets of the $^6H_{15/2}$ ground state is obtained from the high-resolution emission spectrum of the complex at 3.0 K. Tetranuclear complexes **Dy_4_NO_3** and **Dy_4_Cl** exhibit slow relaxation of magnetization under zero external field. Theoretical calculations are utilized to elucidate the pathways of the magnetic relaxations and the distinct SMM behaviours between **Dy_2_MeCN** and the tetranuclear complexes.

4.2 Synthesis details

General procedures

All commercially purchased (Sigma-Aldrich, TCI chemicals, abcr) chemicals and reagents were of reagent grade and used without further purification. Ligand 3(5)-Pyridine-1*H*-pyrazole (Hbpp) was synthesized in two steps, employing modified procedures reported by Yu *et al.*[200] and Jansa *et al.*[201]. All the lanthanide complexes were synthesized following solvothermal synthesis method in either acetonitrile or ethanol solvent.

Synthesis of 3(5)-Pyridine-1*H*-pyrazole (Hbpp)

Hbpp ligand was synthesized using a two-step synthetic procedure, which consists of the synthesis of 1,3-di(2-pyridinyl)-1,3-propanedione from 2-acetylpyridine and methyl 2-pyridinecarboxylate, and the condensation reaction with hydrazine hydrate to obtain the final Hbpp ligand (Scheme 4.1). Under the protection of argon, 2-acetylpyridine (3.63 g, 30 mmol) and slightly excessive methyl 2-pyridinecarboxylate (4.24 g, 31 mmol) were slowly added to a dry THF (40 mL) suspension of sodium hydride (60 % dispersion in mineral oil, 1.60 g, 40 mmol) under ice bath. The mixture was then refluxed at 66 ℃ for 24 h, before cooled down to room temperature. The resulting precipitate was then filtered off and re-suspended in water. Dilute hydrochloric acid was slowly added with constant stirring, until the pH value of the mixture reached 5 to 6. The white powder formed was then filtered and dried at 60 ℃ in an oven overnight. The resulting crude product of 1,3-di(2-pyridinyl)-1,3-propanedione (4.54 g, 20 mmol, 67 % yield) and hydrazine hydrate (N_2H_4 64–65 %, 1.50 g, 40 mmol) were added in ethanol (15 mL) successively. The reacting mixture was refluxed at 78 ℃ overnight. After cooling down to room temperature, colorless rod-shaped crystalline product (3.23 g, 73 % yield) was collected by filtration and washed several times with cold ethanol. The purity was verified by performing ^{1}H and ^{13}C NMR measurements in $CDCl_3$ (Figure S27). FT-IR (ATR):3194.14 (s), 1593.81(s), 1569.22 (s), 1484.85(m), 1447.50 (s), 1316.96 (w), 993.94 (m), 972.36 (m), 771.24 (s), 660.53 (w). ESI-MS m/z: $[M+H]^+$ 223.20 (calcd:223.09).

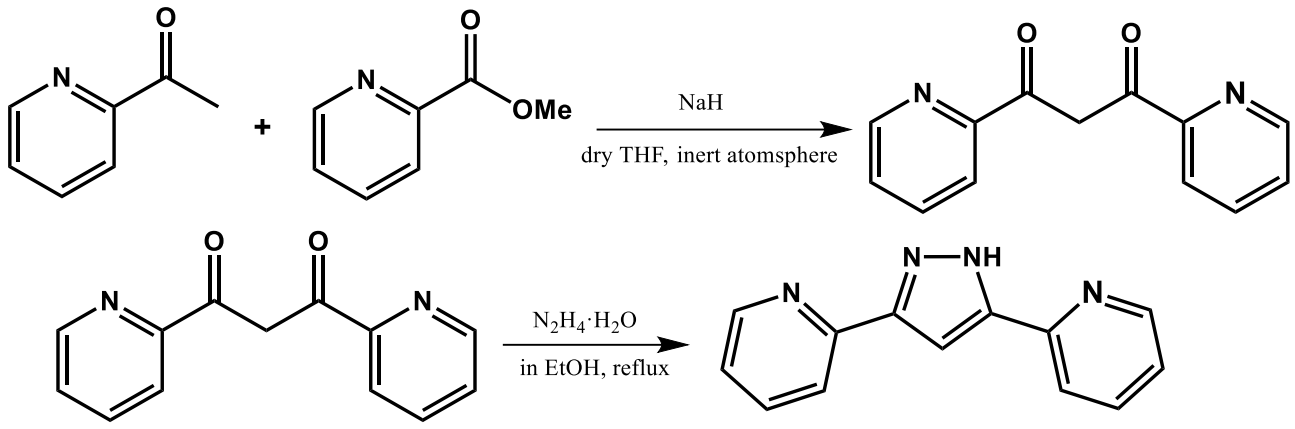

Scheme 4.1. The two step synthesis scheme of 3(5)-Pyridine-1*H*-pyrazole (Hbpp)

Syntheses of $[Ln(Hbpp)_2(NO_3)_3]_2 \cdot 2CH_3CN$ (Ln = Y, La, Ce, Pr, Nd, Sm, Eu, Gd, Tb, Dy, Ho)

The $[Ln(Hbpp)_2(NO_3)_3]_2 \cdot 2CH_3CN$ complexes were prepared employing solvothermal synthesis method in acetonitrile at 120 ℃ for 3 days (Scheme 4.2). Hbpp ligand (22.3 mg, 0.1 mmol) and equimolar amount of the corresponding $Ln(NO_3)_3 \cdot 6H_2O$ were added to 16 mL acetonitrile in a 23 mL stainless steel autoclave, and put into an oven at 120 ℃. After 3 days, the reactions were cooled to room temperature at a speed of 3 ℃ per hour. After reaching room temperature, the stainless-steel autoclave was transferred to a refrigerator set at 0 ℃, to further increase the yield. Crystals of good quality were then collected by filtration. The crystals of $[Nd(Hbpp)_2(NO_3)_3]_2 \cdot 2CH_3CN$ were pale purple, while the others were colorless. The yields were around 40% (based on Hbpp ligands). FT-IR (ATR) of $[Dy(Hbpp)_2(NO_3)_3]_2 \cdot 2CH_3CN$: 3077.07 (br), 2984.82 (w), 2717.90 (m), 1603.77 (m), 1465.87 (s), 1435.01 (s), 1304.93 (s), 1034.00 (m), 1006.50 (m), 814.36 (w), 774.95 (s). The other $[Ln(Hbpp)_2(NO_3)_3]_2 \cdot 2CH_3CN$ have the same infrared absorption peaks within the error range. Elemental analysis: Anal. calcd (%) for $[Dy(Hbpp)_2(NO_3)_3]_2 \cdot 2CH_3CN$ (FW = 1668.16): C, 40.32; H, 2.78; N, 20.14. Found: C, 40.06; H, 2.55; N, 20.32.

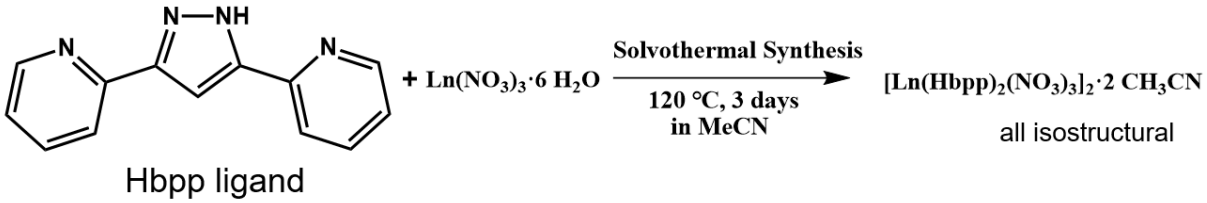

Scheme 4.2. The synthesis scheme of $[Ln(Hbpp)_2(NO_3)_3]_2 \cdot 2CH_3CN$

Attempts were also made to grow $[Er(Hbpp)_2(NO_3)_3]_2 \cdot 2CH_3CN$, $[Tm(Hbpp)_2(NO_3)_3]_2 \cdot 2CH_3CN$, $[Yb(Hbpp)_2(NO_3)_3]_2 \cdot 2CH_3CN$ and $[Lu(Hbpp)_2(NO_3)_3]_2 \cdot 2CH_3CN$ crystals using the same synthetic procedure. However, only amorphous powders were formed, likely due to the smaller ionic radii of Er^{III}, Tm^{III}, Yb^{III} and Lu^{III} compared with other lighter Ln^{III}.

Synthesis of $[Dy_4(bpp)_4(OH)_4(NO_3)_4] \cdot 2CH_3CH_2OH$

$[Dy_4(bpp)_4(OH)_4(NO_3)_4] \cdot 2CH_3CH_2OH$ were prepared by the solvothermal synthesis method in ethanol. Hbpp ligand (22.3 mg, 0.1 mmol) and equimolar of $Dy(NO_3)_3 \cdot 6H_2O$ (22.8 mg, 0.1 mmol) were added to 16 mL ethanol in a 23 mL stainless steel autoclave, and put into an oven at 120 ℃. After 3 days, the reactions were cooled to room temperature gradually at a speed of 3 ℃ per hour. After reaching room temperature, the stainless-steel autoclave was transferred to a refrigerator set at 0 ℃, in order to further increase the yield. The resulting pale pink crystals were then collected by filtration. Yield: 30.6 mg, 63%. FT-IR (ATR) of $Dy_4(bpp)_4(OH)_4(NO_3)_4 \cdot 2CH_3CH_2OH$: 3202.44 (br), 1602.34 (s), 1565.80 (m), 1535.25 (m),

1457.79 (m), 1431.47 (s), 1340.38 (m), 1249.60 (m), 1135.29 (m), 765.68 (s), 736.62 (w), 632.29(m). Elemental analysis: Anal. calcd (%) for $[Dy_4(bpp)_4(OH)_4(NO_3)_4]\cdot 2CH_3CH_2OH$ (FW = 1939.12) C, 34.68; H, 2.70; N, 14.44. Found: C, 34.33; H, 2.52; N, 14.42.

Syntheses of $[Dy_4(bpp)_4(CH_3CH_2OH)_2(OH)_2Cl_6]\cdot 3CH_3CH_2OH$

$[Dy_4(bpp)_4(CH_3CH_2OH)_2(OH)_2Cl_6]\cdot 3CH_3CH_2OH$ were prepared by the same synthetic conditions of $[Dy_4(bpp)_4(OH)_4(NO_3)_4]\cdot 2CH_3CH_2OH$, except for using lanthanide chloride salts instead of nitrate salts. Hbpp ligand (22.3 mg, 0.1 mmol) and equimolar of $DyCl_3\cdot 6H_2O$ (18.9 mg, 0.1 mmol) were added to 16 mL ethanol in a 23 mL stainless steel autoclave, and put into an oven at 120 ℃. After 3 days, the reactions were cooled to room temperature at a speed of 3 ℃ per hour. After reaching room temperature, the stainless-steel autoclave was transferred to a refrigerator set at 0 ℃, in order to further increase the yield. The resulting white crystals were then collected by filtration. Yield: 17.0 mg, 34%. FT-IR (ATR) of $[Dy_4(bpp)_4(CH_3CH_2OH)_2(OH)_2Cl_6]\cdot 3CH_3CH_2OH$: 3235.89 (br), 3073.80 (w), 2970.02 (w), 1601.42 (s), 1565.41 (m), 1458.49 (m), 1342.85 (m), 1150.79 (s), 1137.27 (s), 1019.66 (m), 765.69 (m), 737.30 (w), 633.98 (m). Elemental analysis: Anal. calcd (%) for $[Dy_4(bpp)_4(CH_3CH_2OH)_2(OH)_2Cl_6]\cdot 3CH_3CH_2OH$ (FW = 2012.02) C, 37.01; H, 3.41; N, 11.13. Found: C, 37.24; H, 3.35; N, 10.98.

4.3 Molecular structures of $[Ln(Hbpp)_2(NO_3)_3]_2\cdot 2CH_3CN$

The molecular structures of **Y_2_MeCN**, **Eu_2_MeCN**, **Dy_2_MeCN** were determined employing SC-XRD technique. Meanwhile, Powder-XRD (PXRD) measurements were performed on all the **Ln_2_MeCN** (Ln = Y, La, Ce, Pr, Nd, Sm, Eu, Gd, Tb, Dy, Ho) complexes. The comparable PXRD spectra of all the **Ln_2_MeCN** indicate that they are all isostructural (Figure S28). Therefore, only the structure of **Dy_2_MeCN** will be described in detail and the exact structural parameters regarding **Y_2_MeCN** and **Eu_2_MeCN** will be listed for comparison, when necessary. The detailed crystallographic information for **Y_2_MeCN**, **Eu_2_MeCN**, and **Dy_2_MeCN** are listed in Table S42.

Dy_2_MeCN crystallizes in the $P2_1/c$ space group, monoclinic crystal system. The asymmetric unit consists of two $[Dy(Hbpp)_2(NO_3)_3]$ mononuclear motifs and two acetonitrile solvent molecules in the lattice (Figure 4.2)**.** Inside each mononuclear motif, the central Dy^{III} is ten-coordinated by four nitrogen atoms from two Hbpp ligands and six oxygen atoms from three nitrates. The Dy–O and Dy-N bond lengths are in the range of 2.444(2) to 2.504(2) Å and 2.522(3) to 2.616(2) Å, respectively. Selected bond lengths and bond angles are listed in Table 4.2. Each Hbpp ligand provides one pyridine-N and one pyrazole-N from the same side to coordinate with the Dy^{III} center. The remaining pyridine-N and pyrazole-NH on the other side then participate in the formation of hydrogen bonds together with the pyridine-N and

pyrazole-NH from another Hbpp ligands. Two $[Dy(Hbpp)_2(NO_3)_3]$ motifs are thus bound together by four $N_{pyrazole}$–H···$N_{pyridine}$ hydrogen bonds to form a grid-like dimer, or described in another way, a "corner complex" which can be seen as a [2×2] square grid devoid of two metal ions at diagonally opposite corners. No other hydrogen bonds or any short contacts are found between the neighboring dimers or between a dimer and the surrounding lattice acetonitrile molecules. The intra-grid Dy···Dy distance within one dimer is 8.388 Å. The closest inter-grid Dy···Dy distance between different dimers is 8.777 Å.

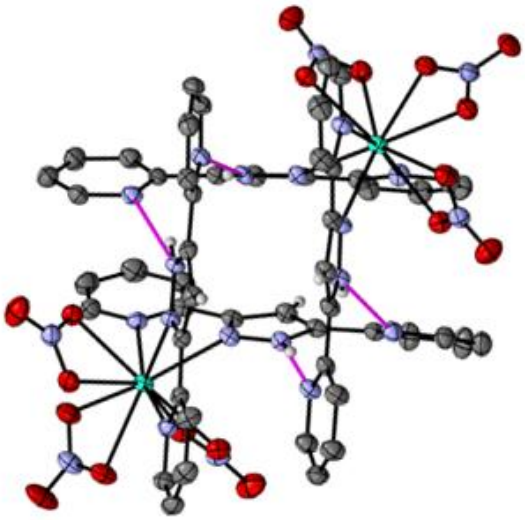

Figure 4.2. Molecular structures of **Dy_2_MeCN**. H atoms on all pyridine rings, and lattice solvents are omitted for the sake of clarity. Colour code: Dy, green; O, red; N, purple; C, grey; H, white. Hydrogen bonds are shown as violet dashed lines.

Table 4.2. Selected bond lengths (Å) and bond angles (°) in **Dy_2_MeCN**.

Dy1 – O1	2.457(2)	Dy2 – O10	2.457(2)
Dy1 – O2	2.470(2)	Dy2 – O11	2.444(2)
Dy1 – O4	2.458(2)	Dy2 – O13	2.471(2)
Dy1 – O5	2.462(2)	Dy2 – O14	2.474(2)
Dy1 – O7	2.504(2)	Dy2 – O16	2.483(2)
Dy1 – O8	2.474(2)	Dy2 – O17	2.468(2)
Dy1 – N1	2.589(3)	Dy2 – N9	2.596(3)
Dy1 – N2	2.527(2)	Dy2 – N10	2.567(2)
Dy1 – N5	2.616(2)	Dy2 – N13	2.590(3)
Dy1 – N6	2.542(2)	Dy2 – N14	2.522(3)
N1 – Dy1 – N2	64.23(8)	N9 – Dy1 – N10	63.27(8)
N5 – Dy1 – N6	62.84(8)	N13 – Dy1 – N14	63.59(8)

It is noteworthy that though the molecule structure of **Dy_2_MeCN** may be centrosymmetric at the first glance, the molecule is in fact asymmetric as the two $[Dy(Hbpp)_2(NO_3)_3]$ mononuclear motifs are structurally inequivalent. This is evidenced by the differences in bond lengths and bond angles around the two Dy^{III} centers (Table 4.2). The continuous shape measures (CShM) were performed on SHAPE 2.1 program to evaluate the degrees of distortion from standard reference shapes for the coordination polyhedra of the two Dy^{III} centers individually (Table 4.3 and S43). The results revealed the symmetries of the polyhedrons around the Dy^{III} centres are, though not exactly the same, quite similar, both being closest to JSPC-10 (Sphenocorona, C_{2v}).

Table 4.3. Continuous Shape Measures for Dy^{III} ions in **Dy_2_MeCN** showing the closest geometries.

	JSPC-10 (C_{2v})	**SDD-10 (D_2)**	**TD-10 (C_{2v})**	**1st Dy as reference**
1st Dy	**2.209**	3.508	3.009	
2nd Dy	**2.169**	3.977	3.536	0.205

The structures of **Y_2_MeCN** and **Eu_2_MeCN** differ from those of **Dy_2_MeCN** only in some bond lengths and bond angles (Table S44, S45). The average Ln–O and Ln–N bond lengths both follow the order: Eu > Dy > Y (Table S46). The trend is in accordance with the order of ionic radii (Table 1.2).

4.4 Magnetic behaviours of $[Dy(Hbpp)_2(NO_3)_3]_2 \cdot 2CH_3CN$

Direct-current (DC) magnetic susceptibility measurement of **Dy_2_MeCN** was performed on polycrystalline samples in the temperature range of 2.0 to 300 K under an applied magnetic field of 1000 Oe. The $\chi_M T$ value of 28.41 $cm^3mol^{-1}K$ at 300 K obtained from the DC magnetic measurement on **Dy_2_MeCN** polycrystalline sample is close to the theoretical value 28.34 $cm^3mol^{-1}K$ expected for two uncoupled Dy^{III} ions (Figure 4.5). Upon lowering the temperature, the $\chi_M T$ value of **Dy_2_MeCN** decreases gradually to 16.60 $cm^3mol^{-1}K$ at 2.0 K. The decrease of $\chi_M T$ is mainly ascribed to the thermal depopulation of the m_J levels of the $^6H_{15/2}$ ground-state multiplet of Dy^{III} ion. Intra- and inter-molecular magnetic coupling may also have influence on the $\chi_M T$ value at cryogenic temperatures. However, their contribution is not significant, since there is no direct exchange-coupling pathway between Dy^{III} ions and

the distances between them are relatively large (8.388 Å and 8.777Å for closest intra- and inter-molecular Dy···Dy distances, respectively). The negligible contribution is also proven by the DC magnetic susceptibility of **Gd$_2$_MeCN**, as the $\chi_M T$ value remain at around 14.5 cm^{3}mol^{-1}K in the 2.0–300 K temperature range (Figure 4.3).

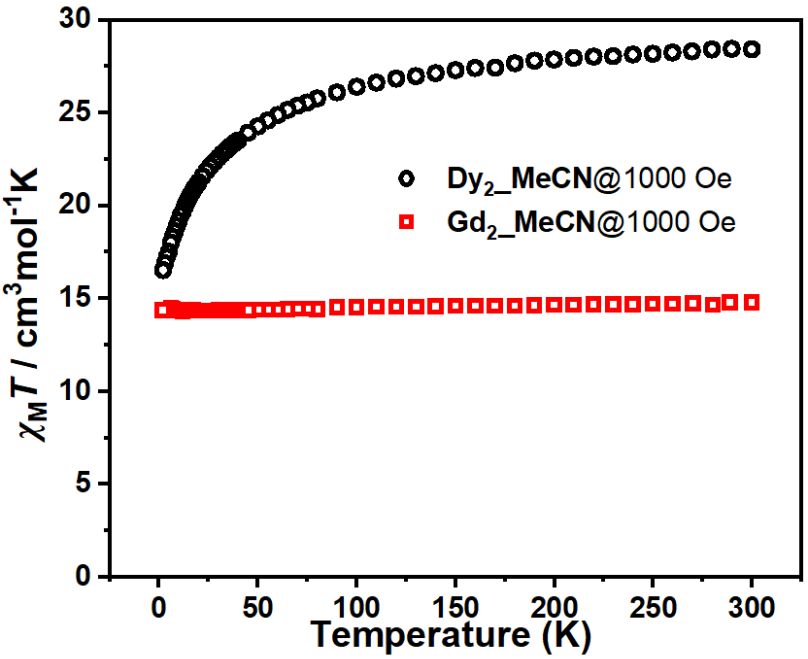

Figure 4.3. $\chi_M T$ versus T plots for **Dy$_2$_MeCN** and **Gd$_2$_MeCN** under an applied DC field of 1000 Oe.

Alternating current (AC) susceptibility measurements were performed on **Dy$_2$_MeCN** with an AC amplitude of 3.5 Oe, with the oscillation frequency varying from 1 to 1500 Hz. Measurements under zero field revealed no out-of-phase susceptibility (χ_M'') signals (Figure 4.4), indicating the absence of the slow relaxation of magnetization. This is a normal phenomenon for **Dy$_2$_MeCN** under zero field, since sufficient QTM can be expected due to the low symmetry of the coordination environment around Dy^{III} ions. The dynamic magnetism of **Dy$_2$_MeCN** was then investigated under applied magnetic fields, which is expected to mitigate QTM. Clear frequency-dependent χ_M'' signals started to appear upon the application of external field, starting from 200 Oe, confirming the field-induced SMM property of **Dy$_2$_MeCN**. The optimal external field, where the maximum of χ_M'' showed up at the lowest oscillation frequency, was found to be 1000 Oe (Figure 4.4).

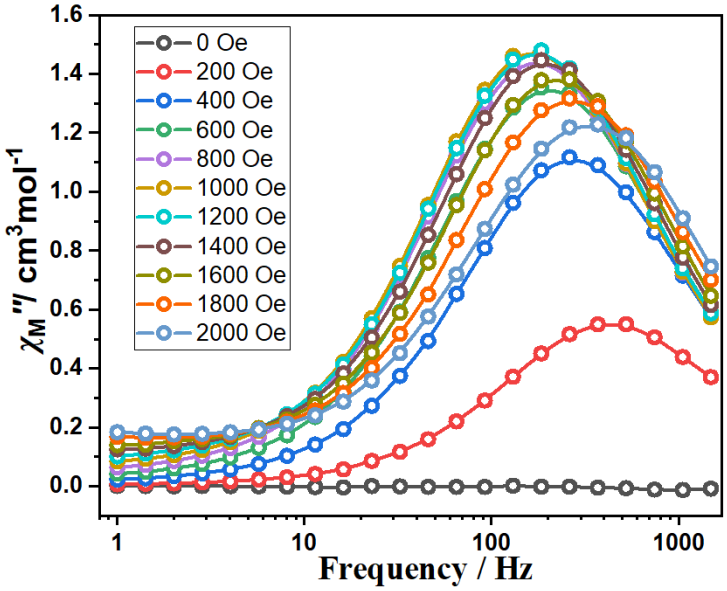

Figure 4.4. The out-of-phase susceptibility (χ_M'') versus frequency plot for **Dy_2_MeCN** under different external fields. The lines are guides for the eye.

The frequency-dependent behaviour of the in-phase (χ_M') and out-of-phase (χ_M'') components of the magnetic susceptibility under 1000 Oe applied field at various measured temperatures were shown in Figure 4.7. The χ_M'' vs. frequency peak was observed up to 2.5 K at the frequency of 868 Hz. The results were shown up to 3.1 K since the relaxation time could be still extracted with a high degree of confidence.

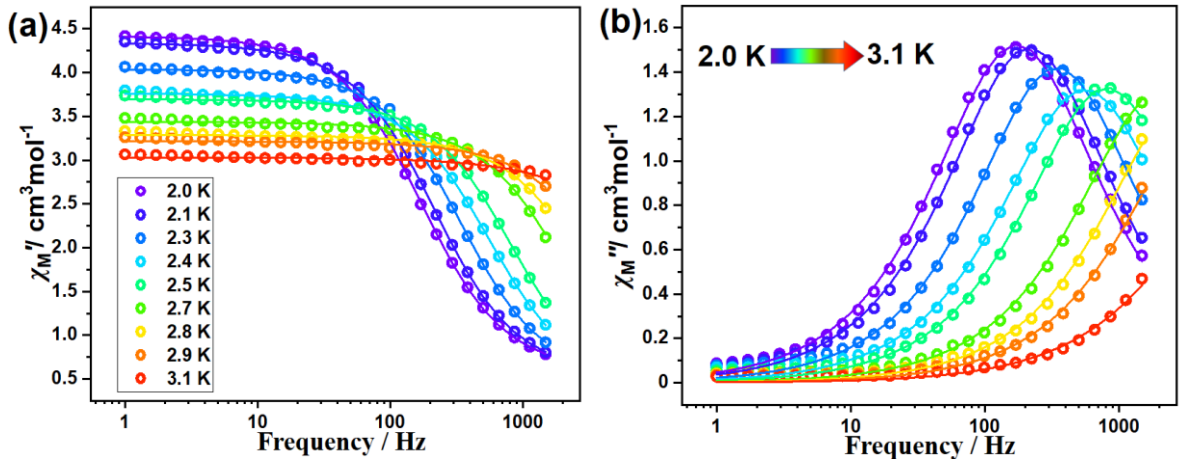

Figure 4.5. Frequency dependency of the in-phase (a) and out-of-phase (b) components of the magnetic susceptibility for **Dy_2_MeCN** under 1000 Oe applied field. The solid lines are the best fits to the generalized Debye model.

The relaxation time (τ) at each measured temperature was calculated according to the generalized Debye model, based on the data from Figure 4.5 and the Cole–Cole (χ_M'' vs. χ_M') diagram (Figure 4.6, a). The calculation was performed on the software CCFIT and the detailed calculation results are given in Table S47. The α values range from 0.139 to 0.218, indicating the existence of multiple relaxation processes throughout the whole temperature

region. By fitting the relaxation time vs. temperature data with the Arrhénius equation—$\tau = \tau_0 \exp(U_{eff}/k_BT)$, the effective reversal energy barrier U_{eff} and the pre-exponential factor τ_0 were determined to be 38.8 ± 2.1 K and 1.14×10^{-10} s, respectively (Figure 4.6, b). However, the Arrhénius equation is not adequate to fit the whole range of data as it displays apparent curvature. This feature indicates the coexistence of multiple relaxation processes, echoing the interpretation of α values. Therefore, a comprehensive equation

$$\tau^{-1} = {\tau_0}^{-1} \exp\left(-\frac{U_{\text{eff}}}{k_B T}\right) + CT^n + AT + {\tau_{\text{QTM}}}^{-1} \qquad \text{Equation 4.1}$$

in which the four terms on the right side represent Orbach, Raman, direct, and QTM processes in sequence, was used to fit the data. To avoid the problem of overparameterization, it was assumed at first that QTM was fully suppressed by the applied field. The assumption was supported by the observation that no plateau was detected in Figure 4.8, b. The best fitting result is $\tau_0 = 4.37 \times 10^{-11}$ s, $U_{eff} = 39.0$ K, $A = 530.4$ s^{-1} K^{-1}. Attempts to include the Raman or the QTM term failed to yield reasonable results. Efforts were also made to fit the data with only Raman and Direct processes. Although the fitting was able to converge at $C = 0.01046$ s^{-1} K^{-n}, $n = 14$, and $A = 460.1$ s^{-1} K^{-1}, $n > 12$ is physically unreasonable for Raman process, suggesting implausible fitting results. The obtained Orbach energy barrier matches well with the energy gap of the ground states and the first excited states deduced from the low-temperature PL study, *vide infra*, demonstrating that the complex undergoes the relaxation of magnetization mainly through the first excited states along with direct process under applied external fields.

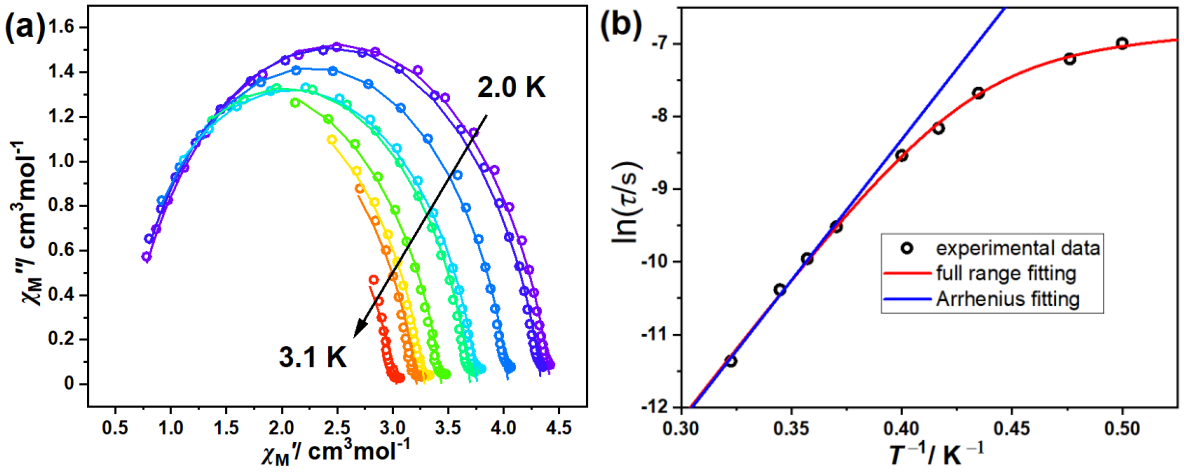

Figure 4.6. a, the Cole–Cole (χ_M'' vs. χ_M') diagram of **Dy$_2$_MeCN** under 1000 Oe applied field, the lines are the best fitting result to generalized Debye model; b, the temperature-dependent relaxation time and the corresponding best fitting results.

The energy barrier for **Dy$_2$_MeCN** under 1000 Oe applied field is relatively low. This is not surprising given the following facts: on the one hand, the neutral Hbpp ligands and nitrate ions are weak field ligands, which cannot provide large electron density around the Dy^{III}

centers; on the other hand, the coordination polyhedra are low in symmetry (C_{2v}), as inferred from the SHAPE analysis presented above. Hence, the complex lacks both the strong magnetic anisotropy and the large energy splitting between Kramers doublets (KDs) to be a high performance SMM. In the meantime, large deviation angles between the easy axes of magnetization of the ground KD and the low energy excited KD can be expected on Dy^{III} centers. The resulting efficient spin reversal transitions through the low energy excited KDs instead of the ones with higher energy further limit the increase of the energy barrier.

CASSCF calculations were carried out with OPENMOLCAS program package on **Dy_2_MeCN** on the basis of single-crystal X-ray determined geometry, excluding lattice solvents. The two inequivalent Dy^{III} ions were calculated individually. For the calculation on one Dy^{III} ion, the other Dy^{III} ion was replaced by Y^{III}. The basis sets for all atoms are atomic natural orbitals from the MOLCAS ANO-RCC library: ANO-RCC-VTZP for Dy^{III}; VDZP for close N and O; VDZ for distant atoms. The calculations employed the second order Douglas-Kroll-Hess Hamiltonian, where scalar relativistic contractions were taken into account in the basis set and the spin-orbit couplings were handled separately in the restricted active space state interaction (RASSI-SO) procedure. For the Dy^{III} fragment, active electrons in 7 active spaces include all *f* electrons (CAS (9 in 7)) in the CASSCF calculation. All the roots were calculated in the active space. The maximum number of spin-free states which was possible with our hardware (all from 21 sextets, 128 from 224 quadruplets, 130 from 490 doublets) was mixed. SINGLE_ANISO program was used to obtain the energy levels, $\boldsymbol{g}$ tensors, m_J values, magnetic axes, *etc.*, based on the above CASSCF/RASSI-SO calculations.

The energy diagrams of the eight Kramers doublets for each Dy^{III} fragments are shown in Table 4.4, together with the calculated $\boldsymbol{g}$ (g_x, g_y, g_z) tensors for each doublet. The g_z values of the two Dy^{III} in the ground Kramers doublet equal to 15.04 and 16.32, respectively, both deviate significantly from 20, indicating less anisotropic nature of the Dy^{III} ions. The lack of strong magnetic anistropy is also evidenced by the definite projections of the total moment $|m_J>$ for the ground Kramers states (Table S48). With the composition of the principle $|\pm 15/2>$ states less than 50% in both Dy1 and Dy2, the highly mixed nature of the ground KDs facilitates the rapid QTM, leading to the absence of slow relaxation of magnetization of **Dy_2_MeCN** under zero field. The first excited doublets for the two Dy^{III} ions in the slightly different configurations are 42.7 K (29.7 cm^{-1}) and 59.0 K (41.0 cm^{-1}) higher than the ground doublets in energy, respectively, similar to the Orbach energy barrier (39.0 K) extracted from AC measurements. This indicates the plausible existence of the Orbach process, where the spin reversal takes place through the first excited Kramers doublet states.

Table 4.4. Calculated energy levels (cm^{-1}), $\boldsymbol{g}$ (g_x, g_y, g_z) tensors and predominant m_J values of the lowest eight Kramers doublets (KDs) of the two Dy^{III} fragments in **Dy_2_MeCN**.

KDs	1st Dy^{III} ion		2nd Dy^{III} ion	
	E/cm^{-1}	$\boldsymbol{g}$ (g_x, g_y, g_z)	E/cm^{-1}	$\boldsymbol{g}$ (g_x, g_y, g_z)
1	0.00	0.379, 2.067, 15.04	0.00	0.320, 1.067, 16.32
2	29.7	1.470, 2.431, 11.85	41.0	1.033, 1.967, 14.34
3	76.2	1.529, 3.064, 12.60	86.5	0.808, 3.375, 13.09
4	116.0	0.840, 2.914, 7.784	131.8	8.057, 5.380, 2.091
5	150.9	0.422, 3.392, 12.23	153.1	0.966, 2.331, 11.99
6	191.6	1.305, 4.364, 8.843	214.4	0.479, 3.241, 11.86
7	250.8	2.447, 6.269, 11.13	272.3	1.315, 4.128, 14.32
8	276.8	2.012, 4.074, 14.12	294.1	1.609, 2.931, 15.20

4.5 Photoluminescence characteristics of $[Ln(Hbpp)_2(NO_3)_3]_2 \cdot 2CH_3CN$

The solid-state photoluminescence (PL) characteristics were investigated on **Ln_2_MeCN** complexes (Ln = Ce, Pr, Nd, Sm, Eu, Gd, Tb, Dy, Ho). At room temperature, upon the excitation ($\lambda_{ex.}$) at 310 nm, **Sm_2_MeCN**, **Eu_2_MeCN**, **Tb_2_MeCN**, and **Dy_2_MeCN** exhibited metal-centered line-like f–f emissive transitions in the visible range (Figure 4.7).

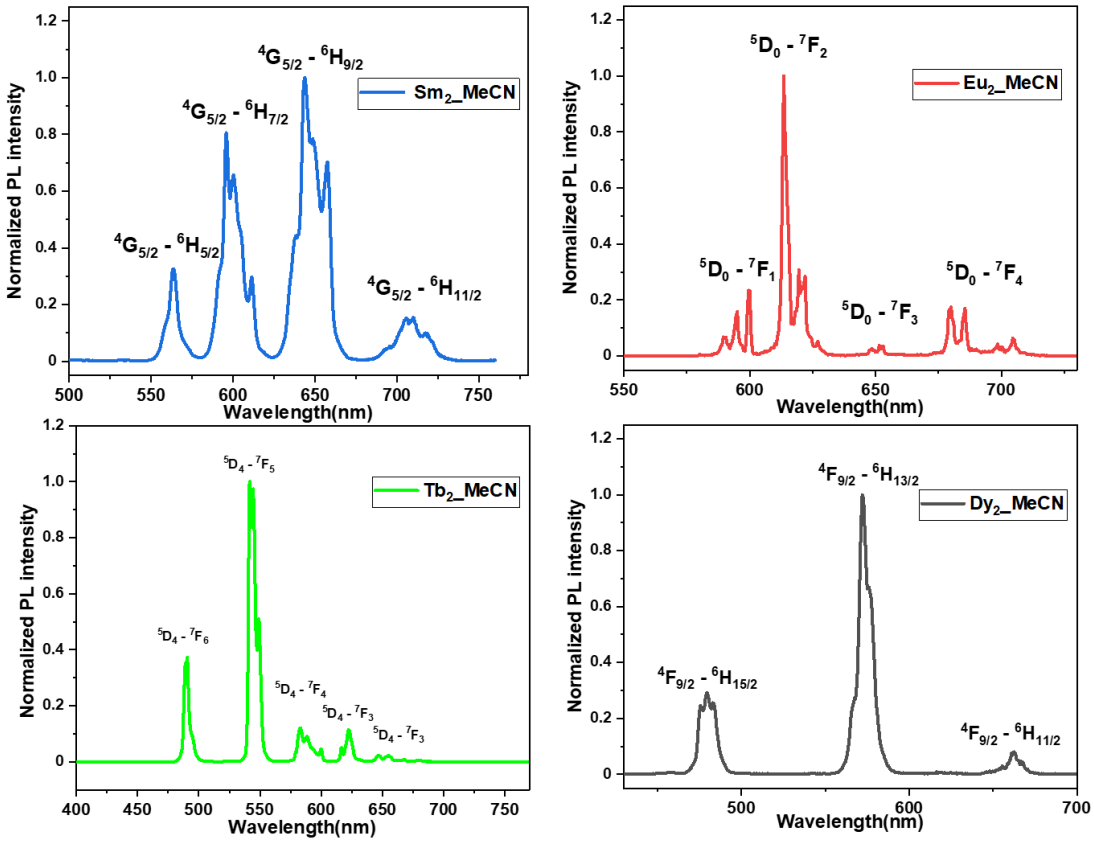

Figure 4.7. Emission spectra of **Sm$_2$_MeCN**, **Eu$_2$_MeCN**, **Tb$_2$_MeCN**, and **Dy$_2$_MeCN** complexes recorded at room temperature in the solid-state. The samples are excited at 310 nm. All f–f transitions are labeled close to the corresponding metal-centered emission peaks.

Nd$_2$_MeCN revealed Nd^{III} ion centered transitions in the NIR region (Figure 4.8). The $^4F_{3/2} \rightarrow {}^4I_{9/2}$ and $^4F_{3/2} \rightarrow {}^4I_{13/2}$ emission peaks, which were blurred at room temperature, became more distinct and intensified at 3.0 K, due to the suppression of the thermal vibrations.

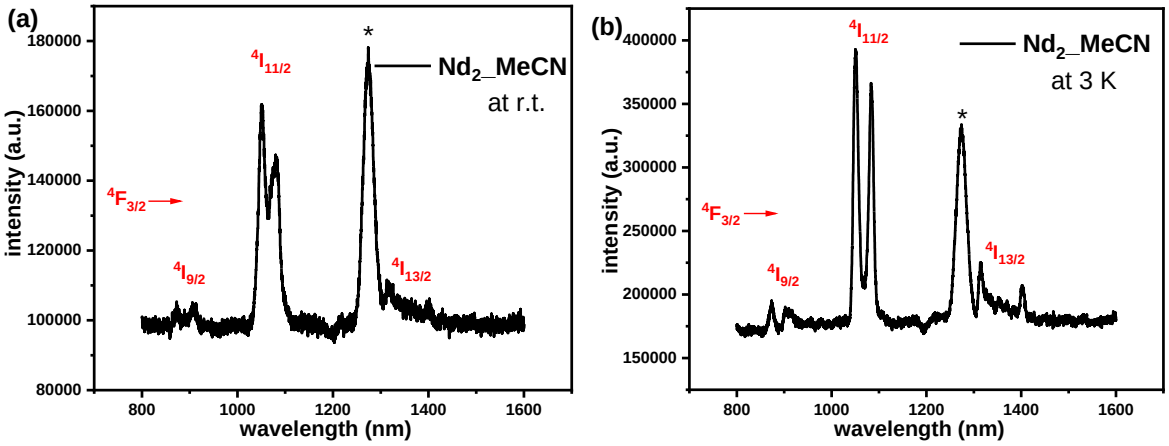

Figure 4.8. NIR emission spectra of **Nd$_2$_MeCN** recorded at room temperature (a) and at 3.0 K (b) with $\lambda_{ex.}$ = 320 nm with f–f transitions are labeled close to the corresponding metal-centered emission peaks. The peaks labeled with * are fourth-order diffraction peaks.

Unlike the Sm, Eu, Tb, Dy, and Nd analogues that exhibit narrow f–f emission bands, **Ce_2_MeCN** showed two broad emission peaks at 416 nm and 440 nm when the complex was excited with $\lambda_{ex.}$ = 370 nm (Figure 4.9). This is typical 5d−4f emission of Ce samples. The energies of the two emission peaks were calculated to be 24038 cm^{-1} and 22727 cm^{-1}. The energy difference (1311 cm^{-1}) falls within the reasonable range of the splitting between ground state levels $^2F_{5/2}$ and $^2F_{7/2}$ of Ce^{III} ions.

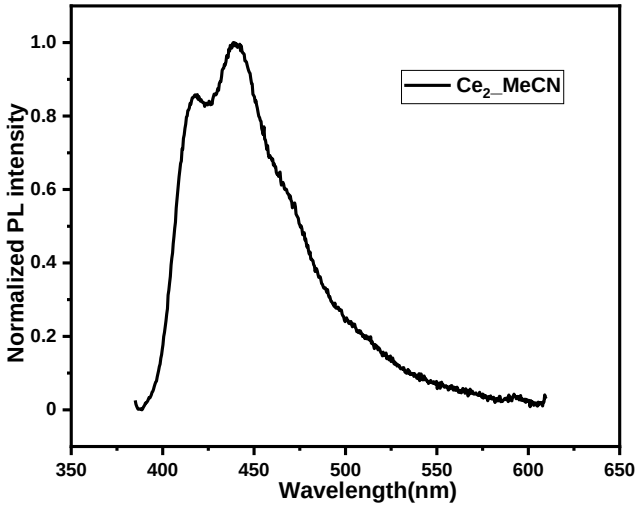

Figure 4.9. Emission spectra of **Ce_2_MeCN** complexes recorded at room temperature with $\lambda_{ex.}$ = 370 nm.

In the case of **Gd_2_MeCN**, when it was excited at 330 nm at room temperature, it exhibited a broad peak around 410 nm (Figure S29). Since the energy of excited states of Gd^{III} are over 30000 cm^{-1}, higher than the triplet states of most ligands, the broad peak originated from ligand-centered emission. The excitation spectrum monitored at 406 nm exhibited a broad peak spanning from 315 nm to 400 nm, with a maximum intensity at 335 nm (Figure S29). Furthermore, the phosphorescence emission spectra of **Gd_2_MeCN** was collected at 77 K (Figure 4.10). The zero-phonon line located at 448 nm in the Gd-emission spectrum was used for the estimation of the triplet energy level of the Hbpp ligands. This estimated energy, 22321 cm^{-1}, was higher than the energies of the emitting levels of Nd^{III} ($^4F_{3/2}$, ~11000 cm^{-1}), Eu^{III} ($^5D_0$, ~17250 cm^{-1}), Sm^{III} ($^4G_{5/2}$, ~17000 cm^{-1}), Tb^{III} ($^5D_4$, ~20500 cm^{-1}), and Dy^{III} ($^4F_9$, ~21500 cm^{-1}), supporting the sensitization of the Ln^{III} luminescence by Hbpp ligand via the antenna effect in these complexes.

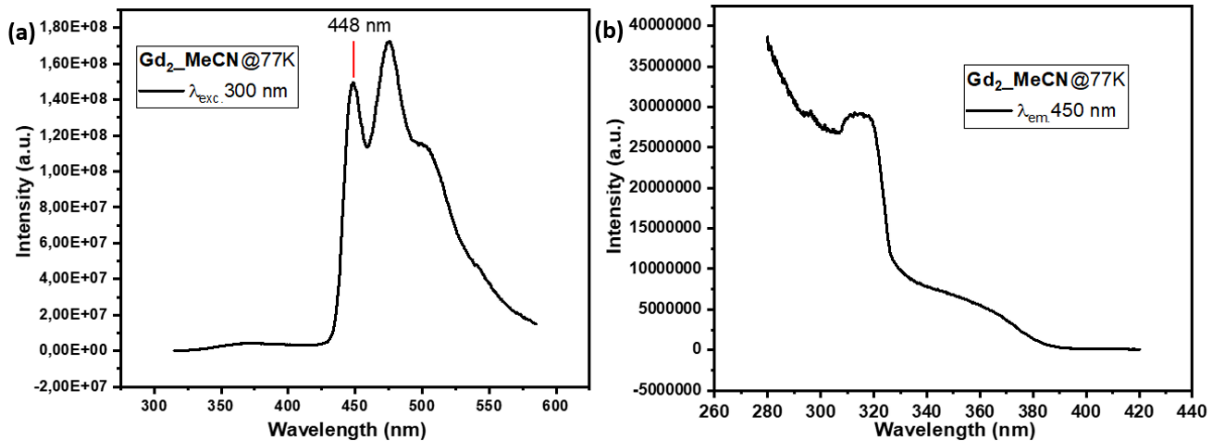

Figure 4.10. Emission (a, $\lambda_{ex.}$ = 300 nm) and excitation (b, $\lambda_{em.}$ = 450 nm) spectra of **Gd_2_MeCN** at 77 K.

The PL measurements on **Pr_2_MeCN** and **Ho_2_MeCN** in the visible range, however, didn't show metal-centered emissions, though Pr^{III} and Ho^{III} have emitting states with lower energies (e. g., $^1D_2$ ~20000 cm^{-1} for Pr^{III}; $^5F_5$, ~15500 cm^{-1} for Ho^{III}) than the triplet states of Hbpp ligand, and the energy transfer from ligand to Pr^{III} or Ho^{III} can occur in principle. In fact, the fluorescence of Pr^{III} or Ho^{III} is generally hard to observe compared with some other Ln^{III} ions. Due to the dense manifolds of closely spaced energy levels, the radiative transitions in Pr^{III} and Ho^{III} often involve states with relatively small energy gaps.[109,110,202] Therefore, these transitions are particularly susceptible to efficient non-radiative relaxations through vibrational coupling with high-energy phonons.

Since **Dy_2_MeCN** showed field-induced SMM behaviour, its high-resolution emission spectrum was collected at low temperature, in order to gain information on the CF splitting of the $^6H_{15/2}$ ground state and energy difference between the M_J sublevels. At 3.0 K, the original peaks corresponding to the $^4F_{9/2} \rightarrow {}^6H_J$ (J = 15/2, 13/2, 11/2) transitions were all split into several obvious peaks (Figure 4.11, a). The fine spectrum of $^4F_{9/2} \rightarrow {}^6H_{15/2}$ is deconvoluted by Gaussian function with 8-components which corresponds to the eight Kramers doublets of the $^6H_{15/2}$ ground state (Figure 4.11, b). The obtained energy levels of the eight doublets are summarized in Table S49.

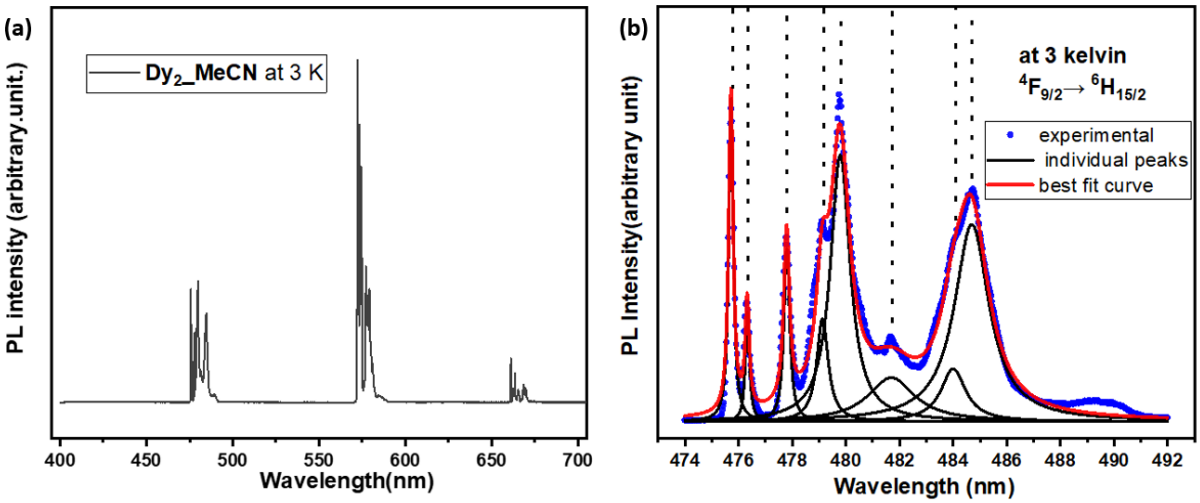

Figure 4.11. a, high resolution emission spectrum of **Dy_2_MeCN** at 3.0 K; b, peak deconvolution of the $^4F_{9/2}$ to $^6H_{15/2}$ transitions

The energy splitting diagram obtained from the fine structures of low temperature luminescence spectrum match well with theoretically calculated results (Figure 4.12). In the meanwhile, the first excited doublets has similar energy with the Orbach energy barrier extracted from the AC measurements.

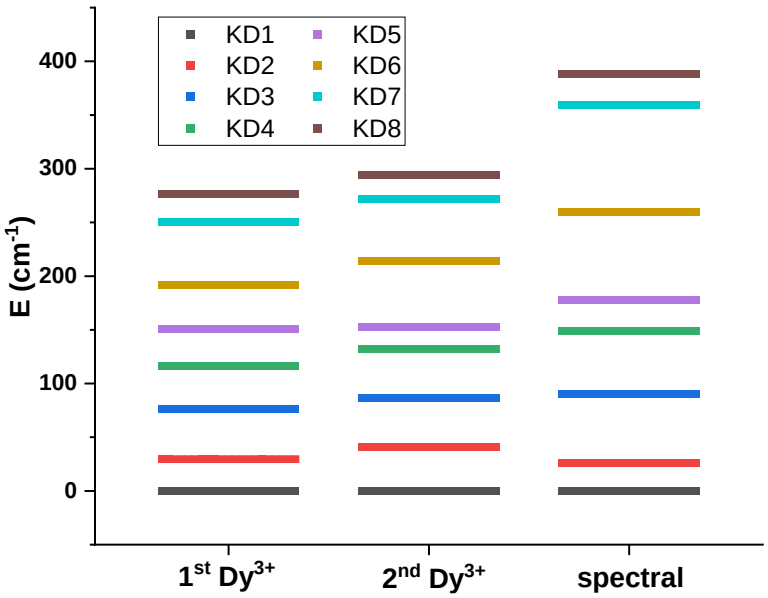

Figure 4.12. Energy diagram of the eight kramers doublets according to the CASSCF calculation or to the deconvolution of low temperature optical spectrum.

4.6 Crystal structures of $Dy_4(bpp)_4(OH)_4(NO_3)_4 \cdot 2CH_3CH_2OH$

The single crystal structure of $Dy_4(bpp)_4(OH)_4(NO_3)_4 \cdot 2CH_3CH_2OH$ (**Dy_4_NO_3**) was determined by SC-XRD technique. The single crystal data of **Dy_4_NO_3** are summarized in Table S50. Powder-XRD measurements confirmed the phase purity of the sample (Figure S30).

Dy_4_NO_3 crystallized in the $P2_1/n$ space group, monoclinic crystal system. The tetranuclear molecule is centro-symmetric, with its four Dy^{III} ions arranged in a parallelogram configuration. The two internal Dy^{III} ions are bridged by two μ_3-OH groups, and each of them is further bridged to an external Dy^{III} by a μ_3-OH group and a μ_2-OH group, thus forming an overall defect-dicubane $[Dy_4(OH)_4]$ core (Figure 4.13, left), as previously reported.[203,204] From one end of the $[Dy_4(OH)_4]$ core to another end, the four hydroxide groups locate above and below the Dy_4 plane alternatively. The Dy–Oμ_2 bond lengths are 2.279(7) Å and 2.243(7) Å for the internal Dy^{III} and external Dy^{III}, respectively, shorter than the Dy–Oμ_3 bond lengths ranging from 2.308(7) Å to 2.413(7) Å (Table 4.5). Every Dy^{III} ion is further coordinated by four nitrogen atoms donated by two bpp^- (Hbpp deprotonated), from the directions of approximately in the Dy_4 plane and approximately perpendicular to the Dy_4 plane. The Dy–N bond lengths range from 2.381(9) to 2.675(2) Å. The remaining coordination sites of the external Dy1 are occupied by two oxygen atoms from one terminal nitrate anion. By contrast, the nitrate anion close to the internal Dy2 is coordinated in a monodentate manner. Its uncoordinated oxygen toward the $[Dy_4(OH)_4]$ core forms an O–H···O hydrogen bond with the neighbouring μ_3-OH group, which stabilizes the monodentate configuration. The Dy–$O_{nitrate}$ bond lengths are in the range of 2.406(8) to 2.470(8) Å. Two lattice ethanol molecules are positioned in the vicinity of the main tetranuclear structure, connected through O–H···O hydrogen bonds (Figure 4.13, right).

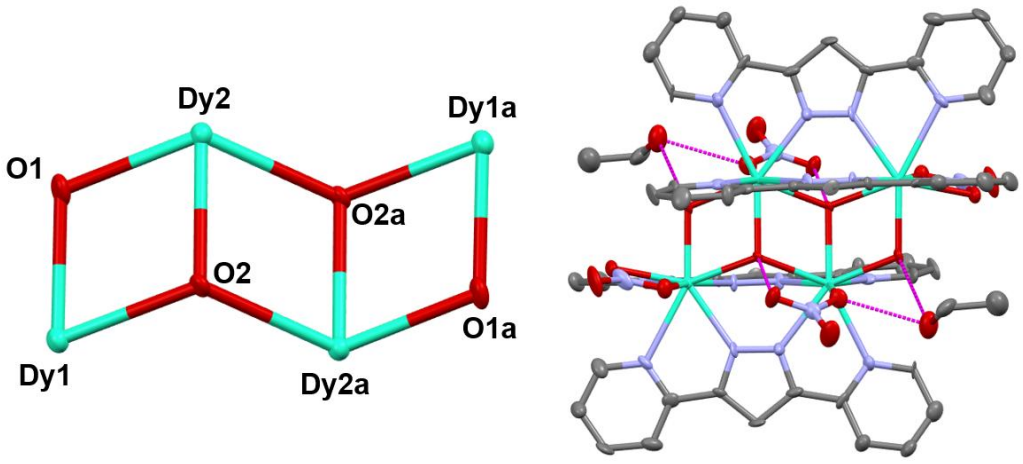

Figure 4.13. (left) The defect-dicubane central core of complex **Dy_4_NO_3**, (right) Molecular structures of **Dy_4_NO_3**. Hydrogen atoms are omitted for the sake of clarity. Colour code: Dy, green; O, red; N, purple; C, grey. Hydrogen bonds are shown as violet dashed lines.

Table 4.5. Selected bond lengths (Å) and bond angles (°) in **Dy_4_NO_3**.

Dy1 – Dy2	3.7173(7)	Dy2 – Dy2a	3.7841(7)
Dy1 – O1	2.243(7)	Dy2 – O1	2.279(2)
Dy1 – O2	2.361(6)	Dy2 – O2	2.308(2)
Dy1 – O3	2.470(2)	Dy2 – O2A	2.413(2)
Dy1 – O4	2.409(8)	Dy2 – O6	2.406(8)
Dy1 – N3	2.381(9)	Dy2 – N1a	2.647(9)
Dy1 – N4	2.545(9)	Dy2 – N2a	2.415(9)
Dy1 – N5	2.675(2)	Dy2 – N7a	2.437(9)
Dy1 – N6	2.412(9)	Dy2 – N8a	2.614(10)
O2 – Dy2 – Dy1	37.73(17)	Dy1 – O2 – Dy2	105.5(3)
O2 – Dy2 – Dy1	99.29(15)	Dy1 – O2 – Dy2a	122.2(3)
Dy1 – O1 – Dy2	110.6(3)	O1 – Dy2 – Dy1	34.39(19)
O1 – Dy1 – O2	71.5(2)	O1 – Dy2 – O2	71.8(3)
O3 – Dy1 – O4	52.5(3)	O1 – Dy2 – O2a	125.2(3)
N3 – Dy1 – N4	64.4(3)	N1a – Dy2 – N2a	63.4(3)
N5 – Dy1 – N6	62.6(3)	N7a – Dy2– N8a	64.5(3)

Symmetry codes: [a]1-X,1-Y,1-Z

Dy1 and Dy2 in **Dy_4_NO_3** are both eight coordinated, and the continuous shape measures (CShM) reveal that the coordination geometry of the external Dy1 and internal Dy2 are closest to BTPR-8 (biaugmented trigonal prism, C_{2v}) and SAPR-8 (square antiprism, D_{4d}), with the values of 2.225 and 1.157, respectively (Table 4.6 and S51). The intramolecular distances between metal centers are 3.784 Å for Dy2···Dy2a, 3.717 Å for Dy1···Dy2, 4.179 Å for Dy1···Dy2a and 6.946 Å for Dy1···Dy1a. The closest intermolecular Dy···Dy distances is 8.705 Å.

Table 4.6. Continuous Shape Measures for Dy^{III} ions in **Dy_4_NO_3** showing the closest geometries.

	SAPR-8 (D_{4d})	**TDD-8 (D_{2d})**	**JBTPR-8 (C_{2v})**	**BTPR-8 (C_{2v})**
Dy1	2.722	2.844	2.906	**2.225**
Dy2	**1.157**	2.323	2.930	1.987

4.7 Magnetic behaviour of $Dy_4(bpp)_4(OH)_4(NO_3)_4 \cdot 2CH_3CH_2OH$

Direct-current (DC) magnetic susceptibility measurement of **Dy_4_NO_3** was performed on polycrystalline samples in the temperature range of 2.0 to 300 K under an applied magnetic field of 1000 Oe. The experimental $\chi_M T$ value of 58.42 $cm^3mol^{-1}K$ for **Dy_4_NO_3** at 300 K was close to the theoretical value 56.68 $cm^3mol^{-1}K$ expected for four uncoupled Dy^{III} ions (Figure S31). $\chi_M T$ decreased gradually to 52.53 $cm^3mol^{-1}K$ at 23 K and then dropped quickly to 24.16 cm^3mol^{-1} K at 2.0 K, upon cooling the temperature. The decrease of $\chi_M T$ is ascribed to the thermal depopulation of the m_J levels of the $^6H_{15/2}$ ground-state multiplet of Dy^{III} ions and/or an overall antiferromagnetic intramolecular coupling between Dy^{III} ions. The short intramolecular distances of Dy1···Dy2, Dy1···Dy2a, Dy2···Dy2a, and to a less extent, Dy1···Dy1a may facilitate effective dipolar magnetic couplings. Furthermore, as Dy1 and Dy2, Dy1 and Dy2a, Dy2 and Dy2a are directly bridged by μ-OH groups, exchange magnetic couplings between them are also expected. However, the ferro/antiferromagnetic nature and the strength of these couplings are difficult to determine based solely on DC magnetic susceptibility measurements.

Alternating current (AC) susceptibility measurements performed on **Dy_4_NO_3** under zero field revealed clear frequency dependent out-of-phase susceptibility (χ_M'') signals (Figure 4.14), revealing the zero field SMM nature of **Dy_4_NO_3**. The χ_M'' vs. frequency peak was observed up to 23 K at the frequency of 1000 Hz.

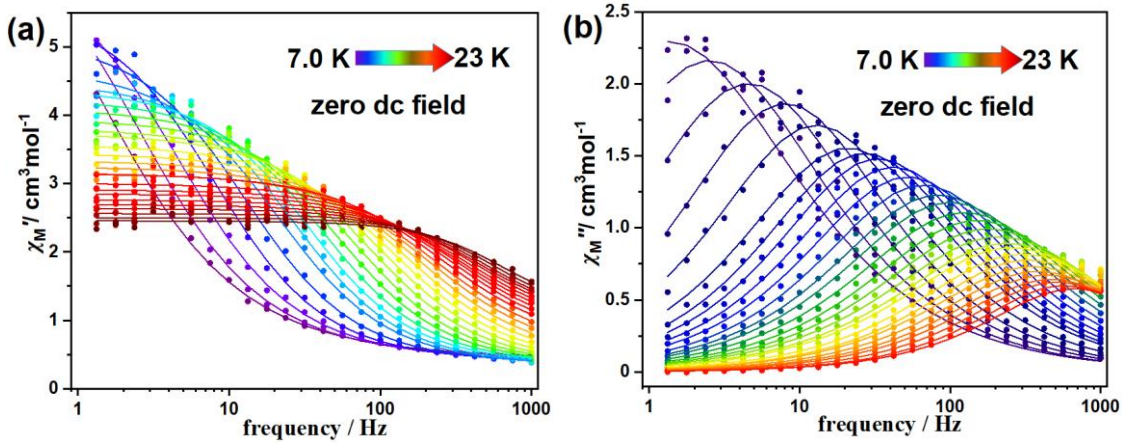

Figure 4.14. Frequency dependency of the in-phase (a) and out-of-phase (b) components of the magnetic susceptibility for **Dy_4_NO_3** under zero field. The solid lines are the best fits to the generalized Debye model.

The Cole–Cole (χ_M'' vs. χ_M') diagram displayed only one single relaxation, as the plot at each temperature showed only one semicircle (Figure 4.15, a), despite the presence of crystallographically inequivalent Dy^{III} in the tetranuclear complex. The relaxation time (τ) at each measured temperature was calculated according to the generalized Debye model on the

software CCFIT, with the detailed calculation results are given in Table S52. The α values showed a gradual decreasing trend from low temperatures to high temperatures, with the maximum 0.317 at the 7.0 K and minimum 0.104 at 22.5 K, indicating more pronounced coexistence of multiple processes in the low temperature regime. At the meantime, the curvature in the relaxation time vs. temperature plot implied the coexistence as well. Since the Direct process can be regarded as absent under zero field for the Kramers Dy^{III} ions, equation 4.2

$$\tau^{-1} = {\tau_0}^{-1} \exp\left(-\frac{U_{\text{eff}}}{k_B T}\right) + CT^n + {\tau_{\text{QTM}}}^{-1} \qquad \text{Equation 4.2}$$

involving only Orbach, Raman, and QTM processes could be used for the fitting of the lifetime versus temperature data. The fitting yielded was $\tau_0 = 4.41 \times 10^{-6}$ s, $U_{\text{eff}} = 96.0$ K, C = 7.09×10^{-3} s^{-1} K^{-n}, n = 3.65. Compared with the energy barrier in **Dy_2_MeCN**, the energy barrier obtained for **Dy_4_NO_3** is nearly tripled.

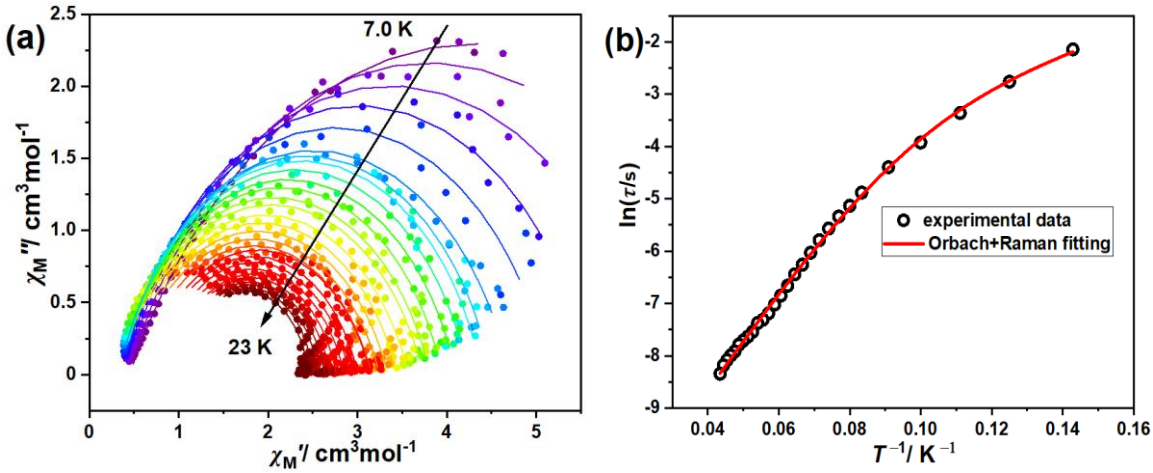

Figure 4.17. a, the Cole–Cole (χ_M'' vs. χ_M') diagram of **Dy_4_NO_3** in the absence of an applied field, the lines are the best fitting result to generalized Debye model; b, the temperature dependent relaxation time and the corresponding best fitting results of **Dy_4_NO_3**.

CASSCF calculations were carried out with OPENMOLCAS program package for **Dy_4_NO_3** on the basis of single-crystal X-ray determined geometry, excluding lattice solvents. The two inequivalent sets of Dy^{III} ions were calculated individually. For the calculation on one Dy^{III} ion, the other three Dy^{III} ions were replaced by Y^{III}. The basis sets for all atoms are atomic natural orbitals from the MOLCAS ANO-RCC library: ANO-RCC-VTZP for Dy^{III} and Ni^{II}; VDZP for close N and O; VDZ for distant atoms. The calculations employed the second order Douglas-Kroll-Hess Hamiltonian, where scalar relativistic contractions were taken into account in the basis set and the spin-orbit couplings were handled separately in the restricted active space state interaction (RASSI-SO) procedure. For the Dy^{III} fragment, active electrons in 7 active spaces include all *f* electrons (CAS (9 in 7)) in the CASSCF calculation. We calculated all the roots in the active space. We have mixed the maximum number of spin-

free state which was possible with our hardware (all from 21 sextets, 128 from 224 quadruplets, 130 from 490 doublets). SINGLE_ANISO program was used to obtain the energy levels, $\boldsymbol{g}$ tensors, m_J values, magnetic axes, *etc.*, based on the above CASSCF/RASSI-SO calculations.

The crystal field splitting energies associated with the eight Kramers doublets of the $^6H_{15/2}$ ground state multiplet for each Dy^{III} fragments are shown in Table 4.7, together with the calculated $\boldsymbol{g}$ (g_x, g_y, g_z) tensors for each doublet. The g_z values of the external Dy1 and the internal Dy2 in the ground Kramers doublet are 19.76 and 19.70, respectively, very close to the ideal value of 20. In contrast, g_x and g_y are approximately 0.01. Meanwhile, the ground KDs are predominantly composed by $M_J = \pm|15/2>$ substates, with contribution being 98.6% and 97.8% for Dy1 and Dy2, respectively (Table S53). These calculation results highlight the strong uniaxial magnetic anisotropy of all Dy^{III} ions in **Dy_4_NO_3**.

Table 4.7. Calculated energy levels (cm^{-1}), $\boldsymbol{g}$ (g_x, g_y, g_z) tensors and predominant m_J values of the lowest eight Kramers doublets (KDs) of the two Dy^{III} fragments in complexes **Dy_4_NO_3**.

KDs	Dy1		Dy2	
	E/cm^{-1}	$\boldsymbol{g}$ (g_x, g_y, g_z)	E/cm^{-1}	$\boldsymbol{g}$ (g_x, g_y, g_z)
1	0.00	0.002, 0.010, 19.76	0.00	0.004, 0.013, 19.70
2	202.1	0.412, 0.845, 16.00	117.8	0.073, 0.120, 16.72
3	257.7	0.166, 0.874, 14.12	201.74	0.725, 0.993, 13.33
4	320.5	3.091, 3.677, 10.13	283.5	1.270, 2.259, 9.815
5	368.9	3.177, 6.127, 9.934	349.1	7.118, 5.839, 2.152
6	426.4	1.138, 1.435, 17.31	214.4	0.479, 3.241, 11.86
7	490.4	0.145, 0.322, 17.56	396.4	2.421, 4.323, 12.09
8	601.5	0.032, 0.055, 19.33	448.2	0.308, 0.790, 17.65

The easy axes of magnetization on Dy1 and Dy2 both align approximately along their bonds with the adjacent μ_2-O, which are their shortest Dy–O bonds (Figure 4.16). This result is in line with the principle that the direction of the easy magnetization axis for dysprosium ions in a low-symmetry coordination environment is often governed by the coordination bond with the shortest bond length, as stated in Chapter 1.2.3. The energy difference between the first excited KDs and the ground KDs are 202.1 cm^{-1} (291.8 K), and 117.8 cm^{-1} (134.2 K)for Dy1 and Dy2, respectively. The latter is close to the energy barrier of Orbach process derived from AC experimental data, which implies that the spin reversal via the Orbach process

happens through the first excited kramers states. The larger energy splitting in Dy1 compared to Dy2 is consistent with the shorter Dy1-Oμ_2 bond length relative to the bond length of Dy2-Oμ_2.

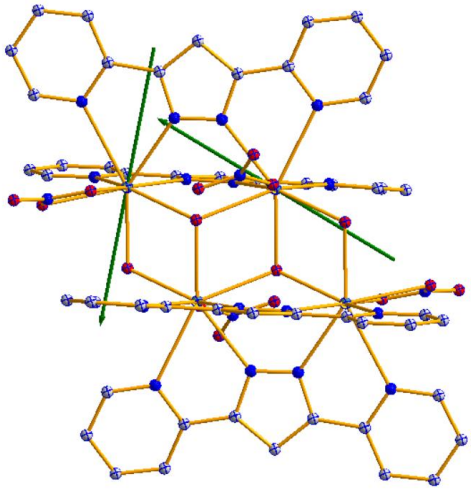

Figure 4.16. Easy axes of magnetization on Dy^{III} ions in **Dy_4_NO_3**.

4.8 Crystal structures of $Dy_4(bpp)_4(CH_3CH_2OH)_2(OH)_2Cl_6 \cdot 3CH_3CH_2OH$

The single crystal structures of **Dy_4_Cl** was determined by SC-XRD technique. Powder-XRD measurements performed on its bulky sample verified the phase purity (Figure S32). The crystal data of **Dy_4_Cl** are summarized in Table S54 and selected bond lengths and bond angles are given in Table 4.8.

Dy_4_Cl crystallized in the *P*2_1/*c* space group, monoclinic crystal system. The centro-symmetric tetranuclear molecule features a defect-dicubane [$Dy_4(\mu_3\text{-}OH)_2(\mu_2\text{-}Cl)_2$] core (Figure 4.17). In comparison to the [$Dy_4(OH)_4$] core of **Dy_4_NO_3** described in Chapter 4.6, the most pronounced difference is the replacement of the two terminal hydroxide groups (OH^-) by two chloride ions (Cl^-). Due to the larger radius than oxygen, the chlorides are located further outward with the Dy–Cl distances being 2.7658(9) Å and 2.7167(9) Å for the external Dy1 and internal Dy2, respectively (Table 4.8). At the meantime, to satisfy to requirement of the longer Dy1–Cl1 bond, Dy1 is also located more remote from Dy2, which is reflected on the increased Dy1–O1–Dy2 angle. The Dy–Oμ_3 bond lengths range from 2.366(2) Å to 2.414(2) Å. On the peripheral of the defect-dicubane [$Dy_4(\mu_3\text{-}OH)_2(\mu_2\text{-}Cl)_2$] core, four bpp^- ligands coordinate with Dy^{III} ions with all the nitrogen atoms on the central pyrazole ring and the terminal pyridine rings. The Dy–N bond lengths range from 2.381(9) to 2.678(3) Å. The remaining coordination sites of the external Dy1 are occupied by one terminal monodentate Cl^- ion, and one oxygen atom donated by a neutral ethanol molecule. Charge balance principle

and the 2.424(3) Å Dy–$O_{hydroxy}$ bond length support the electric neutrality of the coordinated ethanol molecule. Overall, Dy1 is eight coordinated in a $O_2Cl_2N_4$ polyhedron. The internal Dy2 is also eight coordinated in a $O_2Cl_2N_4$ polyhedron, with its last coordination site occupied by a terminal monodentate Cl^-. For every equivalent of the $[Dy_4(\mu_3\text{-}OH)_2(\mu_2\text{-}Cl)_2]$ tetranuclear structure, three equivalent of ethanol molecules are present nearby in the lattice, connecting to the main structure through O–H···O and O–H···Cl hydrogen bonds (Figure 4.19, right).

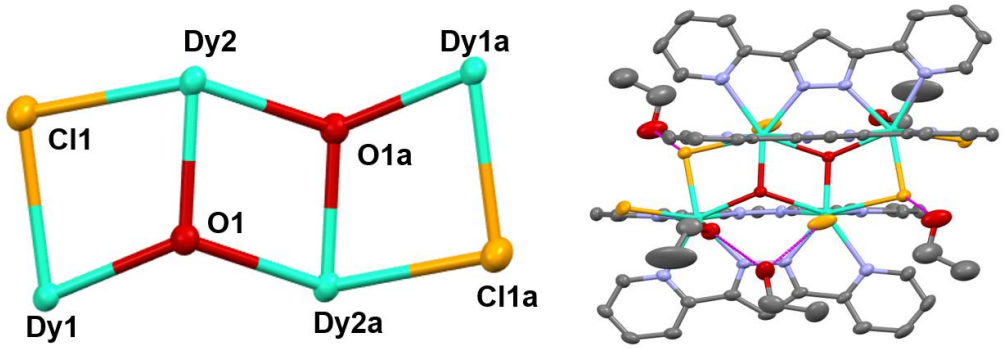

Figure 4.17. (left) The defect-dicubane central core of complex **Dy_4_Cl**, (right) Molecular structures of **Dy_4_Cl**. Hydrogen atoms are omitted for the sake of clarity. Colour code: Dy, green; O, red; N, purple; C, grey; Cl, orange. Hydrogen bonds are shown as violet dashed lines.

Continuous shape measures (CShM) reveal that the coordination geometries of the external Dy1 and internal Dy2 in the **Dy_4_Cl** molecule are both closest to SAPR-8 (square antiprism, D_{4d}), with the values of 1.370 and 1.522, respectively (Table 4.9 and S55). The intramolecular distances between metal centers are 3.819 Å for Dy2–Dy2a, 4.022 Å for Dy1–Dy2, and 7.269 Å for Dy1–Dy1a. The longer distances of Dy1–Dy2 and Dy1–Dy1a in **Dy_4_Cl** compared with that in **Dy_4_NO_3** (see Chapter 4.6) are a result from the aforementioned increased Dy1–O1–Dy2 angle. The closest intermolecular Dy···Dy distances is 9.482 Å.

Table 4.8. Selected bond lengths and bond angles in **Dy_4_Cl**.

Dy1 – Cl1	2.7658(9)	Dy2 – Dy2a	3.8195(3)
Dy1 – Cl3	2.6722(9)	Dy2 – Cl2	2.7018(9)
Dy1 – O1	2.399(2)	Dy2 – Cl1	2.7167(9)
Dy1 – O2	2.424(3)	Dy2 – O1	2.366(2)
Dy1 – N3a	2.381(9)	Dy2 – O1a	2.414(2)
Dy1 – N4a	2.545(9)	Dy2 – N1	2.678(3)
Dy1 – N5	2.675(2)	Dy2 – N2	2.410(3)
Dy1 – N6	2.412(9)	Dy2 – N7a	2.405(3)
Dy1 – O1 – Dy2	115.14(9)	Dy2 – N8a	2.666(3)
O1 – Dy1 – O2	72.73(9)	O1 – Dy2 – Cl2	109.00(6)
O1 – Dy1 – Cl1	74.42(6)	O1a – Dy2 – Cl2	74.00(6)
O1 – Dy1 – Cl3	126.26(6)	O1 – Dy2 – Cl1	75.88(6)
O2 – Dy1 – Cl1	115.26(8)	O1 – Dy2 – O1a	73.91(9)
O2 – Dy1 – Cl3	78.47(7)	N1 – Dy2 – Cl2	85.15(7)
N3a – Dy1 – N4a	63.79(10)	N1 – Dy2 – N2	62.96(9)
N5 – Dy1 – N6	64.41(9)	N1 – Dy2– Cl2	77.12(7)

Symmetry codes: [a]1-X,1-Y,1-Z

Table 4.9. Continuous Shape Measures for Dy^{III} ions in **Dy_4_Cl** showing the closest geometries.

	SAPR-8 (D_{4d})	**TDD-8 (D_{2d})**	**JBTPR-8 (C_{2v})**	**BTPR-8 (C_{2v})**
Dy1	**1.370**	2.122	3.768	2.670
Dy2	**1.522**	2.117	3.031	2.790

4.9 Magnetic behaviours of $Dy_4(bpp)_4(CH_3CH_2OH)_2(OH)_2Cl_6 \cdot 3CH_3CH_2OH$

Direct-current (DC) magnetic susceptibility measurements of **Dy_4_Cl** was performed on polycrystalline samples in the temperature range of 2.0 to 300 K under an external field of 1000 Oe. The experimental $\chi_M T$ value of 55.57 $cm^3mol^{-1}K$ for **Dy_4_Cl** at 300 K was close to the theoretical value of 56.68 $cm^3\ mol^{-1}\ K$ expected for four uncoupled Dy^{III} ions (Figure S33). Upon lowering the temperature, $\chi_M T$ value dropped steadily to reach a minimum of 21.64 $cm^3mol^{-1}K$ at 2.0 K.

Alternating current (AC) susceptibility measurements performed on **Dy_4_Cl** under zero field revealed a clear frequency-dependent out-of-phase susceptibility (χ_M'') signals (Figure 4.18), revealing the zero field SMM nature of **Dy_4_Cl**. The χ_M'' vs. frequency peaks were observed up to 20 K at the frequency of 787.5 Hz.

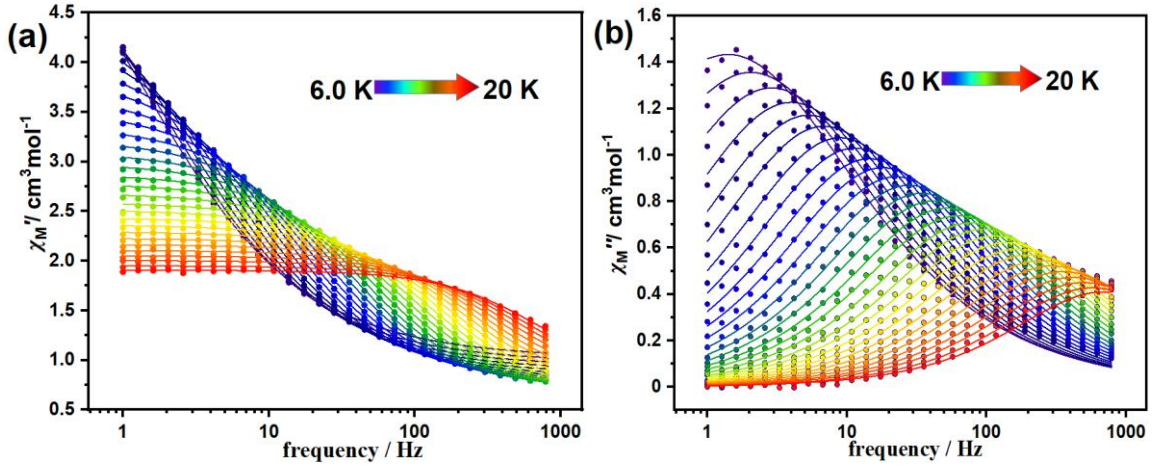

Figure 4.18. Frequency dependency of the in-phase (a) and out-of-phase (b) components of the magnetic susceptibility for **Dy_4_Cl** under zero field. The solid lines are the best fits to the generalized Debye model.

Similar to the case of **Dy_4_NO_3**, the Cole–Cole (χ_M'' vs. χ_M') diagram of **Dy_4_Cl** presented only one single relaxation as the plot at each temperature showed only one semicircle (Figure 4.19, a). The relaxation time (τ) at each measured temperature was calculated according to the generalized Debye model on the software CCFIT, with the detailed calculation results are given in Table S56. The α values showed a gradual decreasing trend from low temperatures to high temperatures, with the maximum 0.378 at 6.0 K and the minimum 0.180 at 19.5 K. The relatively large α values, plus the curvature in the relaxation time vs. temperature plot implied the coexistence of multiple processes. Equation 4.2 was used to fit the temperature dependent relaxation time (τ) plot for the Kramers Dy^{III} ions under zero field. The best fitting result was $\tau_0 = 1.77 \times 10^{-7}$s, U_{eff} = 156.6 K, C = $2.85 \times 10^{-3}\ s^{-1}\ K^{-n}$, n = 4.50. Both τ_0 and n are in the

reasonable range of SMMs.[174-176,189,190] No significant QTM was revealed by the fitting, in line with the observation that no plateau was present in Figure 4.19, b.

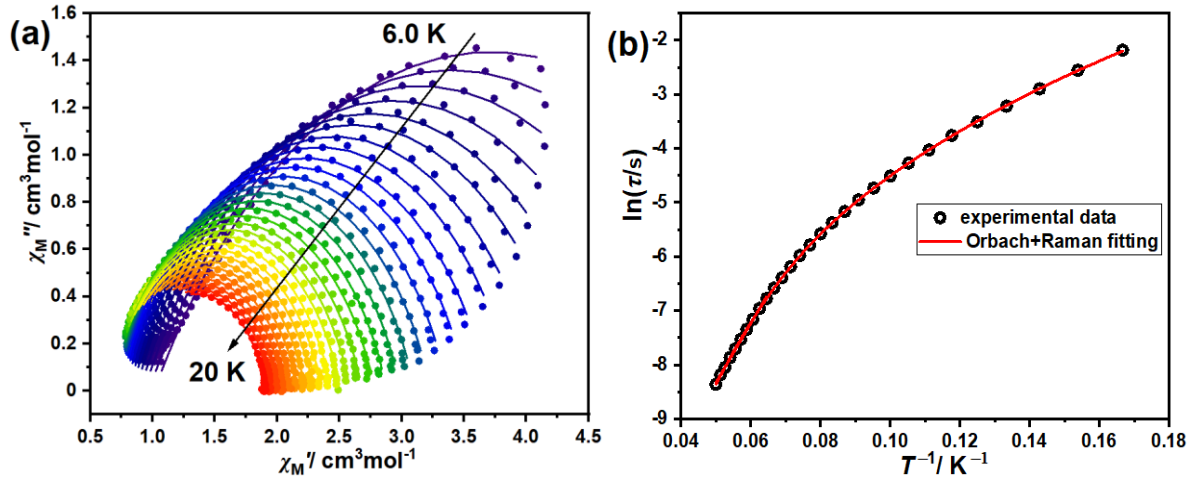

Figure 4.19. a, the Cole–Cole (χ_M'' vs. χ_M') diagram of **Dy_4_Cl** under zero field, the lines are the best fitting result to generalized Debye model; b, the temperature-dependent relaxation time and the corresponding best fitting results of **Dy_4_Cl**.

Concluding remarks

The aim of this thesis was to synthesize new lanthanide-based coordination compounds that exhibit photoluminescence and single-molecule magnet properties and understand the relationship between these physical properties and their molecular structures.

In Chapter 2, nineteen new trinuclear 3d–4f hybrid complexes were synthesized, including thirteen Ni–Ln–Ni complexes **Ln_1** (Ln = Y, Ce, Pr, Nd, Sm, Eu, Gd, Tb, Dy, Ho, Er, Tm, Yb), five Ni–Dy–Ni trinuclear complexes **Dy_2** – **Dy_6**, and one Zn–Dy–Zn complex **DyZn$_2$**. Due to the impact of counter-anions, complexes **Ln_1** and **Dy_2** were highly symmetric with Ln and Ni ions in linear arrangement, whereas complexes **Dy_3** – **Dy_6** were less symmetric and their ∠Ni–Dy–Ni slightly deviate from 180°.

Among all **Ln_1** synthesized, clear intramolecular ferromagnetic Ni–Ln couplings were observed in **Gd_1**, **Dy_1**, **Tb_1**, **Ho_1**, **Sm_1** and **Pr_1**. The oblate or prolate distribution of the electron density on the ground states and the ionic sizes of the Ln^{III} were the influencing factors on the nature of the Ni–Ln couplings. In terms of dynamic magnetism, both **Dy_1** and **Tb_1** exhibited non-zero χ_M'' signals under zero field, indicating the presence of slow magnetic relaxation. However, no χ_M'' peak was observed in the measurable frequency range for **Tb_1**, even under varying applied fields. The rest of **Ln_1** didn't exhibit χ_M'' signals different from zero. **Dy_1** – **Dy_6** are all SMMs, with moderate U_{eff} around 14 K under zero field. Comparative study on **Dy_1** and its isostructural zinc analogue **DyZn$_2$** showed the positive contribution of paramagnetic Ni^{II} to the SMM property by suppressing the fast QTM. The intramolecular ferromagnetic coupling, the uniaxial anisotropy of Ni^{II} and Dy^{III} and the colinear array of their easy axes were supposed to be the reasons for the positive contribution. The relaxation behaviours for **Dy_1** – **Dy_6** showed significant difference when optimal external fields are applied, which probably originates from the counter-anion related phonons among other factors. "Partial dilution" experiments on **1***, in which **Dy_1** molecules were dispersed in a diamagnetic **Y_1** matrix, revealed non-negligible influence of the intermolecular interaction, mediated by paramagnetic Ni^{II} ions in neighboring molecules, in accelerating the magnetic relaxation in **1***.

Sub-kelvin measurements using micro-SQUID revealed open hysteresis loops in **GdZn$_2$**, **Gd_1**, **Dy_1**, **Tb_1**, and **Ho_1**, closed hysteresis loops in **Y_1**, **Yb_1**, **Er_1**, **DyZn$_2$**, and **TbZn$_2$**. Compared to **GdZn$_2$**, where the hysteresis loops were waist-restricted, **Gd_1** exhibited significantly wider hysteresis loop openings, attributed to its "giant spin" behaviour generated by Ni–Gd ferromagnetic coupling. Likewise, the closed hysteresis loops in **DyZn$_2$** and **Y_1** corroborated the "giant spin" origin of SMM behaviours of **Dy_1** instead of the anisotropy of isolated metal centers. In **Yb_1** and **Er_1**, the prolate electron density of Yb^{III} and Er^{III} conflicts with their axial coordination geometry, hindering Ni–Ln ferromagnetic coupling while accelerating spin relaxation—explaining their closed hysteresis loops. Furthermore, **Gd_1** and **Dy_1** exhibited enhanced coercivity and remanence owing to

effective mitigation of zero-field QTM through the protected degeneracy of Kramers systems, as compared to the non-Kramers **Tb_1** and **Ho_1**.

The high symmetry in **Dy_1** simplified the scenarios of zero field splitting and the exchange coupling, facilitates the theoretical analysis. From the analysis, the relaxation pathways were determined to be through the excited exchange states involving both central Dy^{III} and terminal Ni^{II}. Theoretical calculations on different hypothetical scenarios revealed that though the Ni–Dy intramolecular coupling is beneficial as it suppresses the QTM, the low-lying excited states created by it acts as a limiting factor for the SMMs to reach high spin reversal energy. Magnifying the strength of Ni–Dy couplings and adjusting the axial zero field splitting parameter *D* of Ni ions may increase the reversal energy but the effect is limited. The most effective strategy is to ensure that the spins relax via high energy channels, e.g., the KDs of Dy^{III}, which requires a total suppression on the spin transition via the low-lying excited states. Minimizing the transverse CFPs of Dy^{III} and the rhombic zero field splitting parameter *E* of Ni^{II} are the possible means to achieve this goal. A review of previously reported Ni–Ln complexes further underscored the critical importance of precisely tuning the geometry of Ln^{III} ions to achieve high-performance Ni–Ln single-molecule magnets.

In Chapter 3, two sets of trinuclear heterometallic complexes, featuring one central Ln^{III} ion and two terminal divalent M^{II} ions were studied—set 1. $Ln(CoL)_2CF_3SO_3$ (**LnCo$_2$**, Ln = Y, Gd, Tb, Dy), $Ln(FeL)_2CF_3SO_3$ (**LnFe$_2$**, Ln = Y, Gd, Tb, Dy); set 2. $Ln(ZnL)_2CF_3SO_3$ (**LnZn$_2$**, Ln = Ce, Pr, Nd, Sm, Eu, Gd, Tb, Dy) and $Ln(MgL)_2CF_3SO_3$ (**LnMg$_2$**, Ln = Pr, Nd, Sm, Eu, Gd). All 21 heterometallic complexes retained the linear M–Ln–M structural configuration.

Ferromagnetic intramolecular Ln–Co couplings were revealed in **GdCo$_2$**, **TbCo$_2$** and **DyCo$_2$**. On the contrary, among all **LnFe$_2$** samples, only **GdFe$_2$** exhibited ferromagnetic intramolecular Gd–Fe coupling unambiguously. **YCo$_2$** was a field-induced SMM, with the magnetic relaxation governed by the Raman and direct processes. **GdCo$_2$**, **TbCo$_2$** and **DyCo$_2$**, on the other hand, showed slow relaxation of magnetization under zero field, though no peaks in the χ_M'' versus frequency plots were present within the range of measurement, indicating relatively fast QTM processes. Upon applying optimal external fields, temperature- dependent relaxation times were be extracted for **GdCo$_2$** and **TbCo$_2$** and the fitting results of them favored the relaxation via low-lying excited exchange states. As for **LnFe$_2$** complexes, none of them exhibited slow relaxation of magnetization under zero field and only **TbFe$_2$** exhibited that under applied fields.

Photoluminescence properties were collected on **LnZn$_2$** and **LnMg$_2$** on their solid-state samples. The energy of the triplet state in the ligand was calculated to be 19960 cm^{-1} in **GdMg$_2$**, and 18832 cm^{-1} in **GdZn$_2$** from the low temperature emission spectra of **GdMg$_2$** and **GdZn$_2$**, respectively. Characteristic visible light emissions from Ce^{III} and Sm^{III} and NIR emissions from Nd^{III} were detected at room temperature in the corresponding complexes, and their excitation spectra were similar with those of **GdMg$_2$** and **GdZn$_2$**, demonstrating the ability of H_3L ligand to sensitize luminescence in a wide range of lanthanide complexes via the antenna effect. In contrast, the excitation mechanisms in **EuZn$_2$** and **EuMg$_2$** were complicated due to the presence of LMCT process, which exhibited switchable roles at room temperature and low temperature.

In Chapter 4, three different kinds of lanthanide complexes $[Ln(Hbpp)_2(NO_3)_3]_2 \cdot 2CH_3CN$ (**Ln$_2$_MeCN**, Ln = Y, La, Ce, Pr, Nd, Sm, Eu, Gd, Tb, Dy, Ho), $Dy_4(bpp)_4(OH)_4(NO_3)_4 \cdot 2CH_3CH_2OH$ (**Dy$_4$_NO$_3$**), and $Dy_4(bpp)_4(CH_3CH_2OH)_2(OH)_2Cl_6 \cdot 3CH_3CH_2OH$ (**Dy$_4$_Cl**) were synthesized and structurally characterized, where Hbpp standed for the organic ligand 3(5)-Pyridine-1*H*-pyrazole. **Ln$_2$_MeCN** contains two $[Ln(Hbpp)_2(NO_3)_3]$ mononuclear motifs with slight structural differences, which were bound together by hydrogen bonds.

The triplet state energy (E_T) of Hbpp ligand was determined to be 22321 cm^{-1} from the zero-phonon line of the emission spectrum corresponding to the **Gd$_2$_MeCN** complex at low temperature. The determined E_T was higher than the energies of the emitting levels of Ce^{III}, Nd^{III}, Sm^{III}, Eu^{III}, Tb^{III}, and Dy^{III}. As a consequence, ligand-sensitized f–f emissions were observed in **Sm$_2$_MeCN**, **Nd$_2$_MeCN**, **Eu$_2$_MeCN**, **Tb$_2$_MeCN**, and **Dy$_2$_MeCN** spanning both visible and NIR regions, along with 5d–4f emission in **Ce$_2$_MeCN**.

Dy$_2$_MeCN was a field-induced SMM with the optimal external field being 1000 Oe. The energy diagram of the M_J sublevels of the $^6H_{15/2}$ ground state derived from the fine structures of low temperature solid-state luminescence spectrum matched well with theoretical results from *ab initio* calculation. Meanwhile, the energy of the first excited Kramer doublets obtained from both methods were close to the Orbach energy barrier (39.0 K) extracted from AC measurements under the optimal magnetic field, confirming that the spin relaxation occurred via the first excited Kramer doublets.

Dy$_4$_NO$_3$ and **Dy$_4$_Cl** both featured a $[Dy_4(\mu_3\text{-}OH)_2(\mu_2\text{-}X)_2]$ core, where $X = OH^-$ in **Dy$_4$_NO$_3$** and Cl^- in **Dy$_4$_Cl**. They were revealed to be zero field SMMs with the energy barrier of 96.0 K and 156.6 K, respectively. CASSCF calculations suggested that the zero-field SMM behaviour and the significantly higher spin-reversal energy barrier in **Dy$_4$_NO$_3$**, compared to **Dy$_2$_MeCN**, originated from the μ_2-OH anions. These bridging anions created relatively stronger coordination fields around Dy^{III} ions in **Dy$_4$_NO$_3$**, leading to enhanced magnetic anisotropy.

Overall, the optical and magnetic measurements on the newly synthesized lanthanide complexes contributed to a comprehensive understanding of the photoluminescence and the slow magnetic relaxation properties in 3d–4f and pure 4f complexes. The influencing factors on SMMs behaviour, including the crystal field, intra- and intermolecular interactions were extensively explored by comparative studies. Together with theoretical calculations, the present work highlighted the necessity to suppress magnetic relaxations via low-lying exchange states, in the pursuit for high-barrier 3d–4f SMMs. Both the tripodal Schiff base ligand H_3L and the pyrazole-based ligand Hbpp were demonstrated to sensitize f–f emissions spanning both visible and NIR regions, along with 5d–4f emissions in cerium complexes, via the antenna effects. Furthermore, the luminescent field-induced SMM **Dy$_2$_MeCN** demonstrated the utility of optical probes in deciphering spin relaxation pathways in lanthanide-based SMM systems.

Appendix

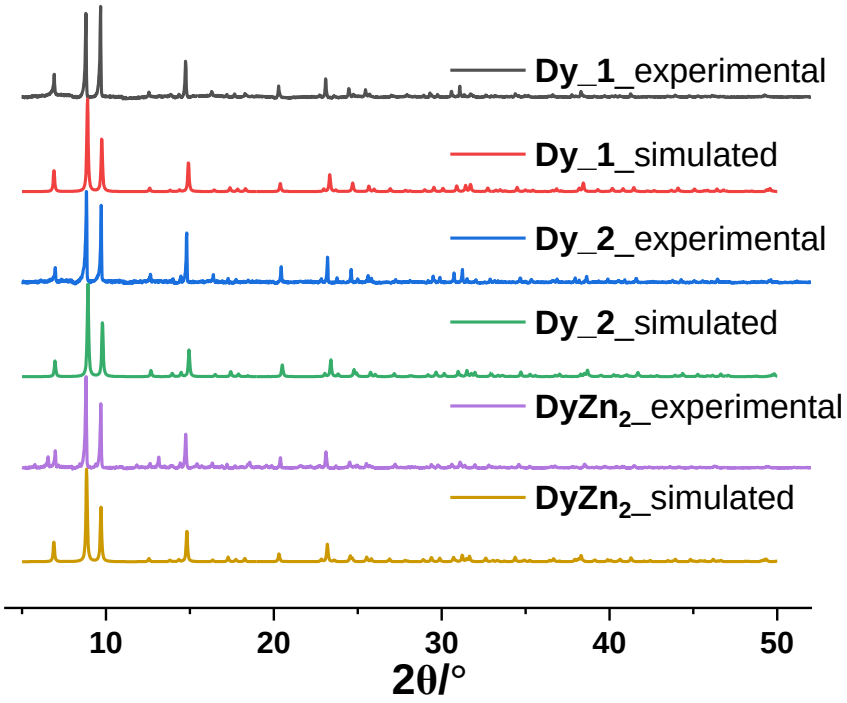

Figure S1. The experimental and simulated powder X-ray diffraction patterns of **Dy_1**, **Dy_2**, and **DyZn2**.

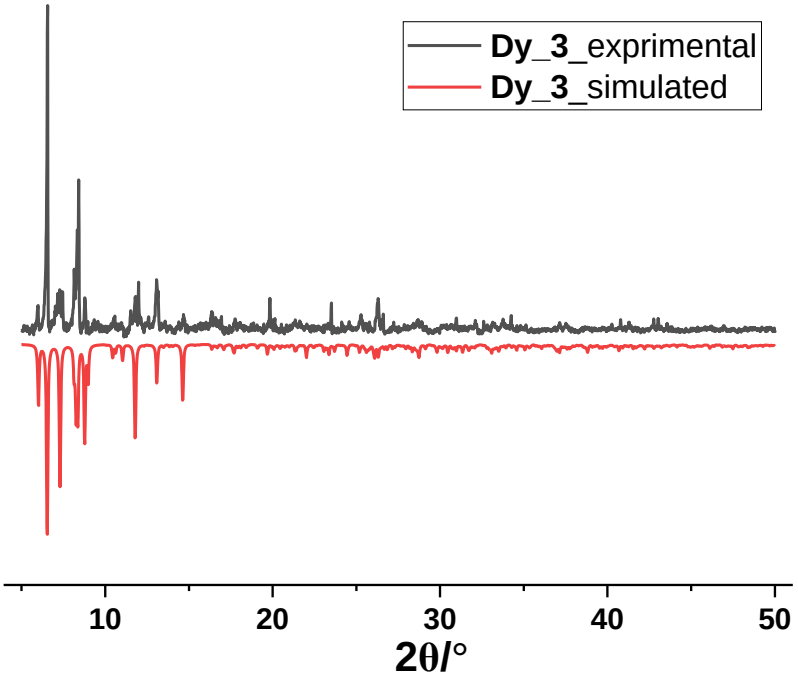

Figure S2. The experimental and simulated powder X-ray diffraction patterns of **Dy_3**.

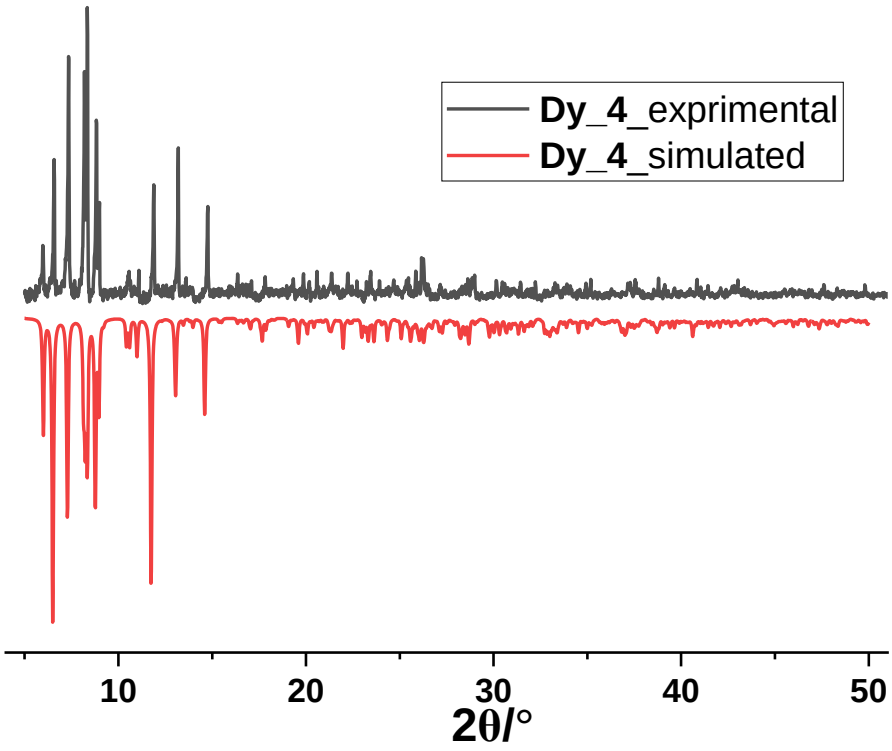

Figure S3. The experimental and simulated powder X-ray diffraction patterns of **Dy_4**.

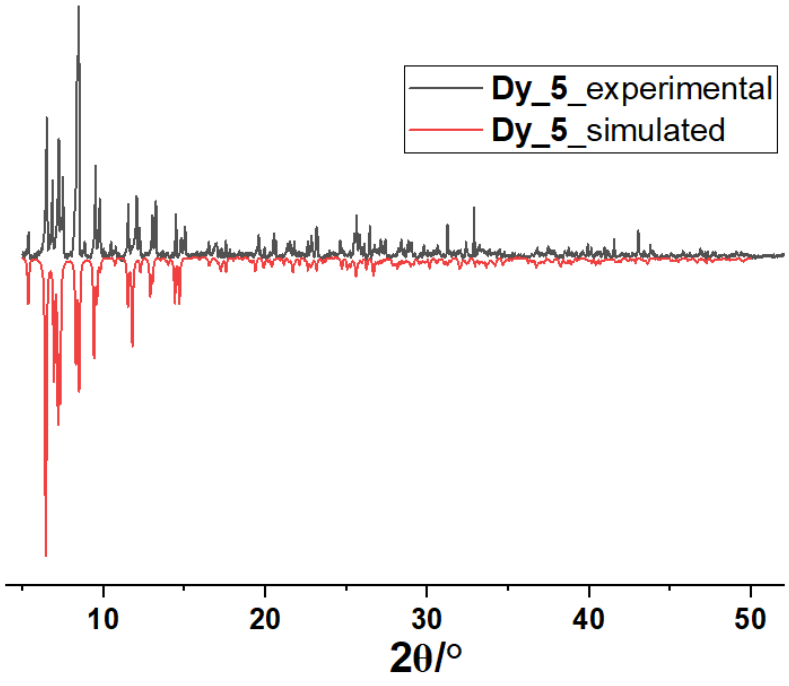

Figure S4. The experimental and simulated powder X-ray diffraction patterns of **Dy_5**.

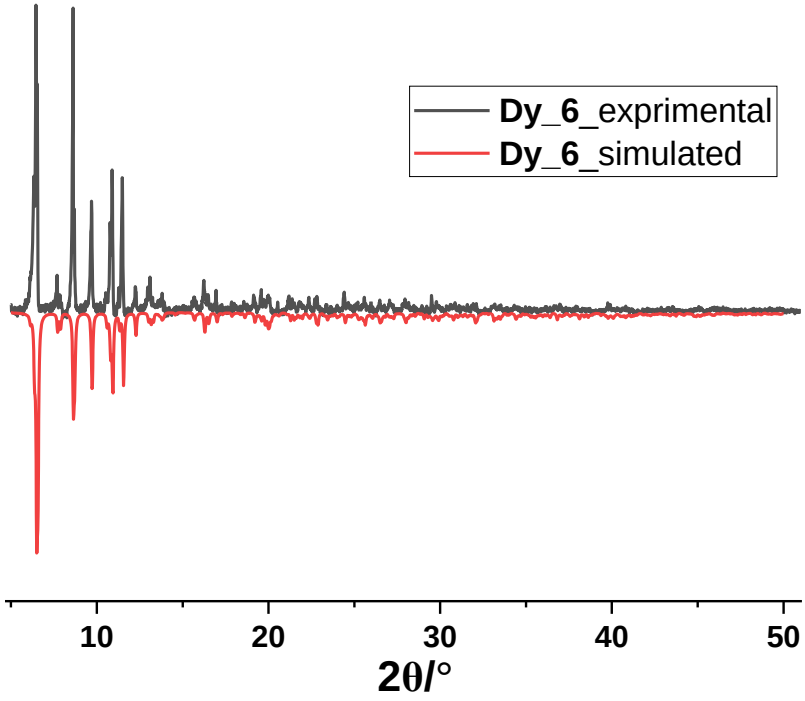

Figure S5. The experimental and simulated powder X-ray diffraction patterns of **Dy_6**.

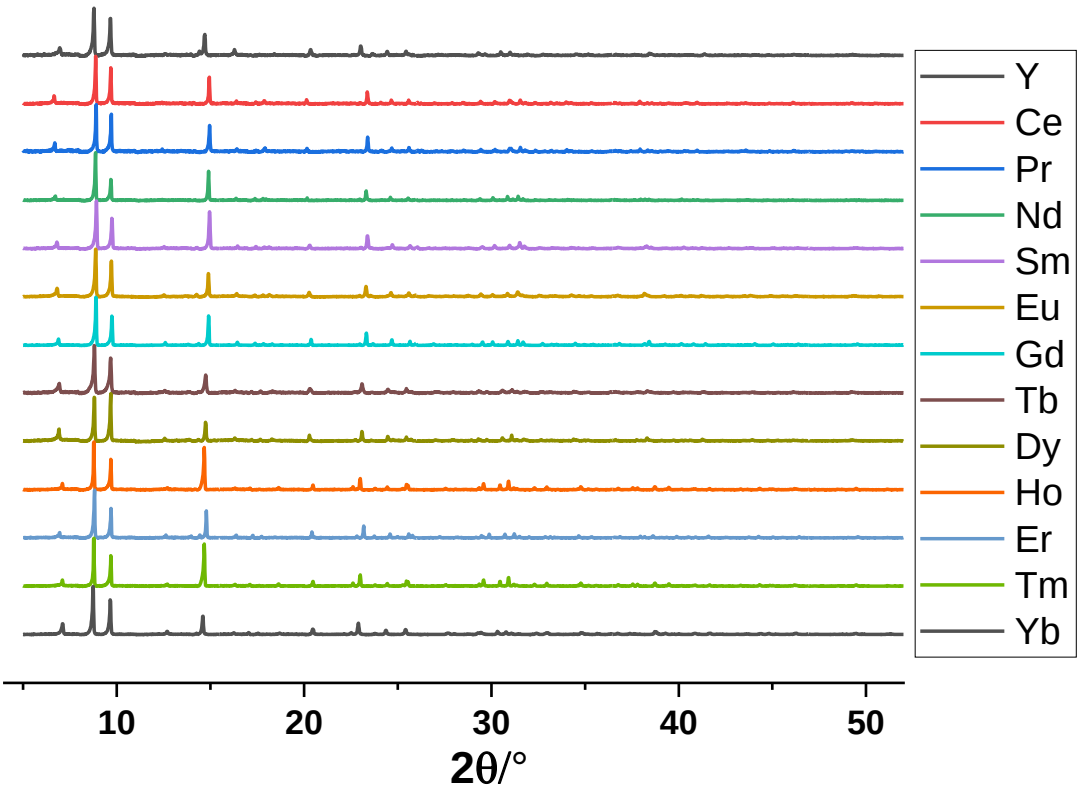

Figure S6. The experimental powder X-ray diffraction patterns of **Ln_1**.

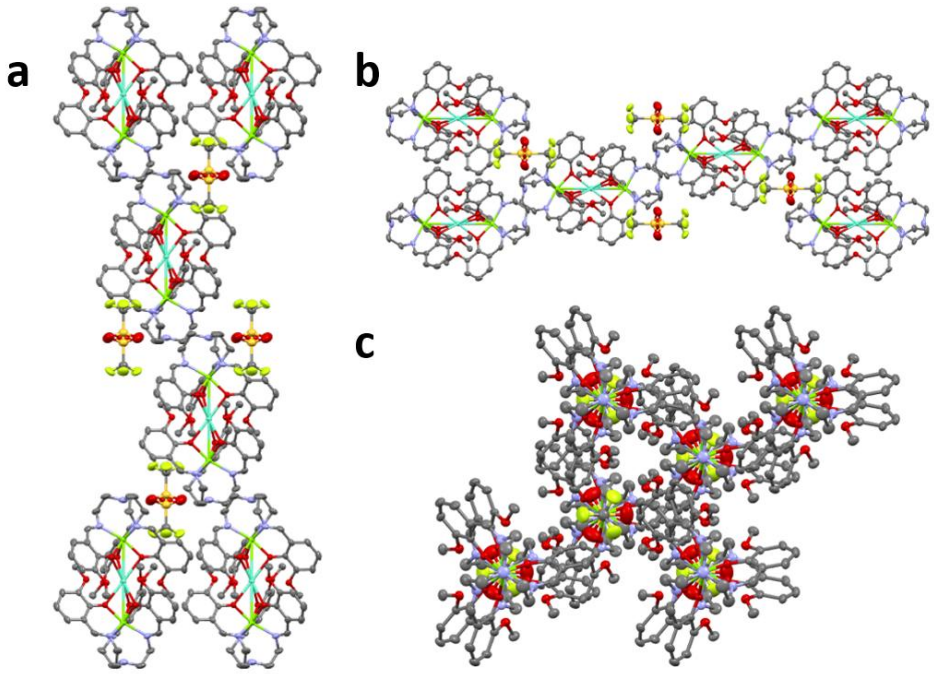

Figure S7. The packing diagram of **Dy_1** along the directions of *a*, *b*, *c* axes.

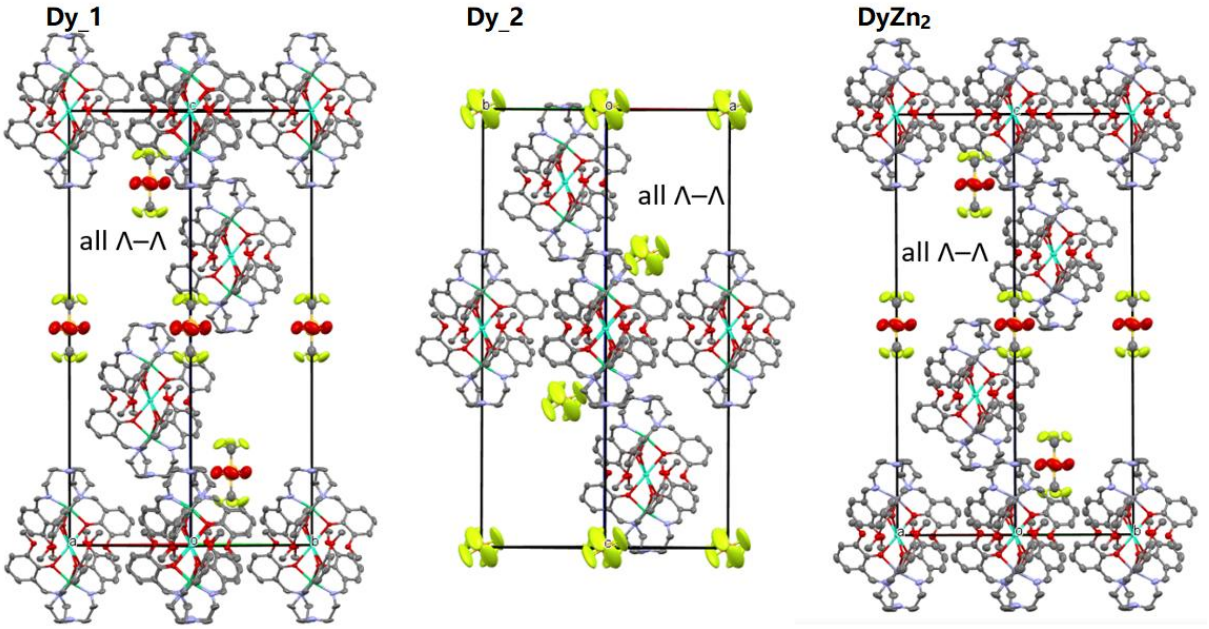

Figure S8. Unit cells of complexes **Dy_1**, **Dy_2**, and **DyZn2**, with the labels of molecular chirality. Black frames are the cell axes.

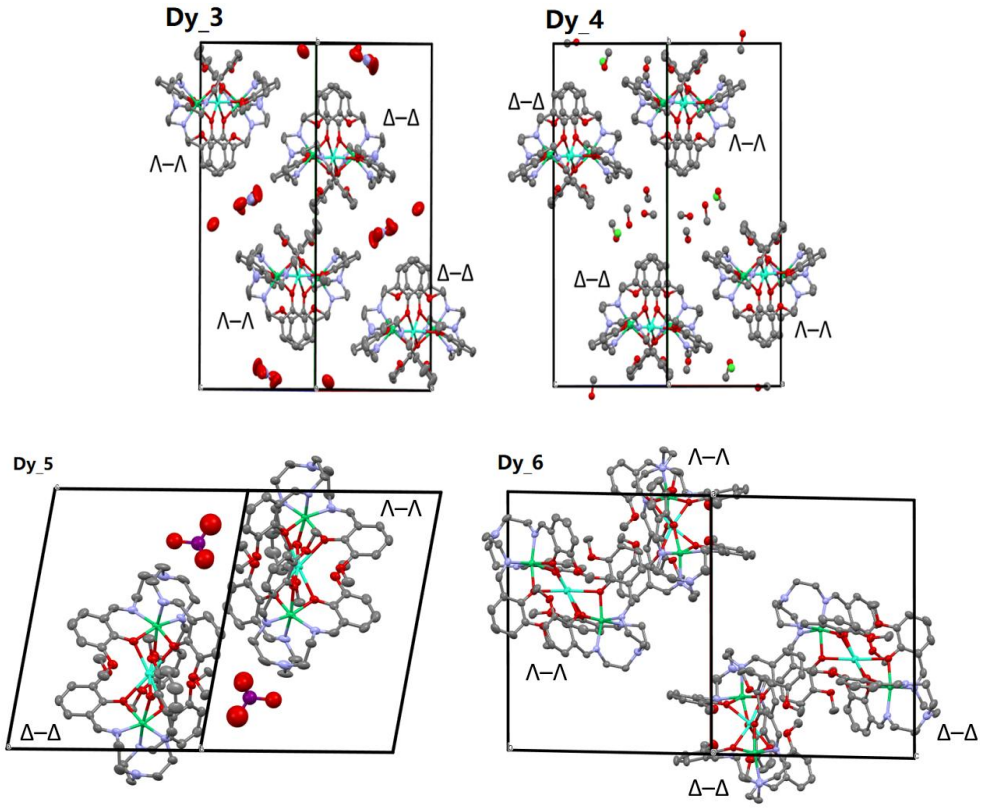

Figure S9. Unit cells of complexes **Dy_3** – **Dy_6**, with the labels of molecular chirality. Black frames are the cell axes. The bulky BPh_4^- anions and the methanol molecules are removed for **Dy_6** for a clear vision of the arrangement of the $[Dy(NiL)_2]^+$ cations.

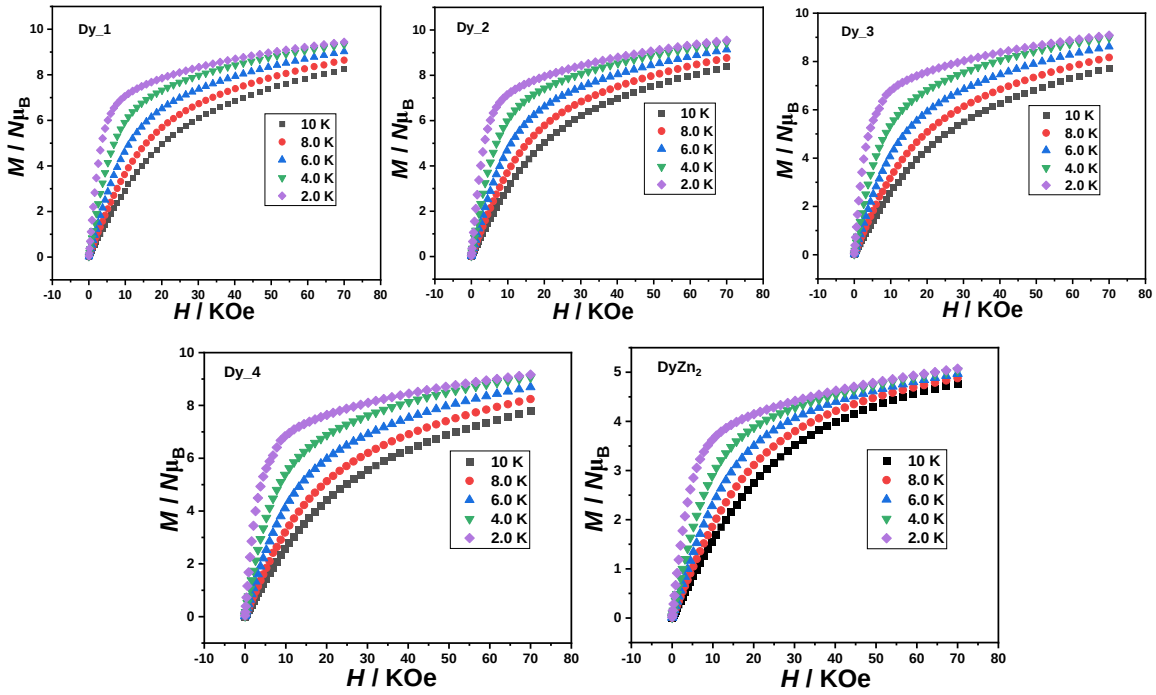

Figure S10. Field dependence of the magnetization for complexes **Dy_1** – **Dy_4** and **DyZn2** at 10, 8.0, 6.0, 4.0, 2.0 K.

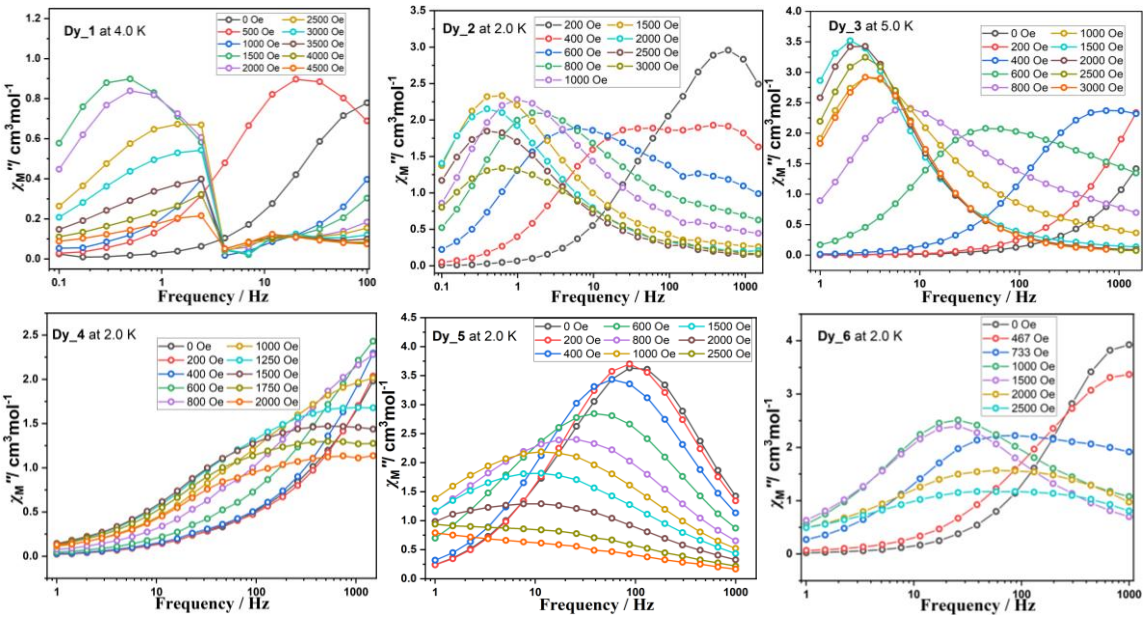

Figure S11. The out-of-phase susceptibility (χ_M'') versus frequency plot for **Dy_1** – **Dy_6** under different external fields. The data for **Dy_1** is collected at 4.0 K, for **Dy_3** at 5.0 K, for the rest at 2.0 K. The lines are guides for the eye.

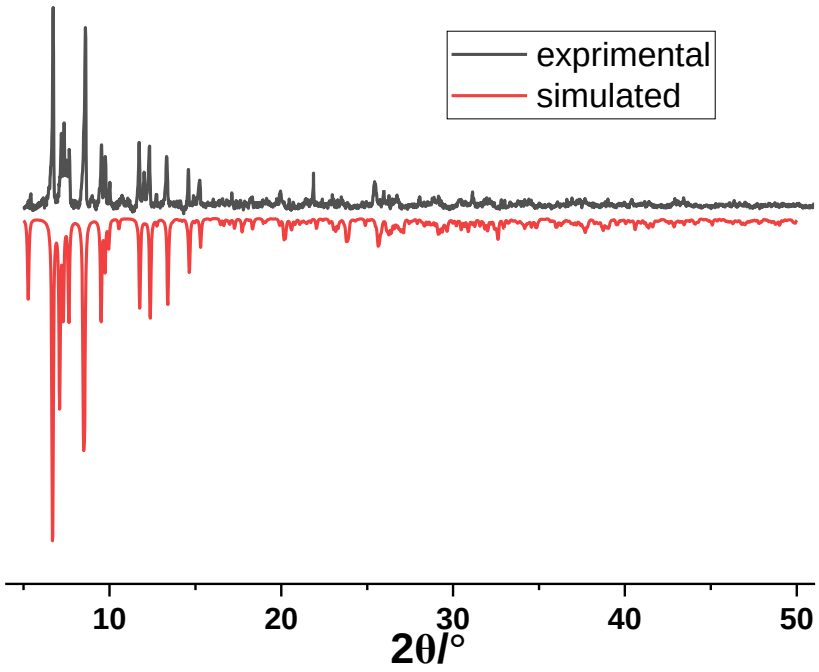

Figure S12. The experimental and simulated powder X-ray diffraction patterns of $[Dy(NiL)_2]NO_3 \cdot 3H_2O$.

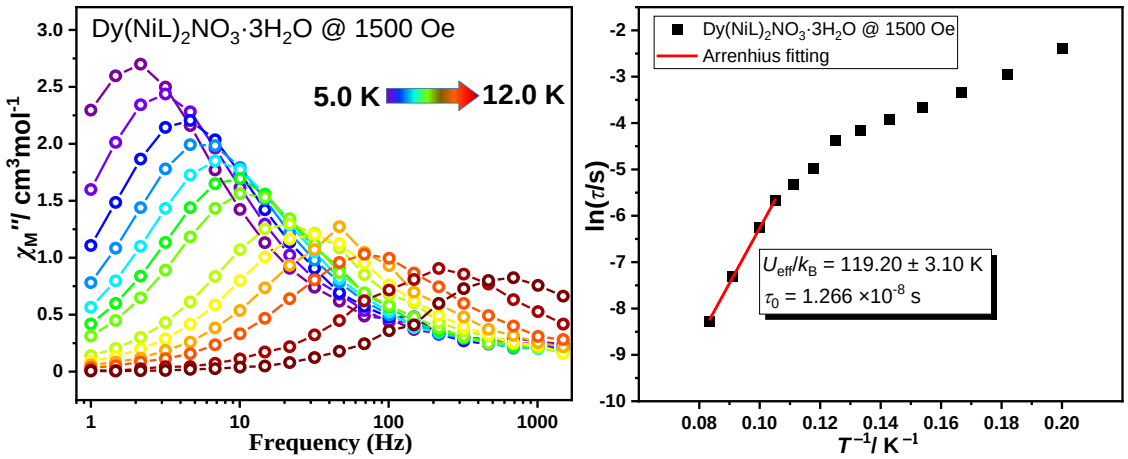

Figure S13. Left, temperature dependence of χ_M'' under optimal fields for complex $Dy(NiL)_2NO_3{\cdot}3H_2O$. The lines are a guide for the eye. Right, ln (τ) versus T^{-1} plot for $Dy(NiL)_2NO_3{\cdot}3H_2O$ under optimal fields, the red line is the linear fitting result.

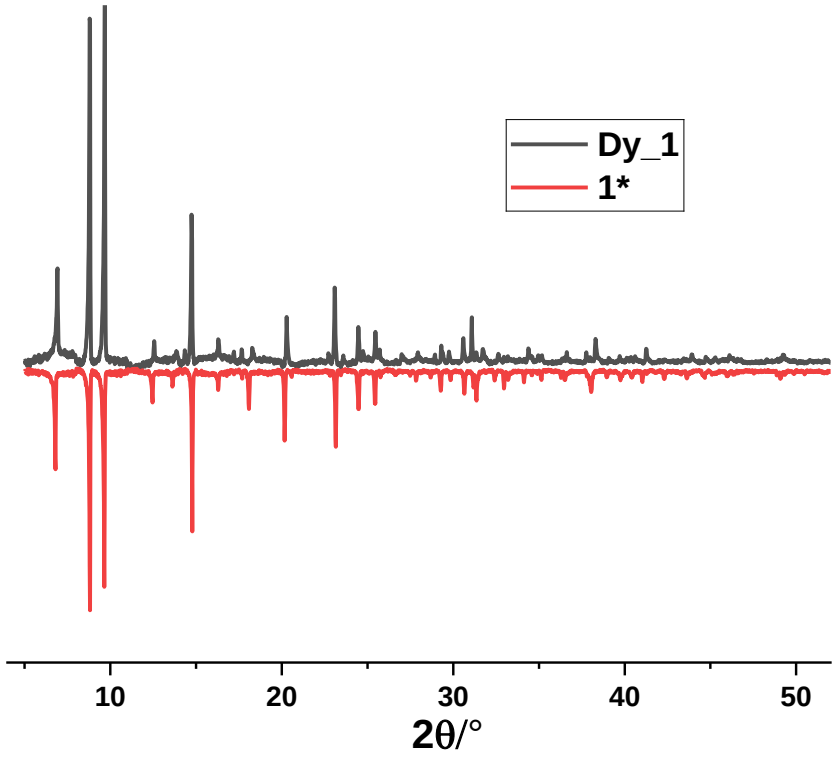

Figure S14. The experimental powder X-ray diffraction patterns of **Dy_1** and **1***.

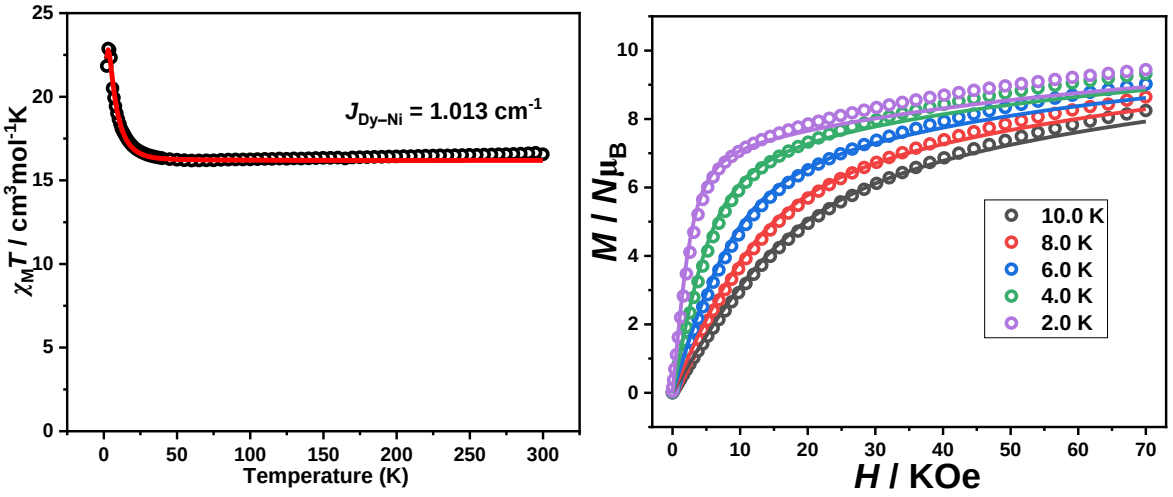

Figure S15. The experimental data (circles) and the fitting results (solid lines) of the $\chi_M T$ *versus* T plot (left) and the M *versus* H plots at varied temperatures (right) for **Dy_1**.

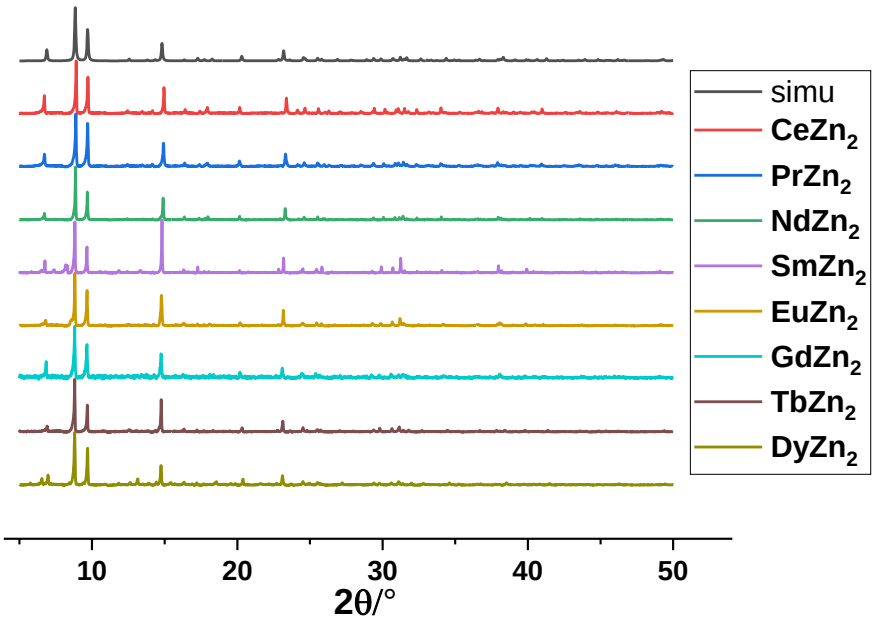

Figure S16. The experimental powder X-ray diffraction patterns of **LnZn2** (Ln = Ce, Pr, Nd, Sm, Eu, Gd, Tb, Dy) and simulated powder X-ray diffraction patterns of **DyZn2**.

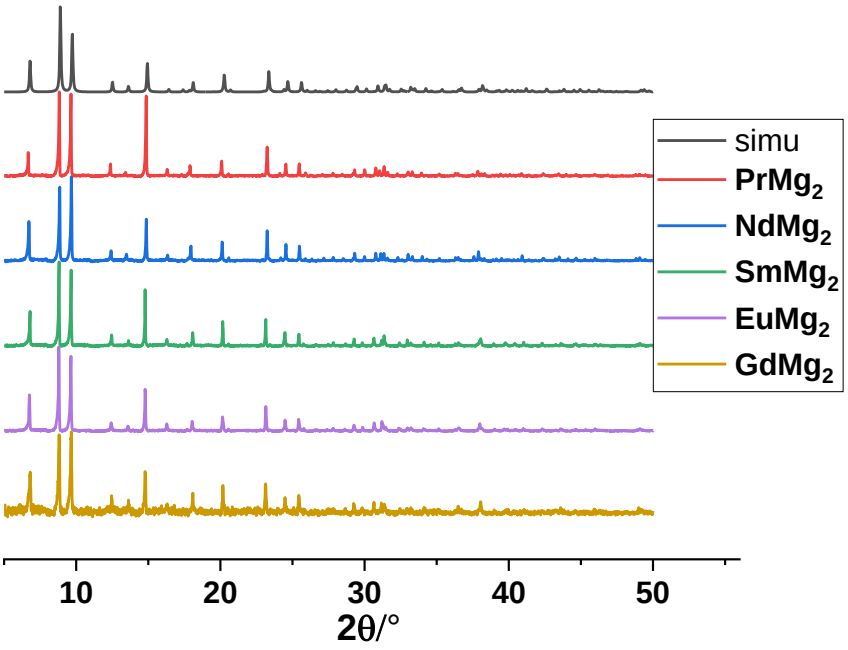

Figure S17. The experimental powder X-ray diffraction patterns of **$LnMg_2$** (Ln = Pr, Nd, Sm, Eu, Gd) and simulated powder X-ray diffraction patterns of **$EuMg_2$**.

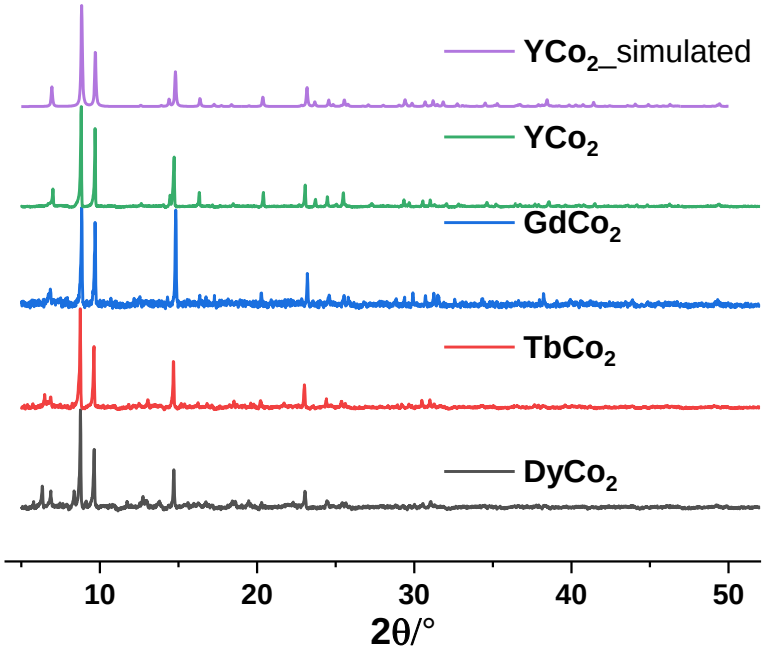

Figure S18. The experimental powder X-ray diffraction patterns of **$LnCo_2$** (Ln = Y, Gd, Tb, Dy) and simulated powder X-ray diffraction patterns of **YCo_2**.

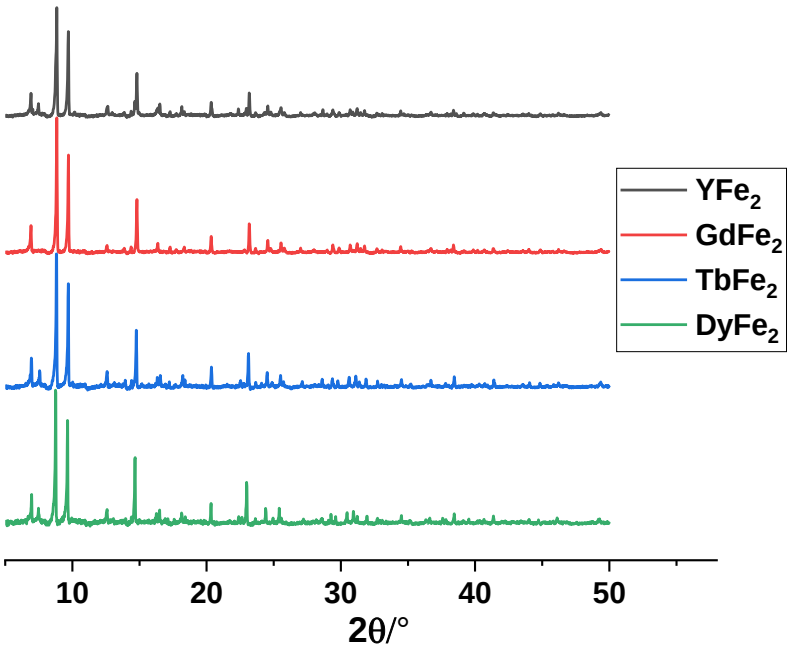

Figure S19. The experimental powder X-ray diffraction patterns of **LnFe2** (Ln = Y, Gd, Tb, Dy).

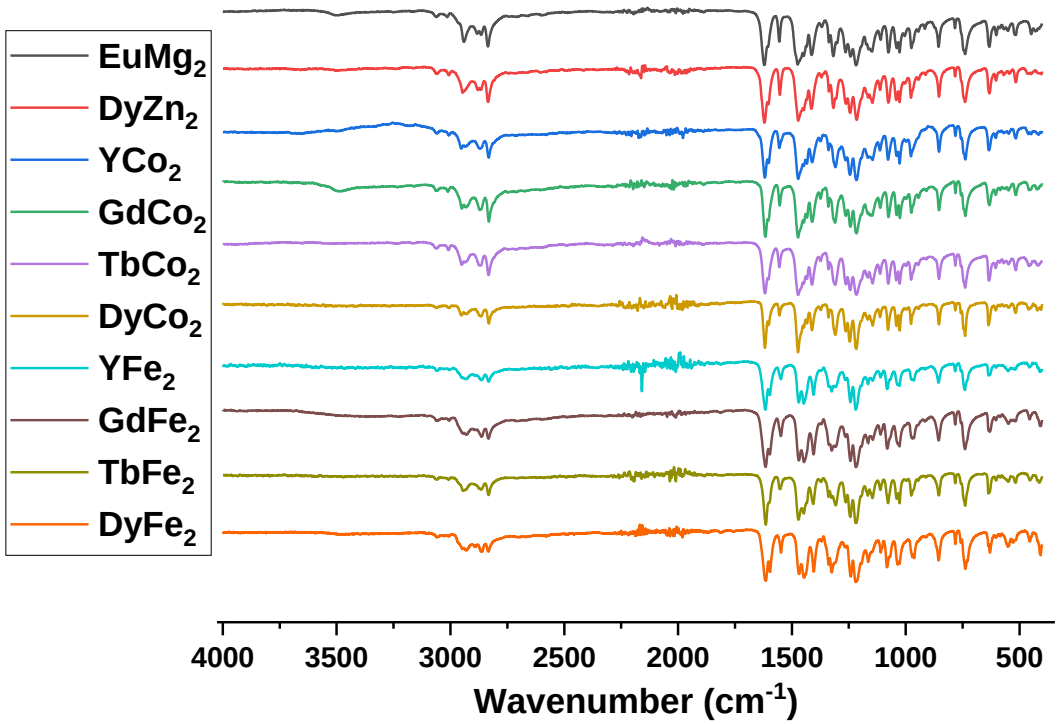

Figure S20. The FT-IR (ATR) spectra of **EuMg2**, **DyZn2**, **LnCo2**, and **LnFe2** (Ln = Y, Gd, Tb, Dy)

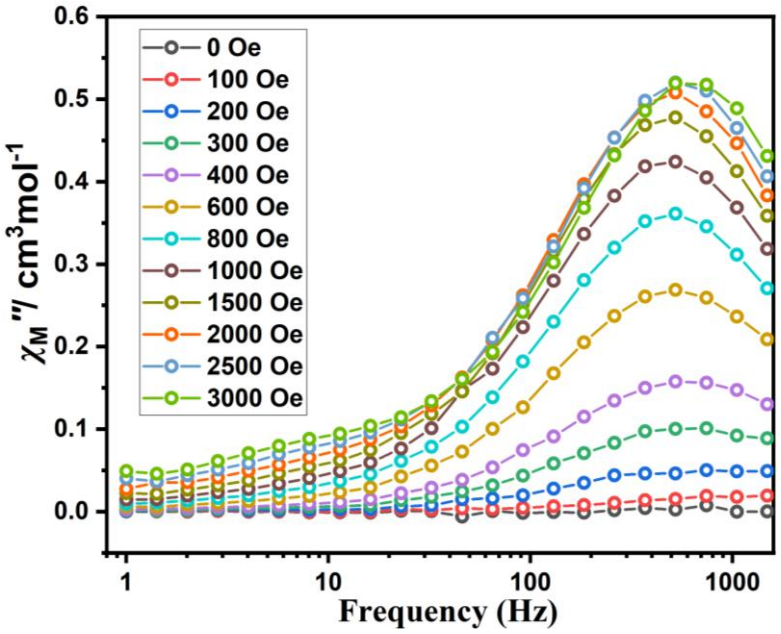

Figure S21. The out-of-phase susceptibility (χ_M'') versus frequency plot for **YCo$_2$** under different external fields. The lines are guides for the eye.

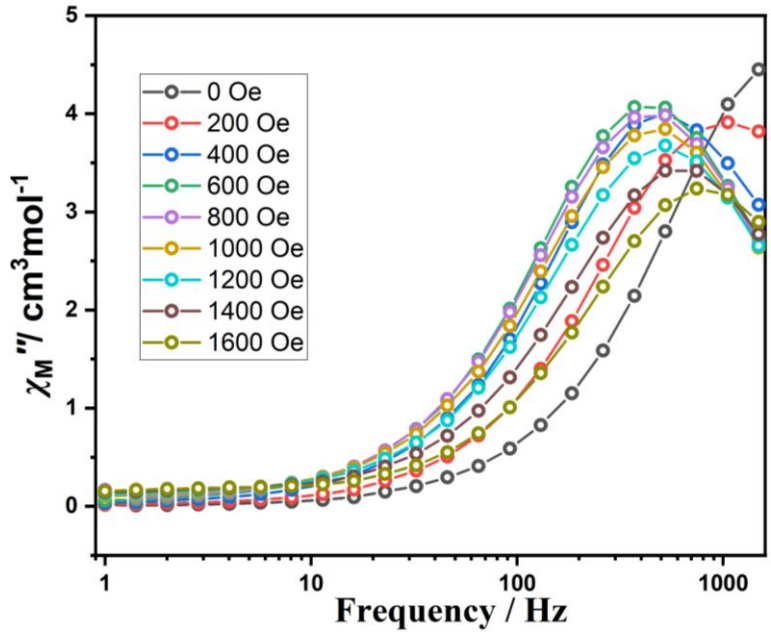

Figure S22. The out-of-phase susceptibility (χ_M'') versus frequency plot for **GdCo$_2$** under different external fields. The lines are guides for the eye.

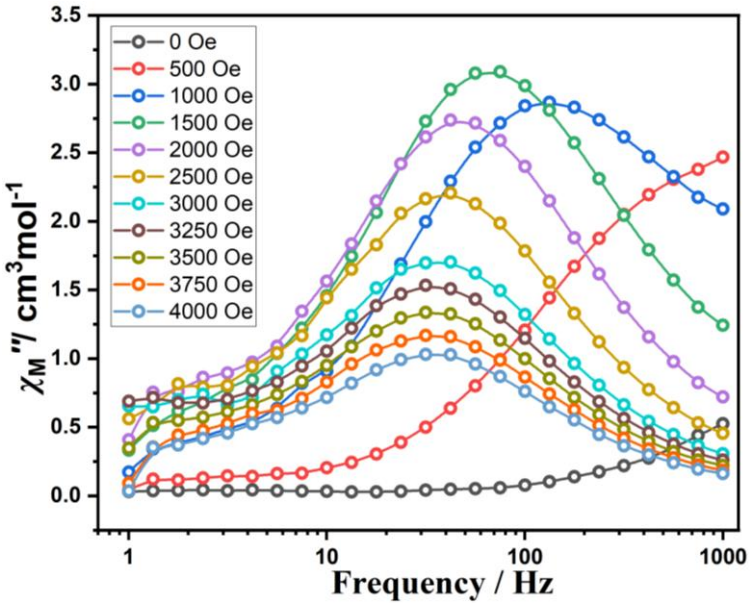

Figure S23. The out-of-phase susceptibility (χ_M'') versus frequency plot for **$TbCo_2$** under different external fields. The lines are guides for the eye.

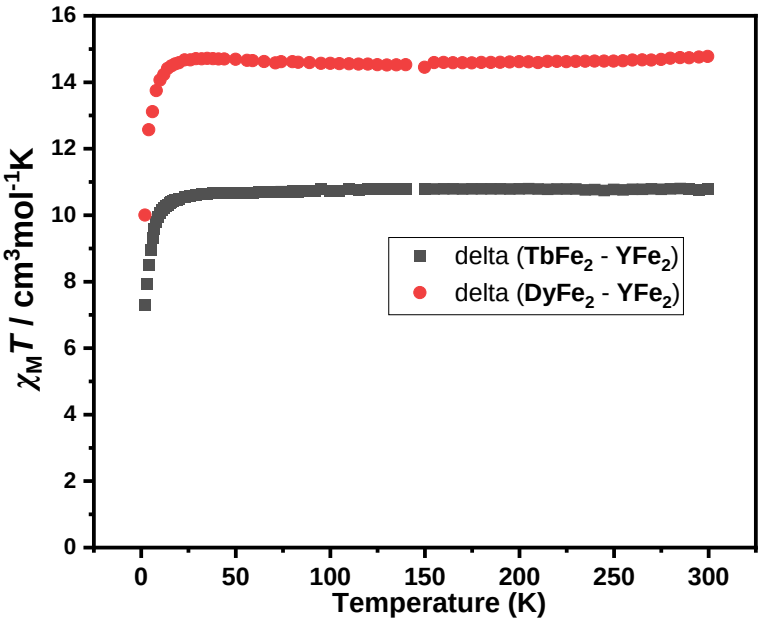

Figure S24. Temperature dependent differences in $\chi_M T$ between **$TbFe_2$** and **YFe_2**, **$DyFe_2$** and **YFe_2**.

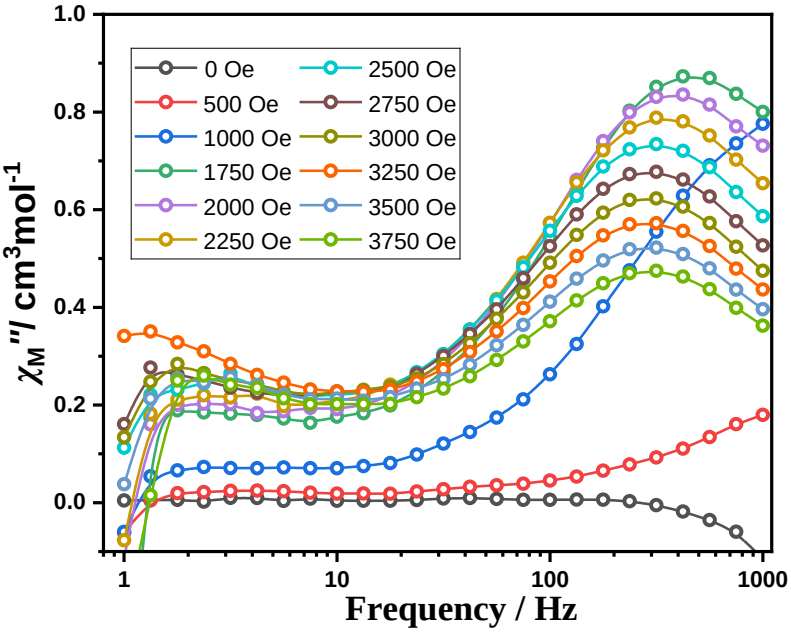

Figure S25. The out-of-phase susceptibility (χ_M'') versus frequency plot for **$TbFe_2$** under different external fields. The lines are guides for the eye.

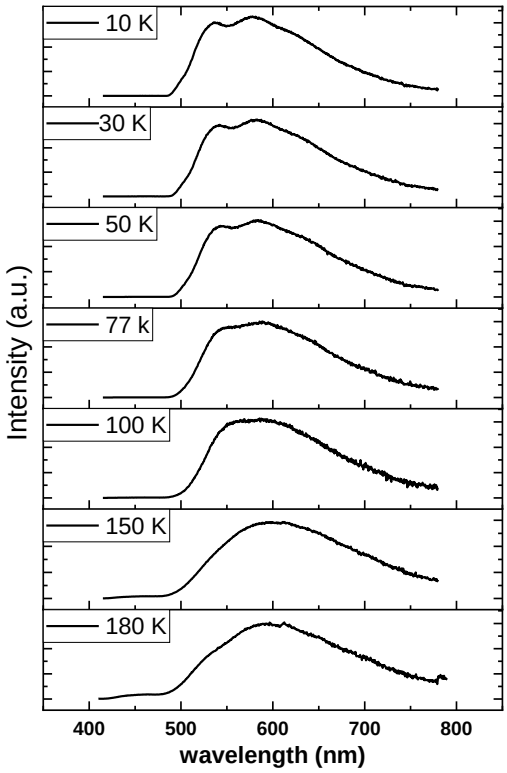

Figure S26. Emission spectra of **$CeZn_2$** ($\lambda_{ex.}$ = 400 nm) at different temperatures.

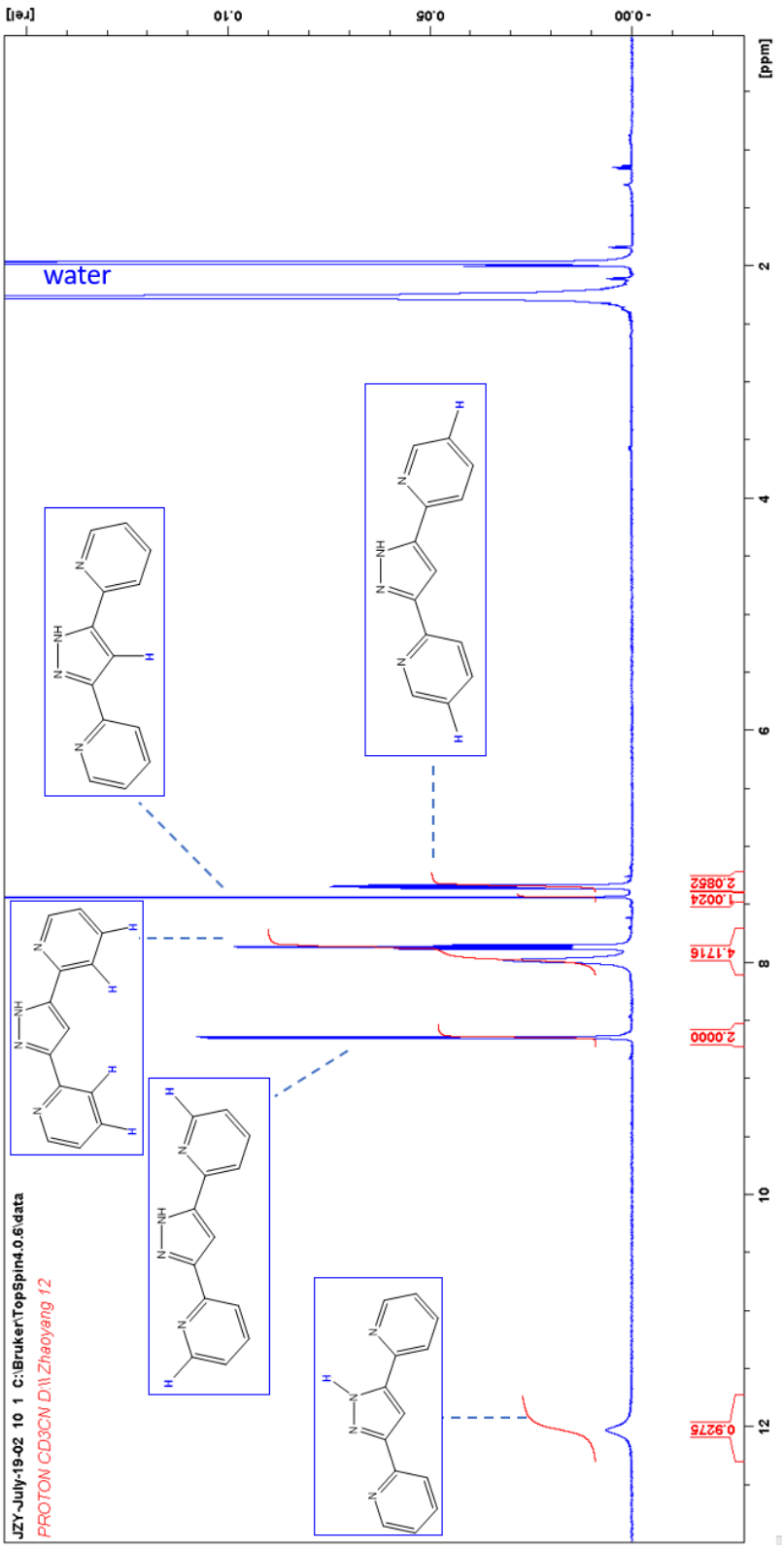

Figure S27. NMR spectrum of Hbpp ligand measured in MeCD solution.

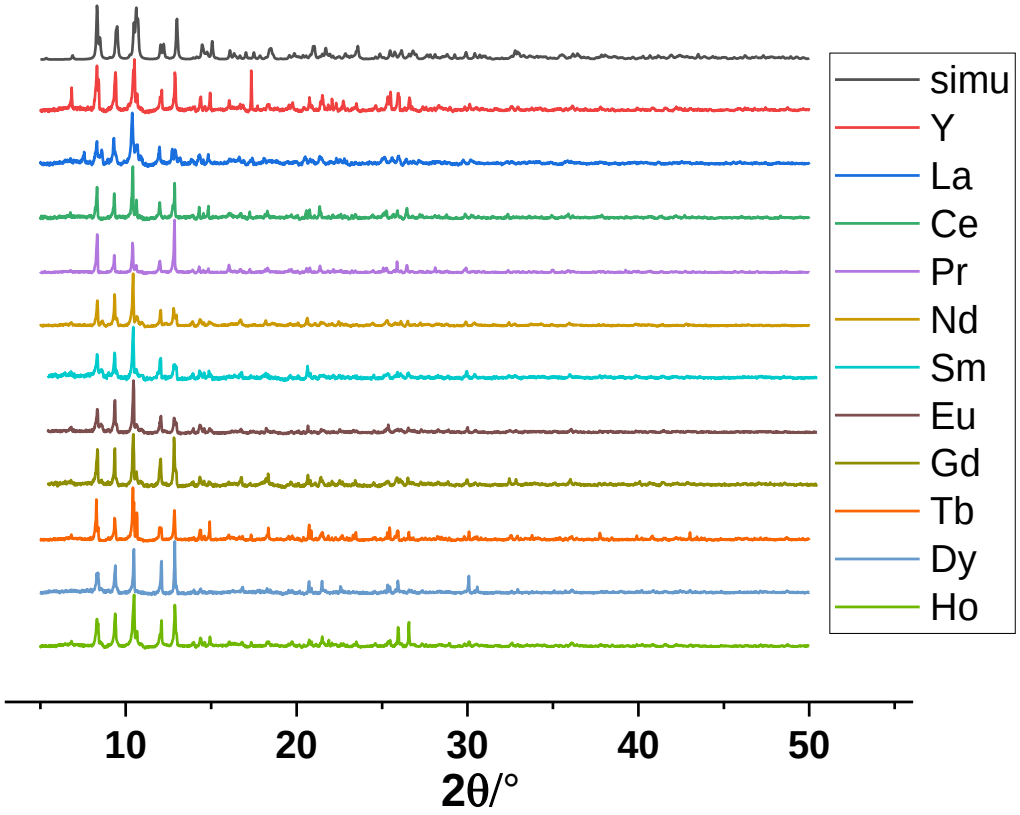

Figure S28. The experimental powder X-ray diffraction patterns of **Ln_2_MeCN** (Ln = Y, La, Ce, Pr, Nd, Sm, Eu, Gd, Tb, Dy, Ho) and simulated powder X-ray diffraction patterns of **Dy_2_MeCN**.

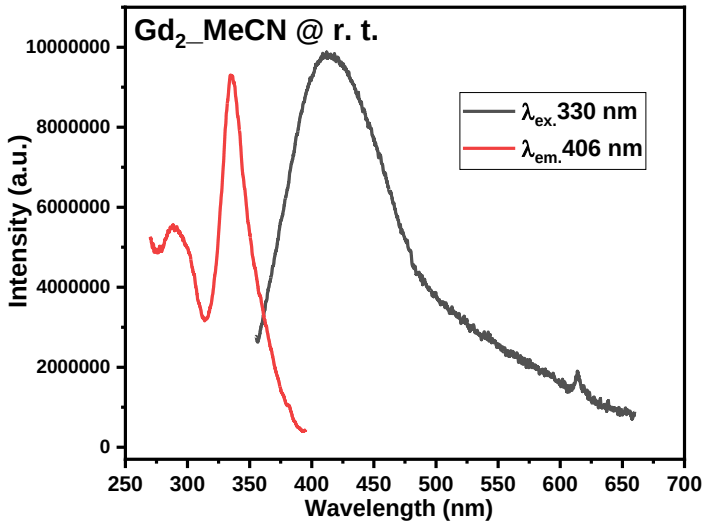

Figure S29. Emission and excitation spectra of **Gd_2_MeCN** ($\lambda_{ex.}$ = 330 nm, $\lambda_{em.}$ = 406 nm) at room temperature.

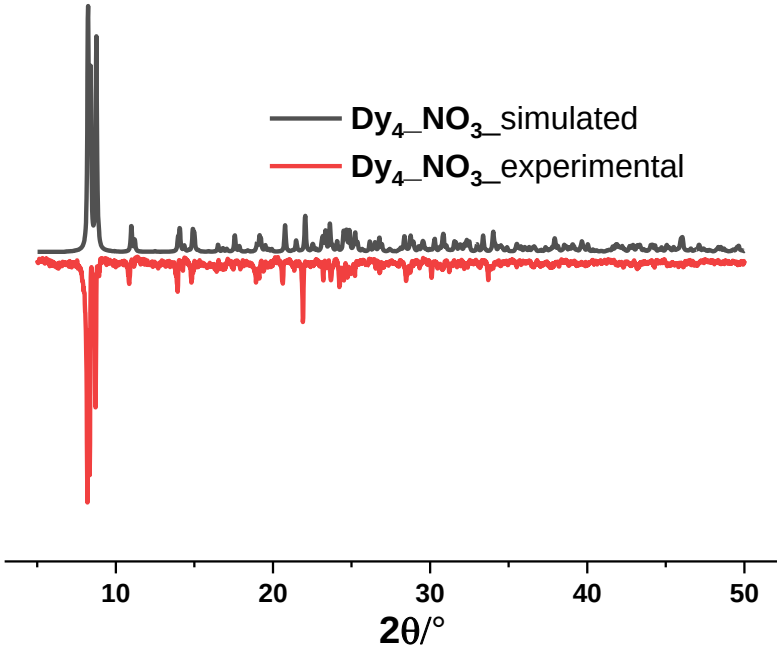

Figure S30. The experimental and simulated powder X-ray diffraction patterns of **Dy_4_NO_3**.

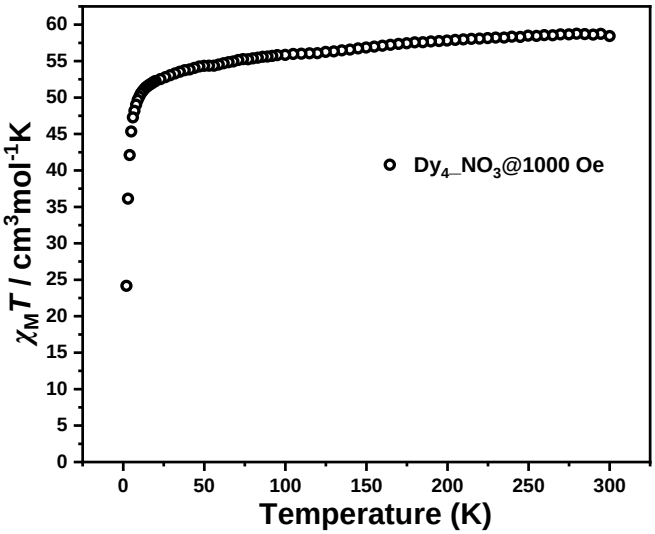

Figure S31. $\chi_M T$ versus T plots for **Dy_4_NO_3** under an applied field of 1000 Oe.

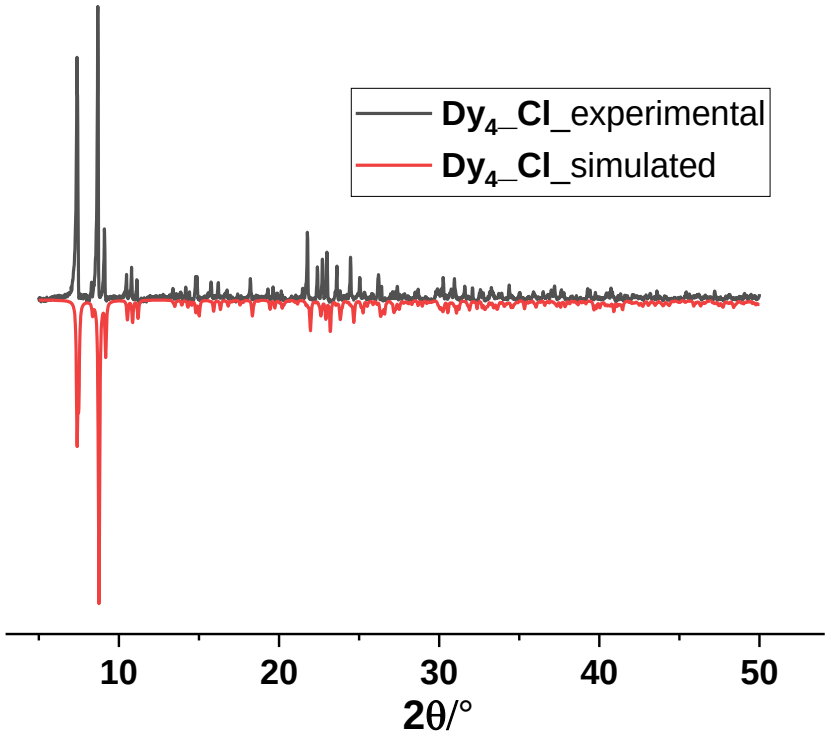

Figure S32. The experimental and simulated powder X-ray diffraction patterns of **Dy$_4$_Cl**.

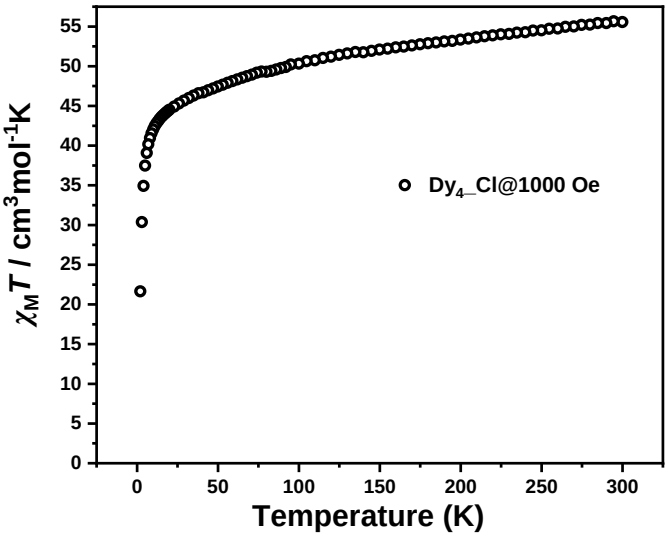

Figure S33. $\chi_M T$ versus T plots for **Dy$_4$_Cl** under an applied field of 1000 Oe.

Table S1. Crystal Data and Structure Refinements for **Dy_1**, **Dy_2**, and **$DyZn_2$**.

Complex	**Dy_1**	**Dy_2**	**$DyZn_2$**
Formula	$C_{61}H_{66}DyF_3N_8Ni_2O_{15}S$	$C_{60}H_{66}DyF_6N_8Ni_2O_{12}P$	$C_{61}H_{66}DyF_3N_8Zn_2O_{15}S$
Fw	1520.19	1516.09	1533.51
Temp (K)	200.0	180.0	200.0
Crystal system	Trigonal	trigonal	trigonal
Space group	*R*32	*R*32	*R*32
a (Å)	11.8738(4)	11.8444(2)	11.9481(3)
b (Å)	11.8738(4)	11.8444(2)	11.9481(3)
c (Å)	38.4123(15)	38.0606(9)	38.4497(11)
α (°)	90	90	90
β (°)	90	90	90
γ (°)	120	120	120
Volume ($Å^3$)	4690.1(4)	4624.15(19)	4753.6(3)
Z	3	3	3
D_{calc} (g cm^{-3})	1.615	1.633	1.607
μ (mm^{-1})	10.034	10.317	7.268
F (000)	2319.0	2307.0	2331.0
R_{int}	0.0494	0.0413	0.0453
R_{sigma}	0.0308	0.0166	0.0150
Refl. (all)	19127	19906	30498
Refl (independent)	2541	2585	30498
R_1 (all)	0.0435	0.0388	0.312
R_1 (> 2σ)	0.0394	0.0388	0.311
wR_2 (all)	0.0988	0.1010	0.0847
wR_2 (> 2σ)	0.0968	0.1010	0.0845
Flack parameter	0.493(7)	0.495(6)	0.390(5)
GOF.	0.994	1.047	1.068

$$R_1 = \sum\big||F_o| - |F_c|\big| / \sum|F_o|,\ wR_2 = [\sum w(F_o^2 - F_c^2)^2 / \sum w(F_o^2)^2]^{1/2}$$

Table S2. Continuous Shape Measures for 3d ions in **Dy_1**, **Dy_2**, and **$DyZn_2$**.

label	shape	symmetry	Distortion for Ni^{II} in **Dy_1**	Distortion for Ni^{II} in **Dy_2**	Distortion for Zn^{II} in **$DyZn_2$**
HP-6	Hexagon	D_{6h}	33.136	33.286	33.920
PPY-6	Pentagonal pyramid	C_{5v}	27.350	26.713	25.199
OC-6	Octahedron	O_h	**1.101**	**1.127**	**2.042**
TPR-6	Trigonal prism	D_{3h}	13.469	12.723	11.060
JPPZ-6	Johnson pentagonal pyramid (J2)	C_{5V}	31.307	30.659	29.168
RP		/	/	0.021	0.257

RP: taking the coordination sphere of Ni^{II} ion in **Dy_1** as the reference polyhedron.

Table S3. Continuous Shape Measures for Dy^{III} ions in **Dy_1**, **Dy_2**, and **$DyZn_2$**.

label	shape	symmetry	Distortion for Dy^{III} in **Dy_1**	Distortion for Dy^{III} in **Dy_2**	Distortion for Dy^{III} in **$DyZn_2$**
HP-6	Hexagon	D_{6h}	29.132	29.444	29.982
PPY-6	Pentagonal pyramid	C_{5v}	28.274	26.601	24.987
OC-6	Octahedron	O_h	**7.734**	**7.823**	**8.567**
TPR-6	Trigonal prism	D_{3h}	11.434	9.532	7.656
JPPZ-6	Johnson pentagonal pyramid (J2)	C_{5V}	31.190	29.643	28.135
RP		/	/	0.098	0.441

RP: taking the coordination sphere of Dy^{III} ion in **Dy_1** as the reference polyhedron.

Table S4. Selected bond lengths (Å) and angles (°) for **Dy_1**, **Dy_2**, and **$DyZn_2$**.

Complex	**Dy_1**	**Dy_2**	**$DyZn_2$**
Dy1—M*1	3.2442(8)	3.2316(7)	3.3493(8)
Dy1—O1	2.346(3)	2.345(3)	2.349(3)
M1—O1	2.602(3)	2.063(3)	2.155(3)
M1—N1	2.090(4)	2.086(3)	2.130(4)
M1—Dy1—M2	180.0	180.0	180.0
O1—M1—O2	77.26(14)	77.63(12)	74.32(12)
N1—M1—N2	97.29(15)	97.54(11)	100.89(14)
Dy1—O1—M1	94.57 (12)	94.07(10)	96.00(11)
O1—Dy1—O2	66.54 (12)	66.95(10)	67.29(11)

*: M = Ni in **Dy_1** and **Dy_2**, M = Zn in **$DyZn_2$**

Table S5. Crystal Data and Structure Refinements for complexes **Dy_3** – **Dy_6**.

Complex	**Dy_3**	**Dy_4**	**Dy_5**	**Dy_6**
Formula	$C_{63}H_{82}DyN_9Ni_2O_{20}$	$C_{64}H_{82}ClDyN_8Ni_2O_{16}$	$C_{62.5}H_{75}ClDyN_8Ni_2O_{18.5}$	$C_{85}H_{91}BDyN_8Ni_2O_{13}$
Fw	1565.29	1534.74	1549.67	1723.38
Temp (K)	180.0	180.0	180	200
Crystal system	monoclinic	monoclinic	triclinic	monoclinic
Space group	$P2_1/n$	$P2_1/n$	P-1	$P2_1/n$
a (Å)	13.5377(2)	13.5501(2)	13.5920(3)	18.3072(4)
b (Å)	27.0330(3)	27.1618(7)	15.9193(3)	20.2770(3)
c (Å)	17.5047(2)	17.5199(3)	17.4132(3)	20.4660(4)
α (°)	90	90	72.447(2)	90
β (°)	91.5900(10)	91.4400(10)	88.148(2)	91.770(2)
γ (°)	90	90	65.440(2)	90
Volume (Å^3)	6403.63(14)	6446.1(2)	3248.48(12)	7593.7(2)
Z	4	4	2	4
D_{calc} (g cm^{-3})	1.624	1.581	1.584	1.507
μ (mm^{-1})	9.608	9.914	9.861	8.232
F (000)	3220.0	3156.0	1586.0	3552.0
R_{int}	0.0425	0.0409	0.0275	0.0422
R_{sigma}	0.0267	0.0456	0.0268	0.0650
Refl. (all)	135518	56387	50024	47687
Refl (independent)	15440	15267	15409	48436
R_1 (all)	0.0748	0.0845	0.0583	0.0815
R_1 (> 2σ)	0.0507	0.0490	0.0475	0.0400
wR_2 (all)	0.1489	0.1297	0.1320	0.0867
wR_2 (> 2σ)	0.1347	0.1157	0.1253	0.0757
GOF.	1.041	1.034	1.058	0.976

$$R_1 = \sum||F_o| - |F_c||/\sum|F_o|, wR_2 = [\sum w(F_o^2 - F_c^2)^2/\sum w(F_o^2)^2]^{1/2}$$

Table S6. Continuous Shape Measures for Ni^{II} ions in **Dy_3** and **Dy_4** obtained using Shape v. 2.1.

Label	shape	symmetry	Distortion for 1st Ni^{II} in **Dy_3**	Distortion for 2nd Ni^{II} in **Dy_3**	Distortion for 1st Ni^{II} in **Dy_4**	Distortion for 2nd Ni^{II} in **Dy_4**
HP-6	Hexagon	D_{6h}	32.766	32.856	32.976	32.722
PPY-6	Pentagonal pyramid	C_{5v}	25.517	25.495	25.609	25.618
OC-6	Octahedron	O_h	**1.355**	**1.373**	**1.361**	**1.377**
TPR-6	Trigonal prism	D_{3h}	11.440	11.626	11.482	11.527
JPPZ-6	Johnson pentagonal pyramid (J2)	C_{5V}	29.416	29.420	29.549	29.394
RP		/	/	/	0.002	0.003

RP: taking the coordination sphere of the 1st and 2nd Ni^{II} ion in **Dy_3** as the reference polyhedron, respectively.

Table S7. Selected bond lengths (Å) and angles (°) for complexes **Dy_3** – **Dy_6**.

Complex	**Dy_3**	**Dy_4**	**Dy_5**	**Dy_6**
Dy1—Ni1	3.2635(5)	3.2724(6)	3.2545(5)	3.2585(4)
Dy1—Ni2	3.2649(6)	3.2669(6)	3.2632(5)	3.2549(4)
Dy1—O1	2.371(3)	2.376(3)	2.370(2)	2.330(2)
Dy1—O2	2.328(3)	2.332(3)	2.370(3)	2.3552(19)
Dy1—O3	2.368(3)	2.366(3)	2.316(2)	2.329(2)
Dy1—O4	2.380(3)	2.383(3)	2.327(3)	2.351(2)
Dy1—O5	2.320(3)	2.364(3)	2.382(2)	2.356(2)
Dy1—O6	2.370(3)	2.333(3)	2.375(2)	2.367(2)
Ni1—Dy1—Ni2	176.633(15)	177.115(17)	176.810(14)	173.516(12)

Table S8. Continuous Shape Measures for Dy^{III} ions in **Dy_3** and **Dy_4** obtained using Shape v. 2.1.

label	shape	symmetry	Distortion for Dy^{III} in **Dy_3**	Distortion for Dy^{III} in **Dy_4**
HP-6	Hexagon	D_{6h}	29.076	28.952
PPY-6	Pentagonal pyramid	C_{5v}	27.625	27.773
OC-6	Octahedron	O_h	**7.684**	**7.655**
TPR-6	Trigonal prism	D_{3h}	10.975	11.254
JPPZ-6	Johnson pentagonal pyramid (J2)	C_{5V}	30.610	30.726
RP1		/	0.028	0.021
RP2		/	/	0.005

RP1: taking the coordination sphere of Dy^{III} ion in **Dy_1** as the reference polyhedron.

RP2: taking the coordination sphere of Dy^{III} ion in **Dy_3** as the reference polyhedron.

Table S9. The experimental room temperature $\chi_M T$ values and the theoretical values for uncoupled two Ni^{II} (S = 1, g_{Ni} = 2.25) and one Ln^{III} for **Ln_1**.

complexes	temperatures at inflection points (K)	$\chi_M T$ at inflection points ($cm^3mol^{-1}K$)	maximum $\chi_M T$ at low temperature ($cm^3mol^{-1}K$)
Gd_1	105	10.28	16.61
Tb_1	35	14.16	18.00
Dy_1	60	16.18	22.88
Ho_1	16	13.29	22.75
Sm_1	9.6	2.37	2.50
Pr_1	26	3.76	4.26

Table S10. The minimum of experimental $\chi_M T$ values at 2.0 K for **Ce_1**, **Nd_1**, **Eu_1**, **Er_1**, **Tm_1** and **Yb_1**.

complexes	minimum of $\chi_M T$ ($cm^3mol^{-1}K$)
Ce_1	1.62
Nd_1	1.55
Eu_1	1.95
Er_1	9.74
Tm_1	2.08
Yb_1	3.37

Table S11. Relaxation fitting parameters from least-squares fitting of $\chi(f)$ between 1 and 1497 Hz under zero dc field for **Dy_1**.

Temperature (K)	χ_T	χ_S	α	*tau* (s)	*tau err* (s)
1.9	11.87289	0.724	0.11775	0.00121	1.17021E-5
2.0	11.2907	0.7734	0.11167	7.85123E-4	7.95764E-6
2.1	10.78689	0.838	0.10531	5.28515E-4	5.55042E-6
2.2	10.33242	0.90029	0.09911	3.70308E-4	4.04746E-6
2.3	10.15923	0.92246	0.0972	3.23454E-4	3.53445E-6
2.4	9.60917	0.98424	0.09087	2.10038E-4	2.81704E-6
2.5	9.23195	1.02819	0.0831	1.58805E-4	2.36963E-6
2.6	8.89082	1.06376	0.07594	1.23444E-4	1.98688E-6

Table S12. Relaxation fitting parameters from least-squares fitting of $\chi(f)$ between 1 and 1497 Hz under zero dc field for **Dy_2**.

Temperature (K)	χ_T	χ_S	α	*tau* (s)	*tau err* (s)
1.9	10.85424	1.29534	0.12784	3.99629E-4	5.22977E-6
2.0	10.41672	1.40067	0.1173	2.75259E-4	3.81317E-6
2.1	10.00347	1.51734	0.10391	1.93401E-4	2.83429E-6
2.2	9.64288	1.67478	0.09151	1.43717E-4	2.1683E-6
2.3	9.4833	1.72612	0.08592	1.2758E-4	2.00284E-6

Table S13. Relaxation fitting parameters from least-squares fitting of $\chi(f)$ between 1 and 1497 Hz under zero dc field for **Dy_3**.

Temperature (K)	χ_T	χ_S	α	*tau* (s)	*tau err* (s)
1.9	16.45002	0.63478	0.05097	0.00172	2.70132E-6
2.0	15.50097	0.64627	0.04809	0.0012	1.53943E-6
2.1	14.61275	0.63924	0.0477	8.73253E-4	1.06653E-6
2.2	13.82287	0.62301	0.04827	6.5489E-4	9.80273E-7
2.3	13.52173	0.62723	0.0472	5.88824E-4	7.73532E-7
2.4	12.57629	0.6121	0.04782	4.17176E-4	6.66478E-7
2.5	11.9598	0.59853	0.0478	3.33599E-4	5.37977E-7
2.6	11.40167	0.58235	0.04827	2.72538E-4	4.97578E-7
2.7	10.88791	0.56946	0.04829	2.26346E-4	4.85291E-7
2.8	10.41455	0.54371	0.04981	1.90528E-4	4.91005E-7
2.9	9.97619	0.53774	0.04947	1.62959E-4	5.31866E-7
3.0	9.57349	0.49725	0.0512	1.40276E-4	5.3397E-7
3.1	9.19858	0.49159	0.05125	1.2274E-4	5.08612E-7
3.2	8.84576	0.46569	0.05176	1.08061E-4	5.92508E-7

Table S14. Relaxation fitting parameters from least-squares fitting of $\chi(f)$ between 1 and 1497 Hz under zero dc field for **Dy_4**.

Temperature (K)	χ_T	χ_S	α	*tau* (s)	*tau err* (s)
1.9	12.73508	1.02805	0.23899	0.00264	7.26394E-5
2.0	12.26036	1.01295	0.23868	0.0018	4.97166E-5
2.1	11.49732	1.02628	0.23155	0.00127	3.24517E-5
2.2	10.85015	1.0291	0.22812	9.23454E-4	2.1441E-5
2.3	10.27183	1.0289	0.22555	7.43965E-4	1.53417E-5
2.4	9.88778	1.0279	0.22434	5.58761E-4	1.22487E-5
2.5	9.38393	1.02798	0.2233	4.33348E-4	9.64276E-6
2.6	8.94113	1.03351	0.22217	3.44659E-4	8.21907E-6
2.7	8.50918	1.07502	0.21646	2.80024E-4	7.60895E-6
2.8	8.1658	1.07831	0.21909	2.30924E-4	6.37257E-6
2.9	7.82436	1.09267	0.218	1.95578E-4	5.91217E-6
3.0	7.50913	1.14399	0.21448	1.67631E-4	5.61955E-6
3.1	7.20793	1.18483	0.21039	1.46827E-4	5.41347E-6
3.2	6.94308	1.24669	0.20776	1.287E-4	5.12262E-6
3.3	6.68699	1.27343	0.20632	1.15763E-4	4.8812E-6

Table S15. Relaxation fitting parameters from least-squares fitting of $\chi(f)$ between 1 and 1497 Hz under zero dc field for **Dy_5**.

Temperature (K)	χ_T	χ_S	α	*tau* (s)	*tau err* (s)
2.0	11.0761	0.21331	0.24308	0.00167	1.08495E-5
2.1	10.44203	0.19308	0.2527	0.00121	8.89987E-6
2.2	9.88146	0.17037	0.26243	8.96767E-4	7.65196E-6
2.3	9.64941	0.15869	0.26713	7.90782E-4	7.40105E-6
2.4	9.00626	0.14417	0.27867	5.56976E-4	6.49133E-6
2.5	8.57066	0.1359	0.28702	4.37925E-4	6.26784E-6
2.6	8.17979	0.12115	0.29506	3.50727E-4	6.45252E-6
2.7	7.81204	0.12584	0.30146	2.8633E-4	6.26253E-6
2.8	7.47189	0.13738	0.30766	2.37162E-4	6.2945E-6
2.9	7.15748	0.19964	0.30833	2.02818E-4	6.22251E-6
3.0	6.87123	0.21906	0.31362	1.73573E-4	6.47372E-6
3.1	6.6026	0.28553	0.31529	1.52773E-4	6.61992E-6
3.2	6.34934	0.34834	0.31603	1.36091E-4	6.77004E-6
3.3	6.11451	0.44308	0.31508	1.23991E-4	6.74981E-6

Table S16. Relaxation fitting parameters from least-squares fitting of $\chi(f)$ between 1 and 1497 Hz under zero dc field for **Dy_6**.

Temperature (K)	χ_T	χ_S	α	*tau* (s)	*tau err* (s)
1.9	11.30694	0.98665	0.15368	2.7148E-4	4.03956E-6
2.0	10.74051	1.15843	0.13725	2.01599E-4	3.31556E-6
2.1	10.22385	1.32654	0.12172	1.54782E-4	2.48817E-6
2.2	9.77148	1.44017	0.1094	1.20285E-4	2.07482E-6
2.3	9.55862	1.52189	0.10181	1.08927E-4	1.90907E-6

Table S17. Relaxation fitting parameters from least-squares fitting of $\chi(f)$ between 1 and 1497 Hz under 1500 Oe field for **$DyZn_2$**.

Temperature (K)	χ_T	χ_S	α	*tau* (s)	*tau err* (s)
1.9	9.29449	0.3897	0.6692	0.00561	8.86758E-5
2.1	8.86851	0.53023	0.68725	0.00423	8.67154E-5
2.3	8.43747	0.74083	0.68771	0.00336	9.20968E-5
2.5	7.56414	1.1555	0.66995	0.00185	7.5872E-5
2.7	6.98805	1.40923	0.66051	0.00122	6.17016E-5
2.9	6.51302	1.59762	0.65406	8.16123E-4	5.01952E-5
3.1	6.08225	1.81993	0.63998	6.04089E-4	4.59835E-5
3.3	5.70313	2.0479	0.62198	4.84103E-4	3.62835E-5
3.5	5.38589	2.20601	0.60678	3.91239E-4	3.41199E-5
3.7	5.10319	2.35899	0.58554	3.32402E-4	2.98084E-5
3.9	4.85003	2.498	0.56159	2.94387E-4	2.70808E-5
4.1	4.63107	2.59452	0.53959	2.54967E-4	2.24869E-5
4.3	4.43667	2.61586	0.52376	2.00195E-4	1.71129E-5
4.5	4.26563	2.70408	0.4989	1.91134E-4	2.14182E-5
4.7	4.0993	2.70417	0.48289	1.48376E-4	1.18513E-5

Table S18. Relaxation fitting parameters from least-squares fitting of $\chi(f)$ between 1 and 1497 Hz under 1500 Oe field for **Dy_1**.

Temperature (K)	χ_T	χ_S	α	*tau* (s)	*tau err* (s)
2.5	12.72772	0.52262	0.24787	0.2775	0.00425
3.0	10.86753	0.57554	0.23257	0.05878	9.48668E-4
3.5	9.56645	0.64761	0.23939	0.01893	2.93171E-4
4.2	8.27968	0.81019	0.28277	0.00539	1.2569E-4
4.4	7.90071	0.8852	0.29032	0.0038	9.83231E-5
4.8	7.27647	1.04047	0.31095	0.00196	6.21568E-5
5.0	6.94805	1.15523	0.31222	0.0014	4.76875E-5
5.2	6.66089	1.25422	0.31576	0.00101	3.78796E-5
5.4	6.3977	1.35934	0.31648	7.34044E-4	3.06629E-5
5.6	6.15042	1.46773	0.31641	5.40984E-4	2.42162E-5
5.8	5.91832	1.59174	0.31111	4.05568E-4	1.92999E-5
6.0	5.69954	1.70995	0.30558	3.07054E-4	1.52807E-5
6.2	5.4991	1.8216	0.30108	2.35496E-4	1.28417E-5
6.4	5.30889	1.93211	0.29254	1.8356E-4	1.02189E-5
6.6	5.13026	2.06017	0.28045	1.47235E-4	8.78848E-6
6.8	4.96464	2.16157	0.27152	1.18508E-4	7.36743E-6

Table S19. Relaxation fitting parameters from least-squares fitting of $\chi(f)$ between 1 and 1497 Hz under 2000 Oe field for **Dy_2**.

Temperature (K)	χ_T	χ_S	α	*tau* (s)	*tau err* (s)
2.2	8.48666	1.15562	0.38967	0.13305	0.00686
2.4	7.92331	1.21486	0.38816	0.05901	0.00264
2.6	7.39592	1.26262	0.39204	0.02486	0.00102
2.8	6.96024	1.29891	0.40369	0.01065	4.03382E-4
3.0	6.57092	1.32734	0.41243	0.00462	1.72985E-4
3.2	6.21864	1.34422	0.42199	0.002	7.46176E-5
3.4	5.91145	1.33063	0.43153	8.70047E-4	3.53874E-5
3.6	5.62546	1.30645	0.43549	3.87312E-4	1.74854E-5
3.8	5.36514	1.35258	0.43401	1.90725E-4	1.07191E-5

Table S20. Relaxation fitting parameters from least-squares fitting of $\chi(f)$ between 1 and 1497 Hz under 1500 Oe field for **Dy_3**.

Temperature (K)	χ_T	χ_S	α	*tau* (s)	*tau err* (s)
4.8	6.5169	0.76628	0.34004	0.11648	2.70132E-6
5.2	5.39382	0.75532	0.27838	0.0638	1.06653E-6
5.6	4.73792	0.73098	0.23953	0.04307	7.73532E-7
6.0	4.26224	0.70221	0.21012	0.03178	5.37977E-7
6.4	3.89235	0.6718	0.19049	0.02477	4.85291E-7
6.8	3.58969	0.64216	0.17572	0.02001	5.31866E-7
7.2	3.33139	0.61343	0.16403	0.01653	5.08612E-7
7.6	3.10531	0.58722	0.1528	0.01381	0.01436
8.0	2.90568	0.56649	0.14143	0.01165	0.00462
8.4	2.52479	0.51641	0.1222	0.00742	0.00223
8.8	2.37655	0.49777	0.11097	0.00581	0.00129
9.2	2.24969	0.47259	0.11284	0.00425	8.61589E-4
9.6	2.13185	0.45334	0.10888	0.003	6.1788E-4
10.0	2.02551	0.4352	0.10443	0.00205	4.7406E-4
10.4	1.92689	0.41511	0.10371	0.00137	3.58955E-4
10.8	1.84134	0.39344	0.10466	9.03516E-4	2.85366E-4
11.2	1.76206	0.37796	0.09742	5.94155E-4	1.52105E-4
11.6	1.68806	0.37491	0.08829	3.97535E-4	1.12791E-4
12.0	1.61587	0.36698	0.07687	2.66141E-4	7.4901E-5
12.4	1.55773	0.3577	0.07518	1.85317E-4	4.88861E-5
12.8	1.50064	0.3563	0.06528	1.31864E-4	2.9178E-5
13.0	1.47429	0.33325	0.07032	1.09216E-4	2.28633E-5

Table S21. Relaxation fitting parameters from least-squares fitting of $\chi(f)$ between 1 and 1497 Hz under 1500 Oe field for **Dy_4**.

Temperature (K)	χ_T	χ_S	α	*tau* (s)	*tau err* (s)
1.9	8.36697	0.27932	0.42267	0.01485	3.98949E-4
2.0	8.15771	0.23207	0.42912	0.00994	2.48061E-4
2.2	7.72729	0.17334	0.43241	0.00494	1.02325E-4
2.4	7.38129	0.1357	0.43462	0.00295	5.1052E-5
2.6	7.01159	0.09707	0.43805	0.00179	2.56413E-5
2.8	6.64738	0.07674	0.44107	0.00118	1.32744E-5
3.0	6.2986	0.07805	0.44285	8.27169E-4	7.94895E-6
3.2	5.95956	0.11129	0.44115	6.15438E-4	6.66026E-6
3.4	5.64374	0.18057	0.43766	4.8715E-4	6.60291E-6
3.6	5.34934	0.24536	0.43336	3.97475E-4	7.53452E-6
3.8	5.06793	0.33544	0.42444	3.38306E-4	7.61084E-6
4.0	4.81528	0.42268	0.41865	2.98078E-4	8.7666E-6
4.2	4.57518	0.4874	0.4116	2.64169E-4	8.48139E-6
4.4	4.35206	0.60545	0.39757	2.47469E-4	8.27463E-6
4.6	4.14727	0.69525	0.3812	2.32923E-4	7.81874E-6
4.8	3.95802	0.73643	0.3755	2.14696E-4	7.14505E-6

Table S22. Relaxation fitting parameters from least-squares fitting of $\chi(f)$ between 1 and 1497 Hz under 1500 Oe field for **Dy_5**.

Temperature (K)	χ_T	χ_S	α	*tau* (s)	*tau err* (s)
2.0	8.73892	0.27998	0.45772	0.01532	1.02574E-4
2.2	8.08729	0.32229	0.43889	0.00712	4.20721E-5
2.4	7.61296	0.35941	0.42433	0.0041	3.78996E-5
2.6	7.12177	0.43557	0.40571	0.00249	3.37879E-5
2.8	6.67327	0.50014	0.39019	0.00163	3.00831E-5
3.0	6.26199	0.57756	0.37291	0.00117	2.69773E-5
3.2	5.89185	0.64277	0.35978	8.78257E-4	2.42974E-5
3.4	5.54935	0.71414	0.34481	6.93832E-4	1.96904E-5
3.6	5.23788	0.7858	0.32967	5.70181E-4	1.74926E-5
3.8	4.94995	0.82889	0.3149	4.75192E-4	1.54625E-5
4.0	4.6878	0.85147	0.30427	4.03746E-4	1.39869E-5
4.2	4.44608	0.91449	0.2899	3.59281E-4	1.27284E-5
4.4	4.22459	0.92904	0.27739	3.16839E-4	1.10165E-5
4.6	4.02812	0.97945	0.26079	2.91963E-4	1.20719E-5
4.8	3.83347	0.95493	0.25563	2.55745E-4	9.0926E-6
5.0	3.65892	0.96749	0.24409	2.34082E-4	8.20222E-6
5.2	3.4976	0.9952	0.2295	2.17568E-4	7.40669E-6
5.4	3.35074	0.97477	0.22201	1.96971E-4	7.15207E-6
5.6	3.21298	0.99338	0.20501	1.85578E-4	6.76071E-6
5.8	3.08401	0.99269	0.19713	1.71116E-4	5.99707E-6
6.0	2.96372	0.99438	0.18452	1.59074E-4	5.53214E-6

Table S23. Relaxation fitting parameters from least-squares fitting of $\chi(f)$ between 1 and 1497 Hz under 1500 Oe field for **Dy_6**.

Temperature (K)	χ_T	χ_S	α	*tau* (s)	*tau err* (s)
2.0	8.63274	0.78803	0.3164	0.00596	1.10079E-4
2.3	7.95812	0.8336	0.30125	0.0026	4.43775E-5
2.6	7.16569	0.91547	0.27593	0.00102	1.91948E-5
2.9	6.54692	0.96809	0.26079	4.98058E-4	1.19916E-5
3.2	6.00173	1.14857	0.23375	2.81019E-4	9.023E-6
3.3	5.83075	1.25543	0.21966	2.39771E-4	8.51451E-6
3.5	5.51948	1.32144	0.19546	1.67563E-4	6.77968E-6
3.6	5.36852	1.42684	0.17462	1.44218E-4	6.38889E-6

Table S24. Relaxation fitting parameters from least-squares fitting of $\chi(f)$ between 1 and 1497 Hz under 1500 Oe field for $[Dy(NiL)_2]NO_3 \cdot 3H_2O$.

Temperature (K)	χ_T	χ_S	α	*tau* (s)	*tau err* (s)
5.0	9.27192	1.1699	0.26674	0.09235	0.00792
5.5	7.77574	1.13732	0.21638	0.05282	0.00293
6.0	6.81803	1.0644	0.18752	0.03541	0.00138
6.5	6.117	1.0024	0.17054	0.02587	8.4962E-4
7.0	5.54246	0.94291	0.15498	0.01982	5.67678E-4
7.5	5.0751	0.89862	0.14771	0.01569	4.34084E-4
8.0	4.65564	0.85	0.12839	0.01271	3.65263E-4
8.5	3.87304	0.77487	0.12346	0.00682	1.70332E-4
9.0	3.59634	0.75613	0.11719	0.00483	1.00749E-4
9.5	3.33001	0.73803	0.06701	0.00345	1.22858E-4
10.0	3.14071	0.67917	0.11545	0.00194	4.41201E-5
11.0	2.77693	0.67946	0.06131	6.73924E-4	3.86085E-5
12.0	2.49707	0.5579	0.10826	2.51259E-4	9.64731E-6

Table S25. Relaxation fitting parameters from least-squares fitting of $\chi(f)$ between 1 and 1497 Hz under zero dc field for **1***.

Temperature (K)	χ_T	χ_S	α	*tau* (s)	*tau err* (s)
1.9	2.34692	0.96836	0.30819	1.62348E-4	3.74028E-6
2.0	2.23648	0.95961	0.29996	1.22429E-4	3.84434E-6

Table S26. Relaxation fitting parameters from least-squares fitting of $\chi(f)$ between 1 and 1497 Hz under 1500 Oe field for **1***.

Temperature (K)	χ_T	χ_S	α	*tau* (s)	*tau err* (s)
2.0	1.95285	1.01524	0.224	0.06623	2.36792E-4
2.3	1.80871	0.93503	0.22868	0.03396	1.94541E-4
2.6	1.62523	0.84903	0.22929	0.01494	1.57918E-4
2.9	1.48768	0.79111	0.23682	0.0081	1.20084E-4
3.2	1.3688	0.74734	0.24786	0.00469	9.4481E-5
3.5	1.26562	0.71279	0.26587	0.00278	7.20136E-5
3.8	1.17829	0.68396	0.29508	0.00167	5.24873E-5
4.0	1.12289	0.66934	0.30223	0.00118	4.18494E-5
4.2	1.0761	0.65385	0.32205	8.28236E-4	3.26549E-5
4.4	1.02236	0.64742	0.31162	5.74074E-4	2.55604E-5
4.6	0.97943	0.63986	0.31199	4.14403E-4	2.62258E-5
4.8	0.93599	0.63012	0.31241	2.84716E-4	1.58108E-5
5.0	0.89769	0.62438	0.30043	2.0731E-4	1.20868E-5
5.2	0.86233	0.62083	0.2892	1.55586E-4	1.05032E-5
5.4	0.8293	0.62337	0.2639	1.26056E-4	8.7377E-6

Table S27. Calculated energy levels (cm^{-1}), $\boldsymbol{g}$ (g_x, g_y, g_z) tensors and predominant m_J values of the lowest eight Kramers doublets (KDs) of the Dy^{III} fragments in **Dy_1**, **Dy_3** and **$DyZn_2$** by CASSCF.

KDs	**Dy_1**			**Dy_3**			**$DyZn_2$**		
	E/cm^{-1}	g	m_J	E/cm^{-1}	g	m_J	E/cm^{-1}	g	m_J
1	0.000	0.000 0.000 19.30	±15/2	0.000	0.009 0.013 19.05	±15/2	0.000	0.000 0.000 19.31	±15/2
2	72.87	0.316 0.316 17.17	±13/2	47.64	0.033 0.205 16.09	±13/2	39.76	0.748 0.749 17.09	±13/2
3	77.83	0.247 0.247 14.20	±11/2	72.06	0.021 0.117 16.44	±11/2	42.42	0.707 0.708 14.17	±11/2
4	140.5	0.000 0.000 11.86	±9/2	113.1	0.175 0.337 12.72	±9/2	103.0	0.000 0.000 11.95	±9/2
5	239.4	4.407 4.408 7.756	±7/2	196.4	4.274 4.708 7.763	±7/2	201.8	3.87 3.88 8.06	±7/2
6	428.5	4.429 4.429 5.303	±5/2	372.0	5.305 4.874 4.026	±7/2	369.0	3.79 3.79 5.56	±5/2
7	586.2	0.002 0.002 4.339	±3/2	517.2	0.203 1.029 4.382	±3/2	510.6	0.000 0.004 4.274	±3/2
8	686.4	10.40 10.39 1.169	±1/2	609.6	11.02 9.768 1.176	±1/2	599.2	10.43 10.42 1.189	±1/2

Table S28. Calculated CFPs of Dy^{III} in **Dy_1**, **Dy_2**, and **$DyZn_2$**.

k	*q*	*B*(*k*,*q*) in **Dy_1**	*B*(*k*,*q*) in **Dy_3**	*B*(*k*,*q*) in **$DyZn_2$**
2	-2	1.1410E-04	7.9543E-02	3.2092E-03
2	-1	7.6512E-04	9.6965E-01	6.4166E-03
2	0	-3.5162E+00	-2.9917E+00	3.8122E+00
2	1	6.3383E-05	-2.0497E+00	-1.2873E-02
2	2	-7.8281E-05	-1.4466E-02	-1.1499E+01
4	-4	1.1584E-06	1.0415E-02	8.4903E-02
4	-3	1.0248E-01	9.7330E-02	-3.6151E-03
4	-2	1.1167E-06	-9.4368E-03	1.7087E-01
4	-1	-1.0377E-05	-9.1808E-03	1.5143E-04
4	0	8.0949E-03	6.5832E-03	1.9935E-02
4	1	-1.3966E-06	2.1567E-02	-4.7627E-02
4	2	4.1908E-06	7.5123E-03	-1.3511E-01
4	3	-6.1383E-02	-2.9791E-02	-1.4223E-01
4	4	4.1539E-06	1.0459E-03	2.3506E-01
6	-6	-1.0502E-04	-6.68789E-05	-6.6709E-03
6	-5	4.8777E-08	-9.05279E-05	-3.1247E-04
6	-4	-2.2860E-08	-2.30769E-04	-7.2449E-03
6	-3	-8.7986E-04	-7.04709E-04	-6.4941E-04
6	-2	-3.6945E-08	1.89859E-04	5.4538E-03
6	-1	7.7489E-08	4.5309E-05	-7.5116E-04
6	0	-3.5252E-05	-2.6043E-05	1.3766E-04
6	1	1.7991E-08	-1.2404E-04	-1.9102E-03
6	2	-7.6153E-08	-1.5809E-04	-3.3438E-03
6	3	5.2701E-04	2.0677E-04	5.2575E-04
6	4	-8.2730E-08	-3.2981E-05	2.7580E-03
6	5	-5.1198E-08	-3.9506E-05	1.1158E-02
6	6	-5.6214E-05	-1.0078E-04	-5.66608E-03

Table S29. Calculated axial and rhombic zero field splitting parameters *D* and *E*, $\boldsymbol{g}$ (g_x, g_y, g_z) tensors the Ni^{II} fragments in **Dy_1** and **Dy_3** by CASSCF.

	Ni^{II} in **Dy_1**	1st Ni^{II} in **Dy_3**	2nd Ni^{II} in **Dy_3**
D (cm^{-1})	-2.0604	-1.9861	-1.4583
E (cm^{-1})	0.0007	0.3619	0.4271
$\boldsymbol{g}$ (g_x, g_y, g_z)	2.281, 2.281, 2.295	2.288, 2.294, 2.310	2.297, 2.299, 2.308

Table S30. Calculated transition probabilities between exchange energy states in **Dy_1**.

states	1	2	3	4	5	6	7	8	9	10
1		5.06E-11	0.50	2.50	4.13E-25	5.42E-25	4.27E-10	1.29E-5	6.22E-30	2.21E-28
2	5.06E-11		2.50	0.50	1.84E-25	8.15E-26	1.29E-5	4.27E-10	2.65E-27	3.02E-26
3	0.50	2.50		2.53E+1	2.67E-24	2.75E-24	1.33	0.27	2.50E-22	2.04E-21
4	2.50	0.50	2.53E+1		1.44E-24	2.02E-24	0.27	1.33	4.85E-23	4.12E-22
5	4.13E-25	1.84E-25	2.67E-24	1.44E-24		4.31E+1	1.07E-21	1.38E-24	0.91	0.59
6	5.42E-25	8.15E-26	2.75E-24	2.02E-24	4.31E+1		1.50E-21	1.89E-24	0.59	0.91
7	4.27E-10	1.29E-5	1.33	0.27	1.07E-21	1.50E-21		3.42E-7	5.70E-24	1.90E-19
8	1.29E-5	4.27E-10	0.27	1.33	1.38E-24	1.89E-24	3.42E-7		5.36E-27	6.71E-28
9	6.22E-30	2.65E-27	2.50E-22	4.85E-23	0.91	0.59	5.70E-24	5.36E-27		3.73E-3
10	2.21E-28	3.02E-26	2.04E-21	4.12E-22	0.59	0.91	1.90E-19	6.71E-28	3.73E-3	

Table S31. The data of {Ln2Ni2} SMMs with “butterfly” shape in literatures.

Complexes	H_{dc}/ kOe	U_{eff}/K	τ_0/s	Geometries	CshM value	Ref.
$[Dy_2Ni_2(H_2L^1)_2(\mu_3\text{-}MeO)_2\text{-}(CH_3CN)_2(NO_3)_4]\cdot 4H_2O$	0	48.5	3.6×10^{-8}	capped square antiprism (C_{4v})	2.873 *	183
$[Tb_2Ni_2(HL^2)_2(\mu_3\text{-}OMe)_2\text{-}(CH_3CN)_2(NO_3)_4]\cdot 4H_2O$	0	86.2	2.3×10^{-7}	capped square antiprism (C_{4v})	3.600 *	183
$[Dy_2Ni_2(HL^2)_2(\mu_3\text{-}OMe)_2\text{-}(CH_3CN)_2(NO_3)_4]\cdot 4H_2O$	0	56.6	3.3×10^{-8}	capped square antiprism (C_{4v})	3.532 *	183
$[Ni_2Dy_2L^3(NO_3)_2(MeOH)_2]$	0	36	8×10^{-8}	triangular dodecahedron (D_{2d})	2.495	205
$[Ni_2Dy_2(L^4)_4(Ac)_2(DMF)_2]\cdot 3CH_3CN$	0	15	6.85×10^{-6}	square antiprism (D_{4d})	9.930	53
$[Ni_2Dy_2(L^5)_4(NO_3)_2(DMF)_2]$	0	18.5	5.4×10^{-7}	square antiprism (D_{4d})	4.090 *	175
$[Ni_2Dy_2(L^5)_4(NO_3)_2(MeOH)_2]\cdot 3MeOH$	0 4	$U_1 = 21.3$ $U_2 = 28.5$	$\tau_1 = 1.5\times10^{-6}$ $\tau_2 = 2.8\times10^{-6}$	square antiprism (D_{4d})		175
$[Ni_2Dy_2(\mu_3\text{-}OH)_2(O_2C^tBu)_{10}[Et_3NH]_2$	0	20	6×10^{-7}	square antiprism (D_{4d})	2.114	160
$[Ni_2Er_2(\mu_3\text{-}OH)_2(O_2C^tBu)_{10}[Et_3NH]_2$	1	12	5×10^{-6}	square antiprism (D_{4d})	1.995 *	160

*calculated by the author from the provided cif files

H_4L^1 = 2-(((2-hydroxy-3-methoxyphenyl)methylene)amino)-2-(hydroxymethyl)-1,3-propanediol;

H_3L^2 = 2-(2, 3-dihydroxpropyliminomethyl)-6-methoxyphenol;

H_2L^3 = 2-ethoxy-6-(((2-hydroxyphenyl)imino)methyl)phenol;

H_2L^4 = 2-((2-hydroxy-3-methoxybenzylidene)amino)-4-methylphenol;

H_2L^5 = 2-(((2-hydroxyphenyl)imino)methyl)-6-methoxyphenol.

Table S32. Crystal Data and Structure Refinements for **$EuMg_2$**

Complex	**$EuMg_2$**
Formula	$C_{61}H_{66}EuF_3Mg_2N_8O_{15}S$
Fw	1440.85
Temp (K)	180.0
Crystal system	trigonal
Space group	*R*32
a (Å)	11.85270(10)
b (Å)	11.85270(10)
c (Å)	38.9623(6)
α (°)	90
β (°)	90
γ (°)	120
Volume (Å^3)	4740.34(11)
Z	3
D_{calc} (g cm^{-3})	1.514
μ (mm^{-1})	5.950
F (000)	2214.0
R_{int}	0.0179
R_{sigma}	0.0085
Refl. (all)	18254
Refl (independent)	2609
R_1 (all)	0.0223
R_1 (> 2σ)	0.0222
wR_2 (all)	0.0613
wR_2 (> 2σ)	0.0613
Flack parameter	-0.004(3)
GOF.	1.144

$$R_1 = \sum||F_o| - |F_c||/\sum|F_o|, wR_2 = [\sum w(F_o^2 - F_c^2)^2/\sum w(F_o^2)^2]^{1/2}$$

Table S33. Continuous Shape Measures for metal centers in **$EuMg_2$** obtained using Shape v. 2.1.

label	shape	symmetry	Distortion for Eu^{III}	Distortion for Mg^{II}
HP-6	Hexagon	D_{6h}	29.852	34.329
PPY-6	Pentagonal pyramid	C_{5v}	26.226	24.712
OC-6	Octahedron	O_h	9.943	**2.206**
TPR-6	Trigonal prism	D_{3h}	**8.856**	10.853
JPPZ-6	Johnson pentagonal pyramid (J2)	C_{5V}	29.192	28.960

Table S34. Crystal Data and Structure Refinements for **YCo_2**.

Complex	**YCo_2**
Formula	$C_{61}H_{66}Co_2F_3N_8O_{15}SY$
Fw	1447.04
Temp (K)	180.0
Crystal system	trigonal
Space group	*R*32
a (Å)	11.95910(10)
b (Å)	11.95910(10)
c (Å)	38.1679(6)
α (°)	90
β (°)	90
γ (°)	120
Volume (Å^3)	4727.44(11)
Z	3
D_{calc} (g cm^{-3})	1.525
μ (mm^{-1})	4.322
F (000)	2232.0
R_{int}	0.0201
R_{sigma}	0.0087
Refl. (all)	19832
Refl (independent)	2550
R_1 (all)	0.0337
R_1 (> 2σ)	0.0333
wR_2 (all)	0.0960
wR_2 (> 2σ)	0.0955
Flack parameter	0.490(10)
GOF.	1.074

$$R_1 = \sum\big||F_o| - |F_c|\big| / \sum|F_o|, wR_2 = [\sum w(F_o^2 - F_c^2)^2 / \sum w(F_o^2)^2]^{1/2}$$

Table S35. Continuous Shape Measures for metal centers in **YCo_2** obtained using Shape v. 2.1.

label	shape	symmetry	Distortion for Y^{III}	Distortion for Co^{II}
HP-6	Hexagon	D_{6h}	29.719	33.494
PPY-6	Pentagonal pyramid	C_{5v}	25.488	25.598
OC-6	Octahedron	O_h	**7.608**	**1.558**
TPR-6	Trigonal prism	D_{3h}	8.324	11.475
JPPZ-6	Johnson pentagonal pyramid (J2)	C_{5V}	28.640	29.627

Table S36. Selected bond lengths (Å) and angles (°) for **$EuMg_2$**.

Eu1 – O1	2.4284(18)	O1 – Mg1 – Eu1	46.57(6)
Mg1 – O1	2.057(2)	N2 – Mg1 – Eu1	118.92(7)
Mg1 – N2	2.206(2)	Mg1 – O1 – Eu1	95.46(7)
O1 – Eu1 – $O1^1$	167.04(8)	O1 – Mg1 – N2	83.46(9)
O1 – Eu1 – $O1^2$	124.28(8)	O1 – Mg1 – $O1^3$	77.94(9)
O1 – Eu1 – $O1^3$	124.27(8)	N2 – Mg1 – $N2^3$	98.58(9)
O1 – Eu1 – $O1^4$	64.40(7)	$O1^3$ – Mg1 – N2	161.36(10)

symmetry code: ^{1}1/3+Y,-1/3+X,2/3-Z; ^{2}1/3-Y+X,2/3-Y,2/3-Z; ^{3}4/3-X,2/3-X+Y,2/3-Z; ^{4}1+Y-X,1-X,+Z

Table S37. Selected bond lengths (Å) and angles (°) for **YCo$_2$**.

Y1 – O1	2.3219(19)	O1 – Co1 – Y1	45.95(5)
Co1 – O1	2.091(2)	N2 – Co1 – Y1	119.53(8)
Co1 – N2	2.132(3)	Co1 – O1 – Y1	93.73(7)
O1 – Y1 – O1^1	139.68(5)	O1 – Co1 – N2	85.82(11)
O1 – Y1 – O1^2	105.35(10)	O1 – Co1 – O1^3	76.99(8)
O1 – Y1 – O1^3	40.32(5)	N2 – Co1 – N2^3	97.79(10)
O1 – Y1 – O1^4	68.17(8)	O1^3 – Co1 – N2	98.39(11)

symmetry code: ^{1}1/3+Y,-1/3+X,2/3-Z; ^{2}4/3-X,2/3-X+Y,2/3-Z; ^{3}1+Y-X,1-X,+Z; ^{4}1-Y,+X-Y,+Z

Table S38. Relaxation fitting parameters from least-squares fitting of $\chi(f)$ between 1 and 1497 Hz under 1000 Oe dc field for complex **YCo$_2$**.

Temperature (K)	χ_T	χ_S	α	*tau* (s)
1.9	1.83633	0.33083	0.23433	3.5873E-4
2	1.75268	0.2928	0.24017	2.97313E-4
2.1	1.67712	0.2696	0.23247	2.46785E-4
2.2	1.6084	0.24512	0.22494	2.05097E-4
2.3	1.58098	0.25292	0.21154	1.9274E-4
2.4	1.50047	0.23351	0.18961	1.51405E-4
2.5	1.44613	0.21908	0.17717	1.25814E-4
2.6	1.39621	0.21828	0.15633	1.0788E-4
2.7	1.34953	0.20488	0.14132	9.00277E-5
2.8	1.30711	0.2003	0.12792	7.66874E-5
2.9	1.26715	0.17591	0.11454	6.39421E-5
3	1.23047	0.16105	0.10785	5.36635E-5

Table S39. Relaxation fitting parameters from least-squares fitting of $\chi(f)$ between 1 and 1497 Hz under 600 Oe dc field for complex **$GdCo_2$.**

Temperature (K)	χ_T	χ_S	α	*tau* (s)
1.95	11.5805	1.80282	0.09291	4.38941E-4
2	11.3334	1.84301	0.08794	3.55207E-4
2.05	11.0996	1.87813	0.0834	2.88399E-4
2.1	10.8718	1.94458	0.07738	2.38533E-4
2.15	10.6593	2.00266	0.07176	1.98551E-4
2.2	10.446	2.04919	0.066	1.66807E-4
2.25	10.2505	2.11448	0.06023	1.4156E-4
2.3	10.1594	2.14461	0.05753	1.32159E-4
2.35	10.1633	2.13987	0.05812	1.32065E-4
2.4	9.7691	2.31809	0.04537	9.6639E-5
2.5	9.41192	2.40183	0.03564	7.2859E-5
2.6	9.08383	2.48851	0.02636	5.63265E-5
2.7	8.77394	2.51288	0.02146	4.36467E-5

Table S40. Relaxation fitting parameters from least-squares fitting of $\chi(f)$ between 1 and 999 Hz under 3000 Oe dc field for complex **$TbCo_2$.**

Temperature (K)	χ_T	χ_S	α	*tau* (s)
2	5.301	0.33296	0.25414	0.00485
2.2	5.49884	0.36335	0.22311	0.00319
2.4	5.56201	0.41747	0.18556	0.00224
2.6	5.61924	0.44433	0.16497	0.00165
2.8	5.62914	0.46892	0.14978	0.00128
3	5.54605	0.51333	0.12724	0.00101
3.2	5.50106	0.52631	0.11945	8.23157E-4
3.4	5.41813	0.53819	0.11167	6.83639E-4
3.6	5.31256	0.55772	0.10161	5.79442E-4
3.8	5.20517	0.56272	0.09722	4.98747E-4

4	5.08327	0.57133	0.09089	4.34813E-4
4.2	4.9423	0.59763	0.0794	3.84714E-4
4.4	4.81876	0.59087	0.07807	3.4239E-4
4.6	4.68889	0.58482	0.07636	3.07458E-4
4.8	4.55357	0.60213	0.07018	2.79811E-4
5	4.40827	0.61144	0.06324	2.55696E-4
5.2	4.28214	0.62234	0.0593	2.3602E-4
5.4	4.1455	0.63404	0.05302	2.18812E-4
5.6	4.02171	0.63159	0.0515	2.03357E-4
5.8	3.89375	0.63671	0.04751	1.89892E-4
6	3.77471	0.65609	0.04117	1.79765E-4

Table S41. Relaxation fitting parameters from least-squares fitting of $\chi(f)$ between 1 and 999 Hz under 3000 Oe dc field for complex **$TbFe_2$.**

Temperature (K)	χ_T	χ_S	α	*tau* (s)
2	3.77675	1.80756	0.29159	4.85903E-4
2.1	3.76897	1.82143	0.26455	3.79241E-4
2.2	3.75851	1.83945	0.23637	3.03553E-4
2.3	3.75441	1.8596	0.2139	2.4948E-4
2.4	3.74725	1.86641	0.19701	2.06837E-4
2.5	3.7231	1.89398	0.17328	1.75074E-4
2.6	3.69756	1.91152	0.15536	1.4894E-4
2.7	3.66759	1.92961	0.1413	1.28097E-4
2.8	3.63174	1.94904	0.1263	1.11064E-4
2.9	3.59612	1.95965	0.11763	9.58272E-5
3	3.55745	1.96941	0.11089	8.326E-5
3.1	3.51435	1.99185	0.09953	7.33322E-5
3.2	3.4726	2.04064	0.0887	6.72299E-5
3.3	3.43213	2.0251	0.09184	5.75246E-5
3.4	3.39006	2.03128	0.0914	5.04514E-5

Table S42. Crystal Data and Structure Refinements for **Y_2_MeCN**, **Eu_2_MeCN**, and **Dy_2_MeCN**

Complex	**Y_2_MeCN**	**Eu_2_MeCN**	**Dy_2_MeCN**
Formula	$C_{56}H_{46}Y_2N_{24}O_{18}$	$C_{56}H_{46}Eu_2N_{24}O_{18}$	$C_{56}H_{46}Dy_2N_{24}O_{18}$
Fw	1520.98	1647.08	1668.16
Temp(K)	180	180	150
Crystal system	monoclinic	monoclinic	monoclinic
Space group	$P2_1/c$	$P2_1/c$	$P2_1/c$
a (Å)	13.6348(2)	13.6687(2)	13.6313(6)
b (Å)	13.9445(3)	13.94010(10)	13.9077(3)
c (Å)	33.0673(5)	32.9437(4)	33.0053(11)
α (°)	90	90	90
β (°)	91.1310(10)	91.2690(10)	91.180(3)
γ (°)	90	90	90
Volume (Å^3)	6285.88(19)	6275.65(13)	6255.8(4)
Z	4	4	4
D_{calc} (g cm^{-3})	1.607	1.743	1.771
μ (mm^{-1})	2.166	6275.65(13)	12.96
F (000)	3088.0	3280.0	3304.0
R_{int}	0.0214	0.0208	0.0424
R_{sigma}	0.0241	0.0127	0.0266
Refl. (all)	56384	107181	42497
Refl (independent)	14673	14999	13585
R_1 (all)	0.0320	0.0240	0.0345
R_1 (> 2σ)	0.0245	0.0216	0.0289
wR_2 (all)	0.0664	0.0551	0.0823
wR_2 (> 2σ)	0.0650	0.0541	0.0804
GOF.	1.008	1.032	1.054

$$R_1 = \sum\big||F_o| - |F_c|\big| / \sum|F_o|, wR_2 = [\sum w(F_o^2 - F_c^2)^2 / \sum w(F_o^2)^2]^{1/2}$$

Table S43. Continuous Shape Measures for Dy^{III} ions in **Dy_2_MeCN** obtained using Shape v. 2.1.

label	shape	symmetry	Distortion of 1st Dy^{III} ion	Distortion of 2nd Dy^{III} ion
DP-10	Decagon	D_{10h}	36.995	37.132
EPY-10	Enneagonal pyramid	C_{9v}	23.691	23.637
OBPY-10	Octagonal bipyramid	D_{8h}	15.675	15.083
PPR-10	Pentagonal prism	D_{5h}	9.806	10.456
PAPR-10	Pentagonal antiprism	D_{5d}	10.914	11.008
JBCCU-10	Bicapped cube J15	D_{4h}	10.965	11.072
JBCSAPR-10	Bicapped square antiprism J17	D_{4d}	5.771	5.082
JMBIC-10	Metabidiminished icosahedron J62	C_{2v}	7.528	8.042
JATDI-10	Augmented tridiminished icosahedron J64	C_{3v}	18.481	19.401
JSPC-10	Sphenocorona J87	C_{2v}	**2.209**	**2.169**
SDD-10	Staggered Dodecahedron (2:6:2)	D_2	3.508	3.977
TD-10	Tetradecahedron (2:6:2)	C_{2v}	3.009	3.536
HD-10	Hexadecahedron (2:6:2) or (1:4:4:1)	D_{4h}	8.254	8.450
RP		/	/	0.205

RP: taking the coordination sphere of 1st Dy^{3+} ion as the reference polyhedron.

Table S44. Selected bond lengths (Å) and bond angles (°) in **Y_2_MeCN**.

Y1 – O1	2.4562(11)	Y2 – O10	2.4490(11)
Y1 – O2	2.4500(11)	Y2 – O11	2.4668(11)
Y1 – O4	2.4476(12)	Y2 – O13	2.4678(12)
Y1 – O5	2.4438(12)	Y2 – O14	2.4560(11)
Y1 – O7	2.4897(11)	Y2 – O16	2.4363(11)
Y1 – O8	2.4558(11)	Y2 – O17	2.4516(11)
Y1 – N1	2.5865(12)	Y2 – N12	2.5910(13)
Y1 – N2	2.5199(13)	Y2 – N13	2.5143(13)
Y1 – N5	2.6102(13)	Y2 – N16	2.5981(13)
Y1 – N6	2.5396(12)	Y2 – N17	2.5577(12)
N1 – Y1 – N2	64.23(8)	N12 – Y1 – N13	63.74(4)
N5 – Y1 – N6	62.84(8)	N16 – Y1 – N17	63.25(4)

Table S45. Selected bond lengths (Å) and bond angles (°) in **Eu_2_MeCN**.

Eu1 – O1	2.5113(15)	Eu2 – O10	2.4966(15)
Eu1 – O2	2.4903(14)	Eu2 – O11	2.5167(15)
Eu1 – O4	2.4921(15)	Eu2 – O13	2.5123(15)
Eu1 – O5	2.4959(15)	Eu2 – O14	2.5061(15)
Eu1 – O7	2.5448(14)	Eu2 – O16	2.4795(14)
Eu1 – O8	2.5001(15)	Eu2 – O17	2.4963(15)
Eu1 – N1	2.6070(16)	Eu2 – N12	2.6117(16)
Eu1 – N2	2.5621(16)	Eu2 – N13	2.5575(16)
Eu1 – N5	2.6318(16)	Eu2 – N16	2.6170(16)
Eu1 – N6	2.5790(16)	Eu2 – N17	2.6038(16)
N1 – Eu1 – N2	63.74(5)	N12 – Eu1 – N13	63.22(5)
N5 – Eu1 – N6	62.48(5)	N16 – Eu1 – N17	62.85(5)

Table S46. Average Ln–O and Ln–N bond lengths (Å) in **Eu$_2$_MeCN**, **Dy$_2$_MeCN** and **Y$_2$_MeCN**.

	Ln–O	Ln–N
Eu$_2$_MeCN	2.503	2.596
Dy$_2$_MeCN	2.469	2.569
Y$_2$_MeCN	2.456	2.565

Table S47. Relaxation fitting parameters from least-squares fitting of $\chi(f)$ between 1 and 1497 Hz under 1000 Oe dc field for complex **Dy$_2$_MeCN**.

Temperature (K)	χ_T	χ_S	α	*tau* (s)
2.0	4.42108	0.56702	0.14774	9.15507E-4
2.1	4.33963	0.53844	0.14481	7.38211E-4
2.3	4.04083	0.50571	0.13754	4.62075E-4
2.4	3.76184	0.42254	0.14624	2.84578E-4
2.5	3.69685	0.38222	0.13893	1.95802E-4
2.7	3.43904	0.02258	0.15926	7.36039E-5
2.8	3.28654	2.66698E-15	0.15443	4.74305E-5
2.9	3.21562	3.89479E-15	0.16046	3.09543E-5
3.1	3.0317	5.41356E-15	0.21842	1.16051E-5

Table S48. Calculated wave functions with definite projection of the total moment $|m_J>$ for the lowest two KDs of individual Dy^{III} fragments for **Dy$_2$_MeCN**.

	E/cm^{-1}	major wave functions*
1st Dy^{III}	0.0	40.5%|±15/2>+11.3%|±13/2>+15.4%|±11/2>+22.3%|±5/2>
	29.7	13.2%|±15/2>+13.0%|±11/2>+34.6%|±9/2>+23.2%|±5/2>
2nd Dy^{III}	0.0	41.7%|±15/2>+25.8%|±13/2>+12.0%|±11/2>
	40.1	11.3%|±9/2>+13.4%|±7/2>+25.4%|±5/2>+27.5%|±3/2>+13.0%|±1/2>

*Only components with contribution over 10% are listed.

Table S49. Energy separation of the eight kramers doublets in **Dy_2_MeCN** by fine structure of luminescence.

KD1	KD2	KD3	KD4	KD5	KD6	KD7	KD8
0.00	26.1	90.7	148.7	177.6	260.0	359.0	388.4

Table S50. Crystal Data and Structure Refinements for **Dy_4_NO_3**.

Complex	**Dy_4_NO_3**
Formula	$C_{56}H_{52}Dy_4N_{20}O_{18}$
Fw	1939.117
Temp(K)	150
Crystal system	monoclinic
Space group	$P2_1/n$
a (Å)	12.6035(4)
b (Å)	20.1706(7)
c (Å)	12.9533(4)
α (°)	90
β (°)	101.952(3)
γ (°)	90
Volume (Å^3)	3221.60(18)
Z	2
D_{calc} (g cm^{-3})	1.999
μ (mm^{-1})	4.672
F (000)	1865.5
R_{int}	0.1894
R_{sigma}	0.1350
Refl. (all)	33562
Refl (independent)	7102
R_1 (all)	0.1196
R_1 (> 2σ)	0.0622
wR_2 (all)	0.1499
wR_2 (> 2σ)	0.1192
GOF.	1.000

$$R_1 = \sum\big||F_o| - |F_c|\big| / \sum|F_o|, wR_2 = [\sum w(F_o^2 - F_c^2)^2 / \sum w(F_o^2)^2]^{1/2}$$

Table S51. Continuous Shape Measures for Dy^{III} ions in **Dy_4_NO_3** obtained using Shape v. 2.1.

label	shape	symmetry	Distortion of Dy1	Distortion of Dy2
OP-8	Octagon	D_{8h}	33.365	30.461
HPY-8	Heptagonal pyramid	C_{7v}	20.453	21.935
HBPY-8	Hexagonal bipyramid	D_{6h}	15.439	16.414
CU-8	Cube	O_h	10.886	10.214
SAPR-8	Square antiprism	D_{4d}	2.722	**1.157**
TDD-8	Triangular dodecahedron	D_{2d}	2.884	2.323
JGBF-8	Johnson gyrobifastigium J26	D_{2d}	13.920	14.183
JETBPY-8	Johnson elongated triangular bipyramid J14	D_{3h}	27.774	27.983
JBTPR-8	Biaugmented trigonal prism J50	C_{2v}	2.906	2.930
BTPR-8	Biaugmented trigonal prism	C_{2v}	**2.225**	1.987
JSD-8	Snub diphenoid J84	D_{2d}	5.124	4.655
TT-8	Triakis tetrahedron	T_d	11.636	11.006
ETBPY-8	Elongated trigonal bipyramid	D_{3h}	22.805	22.850

Table S52. Relaxation fitting parameters from least-squares fitting of $\chi(f)$ between 1 and 1000 Hz under zero dc field for complex **Dy_4_NO_3**.

Temperature(K)	χ_T	χ_S	α	*tau* (s)
7.0	8.17149	0.45034	0.31748	0.11713
8.0	7.15659	0.43656	0.27197	0.06307
9.0	6.32988	0.4081	0.24292	0.03467
10.0	5.63169	0.39041	0.21256	0.01972
11.0	5.15299	0.36189	0.20941	0.01231
12.0	4.70243	0.32966	0.21288	0.00759
12.5	4.49893	0.34364	0.19629	0.00589
13.0	4.39299	0.35429	0.19336	0.00479
13.5	4.23842	0.35311	0.19483	0.00381
14.0	4.10318	0.34081	0.20553	0.00305
14.5	3.9482	0.34561	0.20491	0.0024
15.0	3.81193	0.33625	0.21561	0.00191
15.5	3.7351	0.342	0.22659	0.00159
16.0	3.57355	0.35253	0.23265	0.00128
16.5	3.44451	0.39095	0.23106	0.00106
17.0	3.33926	0.42698	0.23613	8.91056E-4
17.5	3.24981	0.45908	0.24514	7.52845E-4
18.0	3.15733	0.53159	0.23902	6.67848E-4
18.5	3.14814	0.62382	0.23539	6.24653E-4
19.0	3.00546	0.68666	0.21602	5.2998E-4
19.5	2.91171	0.76674	0.19987	4.82922E-4
20.0	2.85182	0.80419	0.2087	4.4638E-4
20.5	2.76417	0.8909	0.18332	4.13859E-4
21.0	2.69345	0.91904	0.17211	3.63622E-4
21.5	2.63445	0.96552	0.1632	3.3657E-4
22.0	2.5627	1.02578	0.12995	3.09007E-4
22.5	2.5006	1.0836	0.10369	2.79238E-4
23.0	2.45605	1.06183	0.11641	2.37266E-4

Table S53. Calculated wave functions with definite projection of the total moment | m_J > for the lowest two KDs of individual Dy^{III} fragments for **Dy_4_NO_3**.

	E/cm^{-1}	major wave functions*
Dy1	0.0	98.6%|±15/2>+0.5%|±11/2>
	202.1	61.7%|±13/2>+7.6%|±11/2>+8.4%|±9/2>+7.6%|±5/2>
Dy2	0.0	97.8%|±15/2>+1.1%|±11/2>
	117.8	81.5%|±13/2>+7.9%|±9/2>

*Only the top two major components or the components with contribution over 6% are listed.

Table S54. Crystal Data and Structure Refinements for **Dy_4_Cl**.

Complex	**Dy_4_Cl**
Formula	$C_{62}H_{68}Cl_6Dy_4N_{16}O_7$
Fw	2012.02
Temp(K)	150
Crystal system	monoclinic
Space group	$P2_1/c$
a (Å)	12.9174(3)
b (Å)	23.9081(6)
c (Å)	12.1938(3)
α (°)	90
β (°)	114.140(2)
γ (°)	90
Volume (Å^3)	3436.49(15)
Z	2
D_{calc} (g cm^{-3})	1.944
μ (mm^{-1})	24.340
F (000)	1948.0
R_{int}	0.0293
R_{sigma}	0.0259
Refl. (all)	42263
Refl (independent)	8256
R_1 (all)	0.0368
R_1 (> 2σ)	0.0270
wR_2 (all)	0.0649
wR_2 (> 2σ)	0.0623
GOF.	1.016

$$R_1 = \sum\big||F_o| - |F_c|\big| / \sum|F_o|,\ wR_2 = [\sum w(F_o^2 - F_c^2)^2 / \sum w(F_o^2)^2]^{1/2}$$

Table S55. Continuous Shape Measures for Dy^{III} ions in **Dy_4_Cl** obtained using Shape v. 2.1.

label	shape	symmetry	Distortion of Dy1	Distortion of Dy2
OP-8	Octagon	D_{8h}	30.234	30.714
HPY-8	Heptagonal pyramid	C_{7v}	22.510	22.769
HBPY-8	Hexagonal bipyramid	D_{6h}	14.637	14.500
CU-8	Cube	O_h	7.931	9.386
SAPR-8	Square antiprism	D_{4d}	**1.370**	**1.522**
TDD-8	Triangular dodecahedron	D_{2d}	2.122	2.117
JGBF-8	Johnson gyrobifastigium J26	D_{2d}	15.611	14.695
JETBPY-8	Johnson elongated triangular bipyramid J14	D_{3h}	27.946	28.202
JBTPR-8	Biaugmented trigonal prism J50	C_{2v}	3.768	3.031
BTPR-8	Biaugmented trigonal prism	C_{2v}	2.670	2.790
JSD-8	Snub diphenoid J84	D_{2d}	5.589	5.083
TT-8	Triakis tetrahedron	T_d	8.793	10.144
ETBPY-8	Elongated trigonal bipyramid	D_{3h}	23.365	24.014

Table S56. Relaxation fitting parameters from least-squares fitting of $\chi(f)$ between 1 and 1000 Hz under zero dc field for complex **Dy_4_Cl**.

Temperature(K)	χ_T	χ_S	α	*tau* (s)
6	6.41418	1.01341	0.37751	0.11243
6.5	5.82588	0.97214	0.34978	0.07766
7	5.34969	0.93488	0.32543	0.05511
7.5	4.94979	0.8994	0.30467	0.03996
8	4.62489	0.86603	0.28821	0.02989
8.5	4.3736	0.83436	0.27735	0.02324
9	4.11302	0.80861	0.26362	0.01777
9.5	3.90182	0.78296	0.25456	0.01395
10	3.70094	0.75936	0.24716	0.01098
10.5	3.53328	0.74009	0.23992	0.0088
11	3.37464	0.72169	0.23441	0.00707
11.5	3.23199	0.70691	0.22959	0.0057
12	3.10436	0.69398	0.22571	0.00464
12.5	2.99137	0.6797	0.2248	0.00378
13	2.8801	0.67127	0.22174	0.00307
13.5	2.78457	0.66453	0.22258	0.00253
14	2.68478	0.66173	0.2199	0.00206
14.5	2.58902	0.66352	0.21446	0.00168
15	2.51479	0.66358	0.21692	0.00138
15.5	2.43673	0.66958	0.21579	0.00114
16	2.36356	0.68555	0.21334	9.49014E-4
16.5	2.29604	0.68359	0.21291	7.75351E-4
17	2.22928	0.70097	0.20875	6.45431E-4
17.5	2.16754	0.71119	0.20512	5.36588E-4
18	2.10836	0.73148	0.20035	4.50141E-4
18.5	2.054	0.76117	0.1934	3.83693E-4
19	2.0057	0.76825	0.19586	3.19703E-4
19.5	1.95216	0.80814	0.18006	2.78284E-4
20	1.90954	0.81233	0.18072	2.33437E-4

References

(1) Balaram, V. Rare earth elements: A review of applications, occurrence, exploration, analysis, recycling, and environmental impact. *Geoscience Frontiers* **2019**, *10* (4), 1285-1303.

(2) Haynes, W. M.; Lide, D. R.; Bruno, T. Abundance of elements in the earth's crust and in the sea. *CRC handbook of chemistry and physics* **2016**, *97* (2402), 14-17.

(3) MacDonald, M. R.; Bates, J. E.; Ziller, J. W.; Furche, F.; Evans, W. J. Completing the Series of +2 Ions for the Lanthanide Elements: Synthesis of Molecular Complexes of Pr2+, Gd2+, Tb2+, and Lu2+. *Journal of the American Chemical Society* **2013**, *135* (26), 9857-9868.

(4) So, Y.-M.; Leung, W.-H. Recent advances in the coordination chemistry of cerium(IV) complexes. *Coordination Chemistry Reviews* **2017**, *340*, 172-197.

(5) Gompa, T. P.; Ramanathan, A.; Rice, N. T.; La Pierre, H. S. The chemical and physical properties of tetravalent lanthanides: Pr, Nd, Tb, and Dy. *Dalton Transactions* **2020**, *49* (45), 15945-15987.

(6) Willauer, A. R.; Palumbo, C. T.; Scopelliti, R.; Zivkovic, I.; Douair, I.; Maron, L.; Mazzanti, M. Stabilization of the Oxidation State +IV in Siloxide-Supported Terbium Compounds. *Angewandte Chemie International Edition* **2020**, *59* (9), 3549-3553.

(7) Willauer, A. R.; Palumbo, C. T.; Fadaei-Tirani, F.; Zivkovic, I.; Douair, I.; Maron, L.; Mazzanti, M. Accessing the +IV Oxidation State in Molecular Complexes of Praseodymium. *Journal of the American Chemical Society* **2020**, *142* (12), 5538-5542.

(8) Zhang, Q.; O'Brien, S.; Grimm, J. Biomedical Applications of Lanthanide Nanomaterials, for Imaging, Sensing and Therapy. *Nanotheranostics* **2022**, *6* (2), 184-194.

(9) Hermann, P.; Kotek, J.; Kubíček, V.; Lukeš, I. Gadolinium(iii) complexes as MRI contrast agents: ligand design and properties of the complexes. *Dalton Transactions* **2008**, (23), 3027-3047.

(10) Marin, R.; Brunet, G.; Murugesu, M. Shining New Light on Multifunctional Lanthanide Single-Molecule Magnets. *Angewandte Chemie International Edition* **2021**, *60* (4), 1728-1746.

(11) Keyes, R. W. The Impact of Moore's Law. *IEEE Solid-State Circuits Society Newsletter* **2006**, *11* (3), 25-27.

(12) Bogani, L.; Wernsdorfer, W. Molecular spintronics using single-molecule magnets. *Nature Materials* **2008**, *7* (3), 179-186.

(13) Ladd, T. D.; Jelezko, F.; Laflamme, R.; Nakamura, Y.; Monroe, C.; O'Brien, J. L. Quantum computers. *Nature* **2010**, *464* (7285), 45-53.

(14) Neese, F.; Pantazis, D. A. What is not required to make a single molecule magnet. *Faraday Discussions* **2011**, *148* (0), 229-238.

(15) Topping, C. V.; Blundell, S. J. A.C. susceptibility as a probe of low-frequency magnetic dynamics. *J Phys Condens Matter* **2019**, *31* (1), 013001.

(16) Guo, Y.-N.; Xu, G.-F.; Guo, Y.; Tang, J. Relaxation dynamics of dysprosium(iii) single molecule magnets. *Dalton Transactions* **2011**, *40* (39), 9953-9963.

(17) Reta, D.; Chilton, N. F. Uncertainty estimates for magnetic relaxation times and magnetic relaxation parameters. *Physical Chemistry Chemical Physics* **2019**, *21* (42), 23567-23575.

(18) Blackmore, W. J. A.; Gransbury, G. K.; Evans, P.; Kragskow, J. G. C.; Mills, D. P.; Chilton, N. F. Characterisation of magnetic relaxation on extremely long timescales. *Physical Chemistry Chemical Physics* **2023**, *25* (25), 16735-16744.

(19) Carilin, R. L. Magnetochemistry, Springer-Verlag, New York, 1986.

(20) Zhu, Z.; Guo, M.; Li, X.-L.; Tang, J. Molecular magnetism of lanthanide: Advances and perspectives. *Coordination Chemistry Reviews* **2019**, *378*, 350-364.

(21) Ding, Y.-S.; Yu, K.-X.; Reta, D.; Ortu, F.; Winpenny, R. E. P.; Zheng, Y.-Z.; Chilton, N. F. Field- and temperature-dependent quantum tunnelling of the magnetisation in a large barrier single-molecule magnet. *Nature Communications* **2018**, *9* (1), 3134.

(22) Ungur, L.; Le Roy, J. J.; Korobkov, I.; Murugesu, M.; Chibotaru, L. F. Fine-tuning the Local Symmetry to Attain Record Blocking Temperature and Magnetic Remanence in a Single-Ion Magnet. *Angewandte Chemie International Edition* **2014**, *53* (17), 4413-4417.

(23) Sessoli, R.; Gatteschi, D.; Caneschi, A.; Novak, M. A., Magnetic bistability in a metal-ion cluster. *Nature* **1993,** *365* (6442), 141-143.

(24) Castro, S. L.; Sun, Z.; Grant, C. M.; Bollinger, J. C.; Hendrickson, D. N.; Christou, G. Single-Molecule Magnets: Tetranuclear Vanadium(III) Complexes with a Butterfly Structure and an S = 3 Ground State. *Journal of the American Chemical Society* **1998**, *120* (10), 2365-2375.

(25) Sangregorio, C.; Ohm, T.; Paulsen, C.; Sessoli, R.; Gatteschi, D., Quantum Tunneling of the Magnetization in an Iron Cluster Nanomagnet. *Physical Review Letters* **1997,** *78*, 4645-4648.

(26) Yang, E.-C.; Hendrickson, D. N.; Wernsdorfer, W.; Nakano, M.; Zakharov, L. N.; Sommer, R. D.; Rheingold, A. L.; Ledezma-Gairaud, M.; Christou, G. Cobalt single-molecule magnet. *Journal of Applied Physics* **2002**, *91* (10), 7382-7384.

(27) Waldmann, O. A Criterion for the Anisotropy Barrier in Single-Molecule Magnets. *Inorganic Chemistry* **2007**, *46* (24), 10035-10037.

(28) Das, A.; Gieb, K.; Krupskaya, Y.; Demeshko, S.; Dechert, S.; Klingeler, R.; Kataev, V.; Büchner, B.; Müller, P.; Meyer, F. A New Family of 1D Exchange Biased Heterometal Single-Molecule Magnets: Observation of Pronounced Quantum Tunneling Steps in the Hysteresis Loops of Quasi-Linear {Mn2Ni3} Clusters. *Journal of the American Chemical Society* **2011**, *133* (10), 3433-3443.

(29) Hu, Z.-B.; Jing, Z.-Y.; Li, M.-M.; Yin, L.; Gao, Y.-D.; Yu, F.; Hu, T.-P.; Wang, Z.; Song, Y. Important Role of Intermolecular Interaction in Cobalt(II) Single-Ion Magnet from Single Slow Relaxation to Double Slow Relaxation. *Inorganic Chemistry* **2018**, *57* (17), 10761-10767.

(30) Pavlov, A. A.; Nelyubina, Y. V.; Kats, S. V.; Penkova, L. V.; Efimov, N. N.; Dmitrienko, A. O.; Vologzhanina, A. V.; Belov, A. S.; Voloshin, Y. Z.; Novikov, V. V. Polymorphism in a Cobalt-Based Single-Ion Magnet Tuning Its Barrier to Magnetization Relaxation. *The Journal of Physical Chemistry Letters* **2016**, *7* (20), 4111-4116.

(31) Zadrozny, J. M.; Xiao, D. J.; Atanasov, M.; Long, G. J.; Grandjean, F.; Neese, F.; Long, J. R. Magnetic blocking in a linear iron(I) complex. *Nature Chemistry* **2013**, *5* (7), 577-581.

(32) Meng, Y.-S.; Mo, Z.; Wang, B.-W.; Zhang, Y.-Q.; Deng, L.; Gao, S. Observation of the single-ion magnet behavior of d8 ions on two-coordinate Co(i)–NHC complexes. *Chemical Science* **2015**, *6* (12), 7156-7162.

(33) Ishikawa, N.; Sugita, M.; Ishikawa, T.; Koshihara, S.-y.; Kaizu, Y. Lanthanide Double-Decker Complexes Functioning as Magnets at the Single-Molecular Level. *Journal of the American Chemical Society* **2003**, *125* (29), 8694-8695.

(34) Kramers, H. General theory of paramagnetic rotation in crystals. In *Proc. Acad. Sci. Amsterdam*, 1930; Vol. 33, p 959.

(35) Guo, F.-S.; Day, B. M.; Chen, Y.-C.; Tong, M.-L.; Mansikkamäki, A.; Layfield, R. A. Magnetic hysteresis up to 80 kelvin in a dysprosium metallocene single-molecule magnet. *Science* **2018**, *362* (6421), 1400-1403.

(36) Izuogu, D. C.; Yoshida, T.; Cosquer, G.; Asegbeloyin, J. N.; Zhang, H.; Thom, A. J. W.; Yamashita, M. Periodicity of Single-Molecule Magnet Behaviour of Heterotetranuclear Lanthanide Complexes across the Lanthanide Series: A Compendium. *Chemistry – A European Journal* **2020**, *26* (27), 6036-6049.

(37) Gould, C. A.; McClain, K. R.; Yu, J. M.; Groshens, T. J.; Furche, F.; Harvey, B. G.; Long, J. R. Synthesis and Magnetism of Neutral, Linear Metallocene Complexes of Terbium(II) and Dysprosium(II). *Journal of the American Chemical Society* **2019**, *141* (33), 12967-12973.

(38) Tang, J.; Hewitt, I.; Madhu, N. T.; Chastanet, G.; Wernsdorfer, W.; Anson, C. E.; Benelli, C.; Sessoli, R.; Powell, A. K. Dysprosium Triangles Showing Single-Molecule Magnet Behavior of Thermally Excited Spin States. *Angewandte Chemie International Edition* **2006**, *45* (11), 1729-1733.

(39) D'Alessio, D.; Sobolev, A. N.; Skelton, B. W.; Fuller, R. O.; Woodward, R. C.; Lengkeek, N. A.; Fraser, B. H.; Massi, M.; Ogden, M. I. Lanthanoid "Bottlebrush" Clusters: Remarkably Elongated Metal–Oxo Core Structures with Controllable Lengths. *Journal of the American Chemical Society* **2014**, *136* (43), 15122-15125.

(40) Wang, Y.; Li, X.-L.; Wang, T.-W.; Song, Y.; You, X.-Z. Slow Relaxation Processes and Single-Ion Magnetic Behaviors in Dysprosium-Containing Complexes. *Inorganic Chemistry* **2010**, *49* (3), 969-976.

(41) Gould, C. A.; McClain, K. R.; Reta, D.; Kragskow, J. G. C.; Marchiori, D. A.; Lachman, E.; Choi, E.-S.; Analytis, J. G.; Britt, R. D.; Chilton, N. F.; et al. Ultrahard magnetism from mixed-valence dilanthanide complexes with metal-metal bonding. *Science* **2022**, *375* (6577), 198-202.

(42) Xin, J.; Hu, Z.; Yao, Y.-R.; Ullah, A.; Han, X.; Xiang, W.; Jin, H.; Jiang, Z.; Yang, S. Short Didysprosium Covalent Bond Enables High Magnetization Blocking Temperature of a Direct 4f–4f Coupled Dinuclear Single-Molecule Magnet. *Journal of the American Chemical Society* **2024**, *146* (26), 17600-17605.

(43) Osa, S.; Kido, T.; Matsumoto, N.; Re, N.; Pochaba, A.; Mrozinski, J., A Tetranuclear 3d−4f Single Molecule Magnet: [CuIILTbIII(hfac)2]2. *Journal of the American Chemical Society* **2004,** *126* (2), 420-421.

(44) Langley, S. K.; Wielechowski, D. P.; Vieru, V.; Chilton, N. F.; Moubaraki, B.; Chibotaru, L. F.; Murray, K. S. The first 4d/4f single-molecule magnet containing a {RuIII2DyIII2} core. *Chemical Communications* **2015**, *51* (11), 2044-2047.

(45) Chatelain, L.; Walsh, J. P. S.; Pécaut, J.; Tuna, F.; Mazzanti, M. Self-Assembly of a 3d–5f Trinuclear Single-Molecule Magnet from a Pentavalent Uranyl Complex. *Angewandte Chemie International Edition* **2014**, *53* (49), 13434-13438.

(46) Li, Q.-W.; Wan, R.-C.; Chen, Y.-C.; Liu, J.-L.; Wang, L.-F.; Jia, J.-H.; Chilton, N. F.; Tong, M.-L. Unprecedented hexagonal bipyramidal single-ion magnets based on metallacrowns. *Chemical Communications* **2016**, *52* (91), 13365-13368.

(47) Cirera, J.; Ruiz, E.; Alvarez, S. Shape and Spin State in Four-Coordinate Transition-Metal Complexes: The Case of the d6 Configuration. *Chemistry – A European Journal* **2006**, *12* (11), 3162-3167.

(48) Liu, J.-L.; Wu, J.-Y.; Chen, Y.-C.; Mereacre, V.; Powell, A. K.; Ungur, L.; Chibotaru, L. F.; Chen, X.-M.; Tong, M.-L. A Heterometallic FeII–DyIII Single-Molecule Magnet with a Record Anisotropy Barrier. *Angewandte Chemie International Edition* **2014**, *53* (47), 12966-12970.

(49) Wu, S.-G.; Ruan, Z.-Y.; Huang, G.-Z.; Zheng, J.-Y.; Vieru, V.; Taran, G.; Wang, J.; Chen, Y.-C.; Liu, J.-L.; Ho, L. T. A.; Chibotaru, L. F.; Wernsdorfer, W.; Chen, X.-M.; Tong, M.-L., Field-induced oscillation of magnetization blocking barrier in a holmium metallacrown single-molecule magnet. *Chem* **2021,** *7* (4), 982-992.

(50) Ling, B.-K.; Zhai, Y.-Q.; Jin, P.-B.; Ding, H.-F.; Zhang, X.-F.; Lv, Y.; Fu, Z.; Deng, J.; Schulze, M.; Wernsdorfer, W.; et al. Suppression of zero-field quantum tunneling of magnetization by a fluorido bridge for a "very hard" 3d-4f single-molecule magnet. *Matter* **2022**, *5* (10), 3485-3498.

(51) Li, X.-L.; Min, F.-Y.; Wang, C.; Lin, S.-Y.; Liu, Z.; Tang, J. Utilizing 3d–4f Magnetic Interaction to Slow the Magnetic Relaxation of Heterometallic Complexes. *Inorganic Chemistry* **2015**, *54* (9), 4337-4344.

(52) Huang, G.-Z.; Ruan, Z.-Y.; Zheng, J.-Y.; Wu, J.-Y.; Chen, Y.-C.; Li, Q.-W.; Akhtar, M. N.; Liu, J.-L.; Tong, M.-L. Enhancing single-molecule magnet behavior of linear CoII-DyIII-CoII complex by introducing bulky diamagnetic moiety. *Science China Chemistry* **2018**, *61* (11), 1399-1404.

(53) Li, G.-P.; Tang, H.-Z.; Gao, R.-C.; Wang, Y.-Y.; Sun, X.; Zhang, K. Tuning Quantum Tunneling in Isomorphic {MII2DyIII2} "Butterfly" System via 3d-4f Magnetic Interaction. *Crystal Growth & Design* **2023**, *23* (3), 1575-1580.

(54) Peng, Y.; Mereacre, V.; Anson, C. E.; Powell, A. K. Butterfly M2IIIEr2 (MIII = Fe and Al) SMMs: Synthesis, Characterization, and Magnetic Properties. *ACS Omega* **2018**, *3* (6), 6360-6368.

(55) Vignesh, K. R.; Langley, S. K.; Murray, K. S.; Rajaraman, G. Exploring the Influence of Diamagnetic Ions on the Mechanism of Magnetization Relaxation in {CoIII2LnIII2} (Ln = Dy, Tb, Ho) "Butterfly" Complexes. *Inorganic Chemistry* **2017**, *56* (5), 2518-2532.

(56) Li, S.; Xiong, J.; Yuan, Q.; Zhu, W.-H.; Gong, H.-W.; Wang, F.; Feng, C.-Q.; Wang, S.-Q.; Sun, H.-L.; Gao, S. Effect of the Transition Metal Ions on the Single-Molecule Magnet Properties in a Family of Air-Stable

3d–4f Ion-Pair Compounds with Pentagonal Bipyramidal Ln(III) Ions. *Inorganic Chemistry* **2021**, *60* (24), 18990-19000.

(57) Ishikawa, N.; Sugita, M.; Tanaka, N.; Ishikawa, T.; Koshihara, S.-y.; Kaizu, Y. Upward Temperature Shift of the Intrinsic Phase Lag of the Magnetization of Bis(phthalocyaninato)terbium by Ligand Oxidation Creating an S = 1/2 Spin. *Inorganic Chemistry* **2004**, *43* (18), 5498-5500.

(58) Demir, S.; Gonzalez, M. I.; Darago, L. E.; Evans, W. J.; Long, J. R. Giant coercivity and high magnetic blocking temperatures for N23− radical-bridged dilanthanide complexes upon ligand dissociation. *Nature Communications* **2017**, *8* (1), 2144.

(59) Tan, G.; Li, J.; Zhang, L.; Chen, C.; Zhao, Y.; Wang, X.; Song, Y.; Zhang, Y. Q.; Driess, M. The Charge Transfer Approach to Heavier Main-Group Element Radicals in Transition-Metal Complexes. *Angewandte Chemie International Edition* **2017**, *56* (41), 12741-12745.

(60) Mavragani, N.; Kitos, A. A.; Brusso, J. L.; Murugesu, M. Enhancing Magnetic Communication between Metal Centres: The Role of s-Tetrazine Based Radicals as Ligands. *Chemistry – A European Journal* **2021**, *27* (16), 5091-5106.

(61) Woods, T. J.; Ballesteros-Rivas, M. F.; Ostrovsky, S. M.; Palii, A. V.; Reu, O. S.; Klokishner, S. I.; Dunbar, K. R. Strong Direct Magnetic Coupling in a Dinuclear CoII Tetrazine Radical Single-Molecule Magnet. *Chemistry – A European Journal* **2015**, *21* (29), 10302-10305.

(62) Liu, J.-L.; Chen, Y.-C.; Tong, M.-L. Symmetry strategies for high performance lanthanide-based single-molecule magnets. *Chemical Society Reviews* **2018**, *47* (7), 2431-2453.

(63) Ding, Y.-S.; Chilton, N. F.; Winpenny, R. E. P.; Zheng, Y.-Z. On Approaching the Limit of Molecular Magnetic Anisotropy: A Near-Perfect Pentagonal Bipyramidal Dysprosium(III) Single-Molecule Magnet. *Angewandte Chemie International Edition* **2016**, *55* (52), 16071-16074.

(64) AlDamen, M. A.; Clemente-Juan, J. M.; Coronado, E.; Martí-Gastaldo, C.; Gaita-Ariño, A. Mononuclear Lanthanide Single-Molecule Magnets Based on Polyoxometalates. *Journal of the American Chemical Society* **2008**, *130* (28), 8874-8875.

(65) Zhang, P.; Zhang, L.; Wang, C.; Xue, S.; Lin, S.-Y.; Tang, J. Equatorially Coordinated Lanthanide Single Ion Magnets. *Journal of the American Chemical Society* **2014**, *136* (12), 4484-4487.

(66) Wu, X.; Li, J.-F.; Yin, B. The interpretation and prediction of lanthanide single-ion magnets from ab initio electronic structure calculation: the capability and limit. *Dalton Transactions* **2022**, *51* (39), 14793-14816.

(67) Rinehart, J. D.; Long, J. R. Exploiting single-ion anisotropy in the design of f-element single-molecule magnets. *Chemical Science* **2011**, *2* (11), 2078-2085.

(68) Gregson, M.; Chilton, N. F.; Ariciu, A.-M.; Tuna, F.; Crowe, I.; Lewis, W.; Blake, A. J.; Collison, D.; McInnes, E.; Winpenny, R.; et al. A Monometallic Lanthanide Bis(methanediide) Single Molecule Magnet with a Large Energy Barrier and Complex Spin Relaxation Behaviour. *Chemical Science* **2016**, *7*, 155-165.

(69) Blagg, R. J.; Ungur, L.; Tuna, F.; Speak, J.; Comar, P.; Collison, D.; Wernsdorfer, W.; McInnes, E. J. L.; Chibotaru, L. F.; Winpenny, R. E. P. Magnetic relaxation pathways in lanthanide single-molecule magnets. *Nature Chemistry* **2013**, *5* (8), 673-678.

(70) Ungur, L.; Chibotaru, L. F., Magnetic anisotropy in the excited states of low symmetry lanthanide complexes. *Phys. Chem. Chem. Phys.* **2011,** *13* (45), 20086.

(71) Ungur, L.; Chibotaru, L. F. Magnetic anisotropy in the excited states of low symmetry lanthanide complexes. *Physical Chemistry Chemical Physics* **2011**, *13* (45), 20086-20090.

(72) Pointillart, F.; Bernot, K.; Golhen, S.; Le Guennic, B.; Guizouarn, T.; Ouahab, L.; Cador, O. Magnetic Memory in an Isotopically Enriched and Magnetically Isolated Mononuclear Dysprosium Complex. *Angewandte Chemie International Edition* **2015**, *54* (5), 1504-1507.

(73) Moreno-Pineda, E.; Damjanović, M.; Fuhr, O.; Wernsdorfer, W.; Ruben, M., Nuclear Spin Isomers: Engineering a $Et_4N[DyPc_2]$ Spin Qudit. *Angewandte Chemie International Edition* **2017,** *56* (33), 9915-9919.

(74) Ruan, T.-T.; Moreno-Pineda, E.; Paul, S.; Schulze, M.; Schlittenhardt, S.; Mizuno, A.; Wernsdorfer, W.; Ruben, M. Modulating quantum tunnelling of magnetization in Dy isotopologue dimers. *Dalton Transactions* **2024**, *53* (42), 17281-17290.

(75) Yu, L.; Reutzel-Edens, S. M.; Mitchell, C. A. Crystallization and Polymorphism of Conformationally Flexible Molecules: Problems, Patterns, and Strategies. *Organic Process Research & Development* **2000**, *4* (5), 396-402.

(76) Aime, S.; Botta, M.; Garda, Z.; Kucera, B. E.; Tircso, G.; Young, V. G.; Woods, M. Properties, Solution State Behavior, and Crystal Structures of Chelates of DOTMA. *Inorganic Chemistry* **2011**, *50* (17), 7955-7965.

(77) Cosquer, G.; Pointillart, F.; Golhen, S.; Cador, O.; Ouahab, L. Slow Magnetic Relaxation in Condensed versus Dispersed Dysprosium(III) Mononuclear Complexes. *Chemistry – A European Journal* **2013**, *19* (24), 7895-7903.

(78) Moreno Pineda, E.; Komeda, T.; Katoh, K.; Yamashita, M.; Ruben, M. Surface confinement of TbPc2-SMMs: structural, electronic and magnetic properties. *Dalton Transactions* **2016**, *45* (46), 18417-18433.

(79) Ungur, L.; Chibotaru, L. F. Strategies toward High-Temperature Lanthanide-Based Single-Molecule Magnets. *Inorganic Chemistry* **2016**, *55* (20), 10043-10056.

(80) Aulakh, D.; Xie, H.; Shen, Z.; Harley, A.; Zhang, X.; Yakovenko, A. A.; Dunbar, K. R.; Wriedt, M. Systematic Investigation of Controlled Nanostructuring of Mn12 Single-Molecule Magnets Templated by Metal–Organic Frameworks. *Inorganic Chemistry* **2017**, *56* (12), 6965-6972.

(81) Habib, F.; Lin, P.-H.; Long, J.; Korobkov, I.; Wernsdorfer, W.; Murugesu, M. The Use of Magnetic Dilution To Elucidate the Slow Magnetic Relaxation Effects of a Dy2 Single-Molecule Magnet. *Journal of the American Chemical Society* **2011**, *133* (23), 8830-8833.

(82) Moreno Pineda, E.; Chilton, N. F.; Marx, R.; Dörfel, M.; Sells, D. O.; Neugebauer, P.; Jiang, S.-D.; Collison, D.; van Slageren, J.; McInnes, E. J. L.; et al. Direct measurement of dysprosium(III)···dysprosium(III) interactions in a single-molecule magnet. *Nature Communications* **2014**, *5* (1), 5243.

(83) Lyu, D.-P.; Zheng, J.-Y.; Li, Q.-W.; Liu, J.-L.; Chen, Y.-C.; Jia, J.-H.; Tong, M.-L. Construction of lanthanide single-molecule magnets with the "magnetic motif" [Dy(MQ)4]−. *Inorganic Chemistry Frontiers* **2017**, *4* (11), 1776-1782.

(84) Guo, Y.-N.; Xu, G.-F.; Wernsdorfer, W.; Ungur, L.; Guo, Y.; Tang, J.; Zhang, H.-J.; Chibotaru, L. F.; Powell, A. K. Strong Axiality and Ising Exchange Interaction Suppress Zero-Field Tunneling of Magnetization of an Asymmetric Dy2 Single-Molecule Magnet. *Journal of the American Chemical Society* **2011**, *133* (31), 11948-11951.

(85) Buchner, M.; Höfler, K.; Henne, B.; Ney, V.; Ney, A. Tutorial: Basic principles, limits of detection, and pitfalls of highly sensitive SQUID magnetometry for nanomagnetism and spintronics. *Journal of Applied Physics* **2018**, *124* (16).

(86) Wernsdorfer, W. From micro- to nano-SQUIDs: applications to nanomagnetism. *Superconductor Science and Technology* **2009**, *22* (6), 064013.

(87) Roos, B. O.; Taylor, P. R.; Sigbahn, P. E. M. A complete active space SCF method (CASSCF) using a density matrix formulated super-CI approach. *Chemical Physics* **1980**, *48* (2), 157-173.

(88) Aquilante, F.; Autschbach, J.; Carlson, R. K.; Chibotaru, L. F.; Delcey, M. G.; De Vico, L.; Fdez. Galván, I.; Ferré, N.; Frutos, L. M.; Gagliardi, L.; et al. Molcas 8: New capabilities for multiconfigurational quantum chemical calculations across the periodic table. *Journal of Computational Chemistry* **2016**, *37* (5), 506-541.

(89) Kollmar, C.; Sivalingam, K.; Guo, Y.; Neese, F. An efficient implementation of the NEVPT2 and CASPT2 methods avoiding higher-order density matrices. *The Journal of Chemical Physics* **2021**, *155* (23).

(90) Fdez. Galván, I.; Vacher, M.; Alavi, A.; Angeli, C.; Aquilante, F.; Autschbach, J.; Bao, J. J.; Bokarev, S. I.; Bogdanov, N. A.; Carlson, R. K.; et al. OpenMolcas: From Source Code to Insight. *Journal of Chemical Theory and Computation* **2019**, *15* (11), 5925-5964.

(91) Aquilante, F.; Autschbach, J.; Baiardi, A.; Battaglia, S.; Borin, V. A.; Chibotaru, L. F.; Conti, I.; De Vico, L.; Delcey, M.; Fdez. Galván, I.; et al. Modern quantum chemistry with [Open]Molcas. *The Journal of Chemical Physics* **2020**, *152* (21).

(92) Chilton, N. F.; Anderson, R. P.; Turner, L. D.; Soncini, A.; Murray, K. S. PHI: a powerful new program for the analysis of anisotropic monomeric and exchange-coupled polynuclear d- and f-block complexes. *J Comput Chem* **2013**, *34* (13), 1164-1175.

(93) Schweizer, T.; Kubach, H.; Koch, T. Investigations to characterize the interactions of light radiation, engine operating media and fluorescence tracers for the use of qualitative light-induced fluorescence in engine systems. *Automotive and Engine Technology* **2021**, *6* (3), 275-287.

(94) Kreidt, E.; Kruck, C.; Seitz, M. Chapter 300 - Nonradiative Deactivation of Lanthanoid Luminescence by Multiphonon Relaxation in Molecular Complexes. In *Handbook on the Physics and Chemistry of Rare Earths*, Bünzli, J.-C. G., Pecharsky, V. K. Eds.; Vol. 53; Elsevier, 2018; pp 35-79.

(95) Carnall, W. T.; Fields, P. R.; Rajnak, K. Electronic Energy Levels in the Trivalent Lanthanide Aquo Ions. I. Pr3+, Nd3+, Pm3+, Sm3+, Dy3+, Ho3+, Er3+, and Tm3+. *The Journal of Chemical Physics* **1968**, *49* (10), 4424-4442.

(96) Carnall, W. T.; Goodman, G. L.; Rajnak, K.; Rana, R. S. A systematic analysis of the spectra of the lanthanides doped into single crystal LaF3 *The Journal of Chemical Physics* **1989**, *90* (7), 3443-3457.

(97) Kariaka, N. S.; Smola, S. S.; Halushchenko, V. S.; Rusakova, N. V.; Sliva, T. Y.; Amirkhanov, V. M. Dual near infrared and visible highly luminescent samarium complexes based on dimethyl-N-benzoylamidophosphate. *Chemical Papers* **2023**, *77* (10), 5989-5997.

(98) Golesorkhi, B.; Nozary, H.; Fürstenberg, A.; Piguet, C. Erbium complexes as pioneers for implementing linear light-upconversion in molecules. *Materials Horizons* **2020**, *7* (5), 1279-1296.

(99) Law, G.-L.; Wong, K.-L.; Tam, H.-L.; Cheah, K.-W.; Wong, W.-T. White OLED with a Single-Component Europium Complex. *Inorganic Chemistry* **2009**, *48* (22), 10492-10494.

(100) Ahmed, Z.; Iftikhar, K. Efficient Layers of Emitting Ternary Lanthanide Complexes for Fabricating Red, Green, and Yellow OLEDs. *Inorganic Chemistry* **2015**, *54* (23), 11209-11225.

(101) Zhang, K.; Kang, J. U. C-band wavelength-swept single-longitudinal-mode erbium-doped fiber ring laser. *Optics Express* **2008**, *16* (18), 14173-14179.

(102) Zheng, X.-L.; Liu, Y.; Pan, M.; Lü, X.-Q.; Zhang, J.-Y.; Zhao, C.-Y.; Tong, Y.-X.; Su, C.-Y. Bright Blue-Emitting Ce3+ Complexes with Encapsulating Polybenzimidazole Tripodal Ligands as Potential Electroluminescent Devices. *Angewandte Chemie International Edition* **2007**, *46* (39), 7399-7403.

(103) Ströh, J.; Ruiz Arana, L.; Polzin, P.; Eliani, I. V.; Lindenberg, P.; Heidenreich, N.; Cunha, C. d. S.; Leubner, S.; Terraschke, H. Real-time Probing the Formation of [M(2,2-bipyridine)2(NO3)3] (M = Ce, La, Tb) Complexes and Influence of Synthesis Parameters. *Zeitschrift für anorganische und allgemeine Chemie* **2019**, *645* (5), 537-543.

(104) Suta, M.; Harmgarth, N.; Kühling, M.; Liebing, P.; Edelmann, F. T.; Wickleder, C. Bright Photoluminescence of [{(Cp)2Ce(μ-Cl)}2]: A Valuable Technique for the Determination of the Oxidation State of Cerium. *Chemistry – An Asian Journal* **2018**, *13* (8), 1038-1044.

(105) Ilichev, V. A.; Silantyeva, L. I.; Grishin, I. D.; Rozhkov, A. V.; Rumyantcev, R. V.; Fukin, G. K.; Bochkarev, M. N. Cerium(iii) complexes with azolyl-substituted thiophenolate ligands: synthesis, structure and red luminescence. *RSC Advances* **2019**, *9* (42), 24110-24116.

(106) Fang, P.; Wang, L.; Zhan, G.; Yan, W.; Huo, P.; Ying, A.; Zhang, Y.; Zhao, Z.; Yu, G.; Huang, Y.; et al. Lanthanide Cerium(III) Tris(pyrazolyl)borate Complexes: Efficient Blue Emitters for Doublet Organic Light-Emitting Diodes. *ACS Applied Materials & Interfaces* **2021**, *13* (38), 45686-45695.

(107) Wang, L.; Fang, P.; Zhao, Z.; Huang, Y.; Liu, Z.; Bian, Z. Rare Earth Complexes with 5d–4f Transition: New Emitters in Organic Light-Emitting Diodes. *The Journal of Physical Chemistry Letters* **2022**, *13* (12), 2686-2694.

(108) Zhan, G.; Wang, L.; Zhao, Z.; Fang, P.; Bian, Z.; Liu, Z. Highly Efficient and Air-Stable Lanthanide EuII Complex: New Emitter in Organic Light Emitting Diodes. *Angewandte Chemie International Edition* **2020**, *59* (43), 19011-19015.

(109) Dang, S.; Yu, J.; Yu, J.; Wang, X.; Sun, L.; Feng, J.; Fan, W.; Zhang, H. Novel Holmium (Ho) and Praseodymium (Pr) ternary complexes with fluorinated-ligand and 4,5-diazafluoren-9-one. *Materials Letters* **2011**, *65* (11), 1642-1644.
(110) Zang, F. X.; Li, W. L.; Hong, Z. R.; Wei, H. Z.; Li, M. T.; Sun, X. Y.; Lee, C. S. Observation of 1.5 μm photoluminescence and electroluminescence from a holmium organic complex. *Applied Physics Letters* **2004**, *84* (25), 5115-5117.

(111) Monteiro, J. H. S. K. Recent Advances in Luminescence Imaging of Biological Systems Using Lanthanide(III) Luminescent Complexes. *Molecules* **2020**, *25* (9), 2089.

(112) Lower, S. K.; El-Sayed, M. A. The Triplet State and Molecular Electronic Processes in Organic Molecules. *Chemical Reviews* **1966**, *66* (2), 199-241.

(113) Bünzli, J.-C. G. On the design of highly luminescent lanthanide complexes. *Coordination Chemistry Reviews* **2015**, *293-294*, 19-47.

(114) Queiroz, E. C.; Franco, C. H. J.; Ferreira, M. S.; Freire, R. O.; Machado, F. C. Photoluminescent complexes of Eu(III), Tb(III) and Gd(III) with 3-thiopheneacetate and 4,4′-dimethyl-2,2′-bipyridine: Synthesis, characterization and photophysical properties. *Journal of Luminescence* **2022**, *249*, 118990.

(115) Klink, S. I.; Grave, L.; Reinhoudt, D. N.; van Veggel, F. C. J. M.; Werts, M. H. V.; Geurts, F. A. J.; Hofstraat, J. W. A Systematic Study of the Photophysical Processes in Polydentate Triphenylene-Functionalized Eu3+, Tb3+, Nd3+, Yb3+, and Er3+ Complexes. *The Journal of Physical Chemistry A* **2000**, *104* (23), 5457-5468.

(116) Yang, C.; Fu, L.-M.; Wang, Y.; Zhang, J.-P.; Wong, W.-T.; Ai, X.-C.; Qiao, Y.-F.; Zou, B.-S.; Gui, L.-L. A Highly Luminescent Europium Complex Showing Visible-Light-Sensitized Red Emission: Direct Observation of the Singlet Pathway. *Angewandte Chemie International Edition* **2004**, *43* (38), 5010-5013.

(117) Yan, H.; Wu, B.; Wei, J.; Zhang, W.-X. Insight into the Ligand-to-Ligand Charge-Transfer Process in Rare-Earth-Metal Diradical Complexes. *Inorganic Chemistry* **2023**, *62* (21), 8052-8057.

(118) Zhang, Z.; Zhou, Y.; Li, H.; Gao, T.; Yan, P. Visible light sensitized near-infrared luminescence of ytterbium via ILCT states in quadruple-stranded helicates. *Dalton Transactions* **2019**, *48* (12), 4026-4034.

(119) Tsaryuk, V. I.; Zhuravlev, K. P.; Gawryszewska, P. Processes of luminescence quenching in europium aromatic carboxylates with the participation of LMCT states: A brief review. *Coordination Chemistry Reviews* **2023**, *489*, 215206.

(120) Pasatoiu, T. D.; Madalan, A. M.; Kumke, M. U.; Tiseanu, C.; Andruh, M. Temperature Switch of LMCT Role: From Quenching to Sensitization of Europium Emission in a ZnII−EuIII Binuclear Complex. *Inorganic Chemistry* **2010**, *49* (5), 2310-2315.

(121) Faustino, W. M.; Malta, O. L.; de Sá, G. F. Intramolecular energy transfer through charge transfer state in lanthanide compounds: A theoretical approach. *The Journal of Chemical Physics* **2005**, *122* (5).

(122) Kovalenko, A.; Rublev, P. O.; Tcelykh, L. O.; Goloveshkin, A. S.; Lepnev, L. S.; Burlov, A. S.; Vashchenko, A. A.; Marciniak, Ł.; Magerramov, A. M.; Shikhaliyev, N. G.; et al. Lanthanide Complexes with 2-(Tosylamino)-benzylidene-N-(aryloyl)hydrazones: Universal Luminescent Materials. *Chemistry of Materials* **2019**, *31* (3), 759-773.

(123) Kovalenko, A. D.; Bushmarinov, I. S.; Burlov, A. S.; Lepnev, L. S.; Ilina, E. G.; Utochnikova, V. V. The peculiarities of complex formation and energy transfer processes in lanthanide complexes with 2-(tosylamino)-benzylidene-N-benzoylhydrazone. *Dalton Transactions* **2018**, *47* (13), 4524-4533.

(124) Pope, S. J.; Coe, B. J.; Faulkner, S.; Laye, R. H. Metal-to-ligand charge-transfer sensitisation of near-infrared emitting lanthanides in trimetallic arrays M2Ln (M=Ru, Re or Os; Ln=Nd, Er or Yb). *Dalton Transactions* **2005**, (8), 1482-1490.

(125) Zhang, L.-Y.; Hou, Y.-J.; Pan, M.; Chen, L.; Zhu, Y.-X.; Yin, S.-Y.; Shao, G.; Su, C.-Y. Near-infrared (NIR) emitting Nd/Yb(iii) complexes sensitized by MLCT states of Ru(ii)/Ir(iii) metalloligands in the visible light region. *Dalton Transactions* **2015**, *44* (34), 15212-15219.

(126) Imbert, D.; Cantuel, M.; Bünzli, J.-C. G.; Bernardinelli, G.; Piguet, C. Extending Lifetimes of Lanthanide-Based Near-Infrared Emitters (Nd, Yb) in the Millisecond Range through Cr(III) Sensitization in Discrete Bimetallic Edifices. *Journal of the American Chemical Society* **2003**, *125* (51), 15698-15699.

(127) Sun, G.; Xie, Y.; Wang, Y.; Mandl, G. A.; Maurizio, S. L.; Zhang, H.; Ottenwaelder, X.; Capobianco, J. A.; Sun, L. Cooperative Sensitization Upconversion in Solution Dispersions of Co-Crystal Assemblies of Mononuclear Yb3+ and Eu3+ Complexes. *Angewandte Chemie International Edition* **2023**, *62* (24), e202304591.

(128) Panguluri, S. P. K.; Jourdain, E.; Chakraborty, P.; Klyatskaya, S.; Kappes, M. M.; Nonat, A. M.; Charbonnière, L. J.; Ruben, M. Yb-to-Eu Cooperative Sensitization Upconversion in a Multifunctional Molecular Nonanuclear Lanthanide Cluster in Solution. *Journal of the American Chemical Society* **2024**, *146* (19), 13083-13092.

(129) An, B.-L.; Zhang, N.; Cheah, K.-W.; Pan, Q.-Y. High yield luminescence of a novel europium complex by excimer excitation and f–f absorption of Eu3+. *Journal of Alloys and Compounds* **2008**, *458* (1), 457-461.

(130) Sun, S.-S.; Wang, Z.; Wu, X. W.; Zhang, J.-H.; Li, C.-J.; Yin, S.-Y.; Chen, L.; Pan, M.; Su, C.-Y. ESIPT-Modulated Emission of Lanthanide Complexes: Different Energy-Transfer Pathways and Multiple Responses. *Chemistry – A European Journal* **2018**, *24* (40), 10091-10098.

(131) Zhu, Y.-X.; Wei, Z.-W.; Pan, M.; Wang, H.-P.; Zhang, J.-Y.; Su, C.-Y. A new TPE-based tetrapodal ligand and its Ln(iii) complexes: multi-stimuli responsive AIE (aggregation-induced emission)/ILCT(intraligand charge transfer)-bifunctional photoluminescence and NIR emission sensitization. *Dalton Transactions* **2016**, *45* (3), 943-950.

(132) Liu, Y.; Lyu, B.-H.; Du, S.-N.; Huang, G.-Z.; Ruan, Z.-Y.; Wu, S.-G.; Liu, J.-L.; Tong, M.-L. Tuning luminescence of didysprosium single-molecule magnets with a π-conjugated/non-conjugated bridging ligand. *Dalton Transactions* **2021**, *50* (20), 6778-6783.

(133) Brites, C. D. S.; Balabhadra, S.; Carlos, L. D. Lanthanide-Based Thermometers: At the Cutting-Edge of Luminescence Thermometry. *Advanced Optical Materials* **2019**, *7* (5), 1801239.

(134) Wang, J.; Zakrzewski, J. J.; Zychowicz, M.; Vieru, V.; Chibotaru, L. F.; Nakabayashi, K.; Chorazy, S.; Ohkoshi, S.-i. Holmium(iii) molecular nanomagnets for optical thermometry exploring the luminescence re-absorption effect. *Chemical Science* **2021**, *12* (2), 730-741.

(135) Zanella, S.; Aragon-Alberti, M.; Brite, C. D. S.; Salles, F.; Carlos, L. D.; Long, J. Luminescent Single-Molecule Magnets as Dual Magneto-Optical Molecular Thermometers. *Angewandte Chemie International Edition* **2023**, *62* (35), e202306970.

(136) Errulat, D.; Marin, R.; Gálico, D. A.; Harriman, K. L. M.; Pialat, A.; Gabidullin, B.; Iikawa, F.; Couto, O. D. D., Jr.; Moilanen, J. O.; Hemmer, E.; et al. A Luminescent Thermometer Exhibiting Slow Relaxation of the Magnetization: Toward Self-Monitored Building Blocks for Next-Generation Optomagnetic Devices. *ACS Central Science* **2019**, *5* (7), 1187-1198.

(137) Marin, R.; Gálico, D. A.; Gayfullina, R.; Moilanen, J. O.; Carlos, L. D.; Jaque, D.; Murugesu, M. A zero-field single-molecule magnet with luminescence thermometry capabilities containing soft donors. *Journal of Materials Chemistry C* **2022**, *10* (37), 13946-13953.

(138) Gütlich, P.; Garcia, Y.; Goodwin, H. A. Spin crossover phenomena in Fe(II) complexes. *Chemical Society Reviews* **2000**, *29* (6), 419-427.

(139) Funck, K. E.; Prosvirin, A. V.; Mathonière, C.; Clérac, R.; Dunbar, K. R. Light-Induced Excited Spin State Trapping and Charge Transfer in Trigonal Bipyramidal Cyanide-Bridged Complexes. *Inorganic Chemistry* **2011**, *50* (7), 2782-2789.

(140) Li, J.; Wu, S.; Su, S.; Kanegawa, S.; Sato, O. Manipulating Slow Magnetic Relaxation by Light in a Charge Transfer {Fe2Co} Complex. *Chemistry – A European Journal* **2020**, *26* (15), 3259-3263.

(141) Liao, P.-Y.; Liu, Y.; Ruan, Z.-Y.; Wang, H.-L.; Shi, C.-G.; Deng, W.; Wu, S.-G.; Jia, J.-H.; Tong, M.-L. Magnetic and Luminescent Dual Responses of Photochromic Hexaazamacrocyclic Lanthanide Complexes. *Inorganic Chemistry* **2023**, *62* (3), 1075-1085.

(142) Pinkowicz, D.; Ren, M.; Zheng, L.-M.; Sato, S.; Hasegawa, M.; Morimoto, M.; Irie, M.; Breedlove, B. K.; Cosquer, G.; Katoh, K.; et al. Control of the Single-Molecule Magnet Behavior of Lanthanide-Diarylethene Photochromic Assemblies by Irradiation with Light. *Chemistry – A European Journal* **2014**, *20* (39), 12502-12513.

(143) Lin, L.-R.; Tang, H.-H.; Wang, Y.-G.; Wang, X.; Fang, X.-M.; Ma, L.-H. Functionalized Lanthanide(III) Complexes Constructed from Azobenzene Derivative and β-Diketone Ligands: Luminescent, Magnetic, and Reversible Trans-to-Cis Photoisomerization Properties. *Inorganic Chemistry* **2017**, *56* (7), 3889-3900.

(144) Li, J.; Kong, M.; Yin, L.; Zhang, J.; Yu, F.; Ouyang, Z.-W.; Wang, Z.; Zhang, Y.-Q.; Song, Y. Photochemically Tuned Magnetic Properties in an Erbium(III)-Based Easy-Plane Single-Molecule Magnet. *Inorganic Chemistry* **2019**, *58* (21), 14440-14448.

(145) Wu, L.; Huang, X.-D.; Li, W.; Cao, X.; Fang, W.-H.; Zheng, L.-M.; Dolg, M.; Chen, X. Lanthanide-Dependent Photochemical and Photophysical Properties of Lanthanide–Anthracene Complexes: Experimental and Theoretical Approaches. *JACS Au* **2024**, *4* (9), 3606-3618.

(146) Wu, J.; Zhu, Z.; Tang, J. Recent advancements of photo-responsive lanthanide single-molecule magnets. *Chinese Chemical Letters* **2024**, 110577.

(147) Ferreira, R. A. S.; Mamontova, E.; Botas, A. M. P.; Shestakov, M.; Vanacken, J.; Moshchalkov, V.; Guari, Y.; Chibotaru, L. F.; Luneau, D.; André, P. S.; et al. Synchronous Temperature and Magnetic Field Dual-Sensing by Luminescence in a Dysprosium Single-Molecule Magnet. *Advanced Optical Materials* **2021**, *9* (24), 2101495.

(148) Sun, G.-B.; Huang, X.-D.; Shang, T.; Yan, S.; Bao, S.-S.; Lu, X.-M.; Zhang, Y.-Q.; Zheng, L.-M. Polar Lanthanide Anthracene Complexes Exhibiting Magnetic, Luminescent and Dielectric Properties. *European Journal of Inorganic Chemistry* **2021**, *2021* (40), 4207-4215.

(149) Pointillart, F.; Atzori, M.; Train, C. Magneto-chiral dichroism of chiral lanthanide complexes. *Inorganic Chemistry Frontiers* **2024**, *11* (5), 1313-1321.

(150) Lefeuvre, B.; Mattei, C. A.; Gonzalez, J. F.; Gendron, F.; Dorcet, V.; Riobé, F.; Lalli, C.; Le Guennic, B.; Cador, O.; Maury, O.; et al. Solid-State Near-Infrared Circularly Polarized Luminescence from Chiral YbIII-Single-Molecule Magnet. *Chemistry – A European Journal* **2021**, *27* (26), 7362-7366.

(151) Liu, J.-L.; Chen, Y.-C.; Zheng, Y.-Z.; Lin, W.-Q.; Ungur, L.; Wernsdorfer, W.; Chibotaru, L. F.; Tong, M.-L. Switching the anisotropy barrier of a single-ion magnet by symmetry change from quasi-D5h to quasi-Oh. *Chemical Science* **2013**, *4* (8), 3310-3316.

(152) Sun, W.-B.; Yan, P.-F.; Jiang, S.-D.; Wang, B.-W.; Zhang, Y.-Q.; Li, H.-F.; Chen, P.; Wang, Z.-M.; Gao, S. High symmetry or low symmetry, that is the question – high performance Dy(iii) single-ion magnets by electrostatic potential design. *Chemical Science* **2016**, *7* (1), 684-691.

(153) Watanabe, A.; Yamashita, A.; Nakano, M.; Yamamura, T.; Kajiwara, T. Multi-Path Magnetic Relaxation of Mono-Dysprosium(III) Single-Molecule Magnet with Extremely High Barrier. *Chemistry – A European Journal* **2011**, *17* (27), 7428-7432.

(154) Liu, J.-L.; Wu, J.-Y.; Huang, G.-Z.; Chen, Y.-C.; Jia, J.-H.; Ungur, L.; Chibotaru, L. F.; Chen, X.-M.; Tong, M.-L. Desolvation-Driven 100-Fold Slow-down of Tunneling Relaxation Rate in Co(II)-Dy(III) Single-Molecule Magnets through a Single-Crystal-to-Single-Crystal Process. *Scientific Reports* **2015**, *5* (1), 16621.

(155) Wu, S.-G.; Ruan, Z.-Y.; Zheng, J.-Y.; Huang, G.-Z.; Vieru, V.; Chen, Y.-C.; Ho, L. T. A.; Liu, J.-L.; Chibotaru, L. F.; Tong, M.-L. Rectangle-like Hysteresis in a Dysprosium Metallacrown Magnet with Linear F-Dy-F Anisotropic Moiety. 2021, arXiv:2105.09586. https://doi.org/10.48550.arXiv.2105.09586.

(156) Wu, S.-G.; Ruan, Z.-Y.; Huang, G.-Z.; Zheng, J.-Y.; Vieru, V.; Taran, G.; Wang, J.; Chen, Y.-C.; Liu, J.-L.; Ho, L. T. A.; Chibotaru, L. F.; Wernsdorfer, W.; Chen, X.-M.; Tong, M.-L., Field-induced oscillation of magnetization blocking barrier in a holmium metallacrown single-molecule magnet. *Chem* **2021,** *7* (4), 982-992.

(157) Xiong, K.; Wang, X.; Jiang, F.; Gai, Y.; Xu, W.; Su, K.; Li, X.; Yuan, D.; Hong, M., Heterometallic thiacalix[4]arene-supported Na2NiII12LnIII2 clusters with vertex-fused tricubane cores (Ln = Dy and Tb). *Chemical Communications* **2012,** *48* (60), 7456-7458.

(158) Bhunia, A.; Yadav, M.; Lan, Y.; Powell, A. K.; Menges, F.; Riehn, C.; Niedner-Schatteburg, G.; Jana, P. P.; Riedel, R.; Harms, K.; Dehnen, S.; Roesky, P. W., Trinuclear nickel–lanthanide compounds. *Dalton Transactions* **2013,** *42* (7), 2445-2450.

(159) Jiang, L.; Liu, Y.; Liu, X.; Tian, J.; Yan, S., Three series of heterometallic NiII–LnIII Schiff base complexes: synthesis, crystal structures and magnetic characterization. *Dalton Transactions* **2017,** *46* (37), 12558-12573.

(160) Moreno Pineda, E.; Chilton, N. F.; Tuna, F.; Winpenny, R. E. P.; McInnes, E. J. L., Systematic Study of a Family of Butterfly-Like {M2Ln2} Molecular Magnets (M = MgII, MnIII, CoII, NiII, and CuII; Ln = YIII, GdIII, TbIII, DyIII, HoIII, and ErIII). *Inorganic Chemistry* **2015,** *54* (12), 5930-5941.

(161) Chakraborty, A.; Bag, P.; Rivière, E.; Mallah, T.; Chandrasekhar, V., Assembly of heterobimetallic NiII–LnIII (LnIII = DyIII, TbIII, GdIII, HoIII, ErIII, YIII) complexes using a ferrocene ligand: slow relaxation of the magnetization in DyIII, TbIII and HoIII analogues. *Dalton Transactions* **2014,** *43* (23), 8921-8932.

(162) Bhunia, A.; Gamer, M. T.; Ungur, L.; Chibotaru, L. F.; Powell, A. K.; Lan, Y.; Roesky, P. W.; Menges, F.; Riehn, C.; Niedner-Schatteburg, G., From a Dy(III) Single Molecule Magnet (SMM) to a Ferromagnetic [Mn(II)Dy(III)Mn(II)] Trinuclear Complex. *Inorganic Chemistry* **2012,** *51* (18), 9589-9597.

(163) Vieru, V.; Pasatoiu, T. D.; Ungur, L.; Suturina, E.; Madalan, A. M.; Duhayon, C.; Sutter, J.-P.; Andruh, M.; Chibotaru, L. F. Synthesis, Crystal Structures, Magnetic Properties, and Theoretical Investigation of a New Series of NiII–LnIII–WV Heterotrimetallics: Understanding the SMM Behavior of Mixed Polynuclear Complexes. *Inorganic Chemistry* **2016**, *55* (23), 12158-12171.

(164) Konieczny, P.; Pełka, R.; Masuda, Y.; Sakata, S.; Kayahara, S.; Irie, N.; Kajiwara, T.; Baran, S. a. Anisotropy of Spin–Lattice Relaxations in Mononuclear Tb3+ Single-Molecule Magnets. *The Journal of Physical Chemistry C* **2020**, *124* (14), 7930-7937.

(165) Masuda, Y.; Sakata, S.; Kayahara, S.; Irie, N.; Kofu, M.; Kono, Y.; Sakakibara, T.; Horii, Y.; Kajiwara, T., Slow Magnetic Relaxation of Linear Trinuclear M(II)–Gd(III)–M(II) Complexes with D3 Point Group Symmetry (M(II) = Zn(II) and Mg(II)). *The Journal of Physical Chemistry C* **2023,** *127* (6), 3295-3306.

(166) Chandrasekhar, V.; Pandian, B. M.; Vittal, J. J.; Clérac, R., Synthesis, Structure, and Magnetism of Heterobimetallic Trinuclear Complexes {[L2Co2Ln][X]} [Ln = Eu, X = Cl; Ln = Tb, Dy, Ho, X = NO3; LH3 = (S)P[N(Me)N═CH−C6H3-2-OH-3-OMe]3]: A 3d−4f Family of Single-Molecule Magnets. *Inorganic Chemistry* **2009,** *48* (3), 1148-1157.

(167) Costes, J.-P.; Yamaguchi, T.; Kojima, M.; Vendier, L., Experimental Evidence for the Participation of 5d GdIII Orbitals in the Magnetic Interaction in Ni−Gd Complexes. *Inorganic Chemistry* **2009,** *48* (12), 5555-5561.

(168) Yao, M.-X.; Zhu, Z.-X.; Lu, X.-Y.; Deng, X.-W.; Jing, S., Rare single-molecule magnets with six-coordinate LnIII ions exhibiting a trigonal antiprism configuration. *Dalton Transactions* **2016,** *45* (26), 10689-10695.

(169) Simon, J.; Horstmann née Gruschka, C.; Mix, A.; Stammler, A.; Oldengott, J.; Bögge, H.; Glaser, T., Evaluation of the binding mode of a cytotoxic dinuclear nickel complex to two neighboring phosphates of the DNA backbone. *Dalton Transactions* **2022,** *51* (7), 2863-2875.

(170) Sasmal, S.; Hazra, S.; Kundu, P.; Dutta, S.; Rajaraman, G.; Sañudo, E. C.; Mohanta, S., Magnetic Exchange Interactions and Magneto-Structural Correlations in Heterobridged μ-Phenoxo-μ1,1-Azide Dinickel(II) Compounds: A Combined Experimental and Theoretical Exploration. *Inorganic Chemistry* **2011,** *50* (15), 7257-7267.

(171) Kahn, O. *Molecular Magnetism*; Dover Publications, 2021.

(172) Borah, A.; Murugavel, R. Magnetic relaxation in single-ion magnets formed by less-studied lanthanide ions Ce(III), Nd(III), Gd(III), Ho(III), Tm(II/III) and Yb(III). *Coordination Chemistry Reviews* **2022**, *453*, 214288.

(173) Lin, P.-H.; Burchell, T. J.; Ungur, L.; Chibotaru, L. F.; Wernsdorfer, W.; Murugesu, M., A Polynuclear Lanthanide Single-Molecule Magnet with a Record Anisotropic Barrier. *Angewandte Chemie International Edition* **2009,** *48* (50), 9489-9492.

(174) Li, Y.; Shang, Q.; Zhang, Y.-Q.; Yang, E.-C.; Zhao, X.-J. Fine Tuning of the Anisotropy Barrier by Ligand Substitution Observed in Linear {Dy2Ni2} Clusters. *Chemistry – A European Journal* **2016**, *22* (52), 18840-18849.

(175) Mondal, K. C.; Kostakis, G. E.; Lan, Y.; Wernsdorfer, W.; Anson, C. E.; Powell, A. K. Defect-Dicubane Ni2Ln2 (Ln = Dy, Tb) Single Molecule Magnets. *Inorganic Chemistry* **2011**, *50* (22), 11604-11611.

(176) Zhao, L.; Wu, J.; Ke, H.; Tang, J. Family of Defect-Dicubane Ni4Ln2 (Ln = Gd, Tb, Dy, Ho) and Ni4Y2 Complexes: Rare Tb(III) and Ho(III) Examples Showing SMM Behavior. *Inorganic Chemistry* **2014**, *53* (7), 3519-3525.

(177) Colacio, E.; Ruiz, J.; Ruiz, E.; Cremades, E.; Krzystek, J.; Carretta, S.; Cano, J.; Guidi, T.; Wernsdorfer, W.; Brechin, E. K., Slow Magnetic Relaxation in a CoII–YIII Single-Ion Magnet with Positive Axial Zero-Field Splitting. *Angewandte Chemie International Edition* **2013,** *52* (35), 9130-9134.

(178) Ruan, Z.-Y.; Lai, J.-J.; Li, J.-X.; Zhao, X.-J.; Huang, G.-Z.; Wu, S.-G.; Liu, J.-L.; Tong, M.-L., Deciphering the Enigma of a Temperature-Dependent Best-Performance Field in Single-Molecule Magnets *The Journal of Physical Chemistry C* **2023,** *127* (29), 14450-14457.

(179) Meihaus, K. R.; Rinehart, J. D.; Long, J. R., Dilution-Induced Slow Magnetic Relaxation and Anomalous Hysteresis in Trigonal Prismatic Dysprosium(III) and Uranium(III) Complexes. *Inorganic Chemistry* **2011,** *50* (17), 8484-8489.

(180) Baniodeh, A.; Mereacre, V.; Magnani, N.; Lan, Y.; Wolny, J. A.; Schünemann, V.; Anson, C. E.; Powell, A. K., Para versus meta ligand substituents as a means of directing magnetic anisotropy in Fe2Dy2 coordination clusters. *Chemical Communication* **2013,** *49* (83), 9666-9668.

(181) Mereacre, V.; Klöwer, F.; Lan, Y.; Clérac, R.; Wolny, J. A.; Schünemann, V.; Anson, C. E.; Powell, A. K. Spin relaxation in antiferromagnetic Fe–Fe dimers slowed down by anisotropic DyIII ions. *Beilstein Journal of Nanotechnology* **2013**, *4*, 807-814.

(182) Zhao, F.-H.; Li, H.; Che, Y.-X.; Zheng, J.-M.; Vieru, V.; Chibotaru, L. F.; Grandjean, F.; Long, G. J. Synthesis, Structure, and Magnetic Properties of Dy2Co2L10(bipy)2 and Ln2Ni2L10(bipy)2, Ln = La, Gd, Tb, Dy, and Ho: Slow Magnetic Relaxation in Dy2Co2L10(bipy)2 and Dy2Ni2L10(bipy)2. *Inorganic Chemistry* **2014**, *53* (18), 9785-9799.

(183) Zou, H.-H.; Sheng, L.-B.; Liang, F.-P.; Chen, Z.-L.; Zhang, Y.-Q. Experimental and theoretical investigations of four 3d–4f butterfly single-molecule magnets. *Dalton Transactions* **2015**, *44* (42), 18544-18552.

(184) Chandrasekhar, V.; Bag, P.; Kroener, W.; Gieb, K.; Müller, P. Pentanuclear Heterometallic {Ni2Ln3} (Ln = Gd, Dy, Tb, Ho) Assemblies. Single-Molecule Magnet Behavior and Multistep Relaxation in the Dysprosium Derivative. *Inorganic Chemistry* **2013**, *52* (22), 13078-13086.

(185) Yu, S.; Hu, H.; Zou, H.-H.; Liu, D.; Liang, Y.; Liang, F.-P.; Chen, Z. Two Heterometallic Nanoclusters [DyIII4NiII8] and [DyIII10MnIII4MnII2]: Structure, Assembly Mechanism, and Magnetic Properties. *Inorganic Chemistry* **2022**, *61* (8), 3655-3663.

(186) Kuppusamy, S. K.; Vasilenko, E.; Li, W.; Hessenauer, J.; Ioannou, C.; Fuhr, O.; Hunger, D.; Ruben, M. Observation of Narrow Optical Homogeneous Linewidth and Long Nuclear Spin Lifetimes in a Prototypical [Eu(trensal)] Complex. *The Journal of Physical Chemistry C* **2023**, *127* (22), 10670-10679.

(187) Hill, C. O.; Lin, S. H. Quenching of Phosphorescence by Paramagnetic Molecules in Rigid Media. II. Quenching of Perdeuderated Naphthalene by Co++, Cr3+, Cu++, and Ni++. *The Journal of Chemical Physics* **1970**, *53* (2), 608-612.

(188) Cook, D. F.; Cummins, D.; McKenzie, E. D. Metal(III) compounds of potentially septadentate[N4O3] ligands derived from tris(2-aminoethyl)amine and substituted salicylaldehydes. Part I. Preparation of gallium, chromium, manganese, iron, and cobalt compounds, and the crystal and molecular structure of the iron compound of tris[2-(5-chloro-2-hydroxybenzylidene)ethyl]amine, [Fe(C27H24Cl3N4O3)]·3H2O. *Journal of the Chemical Society, Dalton Transactions* **1976**, (14), 1369-1375.

(189) Chen, L.; Zhou, J.; Yuan, A.; Song, Y. Slow magnetic relaxation in luminescent mononuclear dysprosium(III) and erbium(III) pentanitrate complexes with the same LnO_{10} coordination geometry. *Dalton Transactions* **2017,** *46*, 15812.

(190) Shrivastava, K. N. Theory of Spin–Lattice Relaxation. *physica status solidi (b)* **1983**, *117* (2), 437-458.

(191) Cuza, E.; Mekuimemba, C. D.; Cosquer, N.; Conan, F.; Pillet, S.; Chastanet, G.; Triki, S. Spin Crossover and High-Spin State in Fe(II) Anionic Polymorphs Based on Tripodal Ligands. *Inorganic Chemistry* **2021**, *60* (9), 6536-6549.

(192) Yamasaki, M.; Ishida, T. Spin-crossover thermal hysteresis and light-induced effect on iron(II) complexes with tripodal tris(2-pyridyl)methanol. *Polyhedron* **2015**, *85*, 795-799.

(193) Latva, M.; Takalo, H.; Mukkala, V.-M.; Matachescu, C.; Rodríguez-Ubis, J. C.; Kankare, J. Correlation between the lowest triplet state energy level of the ligand and lanthanide(III) luminescence quantum yield. *Journal of Luminescence* **1997**, *75* (2), 149-169.

(194) Yang, X.; Jones, R. A.; Wu, Q.; Oye, M. M.; Lo, W.-K.; Wong, W.-K.; Holmes, A. L. Synthesis, crystal structures and antenna-like sensitization of visible and near infrared emission in heterobimetallic Zn–Eu and Zn–Nd Schiff base compounds. *Polyhedron* **2006**, *25* (2), 271-278.

(195) Gouré, E.; Gerey, B.; Molton, F.; Pécaut, J.; Clérac, R.; Thomas, F.; Fortage, J.; Collomb, M.-N. Seven Reversible Redox Processes in a Self-Assembled Cobalt Pentanuclear Bis(triple-stranded helicate): Structural, Spectroscopic, and Magnetic Characterizations in the CoICoII4, CoII5, and CoII3CoIII2 Redox States. *Inorganic Chemistry* **2020**, *59* (13), 9196-9205.

(196) Hong, D.; Ohgomori, Y.; Shimoyama, Y.; Kotani, H.; Ishizuka, T.; Kon, Y.; Kojima, T. Mechanistic Insight into Synergistic Catalysis of Olefin Hydrogenation by a Hetero-Dinuclear RuII–CoII Complex with Adjacent Reaction Sites. *Inorganic Chemistry* **2019**, *58* (17), 11284-11288.

(197) Mognon, L.; Benet-Buchholz, J.; Rahaman, S. M. W.; Bo, C.; Llobet, A. Ru–Zn Heteropolynuclear Complexes Containing a Dinucleating Bridging Ligand: Synthesis, Structure, and Isomerism. *Inorganic Chemistry* **2014**, *53* (23), 12407-12415.

(198) Nakano, K.; Kawata, S.; Yoneda, K.; Fuyuhiro, A.; Yagi, T.; Nasu, S.; Morimoto, S.; Kaizaki, S. Direct two-step spin-crossover through [HS–HS]···[LS–LS] at the plateau in dinuclear diiron(ii) complex [{Fe(NCBH3)(4phpy)}2(μ-bpypz)2]. *Chemical Communications* **2004**, (24), 2892-2893.

(199) Su, N.; Lu, G.-Z.; Zheng, Y.-X. Highly efficient green electroluminescence of iridium(iii) complexes based on (1H-pyrazol-5-yl)pyridine derivatives ancillary ligands with low efficiency roll-off. *Journal of Materials Chemistry C* **2018**, *6* (21), 5778-5784.

(200) Yu, W.-S.; Cheng, C.-C.; Cheng, Y.-M.; Wu, P.-C.; Song, Y.-H.; Chi, Y.; Chou, P.-T. Excited-State Intramolecular Proton Transfer in Five-Membered Hydrogen-Bonding Systems: 2-Pyridyl Pyrazoles. *Journal of the American Chemical Society* **2003**, *125* (36), 10800-10801.

(201) Jansa, J.; Schmidt, R.; Mamuye, A. D.; Castoldi, L.; Roller, A.; Pace, V.; Holzer, W., Synthesis of tetrasubstituted pyrazoles containing pyridinyl substituents. *Beilstein Journal of Organic Chemistry* **2017,** *13*, 895-902.

(202) George, M. R.; Critchley, P. E.; Whitehead, G. F. S.; Bailey, A. J.; Cuda, F.; Murdin, B. N.; Grossel, M. C.; Curry, R. J. Modified pyridine-2,6-dicarboxylate acid ligands for sensitization of near-infrared luminescence from lanthanide ions (Ln3+ = Pr3+, Nd3+, Gd3+, Dy3+, Er3+). *Journal of Luminescence* **2021**, *230*, 117715.

(203) Lin, P.-H.; Burchell, T. J.; Ungur, L.; Chibotaru, L. F.; Wernsdorfer, W.; Murugesu, M., A Polynuclear Lanthanide Single-Molecule Magnet with a Record Anisotropic Barrier. *Angewandte Chemie International Edition* **2009,** *48* (50), 9489-9492.

(204) Guo, P.-H.; Liu, J.-L.; Zhang, Z.-M.; Ungur, L.; Chibotaru, L. F.; Leng, J.-D.; Guo, F.-S.; Tong, M.-L., The First {Dy4} Single-Molecule Magnet with a Toroidal Magnetic Moment in the Ground State. *Inorg. Chem.* **2012,** *51* (3), 1233-1235.

(205) Mandal, S.; Ghosh, S.; Takahashi, D.; Christou, G.; Mohanta, S. Single-Crystal to Single-Crystal Transformations and Magnetic Properties of a Series of "Butterfly" NiII2LnIII2 Compounds: SMM Behavior of the Dysprosium(III) Analogue. *European Journal of Inorganic Chemistry* **2018**, *2018* (24), 2793-2804.

Acknowledgements

First of all, I would like to express my deepest gratitude to my supervisor Prof. Mario Ruben for providing me the chance to join his research group as a PhD student. He is always willing to offer me assistance whenever I need it. His knowledge and scientific thoughts are insightful, up-to-date and inspiring. I am deeply grateful for being able to learn from such an esteemed scholar.

I would also like to thank Dr. Senthil Kuppusamy who provides me essential guidance, in particular, the training for optical measurements and scientific writing. I wish to thank Dr. Svetlana Klyatskaya as well, for her support in creating a convenient and vibrant working environment in the research group. I thank Dr. Nithin Suryadevara and Dr. Jo Komeda for being super friendly officemates with me. I am also profoundly grateful to all my colleagues in the Ruben group. They are always very open for academic exchanges and very helpful to others.

I extend my appreciation to my collaborators for providing invaluable assistance. I would like to thank Dr. Eufemio Moreno-Pineda particularly for helping me with the Micro-SQUID experiments and for sharing with me knowledge on molecular magnetism. I am also grateful to Dr. Olaf Fuhr and Prof. Dieter Fenske for their help on SC-XRD measurements and crystal structure refinements.

At last, my sincere thanks go to my parents and my friends for their unwavering love and support. Their trust and confidence never cease to encourage me throughout my academic journey.